

© Copyright 2007

Kenneth R. Hawkins



Designing the Diffusion Immunoassay (DIA) --  
How Properties of the Analyte Affect DIA Performance

Kenneth R. Hawkins

A dissertation  
submitted in partial fulfillment of the  
requirements for the degree of

Doctor of Philosophy

University of Washington

2007

Program Authorized to Offer Degree:  
Bioengineering

UMI Number: 3252863

Copyright 2007 by  
Hawkins, Kenneth R.

All rights reserved.

### INFORMATION TO USERS

The quality of this reproduction is dependent upon the quality of the copy submitted. Broken or indistinct print, colored or poor quality illustrations and photographs, print bleed-through, substandard margins, and improper alignment can adversely affect reproduction.

In the unlikely event that the author did not send a complete manuscript and there are missing pages, these will be noted. Also, if unauthorized copyright material had to be removed, a note will indicate the deletion.

**UMI**<sup>®</sup>

---

UMI Microform 3252863

Copyright 2007 by ProQuest Information and Learning Company.

All rights reserved. This microform edition is protected against  
unauthorized copying under Title 17, United States Code.

ProQuest Information and Learning Company  
300 North Zeeb Road  
P.O. Box 1346  
Ann Arbor, MI 48106-1346

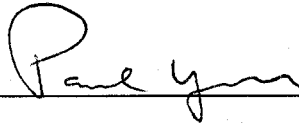
University of Washington  
Graduate School

This is to certify that I have examined this copy of a doctoral dissertation by

Kenneth R. Hawkins

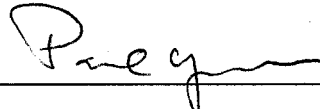
and have found that it is complete and satisfactory in all respects,  
and that any and all revisions required by the final  
examining committee have been made.

Chair of the Supervisory Committee:



Paul Yager

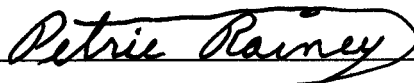
Reading Committee:



Paul Yager



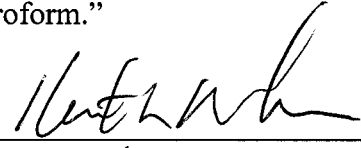
Michael Regnier



Petrie Rainey

Date: 3/14/2007

In presenting this dissertation in partial fulfillment of the requirements for the doctoral degree at the University of Washington, I agree that the Library shall make copies freely available for inspection. I further agree that extensive copying of the dissertation is allowable only for scholarly purposes, consistent with "fair use" as prescribed in the U.S. Copyright Law. Request for copying or reproduction of this dissertation may be referred to ProQuest Information and Learning, 300 North Zeeb Road, Ann Arbor, MI 48106-1346, 1-800-521-0600, to whom the author has granted "the right to reproduce and sell (a) copies of the manuscript in microform and/or (b) printed copies of the manuscript made from microform."

Signature   
Date 3/14/2007

University of Washington

**Abstract**

Designing the Diffusion Immunoassay (DIA) --  
How Properties of the Analyte Affect DIA Performance

Kenneth R. Hawkins

Chair of the Supervisory Committee  
Professor Paul Yager  
Bioengineering

The diffusion immunoassay (DIA) is a novel assay technique based on the difference in diffusivity of an analyte molecule when free in solution, versus when it is bound to a cognate antibody. It is uniquely enabled by the laminar flow conditions found in microfluidic devices, making it an exciting new candidate for a miniaturized clinical assay platform – the kind of platform that is envisioned as enabling technology for delivery of disease diagnosis at the point-of-care.

The DIA principle was originally evinced with the assay of a small molecule – *phenytoin*.<sup>1</sup> Extension of the principle to larger analytes is not trivial, yet larger analytes represent an important class of analytes in the clinic. Larger analytes diffuse more slowly, both in translation (which affects the transport of analyte mass between adjacent flow streams) and rotationally (which affects the association rate of the analyte with its cognate antibody). It seemed obvious that both transport and reaction differences would change the behavior of the DIA, but it was not obvious how, or by how much. A quantitative understanding of the effects of transport and reaction (as well as other important design variables) on the DIA enables intelligent design of a DIA for any analyte through the formulation of power law relationships and design rules. This dissertation identifies the key parameters in the DIA design space, characterizes improvements (leading to a second generation DIA), quantifies the power law relationships between design parameters and important metrics of

performance, and illustrates the conclusions with a second generation DIA for a clinically significant analyte, *C-reactive protein*.



## TABLE OF CONTENTS

	Page
List of Figures .....	iii
List of Tables.....	v
Chapter 1: Prelude.....	1
1.1: Executive Summary .....	1
1.2: Introduction.....	9
1.3: Summary of Thesis .....	10
1.4: Significance.....	11
1.5: Scope.....	12
1.6: Limitations .....	13
1.7: Additional Comments .....	14
Chapter 2: Microfluidic Immunoassay and the DIA.....	15
2.1: General Assay Design Principles.....	15
2.2: The Diffusion Immunoassay (DIA).....	16
2.3: Comparison of the DIA with Other Microscale Assays .....	42
2.4: Anticipated Challenges for a POC Protein DIA .....	49
Chapter 3: Preliminary Work –	
The Germinal DIA for Two Model Proteins Analytes .....	58
3.1: HRP – Challenging the System.....	58
3.2: IgG – An Expectation of Failure.....	64
3.3: Summary of Preliminary Work.....	72
Chapter 4: Improvements to the Germinal DIA Procedure .....	73
4.1: Improvements to the Quality of DIA Raw Data .....	74
4.2: Modification of Data Analysis.....	120
4.3: Biochemical Modification of Capture Species .....	149
Chapter 5: Exploring the Limits of the DIA with Modeling.....	159
5.1: Dimensional Analysis .....	159
5.2: Numerical Simulation .....	166
5.3: Noise Simulations .....	179
5.4: Model Validation .....	185
5.5: Summary of Modeling .....	189
Chapter 6: The DIA for C-Reactive Protein .....	190
6.1: Clinical Relevance of CRP .....	190
6.2: Performing the CRP DIA.....	192
6.3: Summary.....	201
Chapter 7: Limits, Design Rules and Closure.....	202
7.1: Defining the Molecular Weight Limits.....	202
7.2: Design Rules .....	205
7.3: Closure .....	206

References ..... 208

## LIST OF FIGURES

Figure Number	Page
2.1	General Immunoassay Block Diagram ..... 16
2.2	DIA in a T-sensor..... 18
2.3	Schematic Cartoons of the DIA Principle..... 20
2.4	Results of the DIA for Phenytoin..... 27
2.5	Block Diagram Specific to the DIA ..... 32
3.1	Results for the Germinal DIA for HRP..... 63
3.2	Results for the Germinal DIA for IgG ..... 68
3.3	4PLL Curve Fit for the IgG DIA..... 69
3.4	Aggregation in the IgG DIA ..... 70
4.1	Decrease in Autofluorescence Over Time ..... 77
4.2	Normalized Initial Intensity ..... 80
4.3	Slopes of Decay Curves ..... 84
4.4	Adsorption Chromatography Channel ..... 88
4.5	Adsorption Chromatography Set-Up ..... 89
4.6	Chromatograms for Four Analytes..... 94
4.7	BSA Control Chromatograms..... 95
4.8	Revised Channel and Its Effect..... 103
4.9	T-sensor Used for SATW Studies..... 108
4.10	Five-layer SATW Device..... 109
4.11	Results of Early Attempts at SATW ..... 113
4.12	Effects of Jig Roughness..... 114
4.13	Effects of Applied Pressure..... 116
4.14	Effects of Platen Temperature..... 118
4.15	Comparison of Smoothers..... 126
4.16	Improvement in HRP DIA Results ..... 127
4.17	4PLL Curve Fit for HRP DIA..... 128
4.18	Transformed DIA Responses ..... 133
4.19	Fourier Transformed DIA Responses ..... 137
4.20	Regression Segregates Sources of Variation..... 139
4.21	Efficacy of PLS Calibration ..... 142
4.22	Predictions of the HRP Dose Response ..... 143
4.23	Simulations of the HRP DIA at high [Ag]..... 144
4.24	HRP DIA Simulations with Revised Algorithm ..... 146
4.25	Application of the Internal Diffusion Standard..... 147
4.26	DIA with Capture Microspheres ..... 152
4.27	DIA with Decreased Capture Diffusivity..... 155
4.28	DIA with Antibody/Dextran Conjugates ..... 157
5.1	Effects of $\tau k_{\text{off}}$ ..... 167
5.2	Effects of $\tau k_{\text{on}}[\text{Ag}^*]$ ..... 171

5.3	Effects of $D_{Ag^*}/D_{Ab}$ .....	173
5.4	Effects of $[Ab]/[Ag]$ .....	175
5.5	Effect of $D_{Ab}/D_{AbAg^*}$ .....	176
5.6	Design for Study of Noise Sources .....	181
5.7	Variation of a Middling Signal .....	182
5.8	Variation of a Vanishing Signal .....	183
5.9	Variation of a Moderately High Signal .....	184
5.10	Observed vs. Predicted Accumulations for the CRP DIA .....	187
5.11	Observed vs. Predicted Responses for the CRP DIA .....	188
5.12	Observed vs. Predicted Initial Slopes for the CRP DIA .....	189
6.1	Ribbon Diagram of CRP .....	191
6.2	Observed vs. Predicted Blank with Noise for CRP DIA .....	197
6.3	Figures of Merit for the CRP DIA .....	200

## LIST OF TABLES

Table Number		Page
2.1	Key Parameters for the Protein DIA .....	50
4.1	Polymer Films Surveyed for Autofluorescence .....	75
4.2	Quantitative Analysis of Autofluorescence Curves .....	79
4.3	Fraction of Analyte Eluted.....	96
5.1	Dimensional Variables in the DIA .....	163
5.2	Dimensionless Groupings in the DIA .....	165
5.3	Values of Dimensionless Groups Investigated .....	169
6.1	Reference Methods for CRP .....	192
6.2	CRP DIA Formulations Investigated .....	193

## ACKNOWLEDGEMENTS

I would like to acknowledge the guidance and patience of my advisor, Professor Paul Yager, over the many years it took to complete the research for this dissertation. We did not always agree, but the discussions were always stimulating and brought the work into focus. I would also like to recognize my supervisory committee: Professors Lloyd Burgess, Albert Folch, Mehran Mesbahi, Michael Regnier, and Petrie Rainey for making this dissertation much more relevant. I should have used your expertise more than I did.

My colleagues in the Yager Laboratory have been a resource and a diversion over the course of this research, and I owe them *all* a huge debt. I would like to single out a few, however, for individual recognition. Dr. Andrew Kamholz, Dr. Anson Hatch, Hugh Chang, Dr. Matt Munson, Jennifer Foley, Kristen Helton, Mark Steedman, Richard Baldwin, and Dr. Elain Fu have all made significant contributions to my thinking about the content of this dissertation.

Graduate school would not have even been a possibility if it were not for the financial and emotion support of my wonderful wife, Linda Hawkins. Special thanks to my daughters, Emma and Honor, for encouraging their atypical father in his pursuit of his goals. Now maybe I will “get a real job” and be able to give and do all those things we have missed during this time.

This research was funded by NIH grant 1 R01 RR 15309-01A1.

## Chapter 1: Prelude

### *1.1. Executive Summary*

The diffusion immunoassay (DIA) is a novel assay technique based on the difference in diffusivity of an analyte molecule when free in solution, versus when it is bound to a cognate antibody. It is uniquely enabled by the laminar flow conditions found in microfluidic devices, making it an exciting new candidate for a miniaturized clinical assay platform – the kind of platform that is envisioned as enabling technology for delivery of disease diagnosis at the point-of-care. This dissertation identifies the key parameters in the DIA design space, characterizes improvements, quantifies the power law relationships between design parameters and important metrics of performance, and illustrates the conclusions with a second generation DIA for a clinically significant analyte, *C reactive protein*.

#### **1.1.1: Background and Significance**

The DIA principle was evinced with the assay of a small molecule – *phenytoin*.<sup>1</sup> Extension of the principle to larger analytes is not trivial, yet larger analytes represent an important class of analytes in the clinic. Larger analytes diffuse more slowly, both in translation (which affects the transport of analyte mass between adjacent flow streams) and rotationally (which affects the association rate of the analyte with its cognate antibody). It seemed obvious that both transport and reaction differences would change the behavior of the DIA, but it was not obvious how, or by how much.

A quantitative understanding of the effects of transport and reaction (as well as other important design variables) on the DIA, enables intelligent design of a DIA for any analyte through the formulation of power law relationships and design rules. Such an understanding also facilitates identification of improvements to the assay protocol,

leading to a second generation DIA. These are the accomplishments of this dissertation.

### 1.1.2: Preliminary Work

An initial assessment of the suitability of the DIA protocol used for phenytoin for larger analytes was done under the following **conditions**:

- All **signal processing** steps **identical** to **DIA for phenytoin**.
- Reagent **concentrations** and device **dimensions** are **specific** to the analyte, based on modeling.
- **Two model protein analytes** tested (horseradish peroxidase, *HRP* and Immunoglobulin G, *IgG*).
- ANCOVA analysis for **significance** of linear correlation between **response** and **analyte concentration**.

The most important **results** of these studies can be summarized as follows:

- DIA analytical signal **is not significantly modulated** by changing **HRP** concentrations due to low signal to noise ratios.
- Low signal for **HRP DIA as predicted** by modeling.
- High spatial frequency **noise not adequately filtered** by smoother used for phenytoin.
- DIA signal **is significantly modulated** by changing **IgG** concentrations.
- Replicable high signal for **IgG DIA is not predicted** by modeling.
- **Aggregation** of immune complexes is most likely source of higher signal.
- This aggregation represents an important **new assay principle** for bivalent analytes, but goes **beyond the scope** of this dissertation.



Based on the observations of this preliminary work, possible improvements to the DIA protocol were investigated

### 1.1.3: Improvements

The many **improvements assessed** are listed below, along with a very brief conclusion for each:

- Identified **plastics with low auto-fluorescence** to reduce confounding background – *successful*.
- Developed system to **assess** significance of problematic **protein adsorption** to actual microfluidic devices used in DIA – *successful*.
- Developed a **lamination method** (solvent assisted thermal lamination) that eliminates proprietary adhesives – *successful*.
- Identified **digital noise filters** that could remove the confounding noise in the HRP assay – *successful*.
- Investigated **data transformations** to improve the quality of statistical inference – *inconsistent result, deemed unnecessary*.
- Investigated **discrete Fourier transforms** and **multivariate calibration** as techniques to increase signal to noise – *showed potential, deemed unnecessary*.
- Developed a **new response calculation algorithm** (an integrated non-directional difference from free diffusion) to increase signal to noise – *successful, required a new experimental method to correct for midline drift*.
- Modified capture antibody with **microspheres to increase signal** – *smaller spheres showed potential, but fluidic and optical problems reduced impact severely*.
- Modified capture antibody with **soluble protein to increase signal** – *initial attempt unsuccessful, no further work*.

- Modified capture antibody with soluble **high molecular weight dextran** to **increase signal** – *showed some potential, improvement in signal from changing transport cancelled-out by reactivity losses.*

The most promising of these improvements were incorporated into a **second generation DIA** including:

- **Solvent-assisted thermal lamination of poly(methyl methacrylate)** to create microfluidic devices that are adhesive-free, rugged, and have very low fluorescence background.
- **A validated antifouling treatment** (pretreat device with 1 mg/mL BSA solution, and use 1 mg/mL BSA in all reagent diluents).
- **A penalized least-squares regression smoother** used when slope calculations are required.
- The “**integrated non-directional difference from free-diffusion**” response calculation algorithm to increase signal to noise.
- Incorporation of an **internal diffusion standard** in the assay reagents and a change in the data collection methods to enable its use as a midline correction.

It is this second generation DIA protocol that has been analyzed quantitatively to determine the limits of the assay and the design rules.

#### **1.1.4: Modeling the Second Generation DIA**

Several common **engineering techniques and numerical models** have been employed to create a comprehensive data set for the DIA without recourse to extensive laboratory “wet chemistry”:

- **Dimensional analysis** of the most important performance criteria (**blank response, initial slope of response versus dose curve**) expressed as a function of the important design parameters (**interaction time, diffusivity of reactants, concentration of reactants, reaction rate constants**) resulted in the expression of DIA performance in terms of a set of dimensionless parameters; thus enabling a complete description of the states of dynamic similitude and a more efficient exploration of the design space.
- A **numerical (finite difference technique, *FDT*) model** was used to model **individual experiment results** for each set of values for the dimensionless parameters.
- Close to **two-thousand individual simulations** were performed to enable prediction of the blank response and the initial slope of the response versus dose curve, for almost 500 combinations of parameter values. The **comprehensive domain** of individual parameter sets of **design parameters** investigated. encompasses most of the physically achievable embodiments of the DIA
- Log-log plots of the resulting dimensionless blank response and initial slope versus each individual parameter (while holding the other parameter values constant) enables inference of the **power law relationships** between the performance metric (blank response, initial slope) versus the dimensionless groupings of design parameters. The slope of the plot is the exponent of the power law. Simple algebra enables reconstitution of the power laws in terms of the original design variables.
- The most important **noise sources** were also investigated through a simple Excel based model. When combined with the inferences resulting from the FDT modeling, these noise estimates enable **prediction of clinical figures of merit**, such as limit of detection (LOD), sensitivity, and quantitative precision.

The results of the quantitative analysis above yielded **important insight into the design** of the DIA:

- Any single DIA formulation (combination of the physicochemical properties of the analyte, the concentrations of the reagents, the device design and operating conditions) can be thought of as occupying one of **three “regimes” in the design space**: *low signal, high signal, or transitional*.
- The **low and high signal regimes** can be adequately described by **simple power laws** (one for each performance metric, two for each regime). In the **transitional regime** the slopes for most of the log-log plots are changing so inferences require direct **consultation of the plots** or recourse to the FDT model.
- In the **low signal regime**, performance is improved by any **increase in signal**, even when the route to improvement is counterintuitive. For example, increasing the concentration of the labeled antigen reagent will increase the initial slope in the low signal regime – opposite of most competitive assays.
- In the **high signal regime**, **fine tuning** reactant concentration and diffusivity ratios is most productive.
- In the **transitional regime**, generalizations are **difficult** to make
- **Long interaction times** are beneficial until dissociation begins to become important.
- Long interaction times should be accompanied by device **width increases** to maintain the margins of undiluted feed solutions for consistency in signal processing.
- **High affinity antibodies** should be used to enable long interaction times
- **High spatial frequency noise** greater than ~2% can be an important source of **inaccuracy** in signal prediction, but should not be a major source of variation unless the fluorescence intensity of the labeled antigen reagent is

changing over time. Setting the integration time to use the most of the dynamic range of the camera should obviate any problems.

- **Variation in the position of the midline** can be a major source of **variation** if not corrected for. The effectiveness of a midline correction algorithm can be evaluated by the residual noise.

### 1.1.5: A Second Generation DIA for *C Reactive Protein*

A **clinically interesting** analyte, *C reactive protein (CRP)* was assessed to demonstrate the functionality of the **second generation DIA** with a protein analyte, and to verify some of the most important conclusions of the modeling:

- **Five formulations** were investigated, chosen to verify power laws and give good performance versus established clinical benchmarks.
- Streptavidin labeled with a spectrally distinct fluorophore was added to labeled CRP reagent as **internal diffusion standard to enable midline variation correction**. During pump run, the microscope filter set was manually toggled and images taken to create interleaved data set.
- Sufficient spiked CRP levels were performed to **validate the standard curve**.
- Sufficient replication was performed to give **good estimate of variation**.
- Mock samples were prepared and assayed with DIA and by nephelometry at UW, Research Testing Services, for a **method comparison**.

The following **results** were observed:

- The **noise in the response** observed was essentially **constant** for all responses generated, even from different formulations. It was  $s = \sim 1.7$  RU. This is consistent with  $s = \sim 8$  pixels of midline variation. Even after the midline correction was performed, this amount of midline variation was seen

in the diffusion curves used for the correction. Thus, **residual midline variation** appears to be the **dominant source of noise** in the second generation DIA.

- The results of individual experiments **matched predictions well**. A plot of observed versus predicted response showed a substantially linear relationship ( $R^2 = 0.97$ ) with good agreement between the values (slope=1.03, intercept 0.24 RU) within observed noise.
- The counterintuitive conclusion of the low signal regime power law that **increasing the concentration of labeled analyte** in the reagent could **increase the initial slope** (up to a point) was **verified**.
- The **LOD** was calculated as **2.0 mg/dL**.
- The **upper end of the dynamic range** of the assay was calculated as **25 mg/dL**
- **Relative precision** throughout the assay range ranged from **18%-30%**.
- The **quantitative method comparison** was **adequate** given the relative noise (slope =0.82, intercept = 6.0,  $R^2 = 0.49$ ).
- These results indicate that the **CRP DIA** is too noisy to compete with quantitative reference lab assays, but it **compares well with** other, more appropriate benchmarks; e.g., **point-of-care assays by ABX and Murex**.

### 1.1.6: Conclusion

Using the lessons learned in this dissertation, projections about the largest analyte that could be assayed reliably by the DIA can be made. With the noise levels seen with CRP, the **largest analyte** amenable to the DIA is **~33 kD** with an unmodified capture antibody. To **assay larger molecules** with the DIA several problems must first be solved. **Reduction in noise** levels though improvement of the midline correction seems the most feasible. Alternatively (or in concert), the **modification of capture antibody** could eventually produce the dramatic improvements predicted by

modeling, but the fluidic, optical, and reactivity problems encountered must first be overcome. The **quantitative characterization of DIA** performance described herein should make convergence on the final optimum DIA much easier.

## ***1.2. Introduction***

There is an old bromide that is frequently produced in answer to design problems in clinical immunoassay development: *cheaper, faster, better – pick any two*. Like many statements of this type, it is rooted in truth. Typical 96-well enzyme-labeled immunosorbant assays (ELISAs) give good results at a relatively low cost per test; but are very slow, as measured by both turnaround and throughput. High-throughput clinical analyzers rapidly achieve excellent performance via massively-parallel, liquid-handling robotics; but typically require a capital investment of tens-of-thousands of dollars. Paper immunochromatography “dipsticks” yield inexpensive results with good turnaround, but suffer many performance problems. When evaluated using these macro-scale examples, the “pick two” paradigm appears to be absolute.

The advent of microfluidics may finally challenge this paradigm. The cost savings that accrue from microfabrication have been conclusively demonstrated in the fields of personal electronics and information technology. It is, perhaps, less appreciated that miniaturization has frequently been accompanied by speed and performance advantages that arise from the small scale. A miniature clinical immunoassay chip is complicated – involving fluid dynamics, mass transport, dynamic surface and bulk chemistry, and photonics... as well as electronics. However, the cost and performance advantages realized in the electronics industry should translate to microfluidics. The concept of the portable analyzer that quickly gathers high-quality, quantitative assay results and sends them on to the physician is no longer in the realm of science fiction.

Nevertheless, this concept is still a long way from being realized science *fact*. Many discoveries and advances are required before the vision becomes reality. Microfluidic assay techniques are still a fertile area for research – the existing macro-scale assays do not always miniaturize well, or may not fully exploit the advantages of physics at the micro-scale. This is the focus of this dissertation: the continued characterization of one novel microfluidic immunoassay technique – the diffusion immunoassay (DIA).

The primary focus of this dissertation is to determine the effect of the properties of the analyte; e.g., size (and, therefore, diffusivity) and reactivity, on the performance of the DIA. This goal is accomplished through dimensional analysis, numerical simulation, and direct experimentation with several analytes and DIA formulations chosen to encompass the domain of analyte properties expected for realistic analytes. However, to adequately answer this question, many other analytical problems had to be solved. Thus, in addition to numerical simulation and data that directly address the central thesis, this dissertation characterizes background fluorescence of plastic devices, adsorption of protein analytes to devices, describes a novel adhesive-free lamination technique, and discusses the impact of signal and data processing algorithms on the final results.

### ***1.3. Summary of Thesis***

This dissertation explores the limits of a novel microfluidic immunoassay technique – the diffusion immunoassay (DIA) – with respect to the physicochemical properties of the analyte. The limits are defined using a combination of dimensional analysis, numerical modeling, and empirical noise determination. The validity of these conclusions is verified through the performance of the DIA in a research instrument for several protein analytes and assay formulations, and comparison of these results to



modeling and conventional metrics for clinical assays (accuracy, sensitivity, etc.). A set of design rules is proposed that codifies how the interaction between analyte properties and assay formulation results in the desired assay performance and, ultimately, the limits defined. Several methods are used to modify the *germinal DIA* (the DIA as defined at the outset of this research) to create an improved, second generation DIA to test these design rules and illustrate the nature of the limitations. In addition, this exploration is shaped by the consideration of point-of-care (POC) applications; e.g., emphasis is placed on plastic devices because they represent the most likely low-cost disposable.

#### ***1.4. Significance***

This research advances the understanding of an important new immunoassay technique – the DIA. The DIA has great potential as a POC microfluidic immunoassay technique, due to: its relatively short analysis time; the small sample and reagent volumes required; the small volumes of waste produced; and its amenability to simple, disposable “assay cards.” The first demonstration of the proof-of-principle of the DIA was with a small, quickly diffusing analyte – phenytoin, an anti-epileptic drug (274D). Proteins are an important class of analytes; and are good models of other large, slowly-diffusing analytes. The ability to perform protein assays on a POC DIA platform will represent an important advance in patient care for many disease states, and this research builds a solid foundation for the realization of that goal.

### ***1.5. Scope***

The primary motivation of this research is the investigation of the limits of the DIA engendered by the properties of the analyte. The DIA relies on the differential diffusion of the free and antibody-bound forms of an analyte in solution to quantify the amount of analyte. The size (and, therefore, the diffusivity) of the analyte is a key determinant of the magnitude of the analytical signal and response. (This topic will be explored in Section 2.4.) In addition, the thermodynamic and kinetic properties of the binding reaction between the antibody (*Ab*) and antigenic analyte (*Ag*) is expected to affect the results, and can vary over several orders of magnitude for different *Ab/Ag* pairs. Thus the extension of the DIA principal to larger analytes is not trivial.

In addition, there are a number of parameters that can be varied in the assay formulation; such as, concentration of reactants, channel dimensions, and flow rates. It became clear during the work on the phenytoin DIA how these parameters had significant, and sometimes contradictory effects on the final assay result. Further development in understanding their interactions was another important goal of this research. This dissertation proposes a set of dimensionless parameters and general design rules that should enable prediction of the expected performance of the DIA for an arbitrary analyte.

One important potential application of the DIA is as a POC clinical system, and this research will be conducted with consideration of that end goal in mind. It is likely that any practical POC system will use plastic, disposable, microfluidic-cartridges. Thus, this research also investigates how the use of plastic devices may affect the performance of a protein DIA, with specific attention to the auto-fluorescence of the plastics and the adsorption of the protein analytes and reagents to the device under realistic conditions. In addition, it is assumed that a POC system will not use sophisticated detection optics; therefore, experiments are performed on a test-bed that is relatively unsophisticated, to mimic the expected final system configuration.

## ***1.6. Limitations***

This research is not intended to evince the proof-of-principle of the DIA as an immunoassay technique. This has been already accomplished with the phenytoin DIA, and can be considered validated by the issuance of a US patent,<sup>2</sup> and a publication in a prestigious peer-reviewed journal.<sup>1</sup> It should be noted that the initial proof-of-principle of the phenytoin DIA was primarily the work of Dr. Anson Hatch, and comprises a significant portion of his Ph.D. dissertation. The obvious potential of the DIA has made it the subject of several M.S. and Ph.D. theses, and the proposed dissertation has been structured to minimize overlap with that research.

It is not intended that this research provides fully optimized assays or systems. Given the infant and protean nature of the DIA, the advance in the understanding of those parameters is a significant result; but, necessarily falls short of any ultimate optimum. Nevertheless, the generalization of the conclusions strongly suggests where future improvement may prove most fruitful, and which directions will be less productive.

It is not intended that this research will provide any marketable products. The analytes investigated in the preliminary studies are model compounds chosen to represent classes of potential assays (e.g., globular proteins with molecular weight  $\leq 45$  kD). The results of that research should be immediately applicable to clinically important members of that analyte class, but assay formulation and performance specific to those analytes must be determined to evince the efficacy of the DIA in that particular context. The “capstone” DIA for C-reactive protein was performed primarily to assess the conclusions of the modeling, and illustrate the design rules, but a “clinically interesting” analyte was chosen to leverage that work into conclusions that might have more impact on clinicians than the models chosen for preliminary work.

### ***1.7. Additional Comments***

At the outset of this research, we anticipated four primary challenges in adapting the germinal DIA to protein analytes performed in plastic devices. 1) A reduction in the maximum DIA signal available was expected, due to differences in some of the key design parameters that are unavoidable when a protein is the analyte. 2) The auto-fluorescence of the materials used for plastic device fabrication was expected to significantly complicate data analysis. 3) The uncontrollable adsorption of the proteins in the reagents and/or the analyte could complicate the interpretation of results. 4) It was not obvious that the relatively unsophisticated signal processing algorithms used in the germinal DIA would be sufficient for resolving the smaller responses anticipated with a protein DIA. The genesis of these concerns is discussed in detail (Section 2.4) after the germinal DIA is reviewed. It is sufficient to state here, that these challenges motivated the aims of this research. Thus, the research plan was shaped by the preliminary observations about the DIA.

## **Chapter 2: Microfluidic Immunoassay and the DIA**

To facilitate the detailed understanding of this dissertation, a review of the pertinent background and theory is required. This review has been organized under the following major topics:

1. General assay design principles
2. The diffusion immunoassay as defined at the outset of this research
3. A brief comparison of the DIA with other popular microfluidic techniques
4. Challenges anticipated at the outset of this research.

### ***2.1. General Assay Design Principles***

Clinical assay design has its lexicon; which concisely describes the general principles that underlie the design. These terms and concepts are briefly reviewed.

Any quantitative analytical system can be abstractly described as a series of elements that interact to produce the system performance (Figure 2.1). These modules include: signal generation, signal modulation, signal transduction, noise filtering, amplification, response extraction, dose/response modeling, and others<sup>3,4</sup>. These modules can be used as differentiating factors in discussing different assay systems.

The designer manipulates some or all of these elements to achieve the specifications of the assay. The DIA is both relatively uncharacterized and unique for some of these elements (Section 2.2). By better characterizing them, we hope to significantly improve the performance of the DIA, and facilitate intelligent design decisions.

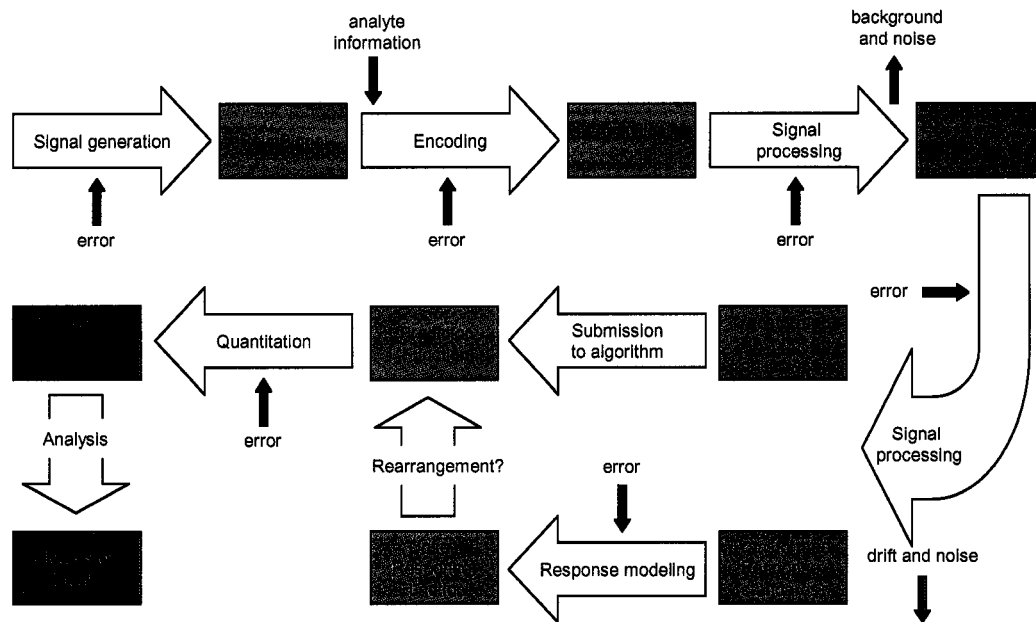


**Figure 2. 1:** A block diagram of the various modules or elements that comprise a generalized immunoassay design. The raw signal is encoded with the analyte information in the sample. The analyte response is extracted from the complex analytical signal. Various signal processing steps (amplification, noise filtering, data transformation, background correction, etc., may be required to achieve a response-to-noise ratio favorable to facilitate modeling and quantitation. Empirical response modeling (a.k.a. *calibration*) is enabled by the assay of standards. The dose/response function (a.k.a. *standard curve*) that results is used to determine the predictor function that is used to quantitate unknowns. Error is introduced at each step. Validation is demonstrated by the figures of merit.

## 2.2 The Diffusion Immunoassay (DIA)

The diffusion immunoassay is a novel immunoassay technique (developed in the Yager Lab) that uses the differential diffusion of the analyte and its immune-complex to transduce information about analyte concentration into a response based on the spatial distribution of mass<sup>1,5</sup>. This is the unique feature of the DIA. It is only possible when convective mixing is absent; e.g., in a microfluidic device or gel. The original proof-of-principle was demonstrated with a small analyte – phenytoin (274D) – and

under a set of conditions which are referred to in this document as the *germinal DIA*.<sup>i</sup> This set of conditions is defined below (Section 2.2.1). Some possible modifications to the germinal DIA that have been investigated by other researchers are discussed briefly (Section 2.2.2). Several interesting consequences of peculiarities of the germinal DIA are also discussed (Section 2.2.3). Finally, the numerical method used to predict the DIA response herein is outlined (Section 2.2.4).

## 2.2.1: Detailed Description of the Germinal DIA

*2.2.1.1. The Assay Principle:* The germinal DIA is performed in a simple microfluidic *T-sensor* (two inputs, one outlet) operating at low Reynolds number (*Re*) flow. One input is a solution of antibody (*Ab*) specific to the analyte, the other inlet is an analyte solution. In the T-sensor, the laminar flow characteristic of low-*Re* insures that the two inlet-streams are axially apposed in near-perfect opposition across the midline of the channel (i.e., “side by side”) without convective mixing orthogonal to the axis.<sup>ii</sup> In the absence of reaction, solutes in the two laminar flow streams diffuse into the opposite streams – creating an *interdiffusion zone* which becomes broader with increasing interaction time between the two flow streams (Figure 2.2). In the germinal DIA, when the analyte encounters *Ab* it binds with characteristic avidity and specificity. The immune-complex of *Ab* and analyte is less diffusive than the unbound analyte, resulting in an accumulation of total analyte mass (bound and unbound) near the interface of the two flow streams relative to the distribution that would result from the diffusion of analyte in the absence of *Ab* (Figure 2.3). Depletion of analyte in the lamina adjacent to the accumulation is an important secondary effect resulting from the overall conservation of mass. Thus, the spatial

---

<sup>i</sup> The DIA for phenytoin was primarily the work of Dr. Anson Hatch and comprised a significant part of his doctoral thesis. As such, it is not considered part of this thesis proposal.

<sup>ii</sup> The interface of the inlet streams is located at the midline as long as the volumetric flow rates and viscosities of the two inputs are identical. If they are not, the interface is displaced from the midline proportionally to the flow rate ratio and/or viscosity ratio.

distribution of analyte mass in the interdiffusion zone is significantly altered by the specific binding of the analyte to its cognate antibody.

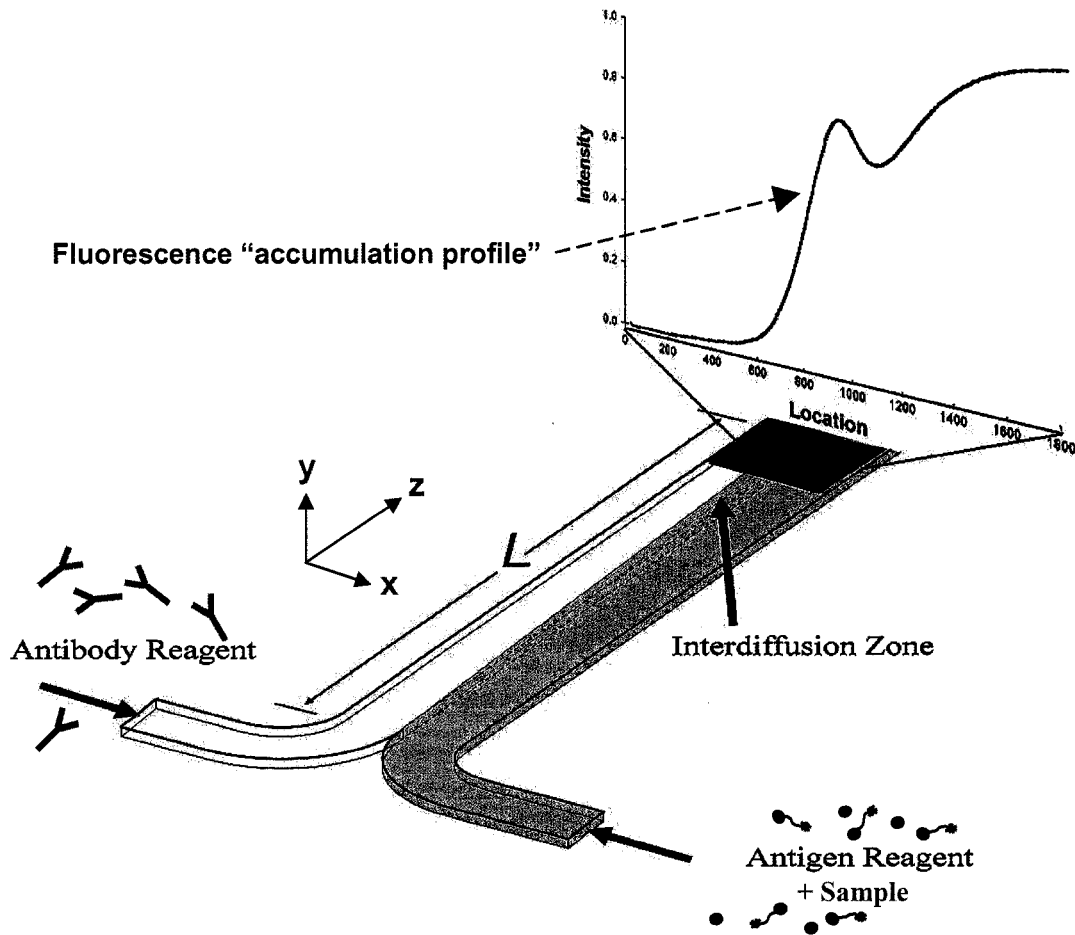


**Figure 2. 2.** A diagram of the DIA as performed in a T-sensor with an actual experimental image of accumulation superimposed at the interrogation zone.. Antibody reagent is introduced into one inlet, and a mixture of a labeled analyte/antigen reagent and the sample is introduced into the other inlet, under conditions that insure completely laminar flow. After a fixed interaction time (determined by the flow rate and downstream length,  $L$ ), interdiffusion and complexation results in an accumulation of the total analyte mass at the interface of the two solutions relative to free diffusion. The mass of labeled analyte that accumulates depends on the mass of unlabeled analyte in the sample because of competition for antibody binding sites, thus modulating the analytical signal with sample analyte concentration. Imaging with a microscope and CCD camera enables calculation of an accumulation profile of fluorescence intensity vs. channel location. See text for more detail.



*2.2.1.2. Fluorescence Detection:* The germinal DIA uses fluorophore-labeled analytes to create a detectable signal. When labels are used, it is desirable to avoid having to label the analyte in samples before performing the assay. To accomplish this with the germinal DIA, a reagent containing a known concentration of fluorophore-labeled analyte ( $Ag^*$ ) was mixed with a sample containing an unknown concentration of unlabeled analyte ( $Ag$ ). The sample analyte ( $Ag$ ) concentration modulates the magnitude of the accumulation of labeled analyte ( $Ag^*$ ) by competing for Ab binding sites – an increase in sample analyte concentration ( $[Ag]$ ) reduces the accumulation detected (Figure 2.3). Therefore, the raw analyte response is the difference in the detected mass of labeled analyte that accumulates with an unknown and the detected mass that accumulates with a *reagent blank* (an assay performed with a standard known not to contain analyte).

The germinal DIA used a 16-bit monochrome CCD camera and epifluorescence microscope (equipped with broad-spectrum source illumination from a mercury-arc lamp, and the appropriate filter sets) to detect the spatial distribution of labeled mass, by imaging a part of the microchannel (the *interrogation zone*.) These images were sampled across a slice orthogonal to the flow (referred to as an *intensity profile*). The mass of labeled analyte was inferred by equating the intensity of fluorescence recorded at any point in the profile with the concentration of labeled analyte. An intensity profile that displays the accumulation of mass characteristic of a DIA response was denoted an *accumulation* or *accumulation profile*.

Integration or averaging was done in the germinal DIA in three ways during the gathering of a raw intensity profile to exploit the associated signal-to-noise gains. (1) Each point in the one-dimensional intensity profile resulted from the fluorescence of numerous voxels (*volume pixels*) extending in the two orthogonal directions. The image taken intrinsically integrated the fluorescence emanating from voxels across the depth of focus; i.e., the *observed* intensity was completely confounded with the

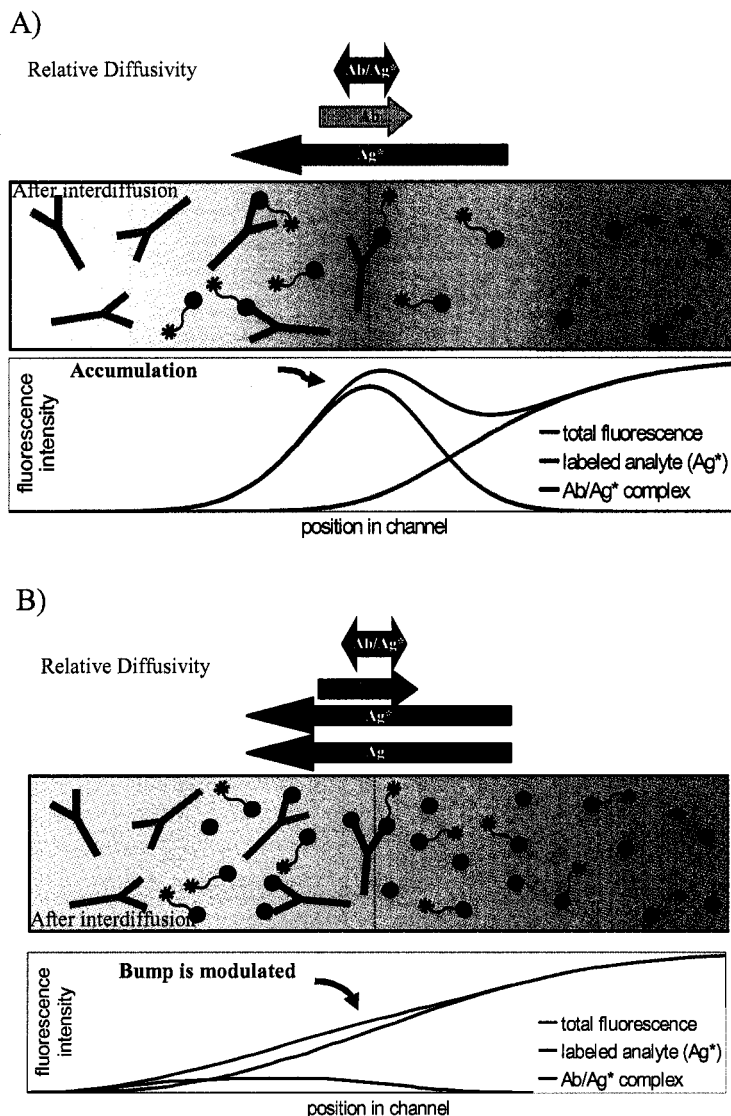


**Figure 2. 3.** Schematic cartoons and charts of the DIA assay principle. Arrows represent the diffusion of the DIA reactants with the length corresponding to relative diffusivity and the arrowhead the dominant direction of transport. Gray “wyes” = antibody, Black dots = antigenic analyte, Red asterisks = fluorophore. Both cartoons represent the states of the system after a set interaction time defined by flow rates and device dimensions. The initial temporal state of the system is a uniform concentration of antibody on one side of the dotted interface, and a uniform concentration of analyte on the other (both labeled and unlabeled, where present.) These states are established in the T-sensor through the junction of two laminar flow streams (Figure 2.2). The plots under the cartoons show the fluorescence intensity that would be observed if the overlying cartoon was sampled horizontally. Only the total fluorescence is physically observable in the germinal DIA – but results from a superposition of the displayed free analyte and immune complex plots. A) The accumulation seen when no sample analyte is present (reagent blank). B) The accumulation when competing sample analyte modulates the blank signal. See text for more detail.

summation of the intensity throughout the  $y$ -dimension (this phenomenon is discussed in more detail in section 2.2.3.) In addition, the slice sampled was two dimensional – covering the entire interrogation zone in the diffusion dimension ( $x$ ; see Figure 2.2) and, typically, ten pixels in the flow direction ( $z$ ). The average of the ten pixels in the  $z$ -dimension is assigned as the intensity at each  $x$ -coordinate, to yield the final one-dimensional diffusion profile.<sup>iii</sup> This resulted in some filtering of high spatial-frequency noise. (2) The image was integrated over time (typically 5-10 s.) to increase the magnitude of the signal and filter high temporal-frequency noise. (Section 2.2.3 discusses why this is uniquely possible in the DIA.) This is the equivalent of a long exposure time in a film-based camera. (3) Ten replicate images were gathered over the duration of each profile-gathering experiment (~ 5 min.). These were averaged and represent a second temporal noise (low pass) filter, as well as giving a pixel-by-pixel estimate of a standard error appropriate for making inferences about intra-run, inter-accumulation differences. The operations can be summarized by the equation 1 for the raw intensity at each pixel  $i$  in the diffusion profile.

$$1) \quad I_i^{raw} \equiv \frac{\sum_{n=1}^{10} \sum_{t=0}^{5s} \sum_{z=z_1}^{z_{10}} I_{iztn}^{obs}}{100} \quad \text{where,} \quad I_{iztn}^{obs} = \sum_{y=1}^w I_{iztny}^{actual} \quad \text{from imaging}$$

The equation of fluorescence intensity to  $Ag^*$  mass required two corrections to the raw accumulation profiles. (1) Background fluorescence from the device or reagents must be corrected for. In the germinal DIA, this *background correction* was done by

---

<sup>iii</sup> There is a slight difference in the actual profiles at each of these ten pixels due to the different interactions times that each represents (see the discussion concerning the collapse of the downstream distance and time dimensions in section 2.2.2.) Therefore, the profile reported represents an average profile for this spatial region.

taking an image of the device filled with flowing diluent<sup>iv</sup>, calculating an intensity profile for this image, and then simply subtracting the background intensity profile from the subsequent raw accumulation profiles on a pixel-by-pixel basis. This simple subtraction algorithm assumes that the background fluorescence does not change over the time period encompassing when the background image is taken and when the experiment is complete. If the device was moved, a new background correction image was determined, because of non-uniformity in the background of the device produced by local defects and outer-surface contamination. (2) Any spatial non-uniformity in the illumination due to the microscope optics must be corrected for. In the germinal DIA, this *flatfield correction* was done by taking an image of the device filled with flowing Ag\* reagent, calculating an intensity profile for this image, correcting this image for the background, and then doing a simple division on all subsequent background-corrected raw accumulation profiles in a pixel-by-pixel fashion. The background and flatfield corrections can be summarized by equation 2.

$$2) \quad I_i^{corr} \equiv \frac{I_i^{raw} - I_i^{bgrnd}}{I_i^{flat} - I_i^{bgrnd}}$$

*2.2.1.3. Signal Processing Algorithms:* To enable direct comparison of different accumulation experiments, all accumulations were *tail normalized* in the germinal DIA. The signal processing steps just described *should* result in intensity values throughout the channel being corrected to values between zero and unity. In regions of the channel that are expected to contain undiluted Ab reagent (near the wall on the

---

<sup>iv</sup> In the germinal DIA, the diluent was phosphate-buffered saline (pH 8.0). A different formulation was used in this research (Section 3.1.)

Ab-inlet side), the value should be zero. In regions of the channel that are expected to contain undiluted Ag\* reagent (near the wall on the Ag\*-inlet side), the value should be unity. In the germinal DIA, this was frequently not the case (for reasons that are still unclear). Thus, tail normalization was adopted to enable the comparison of accumulations without this artifact. The tail normalization step involves calculating the average intensity of twenty pixels at the spatial extremes of the profile (the *tails*), and then using those averages in a simple linear transformation of the entire intensity profile, so that the tails are pegged at zero and unity, and the rest of the profile is rescaled equivalently. This transformation takes advantage of the internal referencing feature of the DIA – each accumulation profile contains an intrinsic background and maximum intensity measurement, temporally linked to the response of interest.<sup>v</sup> The tail normalization can be summarized by equation 3.

$$3) \quad I_i^{BFTN} \equiv \frac{20I_i^{corr} - \sum_{i=1}^{20} I_i^{corr}}{\sum_{i=(d-19)}^d I_i^{corr} - \sum_{i=1}^{20} I_i^{corr}}$$

The end result of the background correction, flatfield correction, and tail normalization to the raw accumulation profile will be denoted in the rest of this document as *BFTN* accumulation profiles.

---

<sup>v</sup> To exploit this unique feature, the interaction time and size of the interrogation zone must be manipulated so that the tails are measurements of their respective inlet solutions before cross-channel diffusion has reduced the solute concentration detectably. This will be discussed in detail in Chapter 2

The signal processing steps summarized above correct for most of the variation between individual accumulation profiles in the germinal DIA; especially, the expected systematic variation. To reduce the remaining high spatial frequency noise, the next step in signal processing in the germinal DIA was a low-pass noise filtering or smoothing of the accumulation profile. A very simple *boxcar* (or *moving average*) filter was applied to the accumulation profile, with a seven pixel *window*. This filter can be summarized by equation 4.

$$4) \quad I_i^{smooth} \equiv \frac{\sum_{j=i-3}^{i+3} I_j^{BFTN}}{7}$$

A simple response-amplification transformation was then performed in the germinal DIA. The algorithm used was based on numerical differentiation: a modified first-order centered-difference equation was used to approximate the first derivative (slope) of the accumulation profile (denoted the *slope profile*.) This algorithm approximates the slope at any point in the profile as the simple difference of the point on either side of it (rescaled to account for the step size). By calculating the slope at each point in the profile, the response becomes the dominant behavior – the peak of the accumulation band shows up as a global maximum in slope, and the valley of the depletion band shows up as a global minimum in the slope<sup>vi</sup>. (Figure 2.4B) Thus, the dominant source of variation in the accumulation profile -- the difference in intensity between the Ag\* reagent and the Ab reagent – is reduced. The differentiation algorithm can be summarized by equation 5.

---

<sup>vi</sup> Numerical differentiation is a notorious high-frequency noise amplifier (i.e., high-pass filter), so smoothing of the BFTN-processed accumulation profiles was required before *any* approximation of the slope was practical.

$$5) \quad \frac{dI_i}{dx} \equiv \frac{I_{i+3} - I_{i-3}}{7\Delta x} \quad \text{where } \Delta x \equiv \text{pixel size (in } \mu\text{m)}$$

Readers familiar with numerical methods might recognize that equation 5 is not the standard first order centered difference equation<sup>6</sup>; rather, it uses a larger step size (three pixels on either side of the smoothed pixel.) The boxcar filter used in the germinal DIA does an adequate job of smoothing for moderately noisy data with a minimum of distortion of the underlying behavior, as evaluated by visual examination of the smoothed profiles for the phenytoin DIA (Figure 2.4A) When the numerical slope approximation was calculated, however, the results were not as good as expected – illustrating the noise-amplification characteristics of the centered-difference algorithm. To offset this, the germinal DIA used a first order centered difference equation where the step size was three points, rather than one. This essentially performs another smoothing step concurrently with the slope calculation. Using a higher-order centered difference equation would have produced a similar or, perhaps, improved result<sup>6</sup>; but, was not attempted.

The slope transformation does not, however, extract a single number from the profile. What results is still a very complex multivariate data set. In the germinal DIA, a univariate response was extracted from the slope profiles. This was done to simplify downstream calculations; e.g., response modeling, quantification of unknowns, and standard error calculations. To convert the slope profile to a univariate response-number a simple difference between the maximum slope and minimum slope was calculated for each slope profile. Calculating a difference amplified the response relative to simply choosing the maximum or minimum, because it actually utilizes the multivariate nature of the response in a primitive way – information from two

locations in the modulated multivariate response (peak accumulation and peak depletion) are leveraged into the univariate response calculation.

The combination of the seven-point boxcar smoother and the first-order centered-difference with the three-pixel step size –used to extract a univariate response number from slope profiles – is denoted the *DIA response* and the *D-A value* in the original publications describing the germinal DIA for phenytoin. This algorithm enabled the extraction of a response number with an adequate response-to-noise ratio to establish the proof-of-principle for the DIA for small molecules. For clarity, the response resulting from the algorithm described above will be referred to as the *germinal DIA response* for the balance of this document. Its adequacy in more demanding applications of the DIA is a major topic of this research (Section 3.3.1).

The germinal DIA procedure up to this point was primarily the work of Dr. Anson Hatch. The author's largest contribution to the germinal DIA was in identifying and implementing the dose-response models and regression procedure that enabled assay calibration and accurate quantification of unknowns.



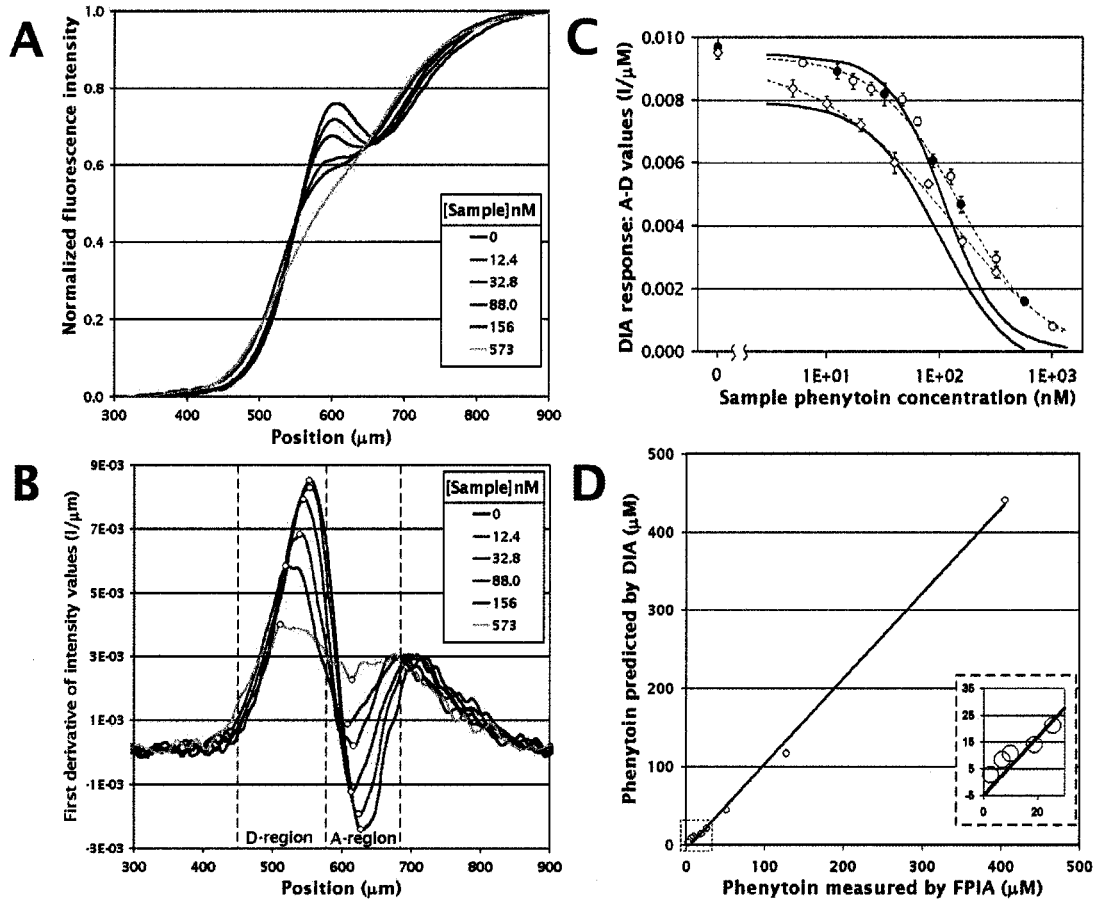


**Figure 2.4** Analysis of DIA diffusion profiles for phenytoin determination. a) Dose dependent diffusion profiles, after BFTN processing and boxcar smoothing. b) derivative of diffusion profiles from a. The maxima and minima from two regions were used as the signal (D-A value). c) Calibration curves (dashed lines) based on D-A values of diffusion profiles. Curves for two assays are plotted on the same graph, as well as numerical predictions (solid lines). Data from the first assay (circles) was for 0.25% blood samples. Six data points (filled circles) were used to generate the calibration curve using four-parameter logit fits and nonlinear least squares method. Error bars represent 1 s.d. based on repeated measurements from 8 samples. The second assay (open diamonds) was for diluted serum calibration standards using a lower Ab concentration (7.5% rather than 10% used in first assay). d) Linear regression analysis of the methods comparison ( $r^2 = 0.998$ ). Figure taken from Hatch *et al.*, 2001.

**2.2.1.3. The Dose-Response Relationship:** The next step in creating a useful assay was to determine the function that enables quantification of unknowns. The germinal DIA response for the phenytoin DIA, expressed as a function of sample analyte

concentration (for a fixed assay formulation) was not linear over much of the hypothetical dynamic range. To enable accurate quantification of unknowns a data transformation or non-linear predictor function was required. The *four-parameter log/logit equation (4PLL)* is frequently used as a univariate predictor function – that is, a *standard curve* – for immunoassays<sup>7</sup>. Its general form is:

$$6) \quad y = \frac{a-d}{1+\left(\frac{x}{c}\right)^b} + d$$

The 4PLL is a sigmoid monotonic function that has sufficient degrees of freedom to fit a data set displaying the curvature apparent in the phenytoin data. It also is an attractive model, in that physical significance can be ascribed to several of the parameters<sup>7</sup>. Using the symbol  $R$  for the response it can be re-written:

$$7) \quad R = \frac{R_0 - R_\infty}{1+\left(\frac{[Ag]}{c}\right)^b} + R_\infty$$

In this formulation,  $R_0$  is the response at vanishing analyte concentration,  $R_\infty$  is the response at infinite analyte concentration,  $c$  is the point on the  $[Ag]$  axis where the point of inflection is located, and  $b$  is the slope of the curve at the point of inflection. In order to empirically determine the standard curve, at least four calibration standards must be assayed: a reagent blank, a very high  $[Ag]$  standard to estimate  $R_\infty$ , and two

intermediate [Ag] standards to account for the degrees of freedom in  $b$  and  $c$ . In practice, at least six standards are usually assayed so that all non-linear parts of the curve are adequately represented in the regression – six calibration standards were used for the germinal DIA.<sup>vii</sup>

In the germinal DIA, the 4PLL standard curve (equation 7) was determined by *non-linear least squares (NLLS)* regression<sup>6,8</sup> using the germinal DIA response as defined above, and the [Ag] of the standards determined by a reference method. The NLLS regression was performed by the *Solver* function in the spreadsheet software *Excel* (Microsoft Corp., Redmond, WA, USA), which uses a generalized-gradient method to iteratively minimize the error function in the multi-dimensional parameter space<sup>9</sup>. The error function for the germinal DIA is summarized by equation 8:

$$8) \quad E \equiv \sum_{std=1}^6 \left[ R_{std}^{obs} - \frac{\hat{R}_0 - \hat{R}_\infty}{1 + \left( \frac{[Ag]_{std}}{\hat{c}} \right)^{\hat{b}}} + \hat{R}_\infty \right]^2$$

To minimize the function  $E$ , the point where the first derivative of  $E$  vanishes is determined. When a linear calibration model is used, the  $\partial E / \partial P_k$  of the error function (where the  $P_k$  are the four parameters of the model being fitted) -- the *normal equations* -- form a simple linear system that can be solved analytically using linear algebra.<sup>6</sup> This process is referred to as the *linear least-squares (LLS)* method, and can be accomplished facily with many commercially available computer programs. For

---

<sup>vii</sup> Even though  $R_0$  and  $R_\infty$  can be estimated empirically; they are fitted parameters in the 4PLL formalism. If one assumes that the empirical estimates for  $R_0$  and  $R_\infty$  are correct, then a *two-parameter log/logit equation (2PLL)* results.

the 4PLL (and many other nonlinear models) an analytical solution is not possible, so an iterative numerical method is used. Iterative methods require initial estimates for the parameters to be fitted.<sup>6</sup>

For the germinal DIA, the initial values for the four parameters were determined by: (1) the observed response for the reagent blank ( $R_0$ ), (2) the observed response for the highest concentration of sample analyte evaluated multiplied by a factor of  $\sim 0.8$  ( $R_\infty$ ), and (3) arbitrary numbers ( $b$  and  $c$ ) determined to give a curve that was reasonably close to the data by operator discretion. When using any iterative technique that searches a non-linear multi-dimensional surface, there is no way of determining if the minimum reached is global or local.<sup>6</sup> To increase the probability that the global minimum was found, a number of initial guesses for  $R_\infty$ ,  $b$  and  $c$  were explored. The nearness of the coefficients of variation to unity indicates that this method yielded curves that fit the data-sets with adequate conformity to the observations (Figure 2.4C).

Another common way to fit the 4PLL model is to use a data transformation to linearize the response and reduce the model to a 2PLL, which can then be fit analytically with the LLS method.<sup>6,7</sup> In the germinal DIA, the NLLS was chosen specifically to avoid transformation of the data. Since most criteria for acceptability of a new clinical assay rely on statistical inference, data transformations should only be performed if they do not introduce mean-dependence into the variances – such mean-dependence violates a basic assumption of common linear statistical models.<sup>10</sup> However, an inadequate number of replicates were performed on the phenytoin DIA to test the effect of a transformation on the variance of different samples; therefore, data

transformation was deemed risky. The appropriateness of data transformation is addressed in this research (Section 4.2.2).

Once the standard curve was determined through calibration and regression, the 4PLL equation was rearranged to enable the quantitation of unknowns from their response:

$$9) [Ag]_{unknown} = c \left( \frac{R_0 - R_\infty}{R_{unknown} - R_\infty} - 1 \right)^{\frac{1}{b}}$$

The tractability of the 4PLL to this type of rearrangement is another attractive feature of the 4PLL. The rearrangement enables the direct algebraic calculation of unknown analyte concentrations without recourse to iterative “back-fitting” methods required for some other non-linear models, e.g., the *five-parameter log/logit*.<sup>11</sup>

Standard curves constructed with the 4PLL-model enabled adequate quantification of unknowns in the germinal DIA for phenytoin.<sup>1</sup> Linked pairs of mock samples were prepared by spiking individual whole blood samples with phenytoin and splitting the samples into two aliquots. One aliquot was centrifuged and submitted to a reference laboratory for determination of phenytoin concentration by fluorescence polarization immunoassay (the established reference method), and the other was assayed using two formulations of the phenytoin DIA. The results of a standard method comparison established that the DIA can be calibrated to quantify whole blood unknowns with good conformance to a reference method (Figure 2.4D).

*2.2.1.4. Germinal DIA Summary:* The elements of the germinal DIA discussed above can be summarized using the same block diagram presented in the general case (Section 2.1). The diagram (Figure 2.5) illustrates those elements targeted for improvement, which will be explicated further below (Section 2.4).

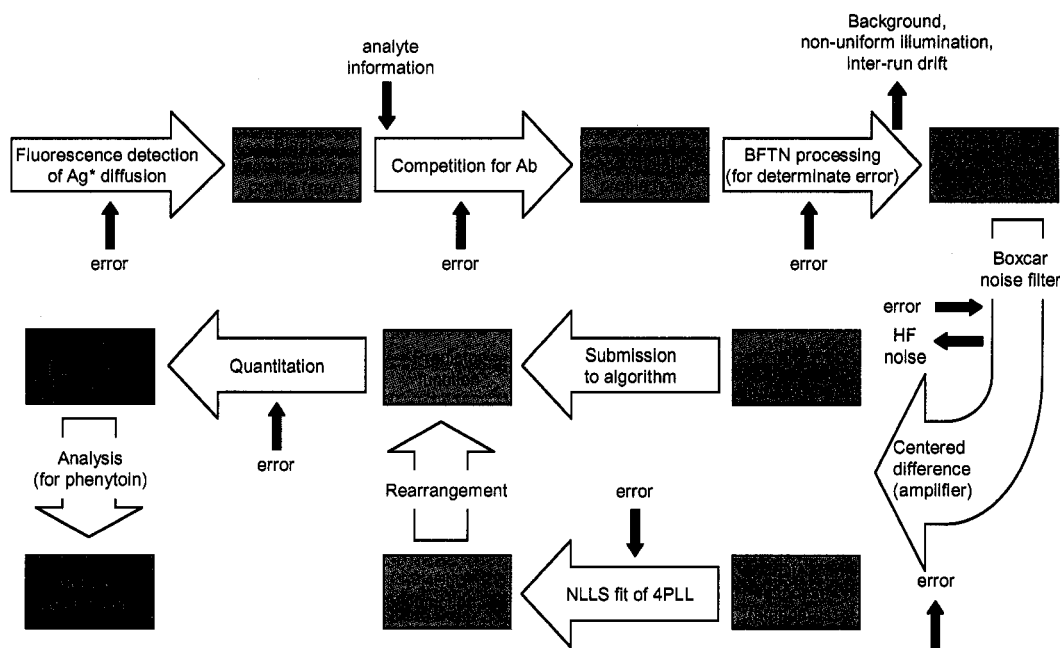


**Figure 2.5:** A block diagram of the germinal DIA design. The analytical signal is produced by the accumulation of the labeled analyte reagent, and modulated by the analyte in the sample. BFTN processing corrects for known systematic error. A boxcar noise filter eliminates some high-spatial-frequency noise. A centered difference amplifies the response. Calibration is accomplished by a non-linear least squares fit of the DIA response to a four-parameter log-logit model. Rearrangement of the model with the fitted parameters enables quantitation. In the germinal DIA for phenytoin, a method comparison with a reference method was the primary figure of merit. Compare this diagram to Figure 2.1.

### 2.2.2: Alternate DIA Formats

The germinal DIA configuration described above is the starting point for the research in this dissertation, but many modifications not investigated here are possible. Some have already been described.

*2.2.2.1. Hydrogels and the Pre-mix Assay:* The germinal DIA used a simple two-inlet T-sensor, with laminar flow, and a competitive format. It has been demonstrated that three inlets will enable the analysis of a reference solution concurrently with analysis

of an unknown – referred to as a “control T-sensor” – and has obvious implications for facile assay standardization.<sup>12</sup> The fluidics are correspondingly more complicated. Flow is also not a requirement – a hydrogel T-sensor has been investigated<sup>5, 13</sup> – arguably, this is not a *microfluidic* device. Relieving the system of the requirement of pumps is a significant advantage, but the advantage of “freezing” the time-course of the binding reaction at a point in space (Section 2.2.3) is lost, and photobleaching of the label confounds detection. A flow DIA configuration that premixes the analyte and the capture antibody has also been investigated.<sup>5, 13</sup> The response of the pre-mixed DIA is much simpler, and the technique may be more robust when the flow is poorly controlled, but it is more sensitive to variation in the dissociation rate of the immune complex.

*2.2.2.2. Other Detection Methods:* The germinal DIA uses fluorophore-labeled analytes to create a detectable signal; but, any signal generation method that enables the detection of the spatial distribution of analyte in solution should be applicable. For example, work is ongoing in the Yager Lab to use surface plasmon resonance (SPR) microscopy<sup>14, 15</sup> as a label-free detection technique for microfluidic immunoassay.<sup>16, 17</sup> This represents a significant change for the DIA because of the introduction of the additional surface effects.<sup>18, 19</sup> The design rules developed for the germinal DIA and in this work may not be applicable to an SPR DIA. Conductivity measurement<sup>20</sup> and refractive-index-gradient detection<sup>21, 22</sup> have both been shown to be able to detect cross-channel diffusion – extending those techniques to the DIA seems possible, under specific solution conditions. Other signal-generation/detection methods can be envisioned (e.g., optical absorbance), but may not be able to provide adequate performance. Fluorescence is used as the signal generator for all of the work described herein – different detection modalities are not the focus of this research.

During the development of the germinal DIA, it became obvious that the auto-fluorescence of the materials used to make the T-sensors could have a significant

effect on the background (Section 2.4.3). One potential solution to this problem is investigated herein (Section 4.1.1.) Another possible solution – the use of a confocal detector to eliminate the confounding effects of the material – has also been investigated.<sup>23</sup> The use of the confocal detector does enable low limit-of-detection DIA in high background materials, but significantly complicates the detection apparatus.

### **2.2.3: Corollary Consequences of the Germinal DIA**

There are several corollary consequences to particulars of the germinal DIA design. These affect the nature of the signal and the analyte response; and can create artifacts if not understood, or can be exploited to improve the assay. Therefore, some explication of these phenomena seems justified.

*2.2.3.1. Degenerate Dimensions:* One of the most interesting and unique aspects of the *flow* DIA is that the Eulerian perspective of fluid mechanics is practically manifested, with consequences for prediction and interrogation of the system. The Eulerian perspective advocates that it is more fruitful to examine what is happening at a particular location in space -- the *control volume* -- rather than tracking individual molecules or populations of molecules<sup>24</sup>. The operation of the T-sensor naturally favors this perspective, as does the method of optical interrogation used for the germinal DIA. In the operation of the T-sensor, the inlet-streams are opposed orthogonally to the direction of laminar flow, and there is an absence of convective mixing. As a result, the distance downstream of the line where the inlet streams first meet corresponds to how long the inlet streams have been in contact (because flow velocity includes both time and distance.) When the inlet feed solutions and flow rates are uniform over time – as they are in the flow DIA – then the downstream distance is directly proportional to the amount of time that the solutes in those solutions have been interdiffusing and reacting with one another; *and remain so, as long as the inlet feed solutions and flow rates stay uniform.* Thus, the time evolution of the diffusion



and reaction of the solutes is “frozen in space”; i.e., one can interrogate a single location for as long as desired and observe what is happening to the system at a particular interaction time, because of the steady state conditions.

This property of the DIA enables integration of the signal over time to increase the magnitude of the signal. Signal integration can also improve the signal-to-noise ratio, since integration acts as a selective filter for high-frequency random noise. This property also enables the simplification of numerical modeling used to predict the behavior of the DIA – one of the four dimensions of spacetime (time since start of interaction) can be collapsed into another ( $z$ -coordinate) as explicated below (Section 2.2.4).<sup>viii</sup>

*2.2.3.2. The Kamholz Number and Detection Artifacts:* A consequence of the optical method of detection used in the germinal DIA is an inability to detect the distribution of mass along the optical axis (the  $w$  dimension in Figure 2.2). To a first approximation the intensity observed at any point in the intensity profile is the integral of the mass distribution (as a function of  $w$ ) from the top to the bottom of the channel.<sup>ix</sup> This fact, coupled with the non-uniform velocity profile intrinsic to duct flow has produced puzzling and difficult to diagnose artifacts in the apparent mass distribution during T-sensor measurements of diffusion coefficients.<sup>25-27</sup> In short, solutes in the slower moving lamina close to the top and bottom of the channel have

---

<sup>viii</sup> The correspondence between downstream distance and time is complicated somewhat by the non-uniform flow velocity in ducts, and by the flow development that is required when two duct-flows with non-uniform velocity profiles merge. Both of these phenomena simply modify the calculation of the distance/time relationship, however; neither invalidate collapsing the two dimensions of the simulation into one.

<sup>ix</sup> This is an imperfect approximation because not all of the fluorescence produced in the entire volume of the channel under one pixel will enter the detector, due to re-absorption by adjacent fluorophores and the emitted photon ray paths. The germinal DIA used dilute Ag\* reagents and low numerical aperture objectives, however; so the approximation is reasonable. The same reagents and detector is used for standardization and the determination of unknowns, so any accuracy errors are corrected for by calibration.

more time to diffuse into the opposing flow stream than do solutes in the central lamina. If predictions are made based on mean residence times calculated from volumetric flow rate, large artifacts in the prediction can arise. These artifacts have received extensive treatment in the literature.<sup>26-30</sup> The artifacts only apply to predictions made with reduced-dimension numerical models (Section 2.2.4) –models that account for the time evolution of all three spatial dimensions have not been impugned.<sup>26</sup> It has been shown that there is a regime of device dimensions, flow rates, and diffusion coefficients that are not significantly affected by these artifacts. A non-dimensional number (here denoted the Kamholz number,  $Kz$ , after the developer of the number) can be constructed from the Peclet number ( $Pe$ ) and the key device dimensions ( $Kz = wPe/L$ ) that can predict if the effect is significant for any set of conditions.<sup>26, 28</sup> A  $Kz$  less than  $\sim 5$  conservatively insures that the effect can be ignored. The  $Kz$  is conceptually related to the Taylor number ( $L_T = 8HPe$ ), which describes the length down a circular duct, at which the Taylor dispersion equations become valid descriptors.<sup>19, 31-33</sup> The germinal DIA for phenytoin was not significantly affected by this artifact, although the calculated  $Kz$  for the Ab did not meet the guideline.

*2.2.3.3. The Multivariate Nature of the DIA Response:* Examination of the modulated accumulation profiles (Figure 2.3) reveals that the nature of the germinal DIA response is multivariate – there is a change in the spatial distribution of mass at many different locations in the channel resulting from modulation by the sample analyte concentration ( $[Ag]$ ). This multivariate response is primarily a result of the diffusion of the Ab-Ag\* immune complex away from the site of its formation. Immune complex that forms at the interface of the inlet streams can sample the lamina surrounding their site of formation as they are transported downstream with the passing of time. New complexes also form from unbound solutes that diffuse across to the interface from the adjacent lamina. With an interaction time sufficient to produce a flux of labeled analyte into the interdiffusion zone adequate for detection,

there is also considerable diffusion of the complex, and the different populations of complex formed at different times differ in the average distance which they have diffused away from the interface. The result is an approximate Gaussian distribution<sup>34</sup> of the complex around the interface of the two flow streams.<sup>x</sup>

Another contributor to the multivariate nature of the response is the modulated removal of Ag\* mass from the unbound Ag\* population by the formation of immune complex. As it becomes bound in immune complexes, less unbound Ag\* is available to diffuse into adjacent lamina, so the mass of unbound Ag\* in those lamina is reduced, and that reduction is modulated by [Ag]. Thus there is not only *accumulation* of fluorescence in the center of the profile, but there is also *depletion* of fluorescence at the zones adjacent to the accumulation (especially on the Ag\* reagent side.) However, because of mass conservation, the phenomenon is not independent of complex formation. Thus, there is no real additional information available from this response. Nevertheless, the form of the response is modified, so that simple Gaussian models of the response are inadequate.

Because of these processes, the response may be detected in as much as one-third of the channel width. Since the intensity at each pixel across the diffusion dimension is a discrete variable, the modulated analyte response in an accumulation profile is intrinsically multivariate, suggesting that a multivariate calibration or response

---

<sup>x</sup> The spatial and temporal distribution of complex has the general

form:  $C(x, t) \cong k \int_0^t C_1 e^{kt'} + C_1 e^{kt}$  where  $C_1$  is a solution to the one-dimensional diffusion equation

without the binding reaction, and  $k$  is a coefficient of distribution in an irreversible reaction (a reasonable assumption for antibody binding reactions on the time scale considered. Note that  $t$  in this expression can represent both time, and the distance along the channel ( $z$ ), as discussed above. This is still an oversimplification. Both the Ab and Ag\* may diffuse into to the opposing stream before encountering their cognate binding partner, and the stochastic nature of the binding event ensures that they do not always bind when they have an opportunity. Thus the site of complex formation becomes a zone which broadens over time. However, given the typical reagent conditions of the germinal DIA – where [Ab] is much greater than [Ag\*], both reagent concentrations are high enough that continuum behavior is valid, and typical antibodies with their high association rates are used -- the effects of this complication are small.

calculation technique could yield superior response to noise ratios – a hypothesis addressed in this proposal (Section 4.2.3).

*2.2.3.4. The Non-linear Nature of the DIA Dose-response Relationship:* The non-linearity of the germinal DIA response as a function of sample analyte concentration for a fixed assay formulation is due a fundamental condition of the DIA – to create a competition between Ag and Ag\* for Ab binding sites that is sensitive to changes in Ag with a low limit of detection and maximal dynamic range, the concentrations of these reactants must be such that the impending saturation of Ab binding sites affects the response at high [Ag]. If there were an excess of Ab to avoid saturation, then the system would not be responsive to small differences in [Ag], because there would be no competition for the abundant Ab. The [Ag\*] could be kept low to enable good modulation by Ag without saturation; but, this would result in a low florescence signal and a reduced dynamic range. These types of design compromises are common to many competitive immunoassay formats, not just the DIA.

## **2.2.4: Predicting Germinal DIA Responses**

*2.2.4.1. The 2-D Model:* A two-dimensional numerical model developed by Kamholz<sup>25</sup> has been used to explore the design space of the germinal DIA. This simple model accounts for convection, diffusion and reaction in the T-sensor. The continuity equation for incompressible flow with chemical reaction<sup>35</sup> is the underlying governing equation for species  $n$  at concentration  $c_n$ , with diffusion coefficient  $D_n$ , undergoing reaction  $R_n$  while flowing in the velocity field  $\vec{v}$  (equation 10).

$$10) \quad 0 = D_n \nabla^2 c_n - \vec{v} \nabla c_n + R_n$$

Assumptions made to simplify the model include: fully laminar plug flow, no axial diffusion, no concentration gradients in channel depth dimension, uniform concentrations and steady state flow of inlet feed solutions. Flow development is also ignored. Applying these assumptions, the governing equation is simplified to:

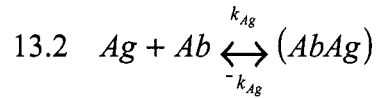
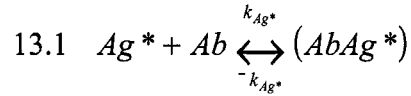
$$11) \quad 0 = D_n \frac{\partial^2 c_n}{\partial x^2} - v_z \frac{\partial c_n}{\partial z} + R_n$$

The assumptions of laminar plug flow, no flow development, and steady state inlet flow imply that  $v_z$  is constant everywhere in the device. Multiplying a constant velocity by a spatial differential creates a temporal differential; therefore,

$$12) \quad v_z \frac{\partial c_n}{\partial z} = \frac{\partial c_n}{\partial \tau} = D_n \frac{\partial^2 c_n}{\partial x^2} + R_n$$

where  $\tau$  is the residence time of a flow element in the main channel before the interrogation zone, which determines the amount of time that inlet streams have had to interact. Equation 12 is a mathematical statement of the steady state that enables interrogation of the system at a single location over long times discussed above (Section 2.2.3).

An additional simplifying assumption of the model -- simple bimolecular binding kinetics -- can be summarized with two reaction equations:



This assumption creates an equation that describes each of the five  $R_n$ :

$$14.1) \quad R_{Ag^*} = \frac{\partial c_{Ag^*}}{\partial t} = -k_{Ag^*} c_{(AbAg^*)} - k_{Ag^*} c_{Ag^*}$$

$$14.2) \quad R_{Ag} = \frac{\partial c_{Ag}}{\partial t} = -k_{Ag} c_{(AbAg)} - k_{Ag} c_{Ag}$$

$$14.3) \quad R_{Ab} = \frac{\partial c_{Ab}}{\partial t} = \frac{\partial c_{Ag^*}}{\partial t} + \frac{\partial c_{Ag}}{\partial t}$$

$$14.4) \quad R_{(AbAg^*)} = \frac{\partial c_{(AbAg^*)}}{\partial t} = -\frac{\partial c_{Ag^*}}{\partial t}$$

$$14.5) \quad R_{(AbAg)} = \frac{\partial c_{(AbAg)}}{\partial t} = -\frac{\partial c_{Ag}}{\partial t}$$

**2.2.4.2. Solution Methods:** The spatial derivatives are discretized with a finite-difference technique (FDT), a method that is based on the same differencing algorithms used to estimate the slope profile. These algorithms are based on the

addition and subtraction of Taylor series expansions of the derivatives of interest. For the one-dimensional derivatives discretized here<sup>6</sup>:

$$15.1 \quad \frac{\partial c_i^{n+1}}{\partial x} = \frac{c_{i+1}^n + c_{i-1}^n}{2\Delta x} + O(\Delta x^2) \quad \text{where, } c_i^n = c(x_i, t^n)$$

$$15.2 \quad \frac{\partial^2 c_i^{n+1}}{\partial x^2} = \frac{c_{i+1}^n - 2c_i^n + c_{i-1}^n}{\Delta x^2} + O(\Delta x^2) \quad \text{and, } O(\Delta x^2) \text{ is the order of the error}$$

The initial condition for this model is the concentration profile of the two joined inlet streams before diffusion and reaction have occurred.<sup>xi</sup> Namely:

$$16) \quad \text{for } x = 0 \rightarrow d/2, \quad c_{Ab} = [Ab], c_{Ag} = c_{Ag^*} = c_{(AbAg)} = c_{(AbAg^*)} = 0$$

$$\text{for } x = d/2 \rightarrow d, \quad c_{Ag^*} = [Ag^*], c_{Ag} = [Ag], c_{Ab} = c_{(AbAg)} = c_{(AbAg^*)} = 0$$

Where the concentrations  $[Ab]$ ,  $[Ag]$ , and  $[Ag^*]$  represent the concentrations in the inlet solutions. A false boundary technique was used at the domain boundary corresponding to the channel walls to properly account for the no-flux boundary condition at the walls. The center node is set to a concentration of half the feed solutions to avoid numerical artifacts resulting from the discontinuity.

The resulting system of five ordinary time-domain differential equations is easily solved with the ODE45 Runge-Kutta solver in MATLAB (The Math Works Inc.,

---

<sup>xi</sup> Ignoring flow development and entrance effects.

Natwick, MA). As coded by Dr. Kamholz, a typical DIA accumulation simulation with a few hundred nodes took a several minutes. During my preliminary explorations with the model it became clear to me that it could be sped up by replacing *for* loops with indicial reference vectors, and typical simulations of this resolution now take about ten seconds.

*2.2.4.3. Validation:* Although several of the assumptions of the two-dimensional model are crude, the model has been shown to adequately describe the important phenomena in the phenytoin DIA.<sup>1</sup> The effects of these assumptions have been examined in detail by Kamholz and others.<sup>5, 19, 26-30</sup> The model is able to describe the behavior of the DIA with adequate accuracy (with some exceptions as noted in Section 2.2.3) within the parameter space of the assays we describe here. It should be noted that analytical solutions to the problem under some subsets of the parameters and assumptions made for the two-dimensional numerical model are possible.<sup>30, 32, 34</sup> In addition, more sophisticated commercially-coded modeling tools have become available recently. Nevertheless, this model has also been proven to be a useful tool for fast prediction of design changes in a number of similar applications in our lab. All of the simulations of diffusion and accumulation contained in this dissertation were done with this model.

### ***2.3. Comparison of the DIA with other microscale assay techniques***

There has been an explosion in the number of micro-scale immunoassay techniques in the last decade, as the field of microfluidics and microelectromechanical systems (MEMS) has grown. (For the purposes of this discussion, *micro-scale* is defined as having at least one characteristic dimension smaller than one millimeter.) Some techniques have received extensive attention with many publications devoted to their characterization; e.g., micro-capillary immunoelectrophoresis, and surface-plasmon



resonance (SPR) immunosorbant assays. Other newer techniques –like the DIA and micro-cantilever immunosorbant assays -- display unique characteristics that deserve additional attention. While a totally comprehensive review of micro-scale immunoassay techniques is beyond the scope of this document, the most important competitors to the DIA are surveyed here, and their strengths and weaknesses discussed.

### **2.3.1. Immunosorbant Arrays**

*2.3.1.1. ELISA:* The enzyme-labeled immunosorbant assay (ELISA) has been a workhorse in clinical and research laboratories for many years.<sup>36, 37</sup> Although, it is not inherently microfluidic, ELISA has been so influential that any discussion of immunoassay techniques would be incomplete without some mention of this technique. In ELISA, a binding species (either antibody or analyte, depending on the exact format) is immobilized in the wells of a microtiter plate, which enables successive reagent additions and washing steps to effect the separation of bound analyte from interfering species. The physical separation steps result in a separation of the analyte response from much of the interfering noise. An enzyme label is used to transduce and amplify the binding information into a detectable optical signal via turnover of a colorigenic or fluorogenic substrate. Several different formats enable response generation. The 96-well culture plate is still used extensively for ELISA, but 384-well and 1536-well plates are available, and miniaturization of 96-well plate assays to these higher-density, smaller-volume formats is possible.<sup>38-43</sup> The reduction in reactant volume comes with a penalty in sensitivity, however. Since ELISA almost always relies on optical detection, the reduction in reaction volume is accompanied by a concomitant reduction in the mass of optically active species available for interrogation, thus dictating the limit-of-detection (LOD) practically achievable.<sup>44</sup> In addition, the precise transfer and dispensing of the small volumes of liquid into the spatially confined array becomes much more challenging, necessitating expensive

robotics for maximum precision and throughput.<sup>45</sup> Nevertheless, the plate-based ELISA remains a popular technique, due primarily to the fact that so many cell line and compound libraries are archived in the plate format.

*2.3.1.2. Microarrays:* Another popular technique that is very closely related to micro-ELISA is protein array chips.<sup>46-53</sup> In essence, the chip is a smaller version of a micro-well plate, but with greater packing densities, and frequently without the topological definition of individual wells. For some materials up to a 10,000 fold savings in material may result compared to a comparable 384-well ELISA.<sup>46</sup> The assay elements are frequently the same.<sup>48, 52</sup> Binding species are adsorbed to the chip as in an ELISA, covalently linked, or absorbed into a hydrogel coating, in a well-defined array.<sup>47, 48, 50, 53</sup> Transport of reactants to the surface may be assisted by electrophoresis.<sup>53</sup> Fluorophore-labels are frequently used to combine simplicity with detection sensitivity.<sup>49, 53</sup> Soluble products of amplifying enzyme reaction are not spatially confined for interrogation so enzymes producing detectable precipitates are preferred.<sup>53</sup> Reagent and sample additions are generally performed on the entire chip, which alleviates the liquid dispensing problems (at least post-fabrication... manufacturing these chips has all of the same problems), but dictates that sample multiplexing is not feasible. Because of the sample multiplexing limitation, this technique is most suitable for drug discovery and proteomics,<sup>46-48, 50</sup> rather than clinical testing of single analytes or small panels. The small interrogation mass creates the same optical detection challenges as micro-ELISA, albeit even more severe—necessitating the use of high-power laser excitation and powerful detection optics.<sup>49, 54</sup> The equipment required is readily available because of the popularity of nucleic-acid array assays.<sup>54</sup> This technique will, no doubt, become increasingly important.<sup>55</sup>

## **2.3.2. Other Approaches to Microscale Flow Assays**

*2.3.2.1. Micro-CE:* One of the most thoroughly studied techniques in recent years has been micro-capillary electrophoresis ( $\mu$ CE).<sup>56-58</sup> In this technique, an electrical

potential is applied to either end of a capillary to produce electrophoretic or dielectrophoretic separation of charged or polarizable species. Bulk fluid manipulation is generally done by electroosmotic pumping, which works well in channels a few hundred nanometers to a few hundred microns.<sup>59</sup> Solutes are also transported by electrophoretic and dielectrophoretic forces, and diffusion -- making the force balance for any solute rather complex.<sup>60</sup> The small dimensions enable field strengths that produce thousands of theoretical plates for highly efficient separations.<sup>58</sup> The connecting of the  $\mu$ CE device to the macro-scale devices required to operate it (sometimes referred to as the *world-to-chip interface*) is simplified by the lack of pressure-driven pump connections. The technique is not without shortcoming, however. A variety of detection methods are used for  $\mu$ CE, and many have poor limits-of-detection;<sup>61-64</sup> however, other researchers have used high intrinsic fluorescence to reach a very low limit of detection.<sup>65</sup> Electroosmotic pumping is notoriously sensitive to the changes in surface charge properties that accompany fouling by reagents and contaminants from complex samples (especially proteins.)<sup>60, 66,</sup>  
<sup>67</sup> The world-to-chip interface is simple, but generally requires a power supply capable of producing significant electrical potential (kilovolts). Despite these shortcomings, this remains a very popular micro-scale technique, and new research appears regularly that claims to overcome these shortcomings.<sup>68</sup>

**2.3.2.2. Micro-FIA:** Flow injection analysis (FIA) is a simple and popular technique that uses automated valves and pumps to introduce a liquid sample plug into a flowing stream of indicator.<sup>69-71</sup> The analyte in the sample and the indicator are then mixed by Taylor dispersion as they flow downstream to a detector.<sup>72</sup> In its original form, a colorogenic or electrogenic reaction between the analyte and indicator was required to generate a detectable signal. The menu of available analytes has been expanded by the sequential injection of multiple reagents and the introduction of functionalized and fluorescently-labeled beads into the FIA system.<sup>73</sup> Specialized detector cells have enabled application of these reagent systems.<sup>74, 75</sup> The tubing used for FI manifolds has

typically been sub-millimeter for some time, so the FIA can be considered one of the first workable microfluidic assay systems. Further miniaturization has resulted in “lab-on-a-valve” systems which consume microliter quantities of reagents.<sup>76</sup> When optical detection is used, however, the usual limits to scale-down are encountered.

### 2.3.3. Label-free Detection and Microfluidic Immunoassays

Three relatively label-free detection techniques have received considerable attention from microscale assay designers. Combined with microfluidic sample delivery and surface functionalization by antibodies, they can greatly simplify assay formats.

*2.3.3.1. SPR:* Surface plasmon resonance (SPR) is a detection principle that enables label-free detection.<sup>77-79</sup> In SPR detection, polarized light reflected from the backside of a metal-coated surface produces an evanescent field in the metal. At a critical wavelength and angle, the oscillations of the incident light are coupled to electrons in the metal and a surface wave (*plasmon*) is produced on the front side of metal. The coupling dramatically reduces the energy of the reflected light. This plasmon resonance is very sensitive to the index of refraction of the medium on the front side of metal layer; thus the presence of biomolecules (either in solution above the surface, or bound to the surface) can be detected by changes in the intensity of the reflected light (or changes in the critical wavelength and angle of the minimum intensity.)<sup>80, 81</sup> The rapid exponential decay of the evanescent field (capable of responding to molecules within ~300 nm of the sensor surface) defines this technique as microfluidic, and the most useful instruments use microfluidic flow-cells to introduce the sample to the surface to without diffusion limitations.<sup>80, 82</sup> (Although, the combination of SPR detection and microarrays could be a powerful combination<sup>55, 83</sup>) This transduction principle is not intrinsically very specific – any molecule that changes the index of refraction is detected – so specific recognition molecules (e.g., antibodies) and separation methods are required.<sup>79, 81</sup> It is also not a terribly sensitive technique, so amplification by secondary binding of more massive species may be

required.<sup>81, 84-88</sup> Nevertheless, the potential for this new method is considered great. As mentioned previously, this label-free detection technique may have application in the DIA.

*2.3.3.2. Acoustic Waves:* Acoustic wave sensors are an example of a MEMS sensor technology that exploits the advantages of the micro-scale. These sensors exploit the predictability of acoustical waves excited in piezoelectric materials as an assay principle.<sup>89</sup> An AC field is applied to generate a wave, and in some devices, the wave is detected via the piezoelectric effect after perturbation by the mass of interest. The wave amplitude and frequency is modulated by the addition of analyte mass to the surface of the crystal. Functionalization of the surface by a specific antibody enables an acoustic wave immunoassay.<sup>90</sup> The mass sensitivity of these devices scale with their size – the smaller they are, the more sensitive to changes in mass they are.<sup>89</sup> So tiny devices can enable label-free detection. In addition, amplification is possible by using specific-binding mass tags.<sup>91</sup> The primary difference between the different types of piezoelectric mass detectors is in the type of wave sensed (e.g., thickness-shear, surface acoustic, flexural, and horizontal-shear) and in the detection circuitry.<sup>89, 92, 93</sup> The biggest limitation of these detectors comes from acoustical coupling of the vibrations to the medium above the detector.<sup>94</sup> Thus, they are most effective in gas or vapor sensing<sup>95</sup>; however, liquid samples can be used with drying after reaction, or if the viscoelastic properties of the sample are characterized.<sup>89, 94</sup>

*2.3.3.3. Microcantilevers:* The use of microcantilevers as mechanical transducers for micro-scale immunoassay is a relatively new technique that exploits the deflection of the microcantilever upon specific binding of an analyte.<sup>96-98</sup> A deflection of the microcantilever results from changes in surface stress due to the specific binding of the analyte. By localizing the specific binding to one of the surfaces of the microcantilever, a differential surface stress between the opposite sides is created, which causes the deflection of the cantilever.<sup>99-101</sup> The specific interaction is localized

to one of the surfaces through selective gold plating and standard gold/thiol functionalization chemistry. The direction of the deflection depends on the sign of the surface stress change at the functionalized surface. The signal measured is the difference in differential surface stress before and after analyte binding, since the functionalized surface is already different from the opposite side. This technique generally operates adequately without labels. In addition to immunoassay, this assay principle has been demonstrated for DNA hybridization, streptavidin/biotin binding, non-specific adsorption of proteins, and pH and gas adsorption into a polymer.<sup>96, 97, 102, 103</sup> Detection of the deflection can be done by several different means: The most common method is to monitor the angle of reflection of a laser directed at the gold surface with a position sensitive photodiode.<sup>98</sup> This method is sensitive to anything can effect the light in its path; e.g., changes in index of refraction of the feed solution, scattering from particles, etc. Interferometry, capacitance monitoring,<sup>96</sup> and piezoresistively-modulated voltimetry<sup>104</sup> have also been used as detection techniques with microcantilevers, and show great promise in advancing the utility of this interesting new technique.

#### **2.3.4. Distinguishing Features of the DIA**

Each of the techniques discussed above has its characteristic strengths and weaknesses. In the context of these competitors, it is instructive to consider those features of the DIA that differentiate it from other techniques. Perhaps the most powerful distinguishing feature of the DIA is the property that enables the time-evolution of the binding reaction to be captured at a point in space (discussed in detail in Section 2.2.2.) Theoretically, this should enable a very low limit-of-detection, as long as other noise sources are controlled. The ability of the DIA to be used in a continuous flow mode is also somewhat unique – no recharging or regeneration of the system is required. This feature may have greater potential in process monitoring or water quality testing, than in clinical diagnostics where the samples are usually small

discrete volumes. The DIA is also faster than many of the other microfluidic immunoassay techniques, because it does not require the equilibration of binding for precise signal generation – the antibody association rate is the key binding parameter. This property also makes it less sensitive to variation in antibody affinity, since most affinity differences arise from dissociation rate differences.<sup>105</sup> Because the DIA is a bulk-phase assay, it does not suffer from the mass transport limitations and unpredictable protein activity changes that frequently accompany immunosorbant techniques. Finally, the self-referencing nature of the accumulation profile enables inter-assay normalization not possible with many other techniques (discussed in detail in Section 2.2.1.) These distinguishing features imply a unique place for the DIA in the armamentarium of the biochemical analyst.

#### ***2.4 Anticipated Challenges for a POC Protein DIA***

Four primary challenges were anticipated in adapting the germinal DIA performed in plastic devices to protein analytes. 1) A reduction in the maximum DIA signal available was expected, due to differences in some of the key design parameters that are unavoidable when a protein is the analyte. 2) The relatively unsophisticated signal processing algorithms used in the germinal DIA were expected to be insufficient for resolving the smaller responses anticipated with a protein DIA. 3) The auto-fluorescence of the materials used for plastic device fabrication in our lab was expected to significantly complicate data reduction. 4) The adsorption of the proteins in the reagents and/or the analyte was expected to complicate the design and/or interpretation of results. This section summarizes what was known about these problems, from literature or preliminary work, at the outset of this research.

### 2.4.1. Differences in Key Design Parameters with Protein Analytes.

The diffusivity of the analyte, the ratio of diffusivity of the analyte and the immune-complex, and the binding reaction coefficients; are the key physicochemical parameters that determine the magnitude of the DIA signal.<sup>106</sup> There are significant differences in these parameters between phenytoin and the model proteins (Table 2.1). The diffusivity ratio of the analyte and complex ( $D_{Ag}/D_{(AbAg)}$ ) is much smaller for a slowly diffusing protein analyte than for a small molecule. The association rate for antibodies and protein antigens are also somewhat lower, due to the slower rotational diffusion of a large protein (compared to a small molecule.) From the description of the germinal DIA (Section 2.1) it can be inferred that both these parameters are both important in producing a DIA response. These parameters are intrinsic properties of the analyte and the necessary reagent components defined by the germinal DIA, and are generally not accessible for manipulation.

**Table 2.1.** A comparison of key physical and biochemical properties of phenytoin, HRP, and IgG that will affect the magnitude of the accumulation signal. Key parameters were estimated from published values for the model protein or similar proteins<sup>107-111</sup>.  $D_{Ag}^*$ = diffusion coefficient of the labeled analyte  $D_{Ag}$ = diffusion coefficient of the sample analyte,  $D_{Ag}:D_{AbAg}$ = ratio of analyte diffusivity to immune-complex diffusivity  $k_{on}$ = forward kinetic constant of Ab/analyte bimolecular binding,  $k_{off}$ = reverse kinetic constant of Ab/analyte bimolecular binding. The binding constants are assumed to be the same for both LA and SA.

Parameter	Phenytoin	HRP	IgG
$D_{Ag}$ ( $\text{cm}^2\text{s}^{-1}$ )	$3.2 \times 10^{-6}$	$6.8 \times 10^{-7}$	$4.3 \times 10^{-7}$
$D_{Ag}^*$ ( $\text{cm}^2\text{s}^{-1}$ )	$5.8 \times 10^{-6}$	$6.8 \times 10^{-7}$	$4.3 \times 10^{-7}$
$D_{LA}:D_{AbLA}$	7.4	1.7	1.3
$k_{on}$ ( $\text{M}^{-1}\text{s}^{-1}$ )	$4 \times 10^6$	$2 \times 10^5$	$2 \times 10^5$
$k_{off}$ ( $\text{s}^{-1}$ )	$1 \times 10^{-4}$	$2 \times 10^{-3}$	$2 \times 10^{-3}$

In the germinal DIA, the choices of reactant concentrations also determine maximum signal magnitude and analytical response throughout the target dynamic range. While these parameters *are* variable in the design space, the choices of these concentrations



are driven by the clinical context. We targeted a limit-of-detection in the nanomolar range in order to make the demonstration of protein DIA clinically relevant.

In planning this research, we anticipated that a protein DIA must be designed differently than a small molecule DIA to achieve useable accumulation signals. The lower diffusivity of a protein necessitates either longer interaction times or more concentrated Ag\* reagents – there must be a sufficient amount of Ag\* flux to create a detectable accumulation. The smaller ratio of diffusivity of the analyte and the immune complex, and the slower association rates of proteins with their cognate antibodies, reduce the magnitude of the accumulation relative to the background signal of freely diffusing analyte. Thus, the first aim of this research was to explore the design space with simulations to find a reasonable formulation of the germinal DIA and then verify that the simulations were accurate (Section 3.1)

Given the high probability that the germinal DIA for proteins would not display signals and responses on the order of the phenytoin DIA, methods to biochemically restore the diffusivity ratio -- through immobilization of the capture antibody onto a bead, macromolecule, or other slowly diffusing species -- were also investigated in this dissertation (Section 4.3.).

#### **2.4.2. Signal Processing Algorithms**

The algorithms used in the germinal DIA to transform the information contained in a raw accumulation image into a predictor function capable of accurately and precisely quantifying an unknown were sufficient to establish the proof-of-principle for the phenytoin DIA.<sup>1</sup> It became obvious in reporting on these results, however; that several of the steps might not be adequate for a protein DIA. As discussed earlier (Section 2.2.1.), the boxcar smoother did not adequately smooth the accumulation

profiles enough to enable the application of a standard centered-difference slope estimation – a larger step-size was required to affect further smoothing. The multivariate nature of the data was not efficiently exploited – only two of the many channel locations that display an analytical response were used in the response calculation (Section 2.2.1.) Finally, the potential of a linearizing and variance-stabilizing data transformation was not exploited (Section 2.2.1.) Given the lower signal-to-noise ratio anticipated for a protein DIA, identifying better algorithms seemed necessary, and perhaps challenging (Section 4.2).

### **2.4.3 Autofluorescence of Plastics**

It was expected at the outset, from both literature searches and anecdotal experience, that the auto-fluorescence of the Mylar® film (polyethylene terephthalate polyester) would be an important lurking variable.

There are many fabrication techniques that can be used to construct plastic and polymer, lab-on-a-chip devices – for several years, the Yager Lab has used direct-write CO<sub>2</sub>-laser cutting of polymer films and adhesive-lamination to achieve finished three-dimensional microfluidic channels within a few hours of completing the design drawings<sup>1, 106, 112, 113</sup> CO<sub>2</sub>-laser photoablation is a well-described technique.<sup>114, 115</sup> This method enables rapid prototyping – a great benefit for iterative device design cycles (although, the intended end-uses of our optimized designs are as disposable analysis chips.) It also enables fabrication of fairly complex three-dimensional structures with straight channel side-walls (an advantage for numerical simulation.) The choice of polymer film type is driven by the physical and optical properties, and the availability of the material. In the past, optical grade Mylar™ film has represented the best compromise by these criteria.

It has long been known that many polymers and plastics are fluorescent, particularly when excited with UV (<400 nm), blue (400-500 nm) and green (500-550 nm)

light.<sup>116</sup> In some cases, the fluorescence is intrinsic to the bulk polymer, in other cases, additives, impurities or degradation products are implicated.<sup>117</sup> From the perspective of the fluorescence-detection device designer, the source of fluorescence is unimportant – as long as it can be characterized, avoided or eliminated. It is beyond the scope of this proposal to comprehensively consider these sources.

Device autofluorescence will impact the on-chip detection of fluorescently-labeled reporters primarily through an increase in the intensity of background fluorescence<sup>116, 118</sup>. In the case where the background noise does not overwhelm the signal of interest, and is constant over the time-scale of the analysis, the simple difference algorithm described for the germinal DIA is sufficient to correct for the background. Robust correction algorithms are more difficult to formulate when the device fluorescence changes systematically on the same time-scale as the signal of interest.

Most investigators have minimized confounding background by employing confocal optics,<sup>23, 119</sup> two-photon excitation,<sup>120</sup> long wavelength fluorophores,<sup>121</sup> modulating the signal of interest and employing lock-in detection,<sup>116</sup> or simply working at a high enough fluorophore concentration that the signal-to-noise ratio is acceptably high. However, these solutions were not compatible with the design goals of the POC protein DIA.

The phenytoin DIA required the detection of small fluorescence signals due to the small volumes and low concentrations of fluorophore solutions interrogated. This was accomplished by integration of the camera signal over several minutes. However, long integration does not always improve signal-to-noise ratios significantly – depending on the dominant sources of noise. For example, the background scales identically with the signal so integration yields nothing. In contrast, CCD-detector noise scales with the square root of the intensity, so integration may help. With the phenytoin DIA, long integration was needed to elevate the signal from the CCD noise; but it also separated the measurement of the background from the measurement of the

signal of interest over enough time that systematic variation in the background was convolved with the results. Thus, while gathering data for the phenytoin DIA, it became obvious that the background fluorescence of a Mylar device was significant compared to the signal of interest. To mitigate these effects, the phenytoin DIA was performed in a device made with glass cover-slips as the capping layers in the three layer laminate – only the channel was made with Mylar.<sup>1</sup>

As discussed previously, (Section 1.5) plastic has significant advantages for POC applications, so the glass-capped devices used for the phenytoin DIA were rejected as unrealistic. In addition, stresses introduced to the cover slips from the drilling of access holes make these devices very prone to breakage, even in the carefully controlled environment of the research laboratory. Thus, a comprehensive investigation of the autofluorescence of commercially available polymer films was included as an aim of the research (Section 4.1.1.)<sup>xii</sup>

#### **2.4.4. Adsorption of Proteins to Plastics**

It was also expected at the outset of this research, from both literature searches and anecdotal experience, that the adsorption of protein analytes and reagent components to the device would require mitigation.

The generality of protein adsorption to surfaces is a topic that has consumed countless researchers in numerous disciplines and resulted in thousands of publications.<sup>122-128</sup> Despite the sustained effort directed at understanding this phenomenon, the field remains quite active. Part of the recalcitrance of the problem is due to its intrinsic complexity.<sup>129-131</sup> Proteins are a diverse class of biomolecules capable of displaying a variety of activities, many of which are not well understood. Surface chemistry can

---

<sup>xii</sup> It should be noted, that results for the HRP germinal DIA were generated using a glass-capped device. The breakage problems noted above were somewhat mitigated by substituting a glass slide for the cover-slip. As will be shown later (Section 3.2.1.) this created an increase in the background fluorescence of its own.

vary greatly as well.<sup>132</sup> The properties of the solvent from which the adsorption occurs is also important<sup>133</sup>, and can vary greatly. Nevertheless, it is not unreasonable to state that “every protein will adsorb to some surface from some solvent to some degree.” In addition, trends can be identified. “Soft” or “globular” proteins tend to adsorb more readily and avidly than “hard” or “rigid” proteins.<sup>129, 131</sup> Highly-charged proteins tend to adsorb more than neutral ones if the surface has an opposite charge, and less if it is the same charge.<sup>133</sup> Some of these trends have obvious physicochemical origins; e.g., electrostatic forces acting on charged species.<sup>129, 133</sup> Other trends require invocation of more complicated theory; e.g., the high avidity of hydrophobic surfaces for globular proteins in aqueous solution is thought to involve the entropy gain that is realized by the water molecules when they are displaced from their more ordered location near the surface by hydrophobic residues in the protein.<sup>131, 134</sup> Other additional trends are cryptic.

Microfluidic systems are particularly sensitive to adsorption of solutes onto their wall surfaces due to the large surface-to-volume ratio of the typical channel. Many microfluidic device designs rely on the delivery of a solute at a specified concentration with precise timing by such a channel. If that solute adsorbs to the walls of the channel, either permanently or transiently, its expected delivery is compromised. In this event, the duct has become a sink, or a chromatography column. Given that many of the proteins used as reagents and/or analytes in the DIA have a high potential for adsorption to common channel materials, adsorption was deemed a potential problem.

From the standpoint of a microfluidic device designer, it is probably more meaningful to approach individual systems of proteins and surfaces, than to attempt to find global solutions. Manipulation of the accessible design parameters (for example; solvent pH, antifouling coatings, antifouling solvent amendments, and device material) should result in system that is free from significant confounding by adsorption. The difficult

problem is how best to demonstrate that adsorption is not a lurking variable for a particular design.

Problems with adsorption are frequently discovered when a system does not behave as expected. Some failures are obvious: a labeled protein that adsorbs can significantly elevate the background signal, and the complete depletion of an assay component generally produces dramatic results. Other problems may be more insidious: a ten-percent reduction in an expected concentration of an unlabeled protein or the slowing of the transport of a reactant due to transient adsorption is more difficult to detect. Sometimes the most powerful indicator of lack of adsorption is the conformance of observations to validated theory. Unfortunately, modeling of transport in the channel is often limited by: 1) overly simple assumptions about surface binding behavior, and 2) lack of information about the kinetic and thermodynamic binding constants required for a fully determined model.<sup>135</sup> Numerical analysis is most effective when used as an adjunct to sensitive experimentation.

Many researchers in microfluidics have addressed the problem of protein adsorption. There has been considerable progress towards understanding the adsorption of proteins in capillary electrophoresis (CE) devices<sup>136-138</sup>, but it is difficult to apply these discoveries outside the CE field because the adsorption affects both the electrokinetic flow and the partition of solute between the solution and the surface.<sup>139</sup> Other microfluidics researchers have been content to look for residual material left on the surface after the analysis or reaction has been completed.<sup>133, 140</sup> This approach is generally one of the easiest, and has the advantage of being directly applicable to the device of interest, since it is usually done *in situ*. The approach suffers the considerable disadvantage, however, of ignoring the effect of transient adsorption. For many applications the slowing of solute transport may be as big of a problem as the permanent loss to the surface, and it is frequently harder to infer from other observations. All of these factors suggest the need for a flexible platform for assessing

the adsorption of a variety of molecules to a variety of surfaces in a channel that is representative of real microfluidic devices, and in a way that gives information about both permanent and transient adsorption without confounding by other effects. Thus, assessment of protein adsorption with such a tool was included in this research (Section 4.1.2.)

## **Chapter 3: Preliminary Work – The Germinal DIA for Two Protein Analytes**

In this chapter, the first attempts at applying the germinal DIA procedure to two model protein analytes (horseradish peroxidase and immunoglobulin G) are detailed (see Section 2.2.1 for a definition and description of the germinal DIA.) This work was performed before the extensive modeling described in Chapter 5, so the formulation used was not optimized for limit of detection or dynamic range. It was the results detailed in this chapter that motivated the work described in Chapter 4.

### ***3.1 HRP - Challenging the System***

Horsradish peroxidase (HRP) is used as a model of a medium sized (~45 kD) globular protein. A germinal DIA for HRP was expected to have a much smaller blank signal than what was observed for phenytoin. A reagent formulation was chosen using the numerical model described previously (Section 2.2.4) to assist in a brief exploration of the design-parameter space. The parameter search was delimited by a target dynamic range, physicochemical properties of the chosen materials, and realistic device dimensions.

#### **3.1.1. Apparatus**

The T-sensor used was a three-layer laminated device with the two outer layers made from glass (a slide and a cover slip) and the center layer made from Mylar with adhesive on either side (Fralock Inc., San Carlos, CA). A rectangular channel was cut into the Mylar layer with a CO<sub>2</sub> laser (Universal Laser Systems Inc., Scottsdale, AZ) to yield a straight channel with final cross-sectional dimensions of 100- $\mu\text{m}$  x 1600- $\mu\text{m}$ . Accumulation images were gathered 40-mm from the confluence of the inlet streams.



The T-sensor device was mounted on the stage of a Zeiss ICM-405 inverted, epifluorescence microscope (Carl Zeiss Inc., Thornwood, NY) and imaged the sensor through a 10x objective. Excitation light came from a Zeiss HB 100W mercury arc source (Carl Zeiss Inc., Thornwood, NY). A rhodamine filter set (excitation bandpass: 520-560 nm; dichroic beamsplitter: 580 nm; emission bandpass: 575-635 nm) conditioned the light. A Retiga 1300 (Q-Imaging, Burnaby, BC, Canada) cooled, 12-bit CCD camera was used for detection.

Two programmable, stepper-motor syringe pumps, both installed with 25  $\mu$ L syringes, provided pressure-driven flow (model # 50300: Kloehn, Las Vegas, NV). Pump control was accomplished with Windows Terminal Version 3.10.0.61 (Microsoft Inc., Redmond, WA).

### **3.1.2. Reagents**

A 100-mM phosphate buffer (pH 6.0) was used as a universal diluent for all solutions. After initial experimentation to assess protein adsorption, 1-mg/mL bovine serum albumin (*BSA*, part # A7030: Sigma, St. Louis, MO) was added to the phosphate buffer to minimize protein adsorption.

Monoclonal anti-HRP clone P6-38 (part #P2419: Sigma, St. Louis, MO) was diluted to 600-nM. Rhodamine isothiocyanate (RITC)-labeled HRP (part # P5031: Sigma, St. Louis, MO) was reconstituted and diluted to 100 nM with diluent. Unlabeled-HRP (part #P6782: Sigma, St. Louis, MO) was reconstituted with diluent. The concentrations of the HRP and RITC-HRP in these stock solutions were quantified by absorbance spectrophotometry using the extinction coefficient of the prosthetic heme group.

Test solutions were prepared by spiking unlabeled-HRP into the 100-nM RITC-HRP stock solution to the desired unlabeled-HRP concentration. The unlabeled-HRP stock was sufficiently concentrated that the dilution of RITC-HRP introduced by this preparation was <1.5%

A cleaning solution of ten percent (v/v) laboratory grade bleach (part # 4000147: Sysco, Houston, TX) was made fresh daily. Deionized water (Culligan Industrial Systems, Hillsboro, OR) was used for all solutions.

### **3.1.3. Procedure**

The T-sensor apparatus was operated as follows. Test solutions were introduced into the pump lines using a custom tubing manifold, so that each feed solution was controlled by a separate pump. The two pumps were both operated at 21 nL/s mean volumetric flow rate. After flow stabilization and feed solution wash in (~300s), ten replicate images were gathered for each sample, with ~30s between replicates. The camera operating software (Q-capture, Q-Imaging, Burnaby, BC, Canada) was manually triggered to integrate intensity data for ten seconds.

Signal processing and response number calculation was carried out as described for the germinal DIA (Section 2.2.1.) using Excel (Microsoft Corp., Redmond, WA, USA)

Solutions containing varying concentrations of unlabeled analyte throughout the expected dynamic range were assayed, for calibration standards and mock samples. Numerous replicates were gathered to enable statistically valid inferences. Numerous experimental runs were performed, over several months, using several reagent preparations, several T-sensors, and two different operators -- to include expected sources of variation. Thus inferences concerning response-to-noise relationships are robust, and probably represent worst-case performance.

### 3.1.4. Results

Initial attempts at obtaining HRP accumulations were invalid due to protein adsorption to the upstream tubing of the manifold. Support for this conclusion is provided later in this document (Section 4.1.2). All results presented in this section were generated with reagents formulated with 1 mg/mL BSA in the diluent to mitigate adsorption.

Examination of the simulations and representative experimental results for the HRP germinal DIA shows that the maximum accumulation signal is predicted and observed to be ~10% of the undiluted fluorescence of the fluorescent antigen reagent (Fig. 3.1A). The accumulation of the blank reagent is modulated by the varying sample analyte concentration, with almost total elimination of the accumulation at 800 nM sample analyte, again in good conformance with the predictions of the 2-D numerical model. Similar conformance to expectation was seen for other sample analyte concentrations (data not shown). It should be noted, that due to the mesh of the model and the field of view of the camera, there were slight adjustments to the abscissa required to create these plots (Figure 3.1A), but in all cases these adjustments were deemed to be within expected noise and systematic error.<sup>xiii</sup>

The slope plots (Fig. 3.1B) display the characteristic shape seen with phenytoin (Figure 2.4.B), but with a reduction in magnitude of the change in accumulation and modulation, and a dramatic increase in noise, relative to phenytoin. Note that it is visually difficult to resolve the slope plots for the three different analyte solutions spanning the dynamic range, primarily due to noise.

An analysis of covariance (*ANCOVA*) with a linear covariation model was performed on the whole data set to determine if the germinal DIA was capable of resolving the different sample analyte solutions, using the a statistical software package (SAS version 9.0, The SAS Institute, Cary, NC, USA). The data set is plotted for visual

---

<sup>xiii</sup> The systematic error included variation in the fluid interface from normal pump variation, and stage positioning error.

evaluation (Figure 3.1C). The results of the ANCOVA indicate that there is insufficient evidence to reject the null hypothesis that the solutions are all from the same population ( $Pr>F = 0.26$ ). No further calculations of figures of merit were performed on the germinal DIA.

### 3.1.5. Discussion

As expected, the reduced diffusivity and slower association rates of proteins results in germinal DIA accumulations that are smaller in magnitude than those observed with the phenytoin germinal DIA (Figure 3.1A and Figure 2.43A). The signal-to-noise ratio is also much smaller, due to the lower dynamic range the assay was designed for and the specific fluorescence of the conjugate (Figure 3.1A and Figure 2.4A). Together, these factors result in slope plots that are unresolved both visually, and using the data reduction algorithms of the germinal DIA (Figure 3.1B and Figure 3.1C), and which differ significantly from the phenytoin germinal DIA (Figure 2.4A).

It appears that the numerical model adequately predicts the accumulations expected from the HRP DIA (Figure 3.1A). This conclusion is not surprising given the conformance to the HRP DIA to the guidelines for the Kamholz number ( $Kz \approx 1.5$  for these assay conditions). The long interaction times required to create a flux of labeled analyte sufficient for detectable accumulation, also acts to eliminate the transverse concentration gradients that create the artifacts described earlier (Section 2.2.3).

The ANCOVA analysis establishes that the HRP germinal DIA as formulated is not functional as either a quantitative or qualitative assay. Nevertheless there is a visible response to sample analyte observed, it is simply unresolvable from the noise. This is fundamentally an apparatus, materials and/or algorithm limitation, not a limitation of the DIA technique itself – there are responses to detect, if the noise can be reduced to sufficiently low levels. This is the topic of the subsequent Aims. The results strongly suggest that the noise filtering algorithms will require examination (Section 4.2.1).

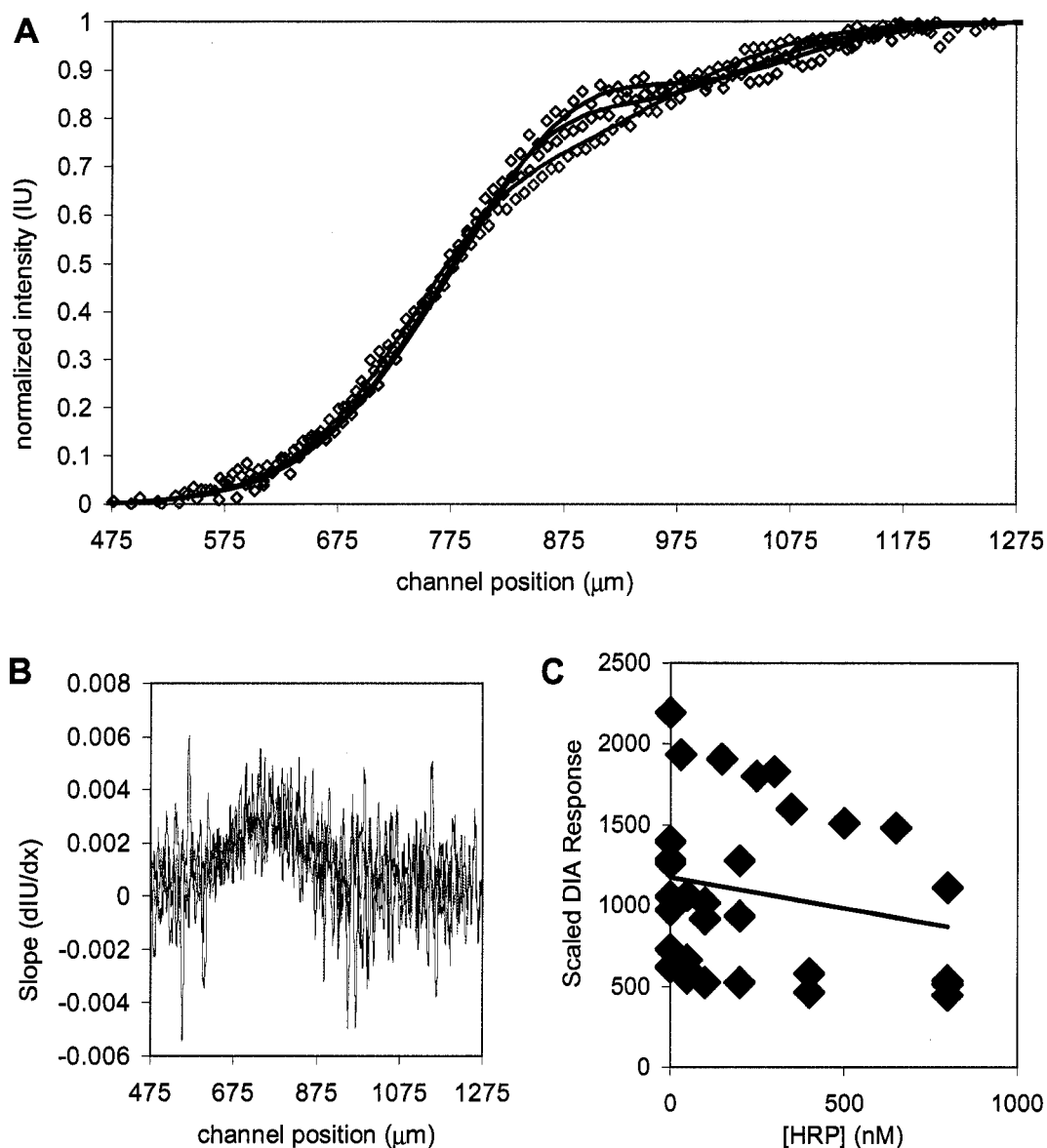


**Figure 3.1:** Representative results for the germinal DIA for HRP. Reagent formulation given in text. For both figures, **blue** is the blank signal, **red** is the response to 200 nM sample Ag, and **green** is the response to 800 nM sample Ag. A) Comparison of predicted and observed DIA accumulations for HRP. Lines are predictions from the 2-D numerical model, and the diamonds are a sparse plotting of the observations (one symbol every ten data points) after BFTN processing, and boxcar smoothing. B) The slope plot of the data in 'A'. C) A plot of the germinal DIA responses of all mock samples (rescaled to match the abscissa scale) as a function of HRP concentration. The fitted line ( $y = -0.3809x + 1172.4$ ;  $R^2 = 0.0422$ ) represents the linear covariation model used in the ANCOVA analysis (discussed in text).

Methods to amplify the analytical signal without increasing the noise should also improve the DIA (Section 4.2.3).

It should also be noted that the ANCOVA analysis as performed may not have substantial statistical power. Examination of the data plot (Figure 3.1C) shows that there may be a mean-dependence of the variance; i.e., there is more noise in the blank observations than there is in the high-analyte-concentration observations. This observation is, perhaps, trivial – the assay *should* be more sensitive to small changes in concentration in the part of the response curve where the response is not saturated. But it does have major implications for an ANCOVA analysis – a technique which assumes that the variances of the different “treatments” (different solution HRP-concentrations) are all identical and independently distributed.<sup>10</sup> In this case a data transformation to stabilize the variances is recommended.<sup>10</sup> The ANCOVA may also be based on an inappropriate model. We do not really expect the dose/response curve to be linear over the entire dynamic range. It is difficult to make any inferences about the appropriateness of the model from a data such with so much variation, however. Data transformation will be considered in Chapter 4 (Section 4.2.2).

### ***3.2. IgG – An Expectation of Failure***

Immunoglobulin G (IgG) is used as a model of a large (~150 kD) stiff protein. A germinal DIA for IgG was expected to have an undetectable blank signal. A reagent formulation was chosen using the numerical model with the same strategy taken with HRP. It should be noted that no formulation *simulated* gave an appreciable blank accumulation or analyte response, so the reactant concentrations chosen were somewhat arbitrary, and (as we shall see) fortuitous.

### 3.2.1. Apparatus

The same T-sensor and microscope set-up used for HRP (Section 3.1.1) was used for this work, with the following exceptions. This device was a three-layer plastic laminate -- the flow channel was cut out of a 0.10-mm thick layer of Mylar D coated on both sides with adhesive (Fralock, Santa Clara, CA, USA); inlet holes were cut through a 0.175-mm thick capping layer of Rohaglas #99524 PMMA (Cyro Industries, Orange, NJ, USA) and a second Rohaglas capping layer sealed the device. On the microscope, a FITC filter set (exciter: 480/30 nm; beamsplitter: 505 nm; emitter: 535/40 nm; Chroma Technology, Battleboro, VT, USA), was required due to the different fluorophore in the labeled analyte reagent.

### 3.2.2. Reagents

A 100-mM HEPES buffer, pH 7.5 (Sigma Chemicals St. Louis, MO, USA) was used as a universal diluent for all solutions. As with the HRP DIA, 1-mg/mL BSA (part # A7030: Sigma, St. Louis, MO) was added to the buffer to minimize protein adsorption. Test solutions preparation procedures and other reagents were the same as used in the HRP DIA (Section 3.1.2)

The MsIgG was obtained in both unlabeled and fluorescein-labeled (FITC-MsIgG) versions from a commercial vendor (Sigma Chemicals St. Louis, MO, USA) The  $\alpha$ -MsIgG (Chemicon International, Temecula, CA, USA) was diluted from the stock solution to a concentration of 381.5 nM (or a concentration of binding sites of 683 nM) with diluent. Numerous mock sample/reagent solutions were made with a constant concentration of FITC-MsIgG (25 nM) mixed with MsIgG to final concentrations spanning the expected dynamic range (0-1500 nM MsIgG), using the same diluent used to dilute the antibody.

### 3.2.3. Procedure

Operating procedures were identical to the HRP DIA (Section 3.1.3). Numerous replicates were performed to enable statistical analysis and include expected variation, as with HRP.

### 3.2.4. Results

Examination of the representative experimental results for the IgG germinal DIA shows that the maximum accumulation signal is observed to be ~15% of the undiluted fluorescence of the fluorescent antigen reagent (Fig. 3.2A). The accumulation of the blank reagent is modulated by the varying sample analyte concentration, with almost total elimination of the accumulation at 1500 nM sample analyte. These observations do *not* match the predictions from the 2-D numerical simulations, except at the highest analyte concentration tested (Fig. 3.2A).

The slope plots (Fig. 3.2B) display the characteristic shape seen with phenytoin (Figure 2.4.B) for the blank signal; but, for the higher analyte-concentration solutions, the shape of the slope profile is somewhat different than that of phenytoin. There is also a similar amount of noise in these plots compared to the phenytoin DIA, even though the analyte concentrations are significantly lower. Note that it is visually easy to resolve the slope plots for the three different analyte solutions spanning the dynamic range.

An ANCOVA analysis with a linear covariation model was done on the whole data set as with HRP, and the results plotted for examination (Figure 3.2C). The results of the ANCOVA indicate that there is sufficient evidence to reject the null hypothesis that the solutions are all from the same population with a high level of significance ( $\text{Pr}>F=0.003$ ) for the fitted linear model ( $y = -0.2525x + 583.33$ ), although the model fit was still poor ( $R^2 = 0.308$ ).



A standard curve (Figure 3.3) was fit to the mean responses by NLLS using the 4PLL model, as was done for the germinal DIA. The fit was reasonably good ( $R^2=0.84$ ) considering the variation in response observed for several of the test solutions. Although only eight replicates of the blank are included in this data set, the standard deviation of those replicates and the fitted 4PLL model were input into the accepted calculation method<sup>xiv</sup> to determine a preliminary limit-of-detection (*LOD*).<sup>141</sup> The preliminary LOD was determined to be ~200 nM.

### 3.2.5. Discussion

These observations are *not* what we expected, either from simple deduction based on first principles, or from the 2-D numerical model. We expected that there would be no detectable accumulation for an analyte this large, even with the reagent blank. Initially, we assumed that the observed accumulation was an artifact, but subsequent experimentation on several days and with several reagent preparations has established that this is a real and replicable phenomenon (Figure 3.2C). The surfaces of the device were treated with fibrinogen to assess if the BSA-containing diluent was not preventing adsorption, but no change in the result was seen (data not shown).

---

<sup>xiv</sup> Limit of detection is calculated here by assaying a number of replicates of a reagent blank (usually >25), determining the standard deviation of the resulting responses, multiplying this statistic by a factor of three, and quantitating the resulting value from an appropriate standard curve. In this small data set, one value was judged to be an outlier (>2s from mean) and was discarded. This step would not be needed if the data set was sufficiently large.

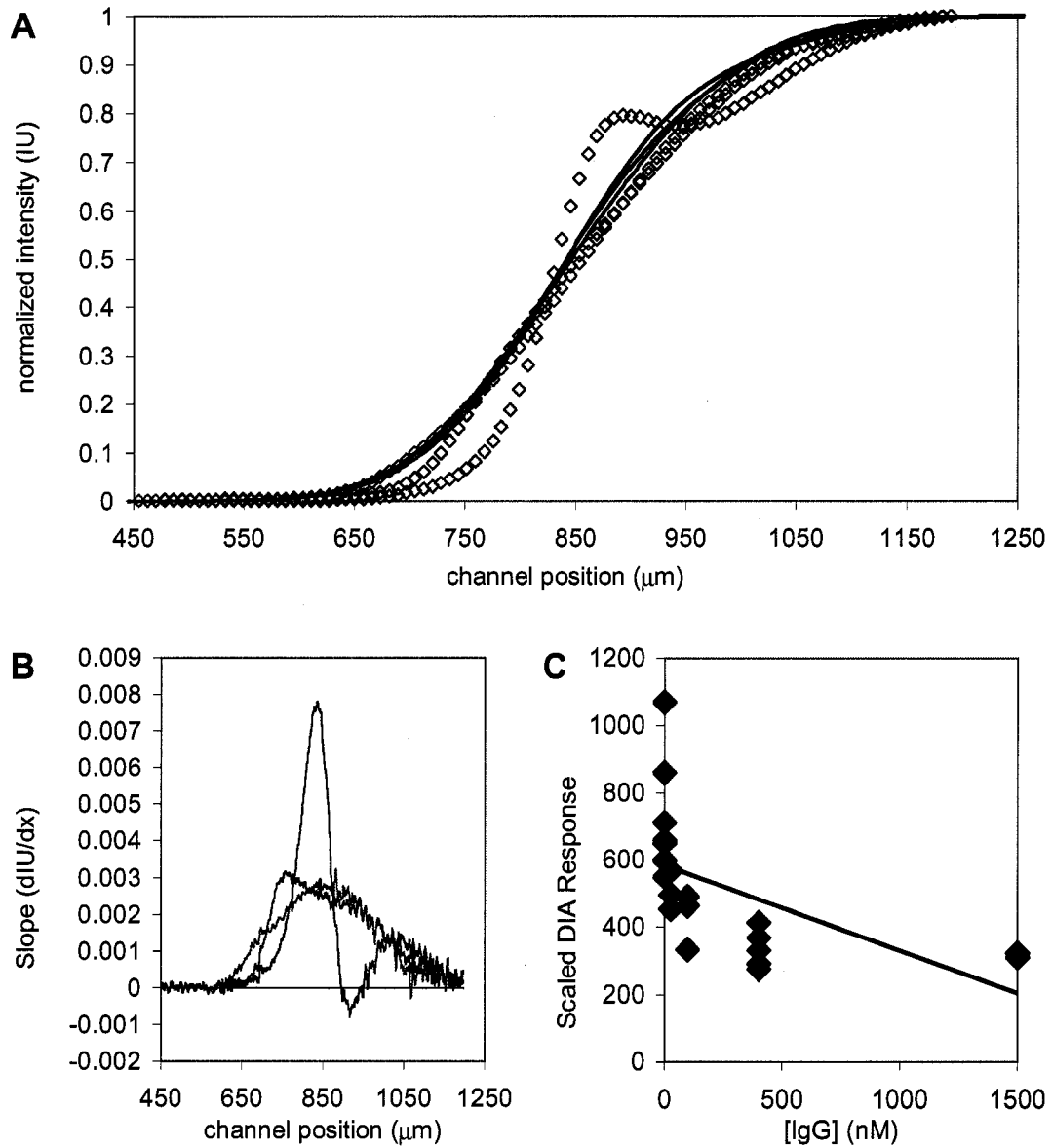


**Figure 3.2:** Representative results for the germinal DIA for IgG. Reagent formulation given in text. For both figures, blue is the blank signal, red is the response to 400 nM sample Ag, and green is the response to 1500 nM sample Ag. A) Comparison of predicted and observed DIA accumulations for HRP. Lines are predictions from the 2-D numerical model, and the diamonds are a sparse plotting of the observations (one symbol every ten data points) after BFTN processing, and boxcar smoothing. B) The slope plot of the data in 'A'. C) A plot of the germinal DIA responses of all mock samples (rescaled to match the abscissa scale) as a function of IgG concentration. The fitted line ( $y = -0.2525x + 583.33$ ;  $R^2 = 0.308$ ) represents the linear covariation model used in the ANCOVA analysis (discussed in text).

The signal-to-noise ratio for this assay is also much larger, due to both the unexpected accumulation, and the high specific fluorescence of the conjugate (Figure 3.2A and Figure 3.2B). Together, these factors result in slope plots that are completely resolved both visually, and using the data reduction algorithms of the germinal DIA (Figure 3.1B and Figure 3.1C). The form of the accumulation (as seen in the slope plots) is somewhat different from what is expected from the simple model of immune-complex formation and diffusion, suggesting that some other process is at work.

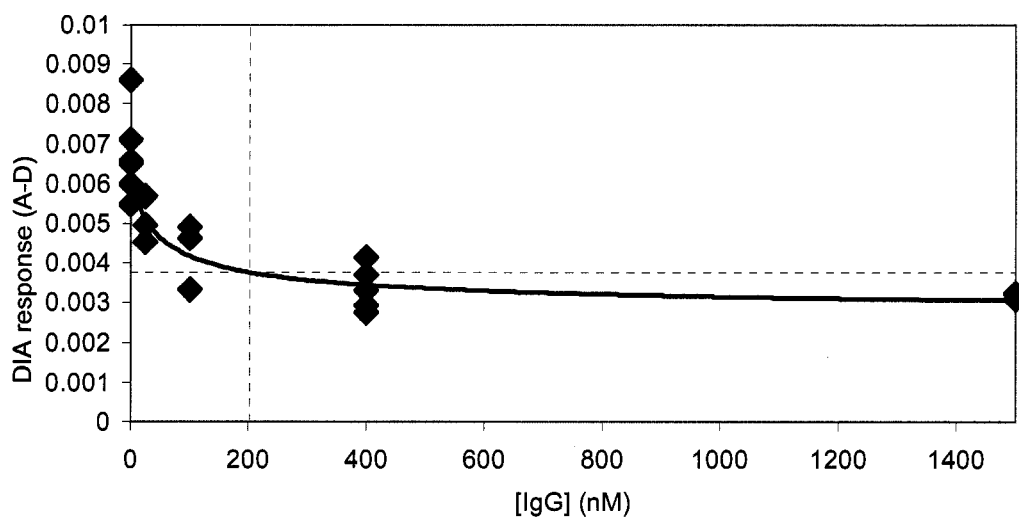


**Figure 3.3:** A 4PLL curve fit to the germinal IgG data set by the NLLS procedure. (---) = graphical representation of the preliminary LOD estimation of ~200 nM.

We hypothesize that the mechanism producing the unexpected accumulation is the formation of soluble or colloidal aggregates of several immune-complexes (Figure 3.4). The bivalent nature of the specific binding activity of whole IgG molecules is well known.<sup>142</sup> Since the  $\alpha$ -MsIgG antibody chosen as a capture molecule was species-specific, it is likely cognate to an epitope on the  $F_c$  fragment of the MsIgG chosen as a model analyte, since that is where most species-specific amino-acid differences are found. The multimeric nature of the IgG, including two identical  $F_c$  fragments makes it likely that at least two copies of the epitope are present, making

the analyte multivalent as well. The combination of multivalent capture antibodies and analytes makes the formation of aggregates quite likely in the right concentration regimes, a fact that has been successfully exploited in the past to create the classic immunoprecipitation assay technique.<sup>142</sup> We have suggested previously<sup>106</sup> that linking the capture antibody to a microsphere will restore the diffusivity ratio expected to be a key parameter in the DIA (Section 2.4.1). In essence, multivalent aggregation is like forming such a particle *in situ*.

One potential limitation of this multivalent-aggregation technique may be a greater sensitivity to reactant concentrations. It is well established that the precipitation reaction occurs only in a small part of the reactant-concentration domain.<sup>142</sup> It may be more difficult to find this “sweet spot” during assay design, and the resulting assays may not have as broad a dynamic range.

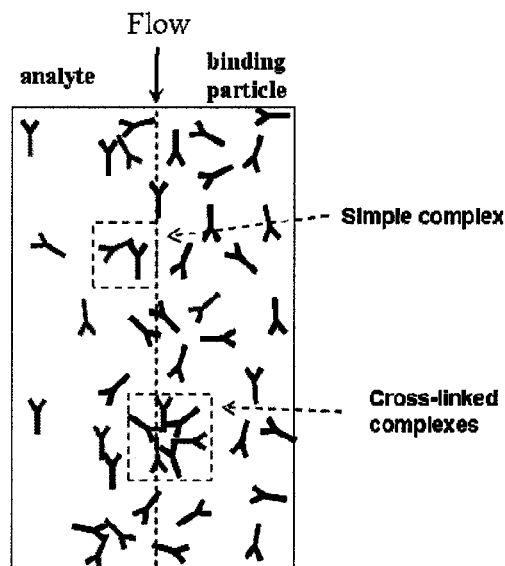


**Figure 3.4:** A schematic representation of what we hypothesize is happening at the interface of the two apposed flow streams in a DIA performed with multivalent analytes. A hypothetical detection region is shown. The “Y”-shaped particles in this diagram represent immunoglobins (not to scale), but the principles apply to other multivalent reactants as well. As analyte (green Y) diffuses across the interface of the flow streams (---) some are captured by the binding particles (black Y) in simple 1:1 complexes, but since the reactants are multivalent, larger cross-linked complexes can also result. The larger complexes will diffuse at a slower rate than the simple complexes, restoring the analyte:binding-particle diffusivity ratio required for a significant response ( $>\sim 2$ ).

The discovery of a multivalent-aggregation format for the DIA is a significant advancement in the basic DIA technique. Many high molecular weight analytes of interest are proteins. Many proteins are multimeric, and therefore, potentially multivalent. It appears that the analyte size domain of the DIA is greatly expanded. Furthermore, this was not a result that was anticipated by earlier investigators of the DIA. It has not been discussed in previous publications, or protected in the patents for this technique. Thus, a UW invention disclosure was prepared for this technique, and a provisional patent filed.<sup>143</sup> These preliminary results have been presented to the community<sup>144</sup> and a refereed publication is in preparation.<sup>145</sup>

The ANCOVA and LOD analyses establish that the IgG germinal DIA as formulated is functional as a qualitative assay with a limit of detection of ~200 nM. It may also be usable as a quantitative assay, with a dynamic range of ~200 to ~1500 nM, although the sensitivity is poor in this range, as evidenced by the low slope of the curve compared to the variation within test solutions (Figure 3.3). Nevertheless, we hypothesize that this assay will also benefit from some of the signal processing algorithms considered later (Section 4.2), and further improvement may be required before it can be considered a robust quantitative technique.

It should also be noted that, as with HRP, the ANCOVA analysis as performed may not have the statistical power that it could. Examination of the data plots (Figure 3.2C, Figure 3.3) again shows that there may be a mean-dependence of the variance. Also, as with HRP, the ANCOVA may also be based on an inappropriate model, an observation supported by the good fit of the 4PLL model by NLLS. Unlike HRP, the variance observed is small enough that the non-linear correlation is clearly visible. While the use of ANCOVA as a figure of merit is not a feature of the germinal DIA, we will consider data transformation to stabilize the variances and linearize the

response as an improvement, since it was not done in the germinal DIA for phenytoin. Data transformation will be considered in Section 4.3.

### ***3.3 Summary of Preliminary Work***

These results suggest that the germinal DIA technique is capable of quantifying protein analytes under specific conditions: 1) The analyte is multivalent with respect to the antibody, and the formulation creates the conditions require for immune-complex aggregation. 2) The fluorescent label has a very high specific fluorescence so that the signal-to-noise ratio remains sufficient for sensitivity in the context of the low reactant concentrations generally required for a protein assay. 3) A combination of these conditions.

For monovalent protein analytes with a molecular weight less than or equal to 45 kD, formulated with common “off the shelf” reagent components, the germinal DIA requires some improvement before the small responses observed with these analytes will be resolvable from the noise. These improvements may include: reduction in systematic noise due to the device materials (Section 4.1) better digital noise filtering and/or amplification algorithms (Section 4.2), and amplification of the signal through biochemical modification of the capture antibody (Section 4.3). No conclusions can be drawn about monovalent analytes with a molecular weight >45 kD from these results; although, the predictions of undetectable signals from the numerical modeling were not refuted.

The results of these preliminary studies suggested that major improvements to the germinal DIA procedure were required to reduce the analytical variation to levels where results were meaningful, much less clinically acceptable. These improvements are the subject of the next chapter (Chapter 4) of this dissertation.

## Chapter 4: Improvements to the Germinal DIA Procedure

In this chapter, several strategies for improving the quality of DIA data are explored. Changes suggested by this exploration were incorporated into a second-generation design used for numerical modeling and the capstone DIA for C-reactive protein. The changes incorporated into the second generation DIA were:

- 1) Adoption of polymethyl methacrylate (PMMA) as the material that caps the channel top and bottom and serves as the “window” through which optical interrogation occurs. This change was made to reduce the confounding effects of autofluorescence of the plastics on the background correction algorithms (Section 4.1.1).
- 2) Adoption of solvent assisted thermal lamination as the means of bonding device layers together. This change was made to eliminate proprietary adhesives of indeterminate chemical composition from the microfluidic channel. (Section 4.1.3).
- 3) Use of a *validated* antifouling strategy – incubation of the device with a buffered 1 mg/mL BSA solution, and the use of the same in the reagent diluents. A specific microfluidic system was developed for the validation (Section 4.1.2)
- 4) Adoption of the Whittaker filter as the smoother of choice when a numerical difference algorithm is required to calculate the slope of an intensity profile. This filter more effectively reduced the high spatial frequency noise that obscured the analyte modulated response in the germinal DIA for HRP (Section 4.2.1.).
- 5) Adoption of an integrated, non-directional difference from free diffusion as the algorithm for calculating the response number. This algorithm was judged superior to the germinal DIA slope algorithm because it leveraged

more of the modulated signal into the response calculation, was less sensitive to high spatial frequency noise, and is defined for all sample antigen concentrations (which the germinal DIA algorithm is not). Use of this response algorithm did require the incorporation of an internal diffusion standard into the reagent formulation (Section 4.2.3.3)

Readers not interested the potential of improvements *not* adopted may wish to skip those sections of this chapter not cited in the paragraph above.

## ***4.1. Improvements to the quality of DIA raw data***

### **4.1.1 Reduction of confounding background**

As discussed previously (Section 2.4.3), the autofluorescence of the Mylar™ typically used in the Yager lab has been problematic in the past. The germinal DIA for phenytoin was done in a glass/Mylar™/glass device<sup>1</sup>, as was the germinal DIA for HRP (Section 3.1.1). This was the most expedient way to eliminate the confounding effects of the high background from autofluorescence, but was not compatible with the final design goals – glass devices are fragile, and not amenable to mass production. Thus a goal of this research was to identify alternative materials that could be used for a rugged, all-plastic device suitable for a POC application.

To accomplish this goal, a survey of some commonly available polymer films (including Mylar™) for their fluorescence behavior under standardized conditions was undertaken, to determine which materials are most suitable for high-sensitivity fluorescence detection lab chips. The first criterion for suitability was low initial fluorescence. For materials where the autofluorescence is not so high that the signal of interest is overwhelmed by the noise in the background, the second important



criterion is an insignificant change in fluorescence over the time-course of a typical analytical experiment (in our case, several minutes) to enable facile background correction.

*4.1.1.1 Materials:* Samples of several different films were obtained (Table 4.1). It was not possible to easily obtain samples of the same thickness. The films were compared to borosilicate glass microscope slides, and fused silica microscope slides – the accepted “low background” reference material.

**Table 4.1:** The polymer films surveyed for autofluorescence in Aim 3. Reproduced from Hawkins and Yager<sup>146</sup>

	Material	Thickness / $\mu\text{m}$	Source
1	Mylar™ (PET polyester)	100	Fralock Santa Clara, CA, USA
2	Mylar™ (PET polyester)*	50	DuPont Wilmington, DE, USA
3	Lexan™ (polycarbonate)	2500	G. E. Plastics Pittsfield, MA, USA
4	polypropylene	60	Exxon Mobil Houston, TX, USA
5	Trycite™ (polystyrene)	50	Dow Chemicals Midland, MI, USA
6	Zeonor™ (polyolefin)	110	Zeon Chemicals Louisville, KY, USA
7	Topas™ (polyolefin)	90	Ticona Summit, NJ, USA
8	Topas™ (polyolefin)	210	Ticona Summit, NJ, USA
9	Rohaglas™ (PMMA)	340	Cyro Industries Orange, CT, USA
10	glass microscope slide	960	Corning Glass Corning, NY, USA
11	glass microscope slide	1970	Corning Glass Corning, NY, USA
12	UV-grade Fused Si	1030	Esco Products Oak Ridge, NJ, USA

*4.1.1.2. Procedure:* A sample of material was mounted on the stage of a Zeiss ICM-405 inverted, epifluorescence microscope (Carl Zeiss Inc., Thornwood, NY, USA).

The sample was imaged through a 10x objective and a reducer for a total magnification of ~6x. At this magnification, a 1.0-mm x 0.8-mm region of the sample was imaged. Excitation light came from a Zeiss HB100W mercury arc source (Carl Zeiss Inc., Thornwood, NY, USA). Light was conditioned by using a fluorescein filter set (excitation bandpass: 385-445 nm; dichroic beamsplitter: 510 nm; emission bandpass: 500-560 nm), and a rhodamine filter set (excitation bandpass: 510-570 nm; dichroic beamsplitter: 580 nm; emission bandpass: 565-645 nm). A Retiga 1300 (Q-Imaging, Burnaby, BC, Canada) cooled, 12-bit CCD camera was used for detection.

Material samples were evaluated without assembling them into a microfluidic device. Prior to evaluation, all samples were sonicated in ethanol for 15 minutes and dried. The background fluorescence of the material was measured at regular intervals over a three-hour period, with continuous exposure to the conditioned illumination.

Several important control experiments were performed. The interpretation of this study is simplified greatly if the intensity of illumination is relatively constant over the timeframe of the study. To assess the variation in the source, a control sample (Mylar™) was measured at the start or end of every experiment. Temperature control experiments were also performed, where the exposure to illumination was interspersed with 5-minute “cool down” periods, to determine the effect of sample heating on the background fluorescence.

The grayscale images of the spatial distribution of intensity were sampled using a custom-coded MATLAB (V6.1.0.450, The Math Works, Inc., Natick, MA, USA) utility. The average of 100 pixels (from a representative 10-pixel by 10-pixel region) was defined as the dependant variable at each time point. The standard deviation of the 100-pixel region was used as the standard error for defining error bars at each time point. For all materials, the field of view appeared essentially uniform in bright field, with occasional obvious surface flaws (scratches, etc.). The flaws were treated as anomalous, and avoided.

4.1.1.3. *Results:* The initial fluorescence intensities of the Mylar™ samples and the polycarbonate sample were significantly higher than the glass and fused silica slides, and decreased over the three-hour period with complex kinetics. The other materials had initial intensities similar to the glass and fused silica, but also displayed a decrease over time, as did the glass and fused silica (Figure 4.1A, Table 4.2). The observations were also normalized to the individual initial intensities to facilitate the comparison of the kinetics of the decrease in fluorescence (Figure 4.1B, Table 4.2). The data shown (Figure 4.1, Table 4.2) resulted from illumination with the fluorescein filter set. Similar results were obtained with the rhodamine filter set, although not all materials were tested, and the initial magnitude was less (data not shown).

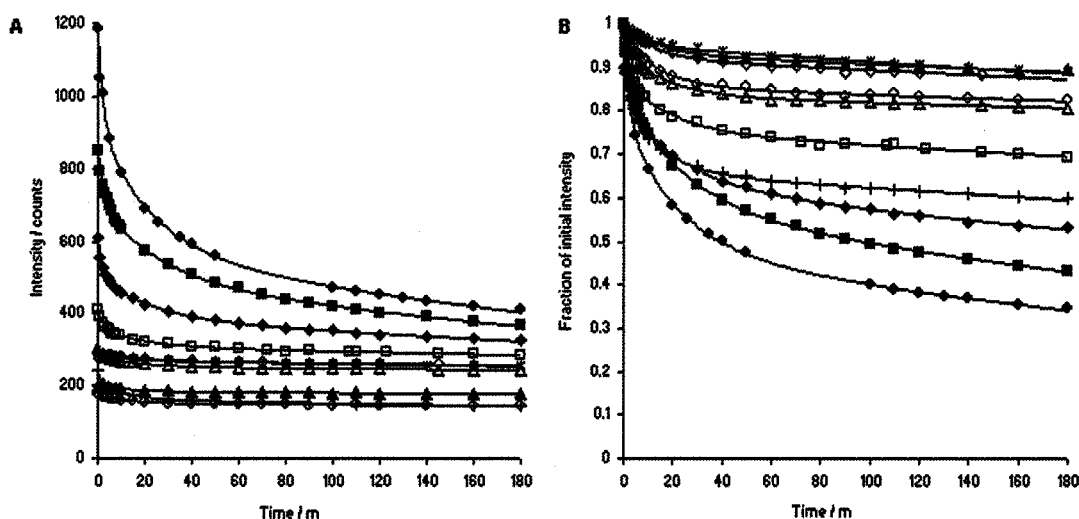


**Figure 4.1:** Plots of the decrease in fluorescence of most of the materials from Table 1 and 2. For the two materials where two different thicknesses were evaluated (glass, Topas™) a single representative plot is shown for clarity. Symbol size approximates the error bars. Each series of discrete observations is accompanied by a best-fit curve (see Table 2 for equation of best fit curve). Curves were fit using non-linear least squared regression by a generalized-gradient method (Excel Solver function, Microsoft, Redmond, WA, USA). A) Fluorescence intensity (CCD counts) versus time. (●)=Fralock Mylar™ data, (▲)=Glass (thin) data, (■)=polycarbonate data, (◆) = Dupont Mylar™ data, (◇) = Zeonor data, (□) = Rohaglas data, (Δ) = Fused Si data, (\*) = polystyrene data, (+) = polypropylene data, (○) = Topas™ (thin) data. B) Fluorescence intensity as a fraction of initial intensity versus time. Symbols and fitted lines are identical to “A” (The multiplicative and additive coefficients are re-scaled to reflect the normalization, the time constants in the exponent remain the same.) Reproduced from Hawkins and Yager<sup>146</sup>

The control experiments indicate that illumination changes or heating effects do not significantly impact these results on the timescale of both an individual experiment and the entire study (data not shown).

Comparison of the magnitude of intensity of two different samples is complicated by the lack of control over sample thickness. The magnitude of intensity observed will be dependent on the thickness of the material in the light-path, because a greater volume of material is being illuminated. Given the low numerical aperture of the objective used (0.25), it is reasonable to assume that the magnitude will be approximately proportional to thickness (at least for the thin-films.) Applying a linear normalization to the initial intensities (Table 4.2) changes the ranking of the materials significantly (Figure 4.2). Even after the normalization to correct for thickness differences, samples of the same polymer material did not always display the same initial magnitude -- Dupont Mylar™ and Fralock Mylar™ were not the same, Zeonor™ differed from Topas™, and even the two Topas™ samples differed from each other. The two glass samples gave essentially identical results upon normalization, however (Figure 4.2).

*4.1.1.4. Discussion:* Our observations of the fluorescence behavior of the polymer thin-films suggest that several polymers are superior to Mylar™ when low and predictable background fluorescence is required. The normalized rankings of initial fluorescence intensity probably more accurately represent the true relative properties of the polymers, but it may not be possible to actually obtain these materials at that thickness. Other material properties must also be considered when choosing the material; for instance, we have found that the polyolefins are difficult to cut cleanly with our laser system (limiting the feature size).

**Table 4.2:** Initial fluorescence intensity, best-fit multiple exponential models, and coefficients of determination for fitted exponential decay models for all materials surveyed. The fitted constants in front of the exponential terms are expressed in the units of “counts”, while the time constants of the exponential decay are expressed in the units “minutes<sup>-1</sup>”. Only the initial fluorescence of the thick glass slide was evaluated. Reproduced from Hawkins and Yager<sup>146</sup>

Material	Initial intensity / counts	“Best-fit” model	R <sup>2</sup> by model			
			at+b	ae <sup>bt</sup> +c	ae <sup>bt</sup> +de <sup>lt</sup> +c	ae <sup>bt</sup> + de <sup>lt</sup> + ge <sup>ht</sup> + c
1 Fralock Mylar™	1184	$y = 257e^{-0.462t} + 355e^{-0.044t} + 535e^{-0.002t} + 37.5$	0.791	0.796	0.994	0.999
2 DuPont Mylar™	613	$y = 104e^{-0.641t} + 119e^{-0.048t} + 353e^{-0.001t} + 37.5$	0.697	0.778	0.988	0.997
3 polycarbonate	849	$y = 135e^{-0.343t} + 217e^{-0.040t} + 458e^{-0.002t} + 37.5$	0.600	0.863	0.981	0.999
4 polypropylene	242	$y = 38e^{-0.731t} + 44e^{-0.075t} + 1221e^{-0.0007t} + 37.5$	0.877	0.641	>0.999	>0.999
5 polystyrene	286	$y = 14e^{-0.113t} + 234e^{-0.0005t} + 37.5$	0.826	0.886	0.988	0.989
6 Zeonor™	293	$y = 5e^{-0.654t} + 20e^{-0.048t} + 231e^{-0.0003t} + 37.5$	0.729	0.829	0.938	0.999
7 Topas™ (thin)	176	$y = 6e^{-0.645t} + 19e^{-0.068t} + 1139e^{-0.0003t} + 37.5$	0.710	0.717	0.992	0.999
8 Topas™ (thick)	294	$y = 18e^{-0.646t} + 14e^{-0.054t} + 225e^{-0.0003t} + 37.5$	0.732	0.742	0.976	0.996
9 Rohaglas™	410	$y = 52e^{-0.427t} + 49e^{-0.052t} + 271e^{-0.0005t} + 37.5$	0.673	0.713	0.989	0.998
10 glass (thin)	198	$y = 14e^{-0.075t} + 147e^{-0.003t} + 37.5$	0.431	0.838	0.988	0.996
11 glass (thick)	419	—	—	—	—	—
12 UV-grade Fused Si	301	$y = 20e^{-0.425t} + 30e^{-0.058t} + 214e^{-0.0002t} + 37.5$	0.660	0.678	0.988	0.999

The differences in magnitudes of the initial fluorescence for similar polymers (Figure 4.2) can be explained by several possible mechanisms: 1) Differences in processes between vendors may result in real material differences that manifest themselves as differences in fluorescence. This is probably implicated in the difference between Dupont Mylar™ and Fralock Mylar™, and the difference in polyolefins from Zeon and Ticona. 2) The post-production age and handling of material from the same vendor can vary, and was not a controlled variable in this study. The decrease in fluorescence observed over time (Figure 4.1) suggests a likely mechanism for some of the variation seen in the two thicknesses of Topas™ examined. Material that has been exposed to the ambient light of a warehouse during prolonged storage could have lost a significant fraction of the fluorescence it displayed when newly manufactured. We have observed similar differences in Fralock Mylar when a new lot was obtained (data not shown), although we did not understand the mechanism at the time. We hypothesize that glass slide production is a better controlled process, and the results

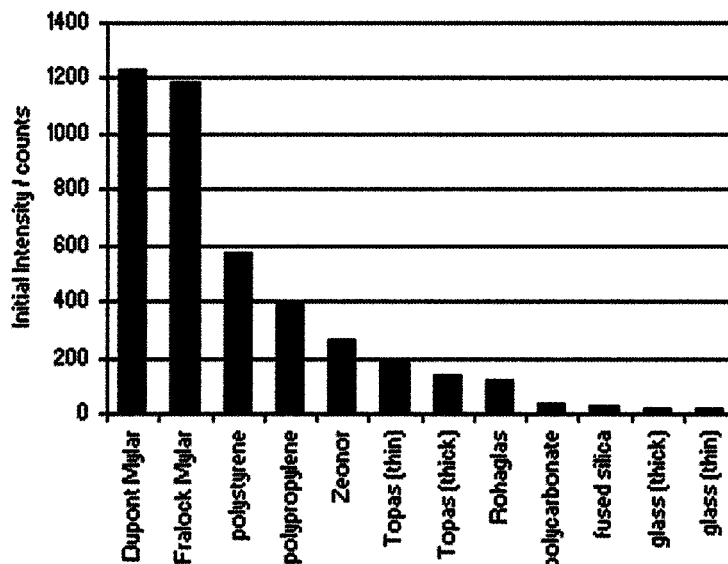


**Figure 4.2:** Initial intensity of materials normalized to 200  $\mu\text{m}$  thickness. (This thickness is representative of a typical device in our lab.) Error estimates are negligible compared to the magnitude of the normalized intensity. Reproduced from Hawkins and Yager.<sup>146</sup>

presented here (Figure 4.1) demonstrate that the autofluorescence of glass is less prone to systematic decrease with exposure to illumination – thus, the two glass samples are not discordant.

One important source of a time-dependant reduction in the intensity of fluorescence of any fluorophore is photobleaching. While the kinetics of fluorescence decrease are well known for a number of important systems,<sup>147-149</sup> the time-scale investigated is usually nanoseconds, not minutes; and the mechanism is the normal relaxation to the ground state, not photochemistry. There is a relative paucity of publications concerning photobleaching of polymer films. Examples include investigations of photobleaching of dyed polymer thin-films for optical waveguides,<sup>150</sup> and for data storage devices;<sup>151</sup> however, to the best of our knowledge, this work represents the first investigation of the kinetics of photobleaching as a lurking variable in microchip fluorescence detection.

Simple models of photobleaching predict an exponential decrease in intensity.<sup>150</sup> In systems where multiple fluorophores are present, linear combinations of exponential decay functions may result (if there are no interactions between fluorophores), or more complex non-linear combinations may result (when energy-transfer between fluorophores occurs).<sup>149</sup> Multiple decay rates may be due to multiple fluorophores, or multiple local chemical environments for the same fluorophore.<sup>117</sup> Exponential decay functions can be fitted to a data set using non-linear least-squared (NLLS) regression to enable the extraction of the individual initial magnitudes and time constants of the decay processes of interest.<sup>152, 153</sup>

To investigate the mechanisms involved in the observed fluorescence decrease, several model decay functions were fitted to the experimental results. Simple linear models (Excel “trendline” function, Microsoft, Redmond, WA, USA) gave poor fits (Table 4.2). Linear combinations of one, two and three exponentials were fit using NLLS regression by a generalized-gradient method.<sup>xv</sup> (Excel “Solver” add-in function<sup>8,9</sup>, Microsoft, Redmond, WA, USA). Using the coefficient of determination ( $R^2$ ) as a measure of model fit, many of the materials appear to have three exponential decay processes operating over the three-hour experiment -- all appear to have at least two (Table 4.2). The coefficients of determination were not always a sufficiently sensitive measure of the quality of curve fit; i.e., visibly obvious differences between two- and three-exponential fits were not always reflected in the  $R^2$  values. The “best-fit” curves plotted (Figure 4.1) were determined using both  $R^2$  values and visual discretion. The time constants of these processes range from about one minute to over eighty hours, complicating potential background correction algorithms. (Note that the numerical constants in the exponential terms have units of *minutes*<sup>-1</sup>; e.g., the numerical constant .02 corresponds to a time constant of 50 min.) When the data

---

<sup>xv</sup> A constant was included in these models to account for the observed dark count of the camera. Numerous iterations of the fitting procedure were performed using different initial conditions in an attempt to reach a global residual minimum. The single exponential was fitted with both the “trendline” function, which does not allow for defining a constant for the dark count, and the NLLS procedure. There was not a significant difference in the  $R^2$  between the two procedures (not shown).

obtained with the rhodamine filter set were analyzed in the same way, the initial magnitude of fluorescence was generally lower, and fewer materials required three exponential terms for fitting (consistent with the lower energy of the longer wavelength excitation light) but the overall trends were similar (data not shown). This suggests that simple photobleaching of two or three species is producing the observed behavior.

Given the stated aim of this investigation, an analysis of how significant these changes are to the germinal DIA was attempted. The conditions of the germinal DIA (Section 2.2) dictate the degree of confounding between the background fluorescence of the polymer films and the signal of interest. The germinal DIA for proteins requires a relatively long reactant interaction time (154 s) and signal integration time (10 s) -- to perform a minimal number of true replicate readings, and perform the associated sample injection and pump control operations, requires about three minutes per accumulation. The only shutter available in the light path of this research instrument is a manually operated slider, positioned such that care must be taken in closing it to avoid moving the device (complicating image registration). Thus, it is impractical to take a background fluorescence image without at least a three minute exposure to illumination between the background and sample images, with our equipment. Consequently, it is the change in background that occurs during any three minute time-window that affects analysis the most. If the background is relatively constant for three minutes, a simple image subtraction can correct for the background. If it changes significantly over three minutes, a more complicated correction algorithm is required. More complex correction algorithms are not robust; given the complex decay kinetics, uncertainty in determining where in the decay curve one starts, and the potential for device-to-device variation. Significant changes in background over the three minute analysis-time were, therefore, deemed unacceptable.



Like the analysis time, the significance of an observed change is context dependant – it depends on the magnitude of the fluorescence signal of interest. The change in intensity over three minutes for a 200- $\mu\text{m}$ -thick Mylar™ layer produces a change in intensity that is as great, or greater than, the signal produced by a 20-nM fluorescein solution (Figure 4.3), throughout the entire three hours we monitored the change. A glass slide never produced a change that was as great as the 20-nM fluorescein signal at any time during the experiment (Figure 4.3). Thus, it is expected that a device that includes 200- $\mu\text{m}$  of Mylar™ in the light path will not perform well in an assay that requires a 20-nM fluorescein limit-of-detection, but a glass device will. This conforms well to our anecdotal observations. The Topas™ produces a change that slightly exceeds the signal of the 20-nM fluorescein for the first few minutes after exposure, but rapidly drops below the 20-nM fluorescein signal (Figure 4.3).

The analysis above also suggests two other inferences: 1) Prior exposure of the film to illumination could improve the limit of detection by moving the decay curve into a region of lower slope. It appears that a device made with Topas™ would require a short “burn-in” of this type if it was used to for an assay that requires a 20-nM fluorescein limit-of-detection. Although we did not comprehensively investigate this, some preliminary experiments suggest that this would be difficult to control precisely. 2) All of the materials investigated, including glass and fused-silica, will have some lower bound to their limit-of-detection caused by the fluorescence change over time, as long as they are in the light path. Only the adoption of a more complex detection scheme (confocal optics or multi-photon excitation) will relieve this constraint.

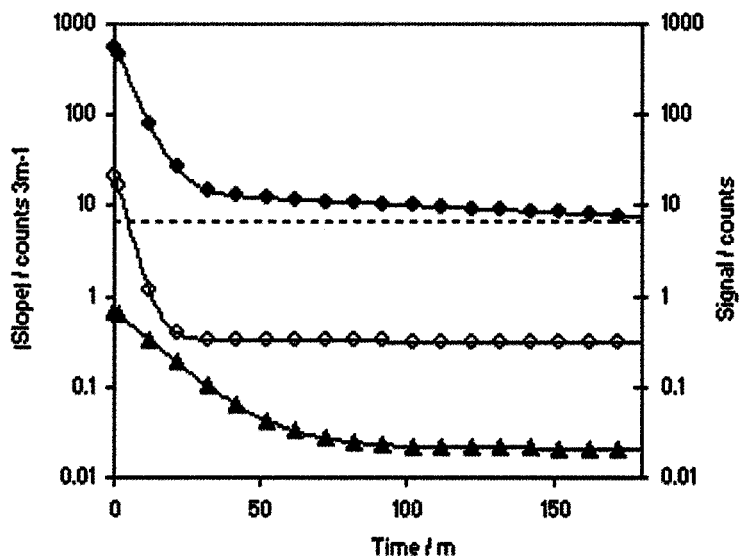


**Figure 4.3:** Slope of decay curves for a three minute analysis time (●)=Fralock Mylar™, (○) = Topas (thin), (▲)=Glass (thin), compared to the fluorescence signal (not slope) produced by 20 nM fluorescein (---). All materials normalized to 200  $\mu\text{m}$  thickness. See discussion for details on this analysis. Reproduced from Hawkins and Yager.<sup>146</sup>

From these results, it appears that there are a number of polymer films better than Mylar™ for sensitive fluorescence-detection devices. The best candidates are the cyclic polyolefins; however, polymethylmethacrylate (PMMA), polycarbonate, polypropylene, and polystyrene may also be an improvement. When optimal design is desired, the fluorescence properties of these polymers will have to be weighed against their other properties of interest and evaluated in the specific analytical context.

It is satisfying to note that the results of this investigation were published in a well-received paper in a peer-reviewed journal<sup>146</sup> which was cited by the Royal Society of Chemistry as being one of the most downloaded publications from their website for three months running, and was chosen by the editor as one of the top ten papers from the first five years of the journal. It appears that these results were applicable to more than just the DIA.

### 4.1.2 Controlling adsorption

Protein adsorption is a very common phenomenon that must be accounted for in any analytical procedure involving proteins as reagents or analytes, as previously discussed (Section 2.4.4).

*4.2.2.1. Preliminary Results:* Initial attempts to perform the germinal DIA for HRP resulted in very inconsistent accumulation data. Occasionally, the results would look promising, usually at the end of an experimental session, but more frequently the raw images were confusing – unexplainably bright, or blotchy, and with a background that changed over the course of the experiment (data not shown).

While operator inexperience was certainly involved in these early results, it also became clear that some other process was at work. Interpreted in the light of the autofluorescence work (Section 4.2.1), some of the anomalies can now be explained. Other anomalies are not as easily explained away, however. In addition, the HRP DIA results from glass/Mylar/glass devices were also subject to these anomalies, despite the low background they displayed.

Based on these observations, and the ubiquity of protein adsorption discussed earlier (Section 2.4.4), a non-fouling amendment was added to the universal HRP DIA diluent – bovine serum albumin (*BSA*) at a concentration of 1 mg/mL. This amended buffer was used to pretreat the device prior to every experimental session, as well as functioning as a universal diluent. “Blocking” with BSA is a very common approach to preventing protein adsorption in immunoassay. After this procedural change was made, easily interpreted results that conformed to expectations became the norm, rather than the exception. All of the DIA results in this thesis were generated from reagents containing the BSA amendment.

Nevertheless, this solution was fundamentally not satisfying – no comprehensive, controlled experimentation was done to determine if the treatment was truly effective

or if the resolution of the anomalies was simply coincidental. In addition, observations of possible confounding adsorption continued to plague other Yager Lab projects (data not shown). Thus, the design and characterization of an adsorption chromatography device was deemed of general interest, as well of specific interest to protein DIA.

*4.2.2.2. Adsorption Chromatography:* Adsorption chromatography is an analytical technique that can give information about both permanent and transient adsorption. Chromatographic peak shape, integrated area, and transit time all contain information about the dynamic adsorption process.<sup>154</sup> The most common embodiment of adsorption liquid chromatography uses a macroscale cylindrical column and the solid phase (the surface) is packed into the column to present maximal surface area. While one could envision triturating the material used to form a microfluidic channel to enable its packing into a column, the result would not be as applicable to a real channel. Fortunately, that approach isn't necessary on the microscale – an excess of surface is already presented to the solute as long as the amount of solute introduced is small. The theory of performing adsorption chromatography in high-surface area, packing-free columns (long capillaries) was developed over fifty years ago.<sup>155</sup> Originally formulated for gas chromatography, the development can be extended to pressure-driven liquid flow capillaries. Because of more recent advances in microfabrication techniques, we now have the capability to realize similar channels in many different materials of interest.

A key to inferring meaningful quantitative results from adsorption liquid chromatography is the precise control of the mass of adsorbate introduced to the column.<sup>154</sup> In a microfluidic embodiment of the long capillary column, the “world-to-chip” interface creates an additional source of potential adsorption that may be as great as the effect of interest and must be accounted for. Some investigators have made inferences that neglect this effect,<sup>156</sup> but this seems a dangerous assumption that could

invalidate their quantitative conclusions. A means of monitoring the material delivered to the column is, therefore, desired. In addition, the plug of adsorbate must be small enough that the effect of depletion and slowing due to adsorption can be detected in a background of eluted adsorbate that does not adsorb because of saturation, binding-kinetics, or transport limitations. Several “micro-injection” valves designed for micro-scale liquid chromatography exist that can meet this constraint.

A flexible platform for understanding the effects of adsorption in the DIA could be comprised of: a long channel as an adsorption column, pressure-driven flow, a sample microinjection valve, provisions to monitor the incoming sample peak as well as the eluted peak, and typical materials with typical dimensions.

*4.2.2.3. Equipment:* The chromatography device is a relatively simple three layer laminate device made from Mylar. The flow channel was cut out of a 0.10-mm thick layer of Mylar D coated on both sides with adhesive (Fralock, Santa Clara, CA, USA), and the capping layers were the same Mylar with no adhesive (Figure 4.4). Note the inlet and outlet legs are positioned so that they can be visualized simultaneously. There is also a small “window” in the Mylar layer that defines the channel which is within the field of view, but does not communicate with the fluid flow. This enables a correction for the changing background due to photobleaching of the Mylar (see Section 4.1.1 for discussion) that is unaffected by adsorption during the experiment. The need for this feature is discussed further below. The device is mounted in a universal Yager Lab manifold to facilitate fluidic connections, and is interrogated with the same microscope camera systems as described previously for the germinal DIA testing (Section 3.1).

The device uses an Upchurch micro-injection valve to introduce a pulse of the solute of interest. With a 5 cm, 0.150  $\mu\text{m}$  internal diameter (*ID*) sample loop and a 56 nL swept volume in the valve, a 940 nL sample pulse was introduced into the device. This is  $\sim 1/10\text{X}$  the volume of the device ( $\sim 9.8 \mu\text{L}$ ) before the outlet detection window.

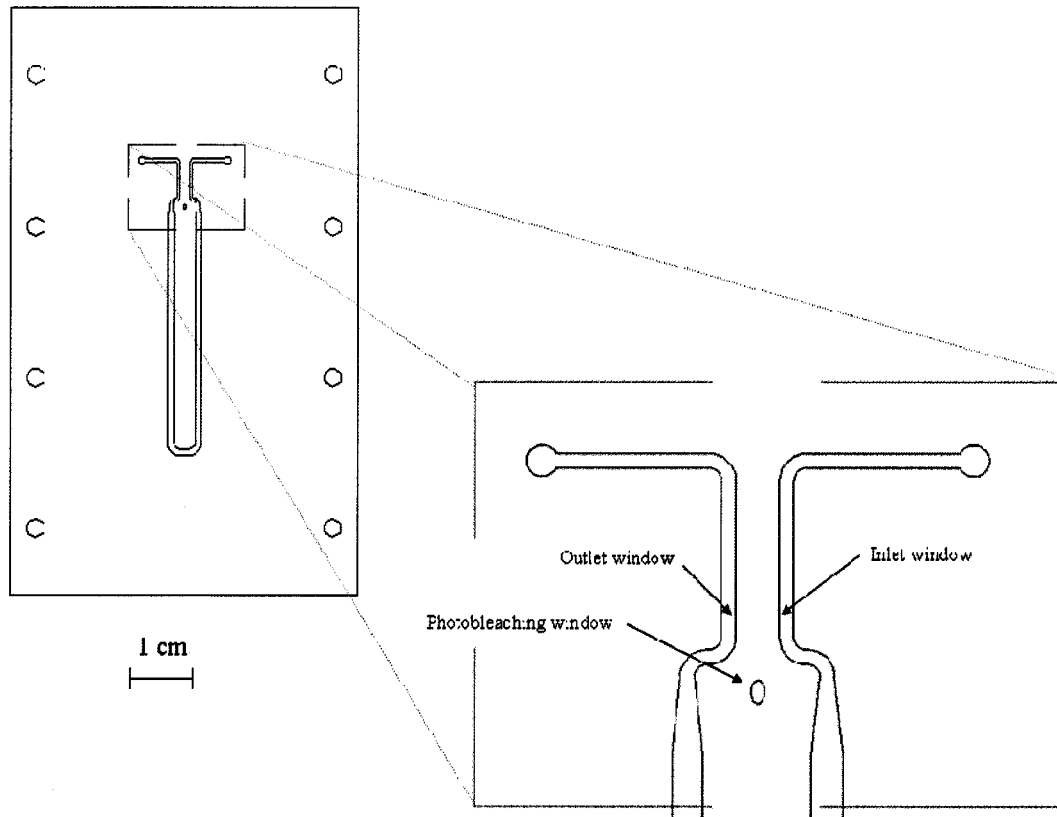


**Figure 4.4:** The microfluidic channel used as an adsorption chromatography device. The main channel is 1-mm wide, and over 70-mm long, so that the device presents  $204 \text{ mm}^2$  of surface to the  $0.94 \text{ mm}^3$  (940 nL) of sample pulse -- a surface to volume ratio of 217 m. Thus, by using dilute solutions of protein, and slow flow rates to allow sufficient time for protein diffusion; it is expected that a significant fraction of the protein in solution will be able to sample the surface, resulting in a detectable change to eluted peaks when adsorption is an important phenomena. The channel shown above is cut into 0.1 mm thick Mylar coated with adhesive on both sides, and laminated with two 0.1 mm Mylar capping layers, one of which is cut with holes to enable fluidic connections. Reproduced from Hawkins et al.<sup>157</sup>

This pulse volume can be tuned by varying the ID and length of the sample loop. The sample loop is as short as possible, but smaller ID tubing is available from Upchurch. There is no upper limit to the pulse volume. Valves of this type generally result in a square-wave input function at the valve.<sup>158</sup> The injection valve is mounted above the manifold so that only a 9.5 cm run of  $150 \text{ }\mu\text{m}$  ID tubing is required between the sample injector and the device to minimize the Taylor dispersion in this section. Thus,

a sharp peak is expected at the inlet window, simplifying interpretation of the effects of the device at the outlet window.

The manifold, valve and mounting are all placed on the microscope stage and loaded with the same tubing manifold used for the DIA (Figure 4.5). Although on-chip valving<sup>159</sup> and fluidic pulse injection<sup>160</sup>, are also viable methods for creating a sample pulse in pressure driven flow, the Upchurch valve chosen represents a robust and facile approach that enables both tuning of pulse volume and a square-wave input.

*4.2.2.4. Reagents:* Several solutions were used to characterize the system. Solutions were prepared of varying concentrations of fluorescein (Sigma Chemicals St. Louis, MO, USA), FITC-labeled dextran (MW 70,000, Sigma Chemicals, St. Louis, MO, USA), and FITC-labeled BSA (Sigma Chemicals St. Louis, MO, USA) in 100-mM HEPES buffer, pH 7.5 (Sigma Chemicals St. Louis, MO, USA); and rhodamine (Sigma Chemicals St. Louis, MO, USA) in phosphate buffered saline, pH 7.0 (Sigma Chemicals St. Louis, MO, USA). The fluorescein and FITC-dextran are assumed to be non-adsorbing; i.e., function as negative controls. The rhodamine and FITC-BSA are expected to adsorb strongly; i.e. function as positive controls.

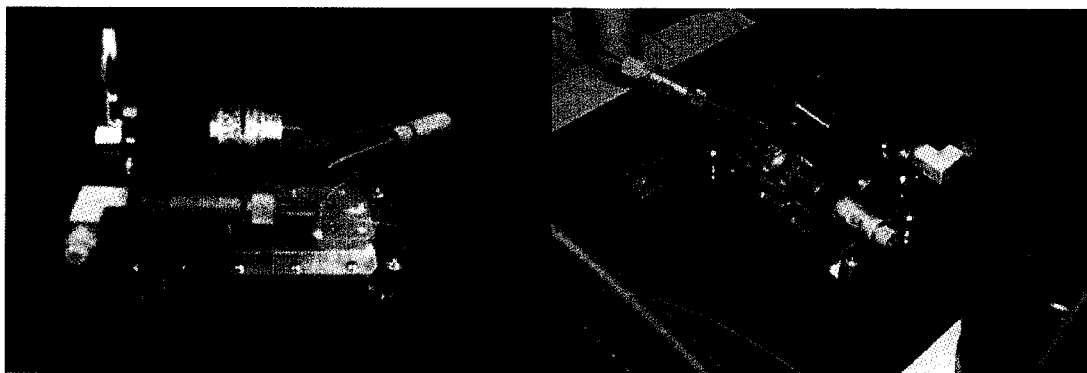


**Figure 4.5:** The adsorption chromatography device. The device is mounted into an aluminum manifold that enables connections to the Upchurch micro-injection valve mounted directly above the device to minimize the length of tubing after sample injection and before introduction to the device (to minimize Taylor dispersion of the peak). Syringe pumps are connected to the valve and the sample loop is moved in-line with the buffer flow by actuating the lever. A (left) The apparatus from the side, clearly showing the sample loop and associated plumbing. B (right) The apparatus mounted on the stage of the epifluorescence microscope.

4.2.2.5. *Procedure:* For each experiment a new device was used, to insure that a clean, un-fouled surface was presented.

Each experiment consisted of five sequential runs. Each run began with a buffer prime, followed by a sample injection. Images were captured once every ten seconds starting at the moment the pulse was injected into the flow stream, using LABVIEW (National Instruments, Austin, TX, USA) to control image capture and image storage automatically; and Terminal (Microsoft Corp., Redmond, WA, USA) to send command strings to the pumps. Image capture continued until well after the intensity observed at the outlet reached a steady state, indicating that the pulse of bulk sample had been entirely eluted from the channel. After the five sample injections, the channel was flooded with the sample solution and an image of the flooded channel was captured, to enable flat-field correction of the images.

Images were sampled as follows. Three 10-pixel by 10-pixel *detection windows* were defined within the inlet and outlet legs of the channel, and within the photobleaching window (Figure 4.4) and the intensity of fluorescence was sampled at these windows at each time point of each experiment. Because the detection windows are imaged simultaneously, this results in a linked set of input, output, and photobleaching data vectors with no uncertainty in the temporal relationship of these data. The elements of these vectors are the observed 100-pixel average intensity of fluorescence at the detection windows, and the index position within the vector corresponds to the time since pulse injection.

The dependence of the output vector on the input vector also enables the normalization of the results to correct for any variation of the inlet peak shape or total mass, insuring that only the adsorption effects of the micro-channel are measured. This insures that the potential confounding effects of upstream adsorption and any resulting dispersion is eliminated or, at least, obvious.



The data vectors for each linked inlet/outlet run were corrected using the following algorithm. They were first corrected for background and photobleaching using the data gathered at the photobleaching window. The data vector from the photobleaching window was fitted to a linear model using the “trendline” function of Excel. The resulting slope and intercept was used to correct the inlet and outlet data vectors for a change in background over the course of the experiment.<sup>xvi</sup> This step assumes that the photon flux at the photobleaching window does not differ significantly from the photon flux at the inlet and outlet windows; i.e., the rate of photobleaching is the same at these locations. The uniformity of illumination across the device was monitored, and occasionally adjusted, to ensure this assumption was valid. The inlet and outlet vectors were then flat-fielded through division by the cognate flood image values. These two steps are analogous to Equation 2 (Section 2.2.1) for the germinal DIA. Finally, the linked input/output data sets thus corrected were then normalized to the area under the input curve, making the normalized area under the output curve an expression of the fraction of input mass that arrived at the outlet of the device. Area under the inlet curve was calculated with a simple additive algorithm, and the resulting sum was used as a divisor to rescale both inlet and outlet data vectors.

Control experiments were also performed where the device and tubing were pretreated with 20  $\mu\text{M}$  unlabeled BSA solution for five minutes (assumed to be sufficient to saturate available binding sites), rinsed lightly with buffer, and then dried before experimentation as above. This control is a mimic of the non-fouling strategy used for the germinal DIA for HRP and IgG (Chapter 3), and is generally accepted as an effective method to prevent non-specific protein adsorption.

---

<sup>xvi</sup> The results of the earlier photobleaching experiments on Mylar (Section 4.1.1) suggest that a triple exponential model would be a more appropriate model; however, the differing experimental conditions in this investigation (slightly different filters, different microscope objectives, etc.) resulted in less dramatic changes over the time course of the experiment. The linear model was adequate in this case. Many of the photobleaching vectors were fit with both models, and very little difference in the quality of fit was observed (data not shown).

*4.2.2.6. Results:* A great deal of work has been done to tune the system to insure adequate sensitivity and precision, and account for sources of error. That exhaustive work is not documented here, but it should be noted that many of the system properties described above were the result of problem solving and optimization of the original system; e.g., the sample volume, the photobleaching correction, and the LABVIEW interface. In tuning the sample pulse, we opted not to use the smallest possible sample loop tubing diameter (50  $\mu\text{m}$ ) and, therefore, the minimum pulse volume; because, the back pressure with this tubing made the purging of bubbles very difficult. Better precision was achieved with the larger tubing. The window for photobleaching correction was adopted after we determined that photobleaching of new devices was effectively masking the permanent adsorption of BSA in that positive control. The LABVIEW interface improved the precision of timing, and eliminated memory and timing limitations arising from using the factory camera operating software. Other examples of optimization exist, as well. In the course of performing these studies a significant number of experiments have been run, and we have developed a strong sense of the robustness of the system and the quality of the conclusions.

Representative results for the non-adsorbing control species investigated here (fluorescein, Figure 4.6A, and FITC-dextran, Figure 4.6B) display completely resolved peaks that approach the original square wave input at the inlet (with some expected Gaussian character) and are more dispersed at the outlet. The amount of dispersion in the peaks is greater for the higher molecular weight negative control (FITC-dextran, MW= 70 kD) relative to the lower molecular weight negative control (fluorescein, MW= ~390D). The negative controls show little variation in the five runs of both inlet and outlet peaks, although the first run of the experiment is different for FITC-dextran, and the slight differences in the outlet peaks of the subsequent runs are correlated with run order, the area under the peak increasing on subsequent runs.

The positive controls (rhodamine, Figure 4.6C, and FITC-BSA, Figure 4.6D) display markedly different behavior than the negative controls, illustrating the difference that adsorption creates in the chromatograms: 1) Rhodamine displays dispersion much greater than expected for its size (MW= $\sim$ 450D). There is a mild upward trend in the area under the inlet peak, but the temporal order does not exactly correlate with the increase. Note that the inlet chromatograms all eventually return to baseline. There is a strong upward trend in the outlet peak area, however. Note that several of the outlet peaks are not detectable; and that, despite continuing observation for 50% longer than for other experiments, the outlet peaks that are visible have not completely passed through the window within that time. Finally note the lack of a flat baseline at the beginning of the experiment for all but the first run. 2) FITC-BSA shows a trend of increasing area under the curve for subsequent runs during a given experiment for both inlet and outlet peaks. Note also, that the inlet chromatograms do not return to the baseline; and, show a trend of decreasing deviation from the baseline with subsequent runs -- a trend that is strongest at the inlet peak. It does display peak dispersion typical for its size (MW=68 kD) if the elevated baselines and are ignored.

Representative results for a device that has been pretreated with BSA and then tested with FITC-BSA (Figure 4.7A) shows that the trends noted with an untreated device (Figure 4.6D) are abolished by the pretreatment step. Note that all peaks for this experiment superimpose, with good precision, as with the non-adsorbing control.

Increasing the concentration of BSA in an experiment with no BSA treatment also partially eliminates the trend of increasing area under the outlet peak (Figure 4.7B) in subsequent runs. For the higher concentration tested the first two runs show the upward trend, but the later runs in the experiment display similar eluted fractions.

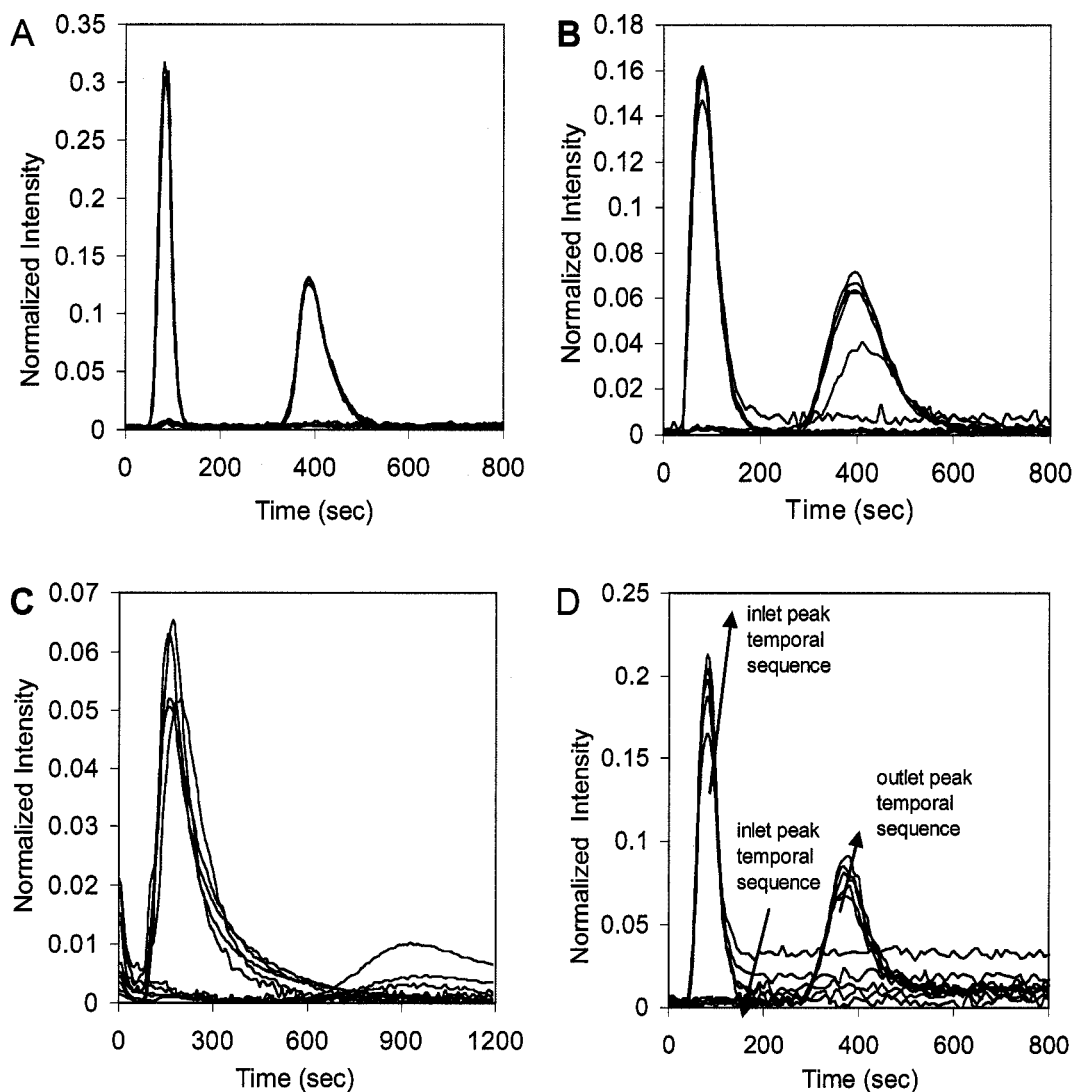


**Figure 4.6:** Results from adsorption chromatography experiments. Blue lines are observations at the inlet, and red lines are observations at the outlet, with the corrections and normalizations described in the text. A) Results for a 1  $\mu\text{m}$  fluorescein solution. B) Results for a 2  $\mu\text{m}$  FITC-dextran solution. C) Results for a 5  $\mu\text{m}$  rhodamine solution. D) Results for a 2  $\mu\text{m}$  FITC-BSA solution. Reproduced from Hawkins et al.<sup>157</sup>

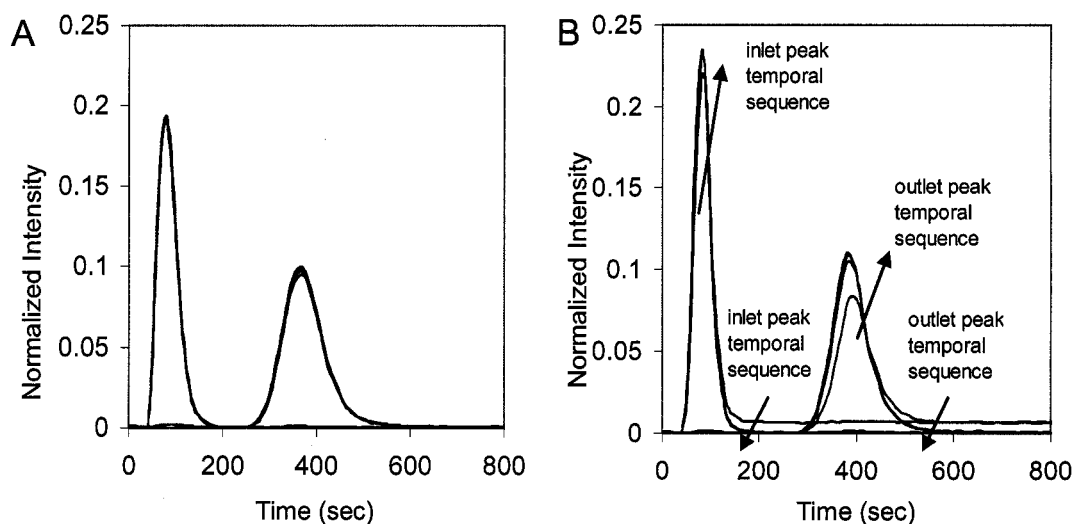


**Figure 4.7:** Experiments that establish that the most likely cause of the results in Figure 4.6D are adsorption, and not some other phenomenon. A) The results for a FITC-BSA experiment when the device is first pretreated with a concentrated solution of unlabeled BSA. B) The results for an experiment with a FITC-BSA concentration of  $20 \mu\text{m}$ , or 10-times the concentration in Figure 4.6D. Reproduced from Hawkins et al.<sup>157</sup>

Quantification of the eluted fraction for each sequential run for these typical experiments also suggests several trends (Table 4.3). The negative controls display complete elution of the inlet mass with reasonable precision ( $\pm 4\%$ ), with the exception of the first three runs of the FITC-dextran experiment. The positive controls (where the results were valid) show an increasing fraction of mass eluted, with the first run in the temporal sequence having the lowest fraction eluted, and rising in a monotonic function of sequence number. Fewer runs were required to recover the full input mass when the inlet concentration was higher.

**4.2.2.7. Discussion:** Results with the adsorption chromatography system described indicate that it is capable of detecting potentially problematic adsorption in a microfluidic device. The device is a realistic model of the types of plastic-laminate devices that we envision for POC diagnostics with the protein DIA

Results with fluorescein (Figure 4.6A) illuminate the performance of the system in the absence of adsorption. The high degree of peak superposition in the five within-experiment-runs, seen in both inlet and outlet peaks, indicates that this system can be operated with the high precision needed to draw statistically powerful inferences about adsorption. The sharp and well-resolved peaks indicate that the Taylor dispersion expected in a pressure-driven flow system is not too great to prevent the detection of subtle peak shape differences. The return to baseline indicates that no permanent adsorption to the detection window has occurred. The progress of the centroid of the peak is an estimate of the retention time of the mobile phase, which can be used to indicate if the elution of a test species (or positive control) has been slowed by transient adsorption. .

**Table 4.3:** Fraction of inlet mass eluted, as observed at the outlet, for each of the five sequential runs in the typical experiments presented. The cardinal numbers assigned to the run sequence correspond to the temporal order in which they were run.

Identification	Function	Figure Ref.	Run Sequence				
			1	2	3	4	5
1 $\mu\text{m}$ fluorescein	Neg. Control	4.6A	1.04	1.02	1.00	1.00	1.00
2 $\mu\text{m}$ FITC-dextran	Neg. Control	4.6B	0.67	0.92	0.92	0.96	1.00
X $\mu\text{m}$ rhodamine	Pos. Control	4.6C	~0	~0	quantitation invalid, but trend is upward with run		
2 $\mu\text{m}$ FITC-BSA	Pos. Control	4.6D	0.74	0.76	0.82	0.87	0.92
FITC-BSA in BSA treated device	Neg. Control	4.7A	1.03	1.07	1.06	1.01	1.02
20 $\mu\text{m}$ FITC-BSA	Pos. Control	4.7B	0.81	0.94	0.96	0.98	0.99

The results for FITC-dextran (Figure 4.6B) suggest that it is not actually a negative control. The pattern of run-dependant changes in inlet baseline and eluted peak area look very similar to what was observed for FITC-BSA, a positive control – especially when BSA was tested at a higher concentration. A better high molecular negative control is required.

Both positive controls (rhodamine, Figure 4.6C, and FITC-BSA, Figure 4.6D) clearly show the presence of adsorption, as evidenced by the differences in the chromatograms compared to negative controls of the same approximate diffusivity, although the differences between these controls suggest the subtle differences in adsorption detectable by this system.

In the FITC-BSA results, the elevation of the chromatogram baselines to a new steady state after the passing of the sample pulse suggests permanent adsorption (at least on the time scale of this experiment). The increased variance of the peak and the asymmetric “tailing” suggest a transient adsorption component as well. The location of the centroid does not appear to be greatly affected (compare Figure 4.6D and 4.6A), however; indicating that most of the adsorbing FITC-BSA attaches with a low dissociation rate – an observation that is consistent with what is known about BSA adsorption.<sup>123, 129</sup> We hypothesize that the peak seen at the outlet is comprised of that FITC-BSA mass which never stuck to the surface at all. A simple calculation using the relationship  $\langle x \rangle = \sqrt{2Dt} = 193 \mu\text{m}$ , which describes an average distance that a molecule can be expected to diffuse in a given time, would suggest that for the residence time in the channel before the outlet (~300s), all BSA molecules should be able to sample the top and bottom surfaces three or four times at least. However, contact with the surface doesn't mean the molecule will adsorb. There is clearly a significant fraction of the BSA population which does not adsorb. This bodes well for the application of this system for the quantitative determination of surface coverage

for a particular material set and flow rate, as permanent adsorption at the outlet window would complicate quantitative analysis.

The results for rhodamine show a different type of adsorption. The location of the centroid of the outlet peak of rhodamine is clearly later than that of fluorescein, and the peaks are very asymmetric and “tailed” -- observations which strongly suggest transient adsorption. The eventual return of the inlet chromatograms to baseline; however, indicate that no permanent adsorption has occurred. This is consistent with the models for small molecule adsorption.<sup>129</sup> The presence of the artifact at the early time points before the inlet peak has entered the inlet window is troubling; however, we hypothesize that rhodamine adsorbs with even higher affinity to the upstream tubing and that insufficient washing was done in between experiments to completely remove residual rhodamine from the tubes. These results may be easier to interpret when the experiment is repeated with additional cleaning and a longer run time.

The eluted fractions calculated (Table 4.3) are consistent with adsorption being the mechanism behind the observed results. No loss of mass with the negative controls indicates lack of permanent adsorption. The upward trend in eluted fraction with sequence number observed for positive controls is consistent with a finite number of surface binding sites for the protein. Since the surface is not cleaned between runs, additional mass introduced in subsequent runs has fewer binding sites available and a greater fraction is eluted. In the lower concentration experiments the eluted fraction never quite reaches unity, indicating the surface is still not saturated. In the higher concentration experiments, the eluted fraction reaches unity after two or three runs, consistent with the faster saturation expected from a higher concentration solution. It should be noted that the baseline is reset after each run through the signal processing algorithms, but examination of the raw data (not shown) reveals that there is a constant upward trend in the baseline over the entire experiment. It should also be noted that the normalization algorithm used is probably not appropriate when the inlet window is



experiencing a constantly increasing signal due to adsorption, rendering the quantitative values thus obtained slightly suspect. (Fluorescent material permanently adsorbed at the window is counted at all time points after the adsorption in the integration – the “duplicate detection” of the adsorbed material results in an overestimate of the input mass.) The qualitative trends have been adequately captured, however. Improvement in the inlet normalization is planned for the future.

It is important when interpreting results from these experiments that the chromatograms of potential adsorbents are compared to negative controls *of similar diffusivity*. Taylor diffusion is greater when the diffusivity is less,<sup>31, 33, 161</sup> so to separate the dispersion due to adsorption from the dispersions due to flow, a similarly diffusive control is required. The results in Figure 3.11 suggest two ways this may be accomplished without resorting to identifying a non-adsorbing species of similar diffusivity (a task whose difficulty is illustrated by the FITC-dextran results). 1) Use of a non-fouling coating will create a negative control; however, that will not be useful if the objective of the experiment is to identify or validate such a coating. There is always the question of the stability of the coating, as well. A useful control experiment to accompany Figure 4.7A would be to pretreat the surface with FITC-BSA and run the experiment with unlabeled BSA, to see if there is any desorption of the non-fouling coating. 2) A high concentration of the adsorbate may create a negative control if the signal from the unadsorbed fraction is so great that it renders the signal from the adsorbed material undetectable. If the material adsorbs permanently, the device can be pre-treated to saturate the binding sites to further reduce the signal from adsorption. Thus an adsorbate can be used as its own control. Nevertheless, it would be useful to have an independent negative control species.

Perhaps the most meaningful and appropriate negative control is analytical or numerical predictions for peak shape in the absence of adsorption specific to the adsorbate of interest. The usual chromatographer's equations do not apply in many

microfluidic situations, and a numerical solution for the temporal evolution of dispersion in arbitrary geometries that accounts for all phenomena requires specialized software and computational power. Therefore, it is useful to determine if simplifying assumptions can be made.

Consider the results for fluorescein. Application of the Taylor/Aris equation<sup>31, 33, 158, 162, 163</sup> requires that the solute concentration be almost uniform in the dimensions transverse to flow. For fluorescein in this device, the time-scale of diffusion in the depth dimension is much smaller than the time-scale for advection (the ratio is on the order of  $10^{-5}$ ). Thus the Taylor assumption applies in the depth dimension. However, the time-scale for diffusion in the width dimension is about an order of magnitude greater than the time-scale for advection -- the Taylor assumption does not apply in the width dimension. Nevertheless, because of the large aspect ratio of the channel and the small size of the sample window, the velocity profile is close to uniform (in the width dimension) across the sample window. In addition, the advective flux of fluorescein is  $\sim 1000$  times greater than the diffusive flux. Therefore, it seems reasonable to neglect the small transverse fluxes and treat the problem as Taylor dispersion in a slit, with a distance  $H$  between the walls. The theory for flow between parallel plates is well known. The dispersion can be expressed with an effective diffusion coefficient,  $D_{eff}$  which is a function of the depth of the channel  $H$ , the molecular diffusion coefficient  $D_m$ , and the linear velocity  $U$  (Equation 17).

$$17) \quad D_{eff} = D_m + \frac{2H^2U^2}{105D_m}$$

Since this system samples the concentration ( $C$ ) at the centerline of the channel, the correct flow velocity is  $3Q/2HW$ , where  $Q$  is the volumetric flow and  $W$  is the channel width<sup>164</sup>.

This effective diffusion coefficient describes the spreading of a delta-function input by  $\sigma_d^2 = 2D_{eff}t$  where  $\sigma_d^2$  is the peak variance. The variance thus calculated is a parameter

in a unity-normalized Gaussian describing the concentration,<sup>163</sup> with a centroid ( $\bar{t}$ ) that is determined by translating the centroid of the input function to a time calculated from the flow velocity and distance between “windows” (Equation 18).

$$18) \quad C(t) = \frac{1}{\sqrt{2\pi}\sigma} e^{-\left(\frac{t-\bar{t}}{2\sigma^2}\right)}$$

For arbitrary input functions ( $\phi_{in}$ ), the input function must be convoluted with the expected dispersion to correctly describe the outlet peak ( $\phi_{out}$ ),<sup>163</sup> where  $G(t,t')=f(t-t')$  is the Green's function for the one dimensional advection diffusion operator (Equation 19).

$$19) \quad \phi_{out}(t) = \int_{-\infty}^{\infty} G(t,t') \phi_{in}(t') dt'$$

The sample injection valve used in this device is assumed to produce a plug of length  $\tau=22.6s$ , which is unity-normalized by the signal processing algorithms. Thus the input function can be written,  $C(t')=C_0/\tau$  for  $0 \leq t' \leq \tau$ . The solution to the integral formed by applying this input to Equation 19 results in a difference of two error functions (Equation 20), where the variables have the same meaning as in Equation 18, except that the location of the centroid is adjusted by  $\tau/2$  to reflect the finite length of the sample plug.<sup>163</sup>

$$20) \quad C(t) = \frac{1}{2\tau} \left[ \operatorname{erf}\left(\frac{t-\bar{t}}{\sqrt{2}\sigma}\right) - \operatorname{erf}\left(\frac{t-\bar{t}-\tau}{\sqrt{2}\sigma}\right) \right]$$

The error functions in Equation 20 determine the shape of the leading and tailing edges of the peak, and the time displacement of their inflection points determines the duration of any plateau in the peak. With sufficiently short sample pulses, no plateau is expected.

The device design in Figure 4.4 creates one additional complication for applying this method: there is a tapered change in cross-section. To account for this change, the taper was modeled simply: half of its length was considered to be narrow channel, and half was considered to be wide channel. Each section of channel was treated as a separate element that introduced its own dispersion, and variances of each of the three sections (narrow, wide, narrow) were added, a common practice in chromatography.<sup>163</sup> The difference in centerline velocity was also accounted for in each section.

The predicted peaks were calculated and compared to experimental data (not shown). Although the magnitude of dispersion is predicted reasonably well, the predicted peaks differ from the observed results for negative controls in two important ways: 1) The peak predictions are always completely symmetrical, because of the underlying Gaussian character. This is not observed for the negative control peaks. Asymmetry can result from elements in the fluidic circuit that produce undesirable mixing.<sup>163</sup> These can be as simple as an abrupt change in cross-sectional area (which motivated the tapered channel sections), especially if an increase in cross-sectional area is rapidly followed by a decrease. It should be emphasized that the inlet peaks are not symmetric either, so even if the dispersion in the channel is Gaussian, the outlet peaks will remain asymmetric on the time-scale considered. The fluidic interface comprising the round inlet tubing, the round inlet hole, and the rectangular channel seems like the most likely location for an upstream mixing element. 2) The calculations suggest that the peak centroids should be moving faster than they are. This could be the result of incorrectly accounting for the tapered section of the channel. This could also be caused by an unintended mixing element<sup>163</sup>, as these features can act as “fluid capacitors”.

We hypothesized that the tapered channel and an unidentified upstream unintended mixing element were responsible for the discord between our observations and the predictions of the simple Taylor model. The device was redesigned to be as simple as

possible; i.e., no changes in channel cross-section between inlet and outlet, and only one turn of the largest radius possible (Figure 4.8A). The inlet peaks were also convoluted with a discrete Gaussian of the expected variance (from Equation 18) using Matlab; i.e., the  $f_i(t_i)$  of Equation 19 constituted the vectors of inlet values. The outlet peaks resulting from this second generation device match the analytical predictions well, and the convolution with the inlet matches more closely than a symmetrical Gaussian-spread plug (Figure 4.8B).

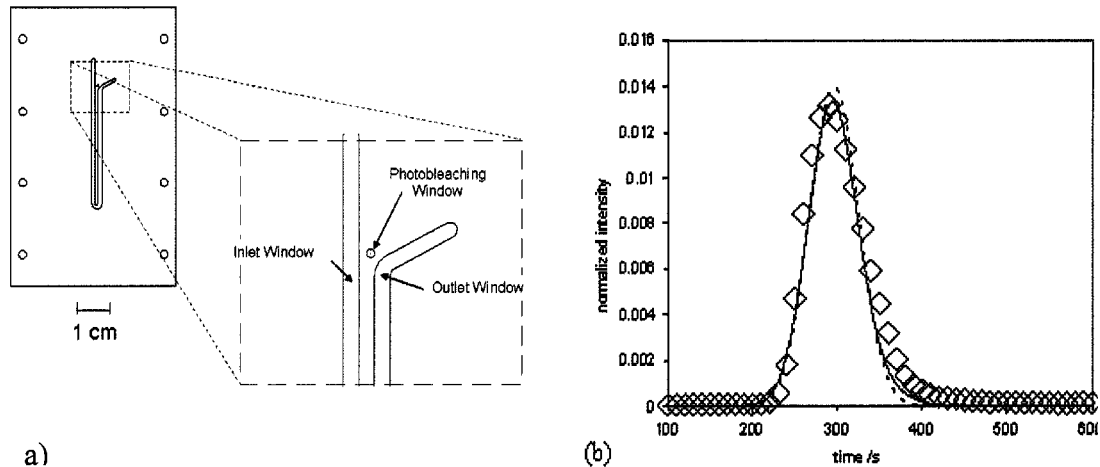


**Figure 4.8** a) The revised channel design eliminates the changes in cross-sectional area and the tapered section, and eliminates unnecessary turns. b) A representative comparison of the observed outlet peaks for fluorescein to predictions for a negative control from a simple Taylor dispersion model with the revised design. (—) = prediction as described in text, (- -) = simple Gaussian-spread plug, (◇) = observed outlet points. Symbol size corresponds to error bars. Observations are the mean of all five runs (not shown elsewhere) and the corresponding values for parameters in the Taylor model have been used. Reproduced from Hawkins et al.<sup>157</sup>

The results gathered on the first generation device are still valid; however, the simple analytical prediction of the negative result is only possible using the redesigned device.

### 4.1.3 Eliminating adhesives in plastic laminated T-sensors

*4.1.3.1. Motivation and Theory:* Adhesive lamination of through-cut films has some inherent problems. The use of adhesives in microfluidic reactors can create problems due to adsorption of reactants to the adhesive, absorption of reactants into the adhesive, leaching of complex adhesive components into the reaction mixture, interference with fluorescence detection from adhesive autofluorescence, and mechanical de-lamination from failure of the adhesive (personal experience). It is also difficult to apply a uniform, thin layer of adhesive without specialized equipment, making the substrate much more expensive than the base films. Lamination “foils” exist that can form a heterogeneous bond (analogous to a solder joint), but this still introduces a second material. Welding uses the same material for all layers, and result in monolithic device that presented a single surface type to the fluids in the network.

Welding plastics can be done with solvents and with heat.<sup>165, 166</sup> Frictional heat created by ultrasonic vibration has been a common plastic joining method for many years.<sup>165</sup> These techniques present challenges for film lamination, however. Uncontrolled melting of the bulk can degrade the dimensional fidelity of the original part, necessitating complex fabrication methods to protect the channel during bonding; such as the sacrificial wax method.<sup>167</sup> Solvents can cause clouding of optically clear substrates, and are also difficult to control. The movement of the layers in relationship to one another required for friction welding makes proper registration of key features difficult, if not impossible. Development of a facile welding-based lamination method would greatly enhance the rapid prototyping potential of the through-cut lamination approach.

The theory behind solvent assisted thermal bonding (SATB) has been described.<sup>168</sup> Briefly, the bulk polymer is incubated with a plasticizer which disrupts the polymer

network enough to depress the glass transition temperature ( $T_g$ ), but diffuses slowly into the bulk and does not actually dissolve it. Bonding is then realized by pressing and heating the parts to above the depressed  $T_g$ , but below the bulk  $T_g$ , involving only the activated surface layers in the bond. The close spatial contact of the layers and the increased mobility of the polymer molecules above the activated-layer  $T_g$  results in considerable interpenetration of the polymer chains across the bonding interface. The result may even approach a true, monolithic weld; although, excellent bonding may occur before this point. By controlling the solvent exposure, the thickness of the activated layer can be tuned to give the best combination of bond quality and channel dimensional fidelity for the application. Good reviews of polymer joining techniques can be consulted for further information.<sup>165</sup>

Elastomers do not in general have a well-defined  $T_g$ .<sup>169</sup> For any sample, the thermal history, and rate of heating and cooling can change the measured  $T_g$ . In addition, different manufacturers frequently add different proprietary additives to films to infer additional functionality (e.g., ultraviolet light absorption) which may change the  $T_g$ . The addition of a plasticizer reduces the  $T_g$  by creating highly mobile voids in the amorphous polymer network, in effect creating additional free-volume into which the polymer chains can move. Pressing serves both to force the lamina to be conformal, and as a means of further manipulating the  $T_g$ . Since the transition from the glassy to the rubbery state generally involves an increase in specific volume as the chains become more mobile, the application of pressure should increase the  $T_g$  somewhat. The application of persistent pressure can also produce shear forces that cause viscous flow. Thus, there is a certain amount of empirical fine-tuning that will be required for any SATB process.

Recently, SATB has been used to create facile bonds for slab-etched microfluidic devices for several different polymer substrates.<sup>114, 170</sup> SATB is similar in many respects to other types of polymer welding; e.g., solvent welding or heat welding.

However, SATB has several advantages for lamination of microfluidic devices: (1) Treatment of the entire surface of the parts means that all surfaces are involved in the weld, even if they are located internally in inner layers and therefore inaccessible to local application of heat or solvent. (2) Tight control over the thickness of the disrupted layer that is actually involved in the weld results a better control over the dimensional fidelity of the process. (3) Bonding is not immediate (with the appropriate choice of materials), so alignment of features can be done during final assembly. This technique should be applicable to any polymer film and plasticizer combination.

The use of SATB lamination in the fabrication of a fairly complex three-dimensional microfluidic sheath-flow device has already been briefly described.<sup>113</sup> This section examines the method in more detail, and explores the parameters for obtaining a strong, high-fidelity bond.

*4.1.3.2. Polymer Film and Plasticizer:* For all of the work described in this dissertation (except controls as noted), 0.175-mm thick optically-clear poly(methyl methacrylate) or *PMMA*, (Rohaglas formulation #99524, Cyro Industries, Orange, NJ, USA) was used. Absolute 200° USP-grade ethanol, (AAPER Alcohol and Chemical Company, Shelbyville, KY, USA) was used as the plasticizer. *PMMA* is a common material for microfluidic devices and has several attractive material properties: compatibility with the laser cutting process, low intrinsic fluorescence, and relatively low affinity for many proteins among them. The published value of  $T_g$  for atactic *PMMA* is 105°C. The effect of ethanol on the bulk  $T_g$  is not well-characterized; however SATB of *PMMA* slabs has been reported at 95°C (with unspecified applied pressure).<sup>114</sup>

*4.1.3.3. Fabrication Equipment:* Several different methods were used to heat and press the part to illustrate the flexibility of the process and to enable adequate control of the parameters being characterized. Usable microfluidic devices of fairly complex design



were made with an inexpensive machinist's vise (Wilton model 30, WMH Tool Group, Elgin, IL, USA) to apply the pressure, and a bench-top laboratory oven to control the temperature (Shel Lab model #1330 GM, Sheldon Manufacturing, Cornelius, OR, USA). An automotive torque wrench was used to tighten the hexagonal nut of the lead screw to achieve the specified pressure. The radius of the lead screw ( $r$ ), the torque applied ( $\tau$ ), efficiency of the lead screw ( $e$ ), and the area of the vise jaws ( $A$ ) roughly determine the pressure applied ( $P$ ), by  $P = \tau e/A$ .

A fully programmable, closed loop temperature- and pressure-controlled platen press (Tetrahedron model MTP-14, Tetrahedron Associates, Inc., San Diego, CA, USA) enabled precise control of the force and temperature applied during process optimization experiments. Once the operating range had been roughly determined, a smaller hydraulic laboratory press with closed loop, temperature-controlled platens (20 ton EZ Press, Part No. 012-6306; and Atlas platens, Part No. 012-6664; International Crystal Laboratories, Garfield, NJ, USA) was employed for the remaining experiments.

Custom fabricated steel or aluminum assembly jigs with registry pins were used to hold the layers during bonding and transfer heat from the platens (or vise jaws) to the parts. Later experiments used a 250  $\mu\text{m}$  thick Mylar sheet on either side of the device to prevent the transfer of tooling marks onto the surface of the device (see Section 4.1.3.5 for explanation of the necessity of this step).

*4.1.3.4. Fabrication Procedure:* We hypothesized that several different parameters in the fabrication procedure would determine the bond strength and dimensional fidelity of the final devices. Thus, cutting parameters, time of incubation in the plasticizer, platen temperature, pressure applied by the press, total bonding time and annealing time were varied to determine their effects and optimum values.

The several layers of the chosen channel designs were through-cut on the CO<sub>2</sub> laser (Model #M360, Universal Laser, Scottsdale, AZ, USA) using appropriate power and speed settings for the material. For all comparison testing, identical two-inlet T-sensor channels were cut (Figure 4.9). To demonstrate the bonding of a more complex design, a stacked serpentine channel design that “braided” three channels together was used (Figure 4.10).

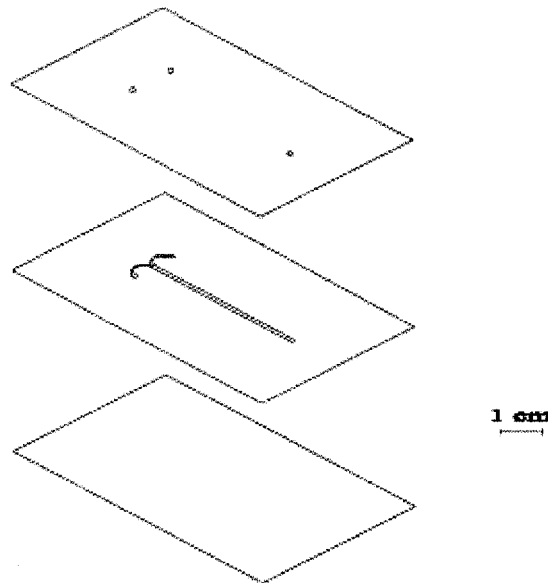


**Figure 4.9:** A scale drawing of the T-sensor microfluidic channel used as the basic test device. The main channel is 1.5mm x 40 mm, cut through the center layer of a three-layer device. The top layer has inlet holes that mate with the two channel inlets and the single outlet. The bottom layer caps the channel. The thickness of the film (0.1 mm) is drawn here to scale also, but is barely noticeable.

The laser cutting process typically causes a rounded burr at the cut edge, produced by local melting of the film and the action of surface tension on the melted material. This burr varies in size with the cutting parameters and conditions. We hypothesized that this burr would affect the SATB bond, so cutting parameters were varied to produce different size burrs. In addition, a sacrificial layer of a different film was investigated (to reduce the burr by changing the surface tension and subsequent “melt-back”). The burr was also reduced by abrading it with sandpaper for some experiments.

Once cut, the parts were sonicated in ethanol for a specified time period (5-min., 15-min., and 30-min.) to both clean and activate the surfaces for bonding. After the specified incubation, the parts were removed, dried of all liquid ethanol with low-shedding paper laboratory wipes, and stacked for lamination onto the assembly jig. Activated parts were pressed within a few minutes of soaking.



**Figure 4.10:** The photograph of a five-layer SATW laminated device. Three separate channels traverse the chip. Each is filled with a different food-coloring solution in the primary colors. The channels wrap around each other like a braid, with several segments superimposed in the XY plane. No leaks or cross-talk was noted, as evidenced by the lack of color mixing.

The assembled parts and pressing jig were placed between the platens of the press (or jaws of the vise when that was used), which had been preheated to the specified temperature (80°C, 85°C, 90°C, 95°C, or 100°C), and the specified pressure (numerous values spanning 2-25 MPa) was then applied. The pressure was maintained for a specified bonding period. Then the heating was ramped down for a specified time (or turned off for the vise/oven combination) to allow the device to cool and anneal – a step recommended by Klank et al. for SATB with PMMA slabs to avoid the formation of stress cracks in the surface.<sup>114</sup>

Several important control experiments were performed. Devices were pressed at a known bonding temperature, but with no ethanol incubation. Devices were incubated

with ethanol for a known effective time and then pressed at room temperature.

Devices were assembled with Mylar as one of the layers in place of PMMA. Solvent lamination (without elevated temperature) was attempted using methylene chloride.

Thermal lamination (without ethanol) was attempted at 120°C -- a temperature above the bulk T<sub>g</sub> -- and minimal pressure. Where possible, the controls were evaluated by the same analytical methods as the SATB laminated devices.

*4.1.3.5. Analytical Equipment and Procedure:* The devices produced were subjected to a battery of different tests to determine the effects of the different process variables. These included visual inspection for cosmetic qualities, pressure testing for leaks and bond yield strength, profilometry for quantification of pre-bonding burr height and post-bonding channel depth, optical microscopy to measure channel width, and pressure distribution testing during selected fabrication runs.

Initial inspection of devices for obvious cosmetic defects was performed by eye. A scoring system was set up to quantify these observations, but will not be presented here. Many of the devices that looked bad actually performed well in the function testing done, but excessive surface roughness could impact optical detection, and discourage device acceptance by the end user – criteria that were not formally tested.

Pressure testing was done with a custom fabricated test station comprised of a pressure transducer (Model PX181-500G5V, Omega Engineering, Stamford, CT, USA) in-line with the inlet to the device and driven by an appropriate power supply (Model PSF151-240C, Phihong USA, Fremont, CA, USA). The inlet to the device was pressurized by a programmable, positive displacement syringe pump (Model 50300, Kloehn Ltd. USA, Las Vegas, NV, USA), pumping an aqueous dye solution for better flow visualization. The voltage output of the pressure transducer was monitored using a portable oscilloscope (TekScope Model THS720, Tektronix, Richardson, TX, USA) as an A/D converter, and a custom LabVIEW (National Instruments, Austin, TX,

USA) utility to collect data. The voltage sampling rate was once per second. For leak testing, the outlet was left open, and a flow rate corresponding to the typical end use in our lab was used ( $500 \text{ nLs}^{-1}$ ). For yield strength testing, the outlet was blocked and the pump was allowed to push until the device began to delaminate. The distinct pressure peak was recorded as the yield pressure. For yield testing, thorough priming was done first to remove any bubbles.

Measurement of burrs was done with a mechanical stylus-type surface profiler (Model P-15, KLA-Tencor, San Jose, CA, USA), scanned across the width dimension of the channel. The burrs were characterized both before bonding on the un-pressed part, and after the bonding procedure by substituting the capping layer of the channel with a similar part cut from Mylar™ D (Fralock, Santa Clara, CA, USA), which does not SATB-bond to PMMA. The after-bonding scan also yielded channel depth information.

Optical microscopy was used to measure the width of the channels. Bright field images were taken with a cooled, 12-bit CCD camera (Retiga Model 1300, QImaging, Burnaby, BC, Canada) mounted on an inverted microscope (Model ICM-405, Carl Zeiss Inc., Thornwood, NY, USA) fitted with a 2.5X objective. The images were sampled with a custom Matlab utility (The MathWorks Inc., Novi, MI, USA), and the edges of the channel were located by their obvious contrast. The width in pixels was then related to the actual linear dimensions using the known pixel size of the camera ( $6.7 \mu\text{m}$ ), and the magnification factor. Channels were measured before and after bonding and normalized to the pre-bonding dimensions to eliminate the imprecision of the laser cutting from the analysis.

The pressure distribution within the jig and parts under pressure was measured using Pressurex Medium film (Sensor Product Inc., East Hanover, NJ, USA). Pressurex is a Mylar™ film that contains a proprietary two-layer microencapsulated

indicator/developer that responds to increasing pressure with increased color development. Within the pressure range (~10-50 MPa, for the “Medium”) the response is approximately proportional and can be related to absolute pressure using the color scale provided. It is easily cut by the laser, so by substituting a layer of Pressurex for one of the parts of the laminated device, the exact distribution of pressure with a fabrication run can be inferred. A pressure range was chosen so that the pressure applied to the jig would fall in the low end of the range. Thus a completely uniform pressure distribution would produce very little (uniform) color development, and any high-pressure regions would be easily visualized because of their high contrast.

*4.1.3.6. Results and Discussion:* The process evaluation occurred naturally in three phases. Early proof-of-principal experiments quickly established a trend in cosmetic criteria and endpoints for functional criteria. More controlled parameter optimization experiments defined the course-grained picture of the process parameter space. Fine tuning experiments resulted in a robust process in our hands and answered questions about controls and alternatives.

Early proof-of-principal experiments with the vise and oven quickly established a trend in cosmetic criteria and endpoints for functional criteria. Relatively short ethanol incubation (10 min. immersed, then towed dry), low temperature (85°C) applied for 90 min, and light platen pressure (~0.1 MPa) resulted in devices that leaked, delaminated easily, and were visibly unattractive (Figure 4.11B). Relatively long ethanol incubation (10 min. immersed, parts left “dripping wet”), higher temperature (90°C) applied for 90 min, and heavy platen pressure (~16 MPa) resulted in devices which were completely monolithic, had severely deformed or blocked channels, and which were visually unattractive (Figure 4.11C). Intermediate values of one or all of these parameters; e.g., ethanol incubation (10 min. immersed, then shaken free of liquid), temperature (90°C) applied for 90 min, and platen pressure (~8 MPa)

resulted in devices which were adequately sealed against typical operating pressures, were not different from their nominal dimensions within typical cutting imprecision, and which were visually more attractive than the non-functional devices (Figure 4.11A).

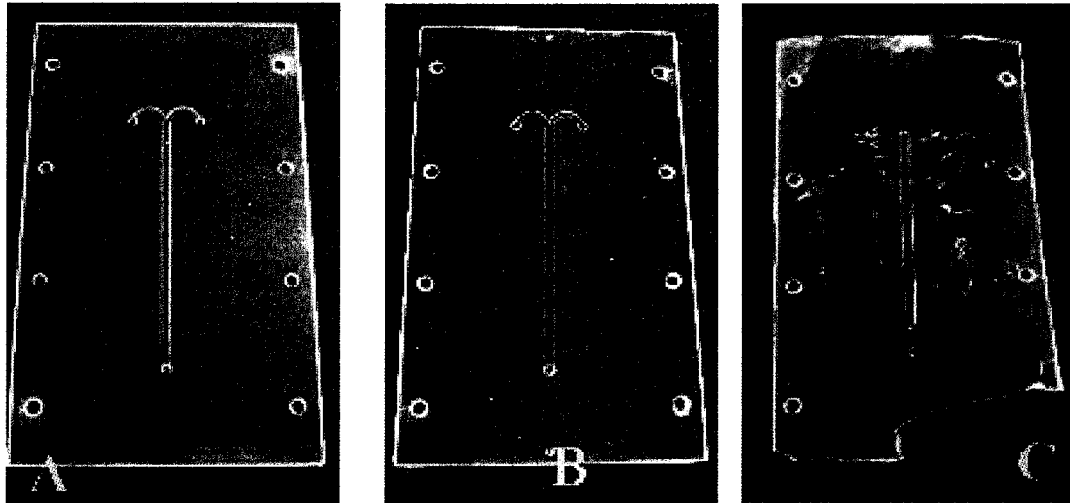


**Figure 4.11.** Some of the results of preliminary experiments into SATW parameters using the T-sensor design in Figure 4.14 (with additional holes for registry and mounting of the device into a fluidic manifold.) (A) A useable device that seals against normal pressure, has no obvious defects, and performs as desired. (B) A device that does not seal due to inadequate pressure during the bonding cycle. The poorly-bonded region can be seen in the center of the device as a milky stripe. (C) A device which has been crushed; notice that the inlet channels have almost disappeared, the main channel does not reach the outlet hole, there are numerous bubbles, and the device became so brittle that the corner was broken off during handling. This device was made before the production parameters were well understood. Devices *B* and *C* were negatively impacted by the flatness in the jig. In device *A* the sealing quality was improved using the technique described below.

This preliminary work also highlighted a major, and unexpected, source of device failure and cosmetic problems – the characteristics of the platens and assembly jig. The first generation jigs – made of aluminum for good heat transfer -- were neither completely planar, nor microscopically smooth. Tooling marks and surface roughness of the jig was transferred into the outer surfaces of the laminated device with excellent fidelity (Figure 4.12A). The lack of planarity resulted in uneven bonding that corresponded exactly to the pressure distribution measured by the Pressurex film. Hand polishing or insertion of a “buffer layer” of 250 mm Mylar between the PMMA part and the jig resolved the transfer of roughness (Figure 4.12B). The planarity issue

was initially thought to be an indicator of uneven pressure from the vise – motivating the switch to the more precise platen presses. While use of the press improved the uniformity of pressure distribution, the bonding problems were not fully resolved until a jig was made that was larger than the device (and previous jigs), and was made from 3/8” plate steel, ground very flat with a surface grinder. Both Pressurex analysis and fabrication results show that this jig has sufficiently uniform pressure distribution.

Leak testing established that the normal operating conditions in our lab produce  $\sim 0.04$  MPa at the in-line pressure transducer in our test station. This pressure was easily withstood by almost all of the devices made that were not failures by our cosmetic criteria. It should be noted that the pressure recorded by this device is most useful for comparing different fabrication parameters with an identical device design (what we have done here), as the force applied to the bond per unit length varies with channel dimensions.



**Figure 4.12.** Optical micrographs (4X) of T-sensor channels showing the effect of jig roughness. (A) A portion of the main channel in a device showing the tooling marks that were transferred from the jig. Note also that this device is showing the channel occlusion characteristic of the endpoint represented in Figure 4.16C. (B) The junction of the inlets in a device that was made with the polished jig. Note the absence of obvious tooling marks. (Some dust and fibers of unknown origin are visible on the device surface. Bubbles indicate possible incomplete bonding; although, this device was fully functional.)



The effect of the cutting burr on the SATB lamination of PMMA films was considerable. The size of the burr was measured before SATB with the profilometer ( $\sim 15 \mu\text{m}$ ). The burr could be removed by abrasion with sandpaper and reduced by cutting through an overlaying sacrificial film layer. Presence of the burr was clearly visible in the Pressurex analysis, and was frequently correlated with incomplete bonding over the entire field of substrate material between channel features. Paradoxically, these devices performed very well in leak and yield pressure testing. It appears that the burr acts to concentrate the pressure at edges of the channel and creates a very robust bond at that very critical location. This is somewhat analogous to the ridges that are usually designed into parts that will be friction welded – the energy of the bonding process gets focused where it is most needed. The burr may also affect the dimensional fidelity of the part, as discussed in more detail below.

The rupture pressure was not significantly correlated to the pressure applied to the jig at a constant temperature at  $80^\circ\text{C}$  and  $85^\circ\text{C}$  (Figure 4.13A). At higher temperatures, the correlation is not statistically significant due to variability at low pressures and (in some cases) relatively few points tested; however, examination of the plot shows an apparent downward trend, especially at higher pressures (Figure 4.13A). The downward slope appears to increase with temperature. The bond strength averaged over all pressures (for a given temperature) went up with temperature (Figure 4.14A). This behavior is quite consistent with the concept of an activated layer with a  $T_g$  lower than the bulk. At the two lowest temperatures, the  $T_g$  of the activated layer has not been exceeded, there is very little molecular mobility, and bonding is poor, regardless of pressure. Around  $90^\circ\text{C}$  to  $95^\circ\text{C}$  the rubbery state has been reached, resulting in better bonds, but at higher applied pressures ( $> \sim 10 \text{ MPa}$ ) either the  $T_g$  is affected by the pressure, or the activated layer is starting to flow and thin. At  $100^\circ\text{C}$  the  $T_g$  is exceeded and bonding is strong, but at higher pressures the activated layer flows excessively and thinning significantly weakens the bond, as evidenced by the increase in variation with increasing temperature in Figure 4.14A.

The presence of flow at higher pressures and temperatures is supported by the channel width measurements. At the lowest temperatures and pressures, the channels retain their full pre-bonded width. As the temperature was increased, the fidelity of the width decreased (Figure 4.13B). Within each temperature the fidelity decreased with increasing pressure, especially for the higher temperatures. As temperature and pressure are increased, the rubbery activated layer begins to flow into the channel and reduce the nominal width, as well as reducing the strength of bonding as discussed above. Devices fabricated from layers with a prominent cutting burr also had poorer width fidelity, suggesting the burr flowed into the channel as well.

Measurements of the channel depth do not show a detectable correlation with the temperature and pressure (not shown). The data set gathered was much less comprehensive than originally planned due to chronic failures of the profilometer in the Washington Technology Center, Microfabrication Lab.

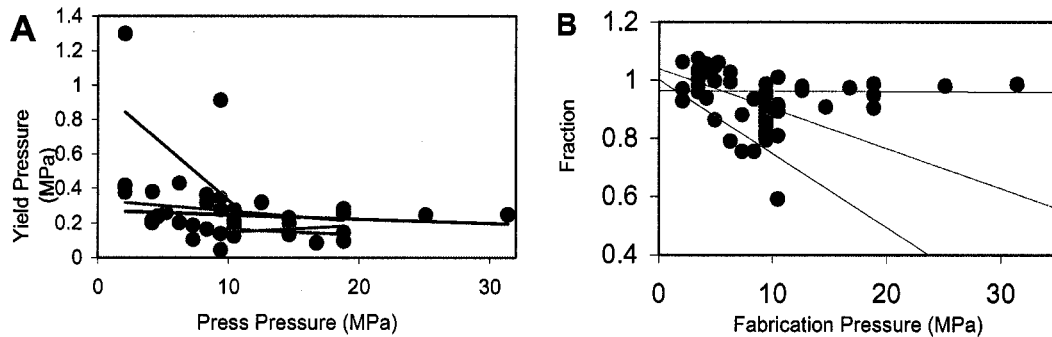


**Figure 4.13:** The effect of press pressure on the quantitative criteria. . A) Yield pressure versus press pressure for different temperatures. ● = 100 C, ○ = 95 C, ◐ = 90 C, □ = 85 C, ■ = 80 C; - = 100 C fitted line ( $y=0.004x+0.11$ ), - = 95 C fitted line ( $y=-0.003x + 0.20$ ), - = 90 C fitted line ( $y=-0.002x + 0.27$ ), - = 85 C fitted line ( $y=-0.006x + 0.33$ ), - = 80 C fitted line ( $y=-0.06x + 0.98$ ); B) Main channel width fidelity versus press pressure for different temperatures. ● = 100 C, ○ = 95 C, ◐ = 90 C; - = 100 C fitted line ( $y=-0.03x+1.00$ ), - = 95 C fitted line ( $y=-0.01x + 1.04$ ), - = 90 C fitted line ( $y=-0.0002x + 0.96$ ); Measurements expressed as a width ratio fraction of a representative unpressed channel cut during the same laser run.

Several important control experiments were performed. Devices pressed at a known bonding temperature (95°C), but without ethanol incubation, did not bond at all. Devices incubated with ethanol for a known effective time (15 minutes) and then pressed at room temperature, did not bond at all. Devices assembled with Mylar as one of the layers in place of PMMA did not bond to the Mylar, although the PMMA layers bonded normally. These results establish that the lamination observed is the result of a SATB process.

A comparison to other common plastic welding techniques was performed to assess the relative robustness of the SATB lamination. Solvent lamination (without elevated temperature) was attempted using methylene chloride. Although functional devices were obtained, the reject rate was unacceptably high. Many of the resulting devices were clouded and cosmetically unattractive, and registry of layers before bonding was challenging at best. Useable devices did have yield pressures that generally exceeded the best SATB laminated devices (~1.5 MPa). Thermal lamination (without ethanol) was attempted at 120°C -- a temperature above the bulk  $T_g$  -- and minimal pressure. While this technique yielded some useable devices with excellent yield pressures (Figure 4.14A) and good transparency, maintaining channel fidelity was very difficult with the equipment used -- the technique was exquisitely sensitive to applied pressure. Solvent assisted thermal lamination was far less sensitive to variations in fabrication parameters, making it a more facile process for rapid prototyping when equipment is limiting.

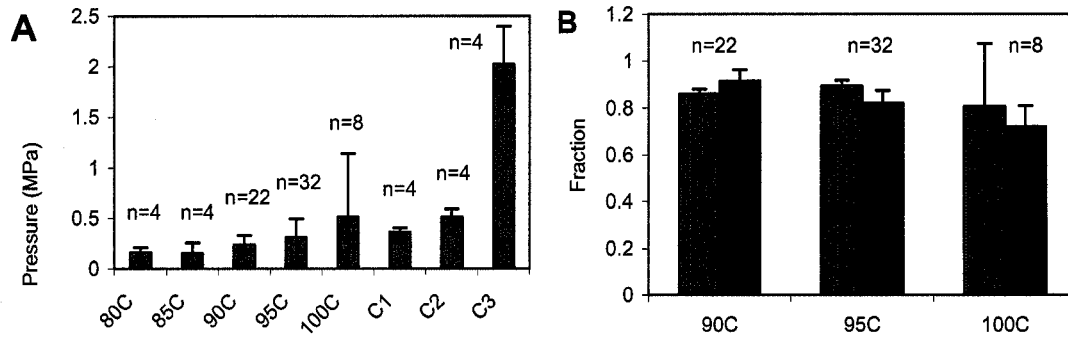


**Figure 4.14:** The effect of platen temperature on the quantitative criteria. A) Yield pressure versus platen temperature with controls. C1= Mylar with adhesives, C2 = PMMA with an adhesive coated Mylar center layer, C3 = thermally bonded (120C) PMMA, no ethanol. B) Channel fidelity versus platen temperature (controls omitted). ■ = Main channel, ■ = Inlets. Measurements expressed as a width ratio fraction of a representative unpressed channel cut during the same laser run.

**4.1.3.7. Conclusions:** Solvent assisted thermal lamination of the Rohaglas PMMA films investigated here is best accomplished with a 30 minute incubation of the parts with ethanol, followed by a 30 minute bonding cycle at 95°C and ~9.4 MPa of applied pressure, and a short annealing cycle (~30 min.) with applied pressure. A brief sonication in water before ethanol incubation can be done if cutting slag is apparent on the parts. The ethanol should be completely dried off of the parts prior to immobilization in the jig. Reduction of the burr may be desirable for some applications, but may be used to aid bonding around channel edges in others.

If other films and plasticizers are used, different optima will result; however, some generalizations from these results are possible. Temperatures below the  $T_g$  of the activated layer will result in poor bonding. Temperatures above the  $T_g$  of the activated layer will result in poor bonding coupled with a loss of dimensional fidelity. Sufficient applied pressure to create conformal contact results in the best combination of bond strength and dimensional fidelity.

The technique as described can be successfully performed with common laboratory equipment. A moderate investment in a benchtop press with temperature controlled

platens make the process very robust and repeatable. A smooth-surfaced, highly planar assembly jig is required for best results, however.

#### **4.1.4 Summary of Improvements in Raw Data Gathering**

Several important improvements that advance the feasibility of a robust POC protein DIA on a plastic disposable have been characterized. Commercially available polymer films with autofluorescence similar to glass and fused silica (the generally accepted low autofluorescence standards) have been identified, and one (Rohaglas PMMA) adopted for the DIA. A method for rigorously investigating the adsorption behavior of protein DIA reactants in channels of similar dimensions and materials, and under similar flow conditions has been developed, and used to evaluate known adsorbing molecules; although, application of this technique has not been required to generate the experimental results in this dissertation. The presence of lamination adhesives in the channel has been eliminated by developing a solvent-assisted thermal bonding process that is enabled by using PMMA. Together these results significantly improve the quality of a protein DIA when plastic chips are used.

The results of the autofluorescence studies have provided important insight into artifacts that have confounded many of the results gathered in the Yager Lab. The kinetics of decay of the autofluorescence of a plastic device (presumably, due to photobleaching) must be accounted for if the initial magnitude at the start of an experiment is significant compared to the signal of interest – a frequent occurrence when sensitive detection is required. A photobleaching correction (as used in the adsorption chromatography experiments) is one method for correcting for significant autofluorescence change. Another method, and perhaps the most expedient, is a material change to a less fluorescent polymer film. As a result of the autofluorescence work, Rohaglas PMMA film has become the new standard material in the Yager Lab

for high-sensitivity fluorescence detection on plastic laminate chips, replacing Mylar for channel-capping layers.

The adsorption chromatography system developed shows great potential as a tool for investigating adsorption to micro-devices with realistic materials, dimensions and flow rates. The results shown in this section evince the system's ability to detect significant adsorption. With further optimization of the analysis techniques quantitative inferences should be possible. The original goal of this aspect of the work – improving the protein DIA by identifying methods to reduce or eliminate reactant adsorption – was accomplished without resort to this system. However, the adaptability of the system should expand its' usefulness far beyond this modest goal. Experimentation with this device could encompass material surveys, protein surveys, treatment surveys, and kinetic studies of sufficient breadth and depth to constitute several PhD theses. It is already the subject of one publication<sup>171</sup>.

The solvent-assisted thermal bonding process developed is a unique adhesive free lamination technique that results in robust and monolithic devices. Our results show that multi-layer devices much more complex than the simple T-sensors required for this research are possible. A T-sensor made with this technique from low auto-fluorescent Rohaglas PMMA has been in use for many months without evidence of delamination, and was the analytical platform for all of the results for the C-Reactive Protein DIA described in Chapters 6 and 7. A US patent application has been filed on this process.

#### ***4.2 Modification of data analysis***

In this section, several digital signal processing algorithms are considered that address the shortcomings of the germinal DIA. Different noise filtering methods are explored

to enable response number calculation for the HRP DIA. A data transformation to stabilize the variances and linearize the response is investigated. Finally, ways to better exploit the multivariate nature of the response are discussed.

#### 4.2.1. Improvements in noise filtering

The signal processing algorithms used for the germinal DIA did not prove adequate for the task when the low specific fluorescence of the RITC-HRP conjugate was the signal generator (Section 3.1.1). Given the crude nature of the boxcar noise filter, it was an obvious target for improvement.

*4.2.1.1 Filtering Theory:* There are many different methods for digitally filtering noise from a data set that has already been gathered. High-frequency noise filtering, or *smoothing*, is the type of filtering that the germinal DIA requires in order to enable meaningful first derivative processing. A brief review of pertinent filtering theory will clarify the direction taken in the research.

Many digital smoothing algorithms employ a convolution integral. The unfiltered data sequence is convolved with a filter sequence. The form of that filter sequence varies depending on the method used. The boxcar filter used in the germinal DIA is a convolution filter with a filter sequence that can be expressed:

$$21) \text{ for } \{x_1, x_2 \dots x_i \dots x_n\}; \quad x_i = \frac{1}{n}$$

In the germinal DIA,  $n = 7$ . This is also frequently referred to a *seven-tap* boxcar (nomenclature that reflects a hardware implementation of the filter in real-time processing). A graph of this boxcar filter convolute is a discrete square wave, with seven points each having the value  $1/7$ .

Another method of constructing a filter convolute is the finite impulse response (*FIR*) filter.<sup>172</sup> This method is usually done in conjunction with Fourier analysis to determine the frequency band in which the information of interest lies, and exploits the fact that convolution in the native domain (in the case of the DIA, *1-D space*), is transformed into multiplication in the frequency domain. After the frequency of interest is identified, a cutoff frequency (or passband) is chosen. A discrete function in the frequency domain (of an appropriate length to insure adequate frequency resolution) is constructed so that all desired frequency bins have a value of unity, and are passed through the filter unchanged; and the unwanted frequency bins have a value of zero, and are rejected (by multiplication in the frequency domain). This frequency domain filter is then converted into a native domain filter sequence by the reverse Fourier transform. This sequence is truncated to an appropriate number of taps required to give adequate filtering, centered around the zero frequency bin (for a low-pass filter, as required here). This process is performed easily in Matlab.<sup>173</sup> A graph of an FIR smoothing convolute is a portion of a discrete sine wave centered around the peak, and incorporating a portion of the period that depends on the cutoff frequency and the number of taps chosen.

All convolution filters share two shortcomings. 1) They severely distort the data at the boundaries of the data domain for the  $n/2$  points ( $n$ = length of filter convolute) where the filter is not completely “engaged” with the data sequence. Because of this the data sequence is usually *clipped*, or shortened by  $n$  points to eliminate these spurious values. Where many taps are required for adequate filtering, this effect can be problematic. 2) Sharp excursions in the data tend to take the form of the convolute. This is, in fact, the desired effect, since high frequency noise can be viewed as many sharp excursions, and filter convolutes are usually “smooth” functions. However, when the information of interest also has sharp excursions (like a steeply peaked chromatograph), convolution filtering can significantly alter this region of the data, introducing systematic error of the kind discussed above. If possible, a convolute with



a similar form to the data should be chosen. Even with the right convolute, there is a shift in the abscissa value of a peak using this method, as the convolute sweeps through (usually referred to as *delay*, given that time is frequently the abscissa).<sup>174</sup>

Another type of filter is a regression filter. The best known of these is the Savitzky-Golay smoother (SGS), based on a *local least-squares* method.<sup>175</sup> This classic technique, well known to chromatographers, uses least-squared regression of low order polynomials to a small local window around the point being smoothed. Once the best-fit local polynomial is determined, the value of that function at the center point is taken as the smoothed value and the algorithm advances to the next point. The filtering characteristics are determined by choosing the size of the window and the order of the polynomial. This choice is somewhat empirical; however, popular convolutes have been characterized and tabulated so that a convolute with the desired characteristics can be chosen by examination. The SGS has no delay, but does have some of the same problems with the data domain boundaries as convolution. These characteristics make most SGS software routines lengthy and slow, but it is a fairly robust smoothing technique.

A different kind of regression filter is the penalized least-squares regression, or Whittaker filter. This filter was invented eighty years ago by Whittaker<sup>176</sup> for actuarial data processing, but has recently been revived for analytical chemistry processing.<sup>174</sup> This, so-called, “perfect smoother”<sup>174</sup> has many advantages and unique characteristics. It is based on a linear least-squares regression technique where the entire data sequence is processed simultaneously. The error function,  $Q$ , to be minimized is a sum of the squared-difference between the smoothed sequence ( $z$ ) and the unsmoothed sequence ( $y$ ), and a weighted (or penalized) measure of the smoothness of the smoothed sequence. The function used to measure the smoothness of the smoothed sequence is a sum of squared-difference of a numerical first

derivative, approximated by a backwards difference equation (Eilers, numerical book]. The result is a linear regression that can be represented in matrix form as:

$$22) \quad Q = |y - z|^2 + \lambda |Dz|^2$$

Where  $D$  is a matrix that creates the backwards differencing,  $Q$ ,  $y$ , and  $z$  are the vectors defined above,  $|a|$  is the quadratic norm of the vector  $a$  defined as  $\sum_i a_i^2$  (and which captures the summing), and  $\lambda$  is the scalar weighting factor that enables the tuning of the smoothing process. When  $\lambda=0$ , there is no smoothing – the minimization of  $Q$  results in  $z=y$ . When  $\lambda$  approaches infinity, the severely over-smoothed  $z$  is defined by the character of the difference equation.

It should be noted that backward difference equations of different orders can be used to define the weighted smoothness function in the Whittaker filter. The primary differences that result in using different order difference equations are that a given weighting coefficient has a smaller effect with higher order differences, and the character of the over-smoothed function changes. If  $k$  is the order of the difference equation, then the over-smoothed sequence approaches a polynomial of degree  $k-1$ .<sup>174</sup> A first-order difference equation produces a constant upon over-smoothing, a second-order equation produces a line, etc. Thus the order of the smoother may be chosen to more closely match the expected form of the data.

The Whittaker filter is easily coded in Matlab in a few lines, and runs very quickly. This smoother has many other interesting properties not developed here, but which may serve useful in the future work planned.<sup>174</sup>

When smoothing data, care must be taken to avoid distortion through “over-filtering.”<sup>174</sup> The introduction of distortion can produce an important source of systematic error. One of the most straightforward ways to evaluate the efficacy of smoothing is to plot the unfiltered data on the same chart as filtered data. The goal is to reduce the scatter of the unsmoothed points around the smoothed, without introducing a systematic deviation of the smoothed data from the unsmoothed. If rigor is desired, coefficients of determination can be calculated for the fit of unfiltered data to filtered data, but this calculation rarely gives insight not available from the simple visual approach.

*4.2.1.2 Procedure:* To investigate the efficacy of several digital filters, ten representative BFTN-processed accumulations at three sample analyte levels from the germinal HRP data (Section 3.1.1) were filtered by a number of candidate filters to determine which gave the best results. A seven-tap, and a 49-tap FIR filter convolute were constructed based on Fourier analysis of the spatial frequency of the modulated accumulation bump (discussed further in Section 4.2.3.1). Several Whittaker filters of first and second order and varying  $\lambda$  were also investigated. These were compared to the seven-tap boxcar filter used in the germinal DIA.

From those results, the best candidate was chosen. To assess the magnitude of the improvement, the entire data set presented earlier for the HRP germinal DIA (Section 3.1) was reprocessed using the candidate filter in place of the 7-tap boxcar filter, with no other changes. The recalculated figure of merit (ANCOVA) was evaluated for any improvement. In addition, the procedure described for HRP was also performed with the germinal IgG data set (Section 3.2).

*4.3.1.3. Results:* An examination of the comparison for a representative blank accumulation (Figure 4.15) shows that seven-tap FIR filter does not smooth the data significantly better than the seven-tap boxcar. The 49-tap FIR smoothes adequately but introduces significant distortion. A first-order difference Whittaker filter with

$\lambda=10^3$  smooths the data adequately without introducing significant distortion; however, a first-order difference Whittaker filter with  $\lambda=10^4$  does introduce significant distortion. A second-order difference Whittaker filter with  $\lambda=10^6$  smooths the data adequately without introducing significant distortion; however, a second-order difference Whittaker filter with  $\lambda=10^8$  does introduce significant distortion.

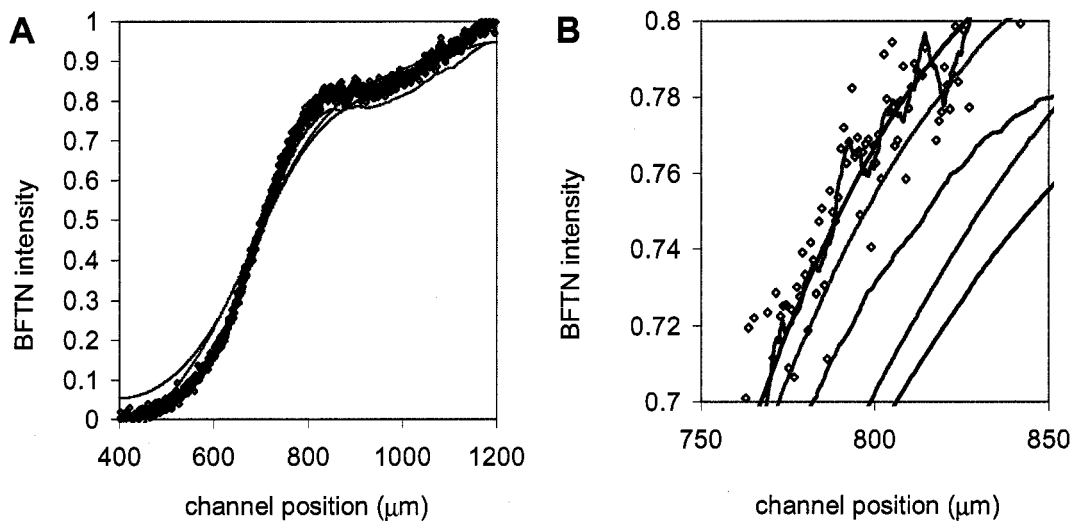


**Figure 4.15:** Comparison of the different smoothers investigated. ( $\diamond$ ) = unsmoothed data points; (—) = 7-tap boxcar; (—) = 7-tap FIR; (—) = 49-tap FIR; (—) = 1° Whittaker,  $\lambda=10^3$ ; (—) = 1° Whittaker,  $\lambda=10^4$ ; (—) = 2° Whittaker,  $\lambda=10^6$ ; (—) = 2° Whittaker,  $\lambda=10^8$ . (All filtered sequences are shown as lines to facilitate comparison; but, of course, are actually discrete sequences like the unsmoothed data.) A) A plot of the comparison over the entire data range is difficult to interpret because of the superposition of many of the plot, but does show the significant distortion of several of the candidate filters over the entire domain. B) A plot of the comparison over the critical range around the diffusion interface illustrates best the degree of smoothing achieved by the candidate filters, and also shows subtle differences in their fidelity to the data. The two 7-tap convolutes are completely superimposed, even at this scale.

The results for a HRP DIA using the best candidate filter (Figure 4.16) instead of the boxcar filter show obvious differences from the same data processed as the germinal DIA (Figure 3.1). The slope plots (Figure 4.16A) are all clearly resolved from one another, and display an obvious decrease in noise, relative to the same three accumulations presented earlier (Figure 3.1B). The plot of all responses in the data set

calculated from the improved slope plots (Figure 4.16B) likewise displays less noise and a clearer trend relative to the germinal HRP DIA (Figure 3.1C).

The results of the ANCOVA indicate that there is sufficient evidence to reject the null hypothesis that the solutions are all from the same population with a high degree of confidence ( $Pr > F = 0.0006$ ) for the fitted linear model ( $y = -0.182x + 372.7$ ), although the model fit evaluated by the coefficient of variation was still poor ( $R^2 = 0.329$ ).

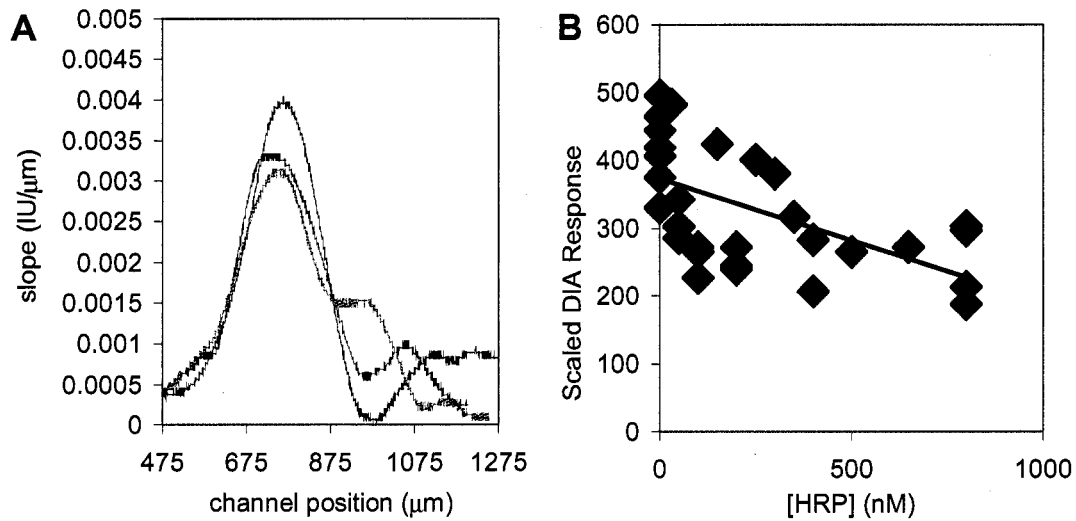


**Figure 4.16:** Representative results for the HRP DIA, improved by replacing the 7-tap boxcar filter with a  $2^\circ$  Whittaker filter ( $\lambda=10^6$ ). The same BFTN-processed accumulations used for the germinal DIA assessment (Section 3.1.1) were used as the starting point for this analysis. A) The slope plot of the three representative accumulations as presented earlier (Figure 3.1B, key identical). B) A plot of the germinal DIA responses of all mock samples (rescaled to match the abscissa scale) as a function of HRP concentration. The fitted line ( $y = -0.182x + 372.7$ ;  $R^2 = 0.329$ ) represents the linear covariation model used in the ANCOVA analysis.

A standard curve (Figure 4.17) was fit to these improved mean responses by NLLS using the 4PLL model, as was done for the germinal IgG DIA (Section 3.2). The fit was significantly better than a linear fit as measured by the coefficient of determination ( $R^2=0.71$ ) and visually seems more appropriate. Only nine replicates of

the blank are included in this data set, but a preliminary LOD was calculated as with the germinal IgG (Section 3.2), and was determined to be  $\sim 114$  nM. It should be noted, that in order to fit the model as described two replicates of the 800 nM sample analyte solution had to be excluded from the SSE calculation. These seem like obvious anomalies, as they show a response higher than some of the blank replicates, and were both determined on the same day separately from the rest of the data set. In addition, single replicates were not included in the fit, given the inherent uncertainty of those observations.

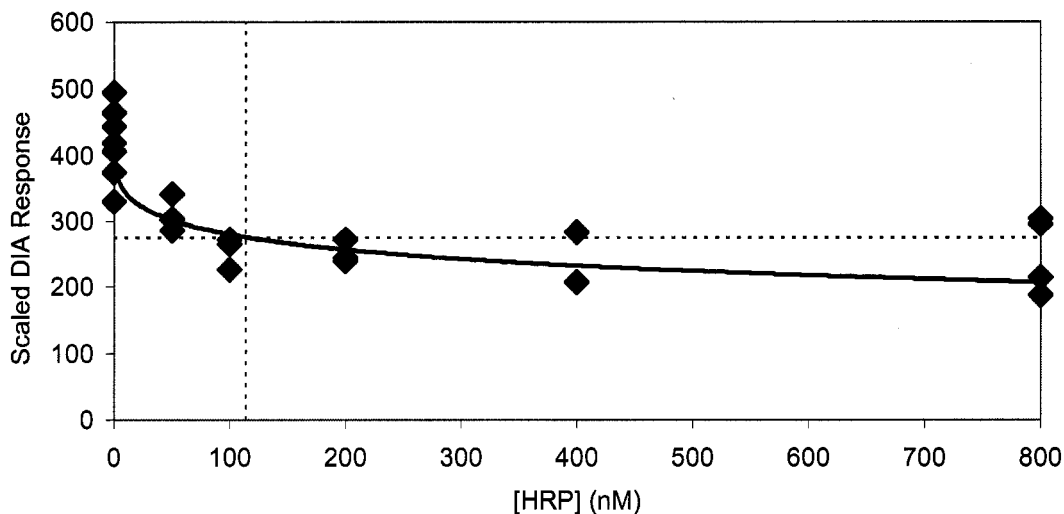


**Figure 4.17:** A 4PLL curve fit to the improved HRP data set by the NLLS procedure. (---) = graphical representation of the preliminary LOD estimation of  $\sim 114$  nM.

The higher specific fluorescence and larger blank signal of the germinal IgG made the application of the Whittaker filter less important to this assay. There was no significant difference relative to the germinal DIA for most of the analysis (plots not shown), and the calculated LOD was actually greater ( $\sim 250$  nM). We hypothesize that this was an artifact resulting from the curve fitting with a small data set, since the variance of the blank response was actually reduced by the application of the Whittaker filter.

*4.2.1.4. Discussion:* That the 7-tap FIR does not smooth significantly better than the 7-tap boxcar is not surprising when the structure of the FIR filter is examined. The Fourier analysis indicated that the correct FIR filter had a spatial frequency cutoff such that the convolute sequence in the space domain did not differ much from  $1/n$  when  $n < 10$ . Thus, the resulting filter was almost identical to the boxcar. Identical performance followed naturally, as evidenced by the total superposition of the two 7-tap smoothed sequences (Figure 4.15).

The results of the comparison strongly suggested that there were several filters from the candidates that could produce the improvement required. The second-order difference Whittaker filter, with  $\lambda=10^6$ , appeared to be the best candidate for giving improved smoothing without data distortion or clipping. It should be noted, that while a number of different Whittaker filters were investigated, there may be a Whittaker smoother with higher order difference equation or different penalty ( $\lambda$ -value) that gives even better results. The second-order difference was chosen because it results in a discrete line at the limit of infinite penalty. This seemed close to the unsmoothed form of the data than a constant or higher-order polynomial. There is a formalism for determining the optimum value of the penalty,<sup>174</sup> but we have not applied it to this analysis.

The application of the second-order difference Whittaker filter, with  $\lambda=10^6$ , resulted in a dramatic improvement in the analytical signal-to-noise ratio of the HRP DIA, as evidenced by the fully resolved slope plots (Figure 4.16A). Note the difference in the form of the slope plots relative to the phenytoin DIA (Figure 3.1B). Even more care must be taken when choosing the region in which to calculate the minimum and maximum (see section 4.2.3.3 for a further discussion of this observation).

The application of the second-order difference Whittaker filter, with  $\lambda=10^6$ , resulted in a dramatic improvement in the response-to-noise ratio of the HRP DIA, as evidenced by the response plots (Figure 4.16B), and the significant ANCOVA results. The

ANCOVA and LOD analyses establish that improved HRP DIA could be functional as formulated as a qualitative assay with a limit of detection of ~114 nM. It may also be usable as a quantitative assay, with a dynamic range of ~114 to ~800 nM, although the sensitivity is poor in this range, as evidenced by the low slope of the curve compared to the variation within test solutions (Figure 4.17), and the difficulty encountered in the NLLS curve fit. Further improvement may be required before it can be considered a robust quantitative technique.

It should also be noted that, as observed with both germinal DIAs (Section 3.1), the ANCOVA analysis as performed may not have the statistical power that it could. The plot of all responses (Figure 4.16B) still suggests a possible mean-dependence of the variance. Also, as with IgG, there is strong evidence that the ANCOVA is based on an inappropriate model. In the section that follows (Section 4.2.2) data transformation to stabilize the variances and linearize the response to determine if it will increase the power of the statistical inference and simplify precise quantitation is investigated.

The slight improvements seen with the IgG DIA, do not refute the universal applicability of the Whittaker filter to the DIA because it was already superior to the germinal DIA for HRP; however, they do highlight the fact that smoothing only reduces one type of noise that was a lurking variable in the germinal DIA.

#### **4.2.2 Transformation of responses to stabilize variance**

In the analysis presented so far there have been several instances where data transformation was considered advisable. The germinal DIA for phenytoin displayed marked non-linearity in its dose/response curves, and in order to achieve maximum sensitivity and dynamic range, a four-parameter log-logit (4PLL) model was used to model the standard curve, with a non-linear least squares (NLLS) regression fit (Section 2.2.1). The results for the HRP and IgG DIAs (Section 3.1 and Section 3.2) also indicate that the dose/response is non-linear for much of its potential dynamic



range. Also discussed was the possible mean-dependence of the variances in DIA response as a function of analyte concentration and the potential impact on the validity of the ANCOVA analysis (Section 3.2 and Section 4.2.1). Thus, transformation was investigated.

4.2.2.1. *Theory:* As discussed earlier (Section 2.2.1), it is possible to use the 4PLL function in a different way: for a given dose/response data pair the concentration (dose) is transformed by a logarithmic transformation, and the response is transformed with the *logit* transformation, expressed as:

$$23) \quad y_i' = \log \frac{y_0 - y_i}{y_i - y_\infty}$$

where,  $y_i'$  is the transformed response,  $y_i$  is the individual response undergoing transformation, and  $y_0$  and  $y_\infty$  are the estimates for the response of the blank and of an infinitely concentration of sample analyte, respectively, as before. The resulting transformation is a 2PLL because the 4PLL parameters  $y_0$  and  $y_\infty$  are used in the transformation. It is also a linear model when plotted on the transformed axis. This represents a significant advantage in model fitting – a linear least squares (LLS) procedure can be used, which has a unique algebraic solution – as opposed to the iterative NLLS procedure with its attendant uncertainties (Section 2.2.1).

Anytime data transformation is considered, and subsequent statistical inference is desired, care must be taken that the transformation does not introduce variance instabilities that violate the assumptions of the subsequent analysis.<sup>10</sup> The ANCOVA analysis relies on the assumption that the variances for all means to be compared are independent, and identically distributed (*IDD*). The data set used for phenytoin did

not include sufficient true replicate responses to evaluate the variance effects from the 2PLL log-logit transformation, so it was avoided. Thus it became a goal of this research to gather enough true replicates to test the effects of the transformation.

In the results gathered so far, the responses of the HRP and IgG DIA both seemed to display some mean-dependence of the variance in the absence of transformation. In this case, a transformation is *recommended* to stabilize the variances, so that inferences are valid, even if it is not required for other reasons. There is a formalism for determining a stabilizing power transformation – the Box-Cox procedure<sup>10</sup> – but does not necessarily yield a linearizing transformation, *per se*. The theory and details of the Box-Cox procedure are not discussed here, but can be found in many statistical texts.<sup>10</sup>

*4.2.2.2 Procedure:* The improved, Whittaker-filtered responses were analyzed by the Box-Cox procedure and an appropriate power transformation determined. The IgG data set was transformed by the power transformation. Both the HRP and IgG data sets were transformed by the log-logit transformation. The ANCOVA analysis was then recalculated with the transformed responses.

*4.2.2.3 Results:* The Box-Cox procedure indicated that a power transformation  $y' = y^{0.8}$  should best stabilize the variances of the IgG data.

The effects of the transformations are apparent upon examination of the data plots (Figure 4.18). The plot of the IgG power transformation (Figure 4.18A) displays less difference in the variance of the data for solutions of differing analyte concentrations relative to the untransformed data. The fitted linear model ( $y = 0.0315x + 71.367$ ) is still a poor fit, as evaluated both visually, and by the coefficient of determination ( $R^2 = 0.5467$ ). The plot of the log-logit transformation for IgG (Figure 4.18B) displays less difference in the variance of the data for solutions of differing analyte concentrations relative to the untransformed data. The fitted linear model ( $y =$

$0.5475x - 2.3782$ ) is a much better fit, as evaluated both visually, and by the coefficient of determination ( $R^2 = 0.7935$ ). The plot of the log-logit transformation for HRP (Figure 4.18C) appears to display less difference in the variance of the data for solutions of differing analyte concentrations relative to the untransformed data.

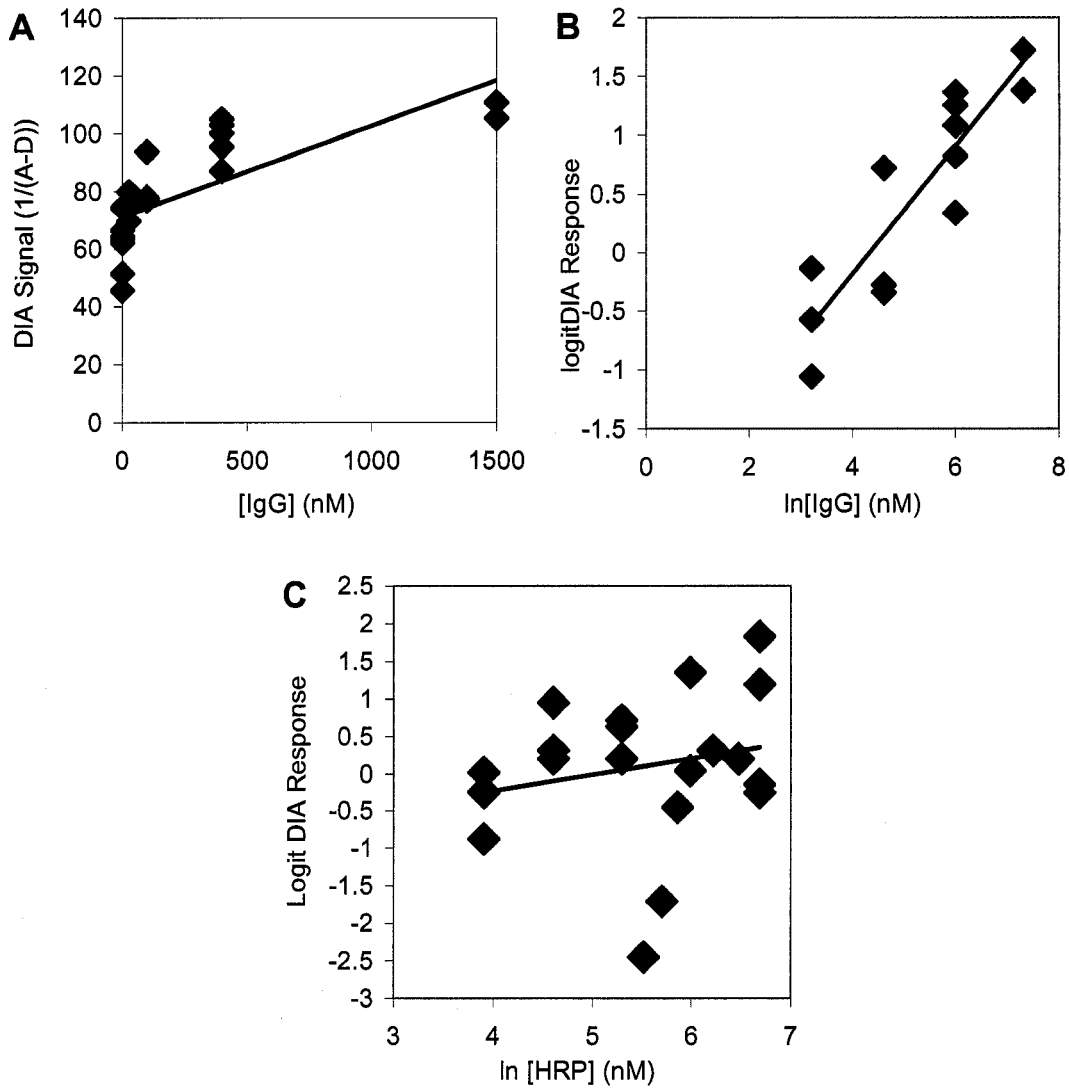


**Figure 4.18:** Data plots for transformed DIA responses for: A) the IgG DIA transformed by a power transformation ( $y' = y^{0.8}$ ) with a fitted line ( $y = 0.0315x + 71.367$ ,  $R^2 = 0.5467$ ), B) the IgG DIA transformed by the log-logit transformation with a fitted line ( $y = 0.5475x - 2.3782$ ,  $R^2 = 0.7935$ ), C) the HRP data transformed by a log-logit transformation with a fitted line ( $y = 0.2124x - 1.0766$ ,  $R^2 = 0.0488$ ).

The fitted linear model ( $y = 0.2124x - 1.0766$ ) may be a better fit, as suggested visually, but the coefficient of determination ( $R^2 = 0.0488$ ) is still very small.

The results of the ANCOVA indicate that there is sufficient evidence to reject the null hypothesis that the solutions are all from the same population with a high degree of confidence for both IgG transformations ( $Pr > F < 0.0001$ , for both). The results of the transformed HRP ANCOVA are barely significant ( $Pr > F = 0.0465$ ), when compared to the usual criterion.

An LOD analysis can be done for the log-logit transformed data if the fitted lines from the data plots are used as standard curves. For the IgG log-logit transformed data, a preliminary LOD of ~1275 nM results. For the HRP log-logit transformed data, a preliminary LOD of ~343 nM results.

*4.2.2.3 Discussion:* The Box-Cox derived power transformation appears to stabilize the variances as expected – that is what the procedure is designed to do. The better conformation of the variances to the assumptions of the analysis is reflected in the increase in the significance of the ANCOVA, but the linear model still seems inappropriate.

The log-logit transformation both stabilized the variances and linearized the dose-response relationship, as best illustrated by the IgG data set (Figure 4.18B). The HRP analysis also appears to be stabilized and linearized; however, a lurking variable(s) that remains in this data set makes the trend less obvious.

The increase in the significance of the ANCOVA results indicates that the transformation has increased the power of the statistical analysis – there is little doubt that both the IgG DIA and the HRP DIA display a real response to changes in sample analyte concentration.

The increase in the calculated LOD may be the result of one or both of two factors: 1) The linearized response is returning a more accurate LOD. This hypothesis is supported by the relative ease of standard curve fitting with the transformed response; however it is refuted by the greater relative weighting given to solutions at the upper end of the dynamic range with this procedure. 2) There are analytical artifacts that result from the small and unbalanced data set, either in curve fitting, or in calculation of the blank variance. This hypothesis seems reasonable, and is easily tested.

These observations suggest the potential of the log-logit transformation to improve DIA calibration and analysis; however, a final judgment as to the efficacy of this transformation requires a larger and more balanced data set that better spans the putative dynamic range. Further investigation was not performed as part of this dissertation – other techniques were deemed to be more fruitful.

#### **4.2.3 Leveraging more of the available information into the signal**

The germinal DIA response algorithm uses only a fraction of the information available in the raw accumulation profile, as discussed earlier (Section 2.2.3). The alteration in mass transport that results from specific binding of labeled antigen is detectable over several hundred sampled pixels, yet the response number calculation uses the information in only two pixels – the points of maximum and minimum slope in the accumulation and depletion regions. In this section, approaches to using more of the available information are investigated.

*4.2.3.1 The Discrete Fourier Transform (DFT):* One conception of the accumulation of fluorescent mass in the DIA is as an addition of a higher spatial-frequency component to the “waveform” that results from free diffusion (or, more accurately, complete competition by unlabeled analyte). The validity of this conception was verified by simple Fourier analysis on simulated data with Matlab, previously mentioned when discussing the design of the FIR smoothers (Section 4.2.1). A plot of

the full DFT sequence of simulated HRP data (Figure 4.19A) shows a large magnitude at the zero-frequency bin, corresponding to the “DC” change in fluorescence signal that results from the two different input solutions. Also noticeable in the full plot are several frequency bins with non-zero magnitude below  $\sim 0.01$  cycles/ $\mu\text{m}$ . A closer view of some of the frequency bins (Figure 4.19B) reveals that the modulated response of the accumulation curve is present in the frequency bins between 0.001 and 0.006 cycles/ $\mu\text{m}$ . There were no modulated changes in the phase plots of the DFT (data not shown).

The Fourier analysis suggested several conclusions. The modulated response of the accumulation did not include any significant frequency changes, thus any response extraction algorithm applied to a DFT of the accumulation would be similar in nature to the algorithms used for the accumulation itself – modulation would have to be detected in the background of the blank signal. The DFT used did not significantly reduce the multivariate nature of the response – the response was visible in  $\sim 90$  frequency bins. The response was clearly present in these simulations, however. Given the other attractive properties of the DFT, we proceeded to investigate its potential as a signal processing step.

Initial simulations with simulated noise and systematic error (not shown) suggested that the DFT would make an effective filter for high frequency noise and would dampen the effect of large (uncorrected) background shifts and scaling changes of the type corrected for by the tail-normalization procedure (Section 2.2.1). The DFT did not seem resistant to midline shifts (as seen with flow instability), but then neither was the germinal DIA algorithms prior to the final response calculation. Nevertheless, we hypothesized that DFT processing could eliminate many or all of the germinal DIA signal processing steps (Section 2.2.1)

Initial attempt to apply the DFT to actual HRP DIA experimental observations were puzzling – even though the observed accumulations matched simulations well

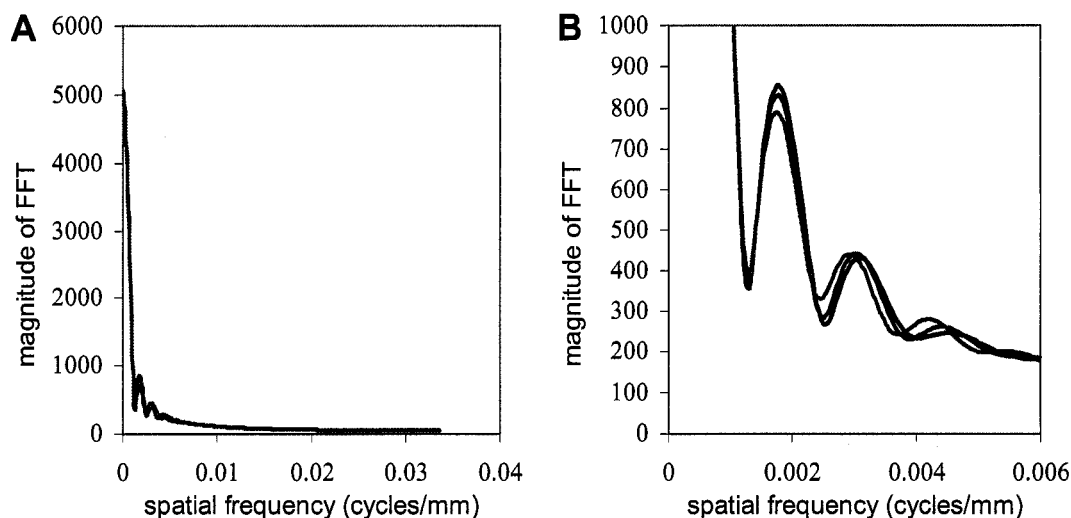


**Figure 4.19:** Discrete Fourier transforms of simulated HRP accumulations. The simulations are identical to those shown earlier (Figure 3.1). For both figures, blue is the blank signal, red is the response to 200 nM sample Ag, and green is the response to 800 nM sample Ag, as before. A) The full DFT. At this scale all three simulations superimpose. B) A zoomed-in plot of the DFT in ‘A’ showing only those frequency bins where modulated response is observed.

(Figure 3.1), the observed DFTs did not match the DFTs performed on the simulations (not shown). Further analysis and simulation (not shown) revealed the cause. We were not observing the entire width (diffusion dimension) of the channel to eliminate the confounding effects of the autofluorescence at and outside the walls. This smaller “window” on the data acted to spread the response out over more frequency bins. This spreading, combined with the presence of all of the usual sources of error in the real data, acted together to reduce the magnitude of the modulation to undetectable levels.

These results indicated strongly that to include the DFT in DIA signal processing would complicate the algorithms, not simplify them. The DFT will only show a DIA response if all of the usual DIA BFTN processing is done first. Thus it does not represent a simplification of processing. In addition, it is well known that the DFT is a technique best suited to frequency analysis of periodic data. The discontinuities at the ends of finite discrete sequence create artifacts that must be mitigated by numerous

periods of the waveform of interest.<sup>172</sup> The typical DIA accumulation resembles only one half-period. While it would be possible to digitally reflect the data to create a full period, and even to concatenate many of these sequences to create multiple periods, this complicates the algorithm greatly. Simulations suggest this process would also be very sensitive to midline shifts and changes in the size of the interrogation window (not shown). All of these factors lead to the rejection of the DFT as a pre-processing method.

It is possible that the DFT could still be a useful pre-processing technique if images of the whole channel were used; however, when adhesive-coated Mylar is used to join the layers autofluorescence at the walls represents a significant interference. In the second generation DIA, solvent-assisted lamination enabled imaging of the whole channel, but use of the DFT was not revisited.

*4.2.3.2 Multivariate Calibration:* The multivariate nature of the DIA accumulation has already been discussed and displayed repeatedly throughout this proposal. Any technique that will exploit this has potential for improving the DIA.

Multivariate calibration techniques have a multiplex advantage over the “bivariate” technique used for the germinal DIA – more of the information encoded in the signal is leveraged into the calibration model.<sup>177</sup> They are also more amenable to automation than the germinal DIA method. Frequently greater precision results from eliminating user discretion in processing decisions. Partial least-squares regression (*PLS*) is the most common of these techniques.

PLS is a regression technique that searches the multidimensional dose-response space to find a coordinate transformation that segregates the observed variance more effectively than the coordinate system imposed by the physical constraints of the system.<sup>177</sup> It is analogous to a simple two-dimensional linear regression of X-Y data set that contains an underlying linear relationship overlaid by noise. In this simple



case the variation from the two sources are present in projections on to both axes (Figure 4.20A). However, the linear regression finds the vector in X-Y space that best describes the variation due to the linear relationship. This vector and the orthogonal vector comprise a new basis set that, when viewed as a new coordinate system, segregate the variance more meaningfully. A projection of the data onto the fitted line shows maximum variation, only due to the underlying correlation; and a projection onto the orthogonal axis shows much reduced variation, now attributable only to noise (Figure 4.20B).

It is straightforward to expand the simple linear algebra that enables a unique solution to the linear least squared (*LLS*) regression equations to a multidimensional domain. The result is multiple least-squares regression (*MLS*). In practice *MLS* does not apply well to many situations, because it requires that the sources of variation in the data set are all independent. Real data generally does not meet that requirement, resulting in ill-conditioned matrices in the solution.<sup>177</sup>

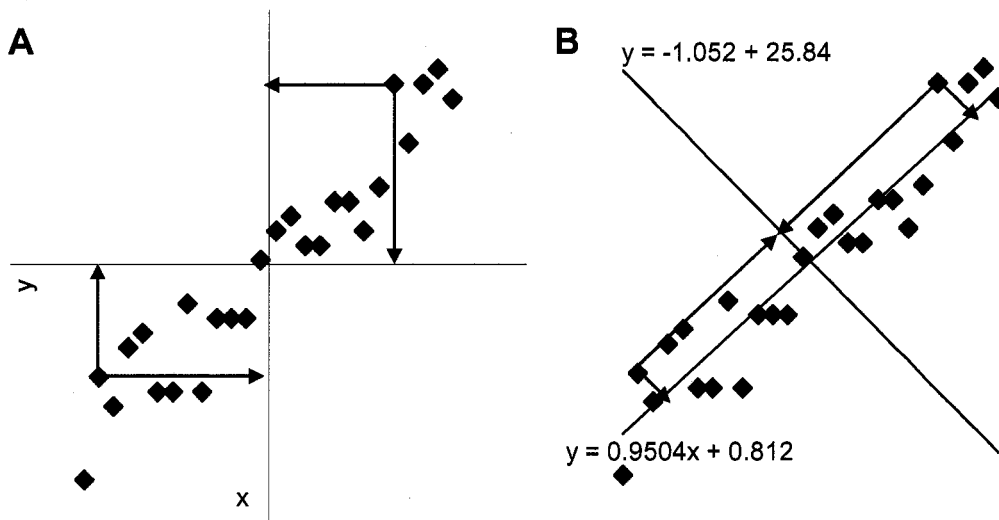


**Figure 4.20:** A simple example of how a regression can segregate sources of variation. The red arrows represent projections of two data points to the axes. A) A scatterplot of the function  $y = x$ , with slight random noise added to the ordinate values. B) The same plot with the axes rotated to the new basis set formed by a fitted line, and the vector orthogonal to it. The rotation clearly segregates the major source of variation (the linear correlation), and the slight random noise along the new axes.

Partial least squares (PLS) is a searching algorithm that is capable of compensating for dependant variation. The PLS algorithm searches for the vector in the multidimensional space that maximizes the variance of the projection of the data onto the vector. Then orthogonal vectors are searched to find the one that maximizes the remaining variance of the projection.<sup>177</sup> This process continues until a new basis set is identified. This then becomes a new coordinate system that enables visualization of the meaningful relationships in the data, and can be used to determine which projections contain the assay response, and which are noise.

In the DIA each pixel in the accumulation profile is one dimension in the domain. Antigen concentration is the single ordinate dimension. The values at each matrix location are the intensities (or slopes) for those coordinates. Prior to the PLS algorithm, each pixel defines an axis in the multivariate abscissa domain. The PLS algorithm determines linear combinations of the pixels that describe the vectors of maximum variation in the projection of the ordinate onto that vector.

PLS can also be a kernel for multivariate calibration in the DIA -- recall that calibration is done "in reverse" by first determining the concentration as a function of assay response, and then inverting this into a predictor function (Section 2.2.1). . . Multivariate calibration uses the new basis set found with PLS to create a predictor matrix, which functions analogously to a standard curve in two dimensions. The multivariate intensity of an unknown is then submitted to the prediction algorithm for quantification.

From this discussion, several inferences about the technique can be made. First, since the PLS algorithm first searches for the vector describing the maximum variation, and all subsequent vectors in the basis set must be orthogonal to this, the best results will result from data where the response is the source of maximum variation in the data set. This is *not* true of DIA accumulation profiles – the largest source of variation in them is "DC offset" in signal that results from the presence or absence of fluorophore on

opposite sides of the channel. What's more, the next largest source of variation is from the blank signal; i.e., the accumulation before it is modulated with the analyte information. The DC offset is easily eliminated through a derivative, as is already done with the germinal DIA. The blank signal is harder to account for. The second inference concerns the size of the data set. A lot of data is needed to account for all the degrees of freedom used by the multiple regressions. Most practitioners of multivariate calibration recommend a minimum of 30-50 calibration objects and similar number of independent test objects.<sup>177</sup>

To investigate the feasibility of this technique for the DIA, the set of seventeen accumulations gathered for the germinal DIA for phenytoin were submitted to the technique.<sup>xvii</sup> The first step was a second derivative calculation. This has the advantage over a first derivative that the peak of the second derivative is in the same place as the peak of the data. Although the size of the data set was woefully inadequate for rigor, a few conclusions were suggested (Figure 4.21). The PLS technique can be used to create a calibration model that adequately estimates the concentration of unknowns when applied to the phenytoin data. It appears that five *factors* (the vectors in the basis set describing the most variation), gives the best calibration model (Figure 4.21B). Three were adequate, but not optimal (Figure 4.21A).

The primary disadvantage to PLS calibration is the difficulty many people have in relating to the result – it is simply *not* a very intuitive technique. The DIA may be more readily accepted as a technique if the immunoassay community does not perceive that complex calibration techniques are required to yield acceptable results.

---

<sup>xvii</sup> At the time this was done, there were very few replicates for HRP and none for IgG. Also, the quantification of the phenytoin mock samples by a reference method gave an additional anchor to this analysis. We would like to acknowledge Dr. David Burns for his assistance with this analysis.

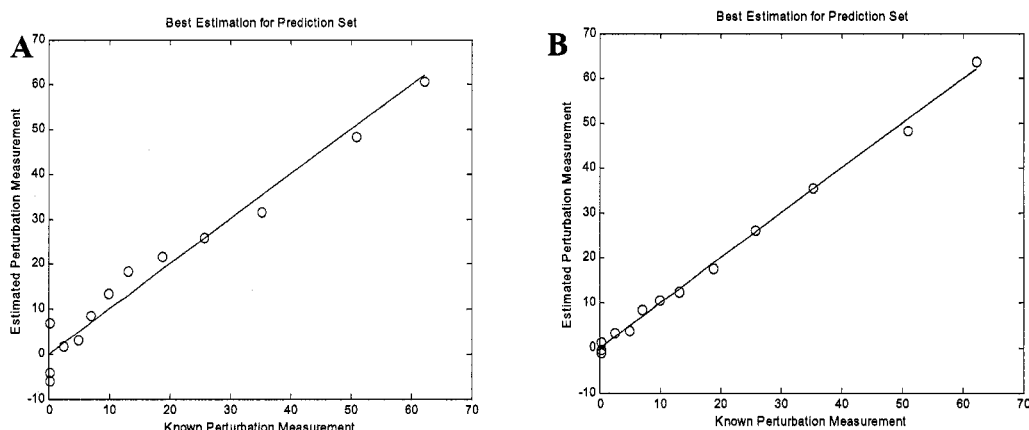


**Fig. 4.21:** Phenytoin method comparisons. The abscissa in these plots is the phenytoin concentration as determined by a commercial fluorescence polarization immunoassay. The ordinate is the phenytoin concentration estimated using the PLS calibration model. (A) Quantification done with the 3-factor PLS model. (B) Quantification done with the 5-factor PLS model.

*4.2.3.3. Integrating the difference from the free-diffusion curve.* Perhaps the simplest and most intuitive method for accounting for the multivariate nature of the response is by integrating an analytical signal over all of the pixels where a response is seen. This approach was investigated during the characterization of the phenytoin DIA, but was deemed unsatisfactory. The result of this algorithm, when it was applied to simulations, was excellent; however, when applied to experimentally derived accumulations, the variation was much greater than that observed with the slope algorithm described for the germinal DIA (Section 2.2.1, data not shown). This was judged to be the result of real variation in the location of the diffusion interface in relationship with the mid-plane of the channel, due to slight variations in flow. The origins of the flow variation appear to be occasional undetected leaks or bubbles in the feed lines, or intrinsic variation in the pumps. The slope algorithm is far less sensitive to fluctuation in the location of the interface – the algorithm looks for a minimum and maximum in a wide range of pixels.

During the preliminary experimentation with HRP, it was observed that the dose/response curve of a simulation was very linear over the entire range of modulated

behavior investigated (Figure 4.22). The sample antigen concentrations simulated were varied from the blank (no sample antigen), to a concentration seen to abolish the characteristic accumulation bump. However, it is expected that the dose/response curve for a DIA should be non-linear over the entire dynamic range, due to the saturation kinetics of an antibody/antigen reaction (see Section 2.2.3.4 for further discussion).

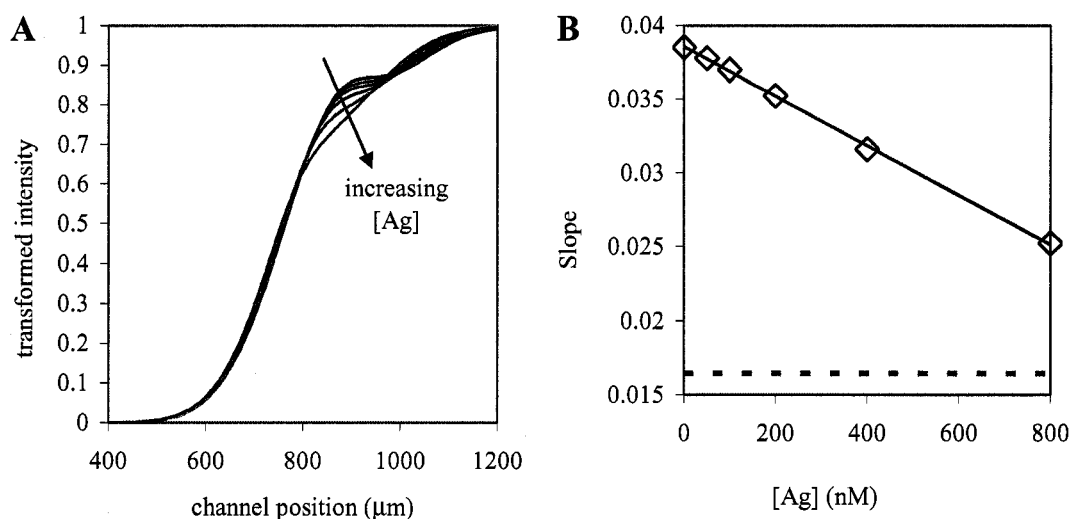


**Figure 4.22:** Predictions of the performance of an HRP DIA. A) Accumulations at [SA] of 0-nM, 50-nM, 100-nM, 200-nM 400-nM, and 800-nM. B) The standard curve corresponding to these accumulations with an estimate of the infinite response plotted for comparison (---). The careful reader may notice that the dose/response in 'B' does not match the experimental results shown in Section 4.2.1 (which is what motivated the detailed analysis). We hypothesize that there was degradation or contamination in some of the solutions used in the experiments used for generating that data set, since the HRP assay was predicted by simulations quite well in most cases.

Additional simulation of the slope algorithm revealed that there was significant modulation of the accumulation profile by high analyte levels that was not captured with the bivariate slope algorithm (Figure 4.23). This result implied that a significant part of the dynamic range was simply being discarded by the slope algorithm. Given the compromise between limit-of-detection and dynamic range that is frequently required of the device designer, this was judged to be unwise, and the idea of integrating over all of the modulated pixels was revisited, with an important difference

– a difference (non-directional) between the accumulation and the free-diffusion of labeled analyte was first calculated.

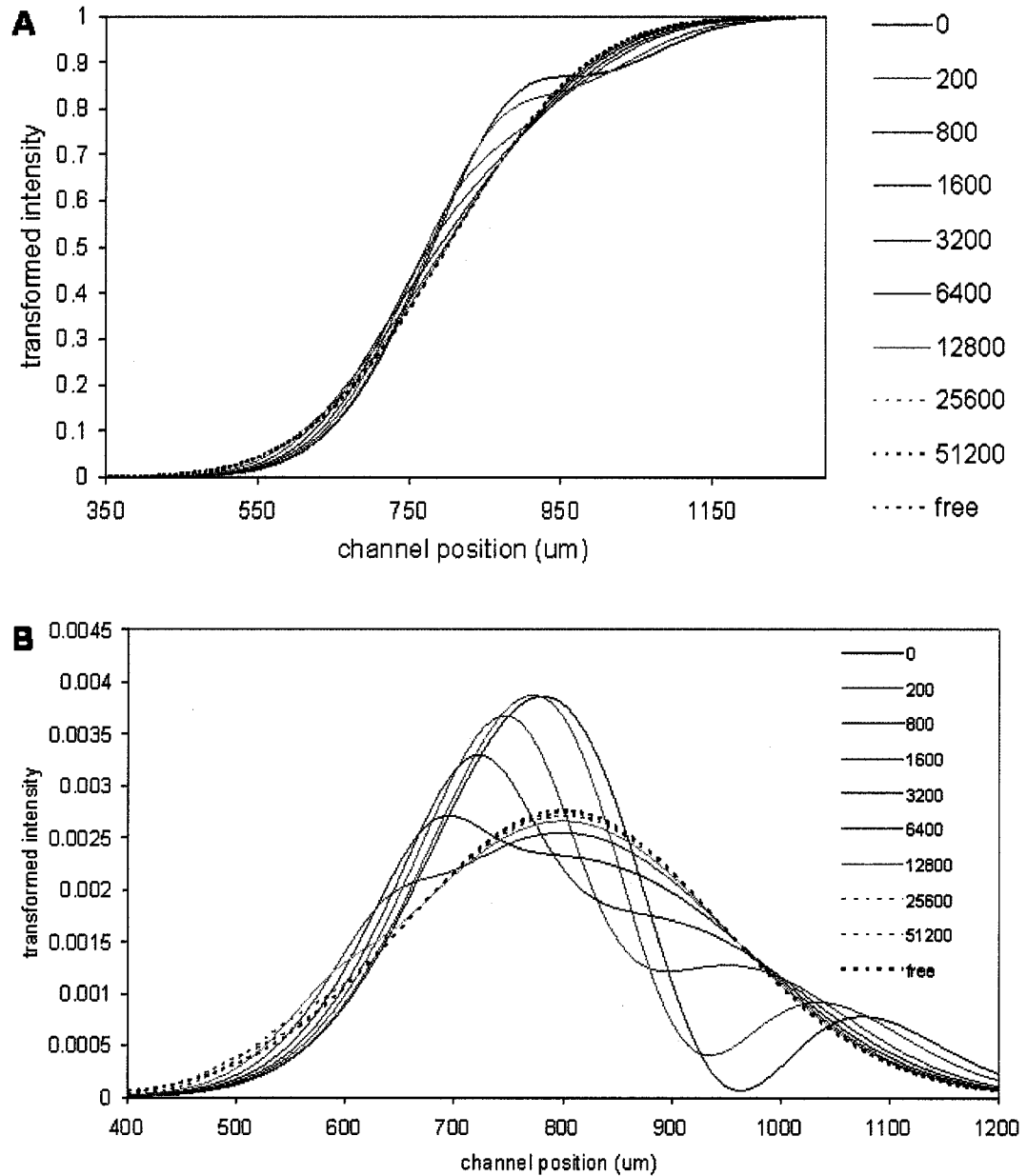


**Figure 4.23:** Simulation of the HRP DIA at higher  $[\text{Ag}]$  (see legend) than previously investigated, including two concentrations assumed in Figure 4.22. (“Free” = free-diffusion.) All other parameters are the same as the previous simulations. A) The accumulations profiles. B) The corresponding slope profiles. Note the presence of modulation to the left of the slope maximum, which is not captured by the germinal IDA algorithm.

There are distinct advantages of calculating a difference from free-diffusion. In the DIA, the free diffusion corresponds to the theoretical “infinite dose” case. As increasing analyte in the sample competes for the antibody binding sites with the labeled antigen in the reagent, the labeled analyte becomes blinded to the antibody – it is as if the antibody isn’t there. Without antibody in the system, a T-sensor experiment measures free diffusion, thus the infinite dose can be measured by introducing an antibody free reagent into the inlet opposite the labeled antigen reagent. The ability to physically measure infinite dose is somewhat unique among immunoassay systems, and provides great advantages in fitting the 4PLL model, where infinite-dose response is a fitted parameter (see Section 2.2.1 for more detail). The fitted models are then asymptotic to the sample analyte concentration axis in the dose/response plot. An additional advantage is that the variation observed for free-diffusion curves can be used to estimate the absolute upper limit of the dynamic range of an assay, as long as a meaningful dose/response curve can be constructed.

Application of this new algorithm to the problematic HRP simulation-set discussed above enables the correct determination of predicted responses throughout the true dynamic range, approaching the infinite response. The possible dynamic range is expanded over several orders of magnitude, relative to the germinal DIA slope algorithm (Figure 4.24), although the sensitivity as the analyte concentration increases will most likely degrade because of the lower slope of the dose/response curve in this region.

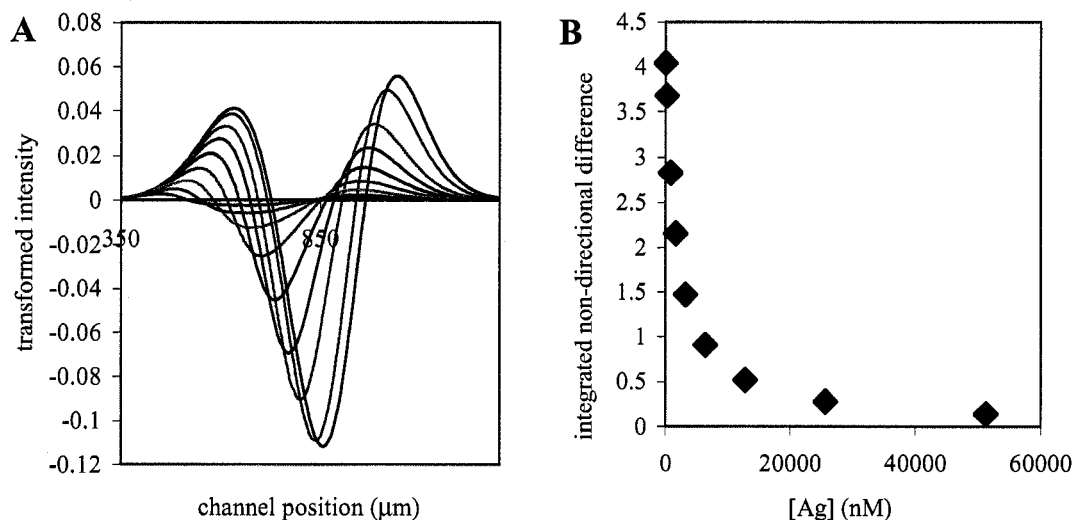


**Figure 4.24:** Simulation of the HRP DIA with the application of a revised signal algorithm eliminating the slope calculation and replacing it integration over the whole channel width of the absolute value of a pixel-by-pixel difference between the accumulation profile and a free-diffusion profile. A) Plots of the difference between simulated accumulations and a free-diffusion of Ag\*. Individual lines are labeled identically to Figure 4.23. B) The dose/response curve constructed from the integrated non-directional differences.

The primary disadvantage to this method is that it is very sensitive to variation in the interface produced by the variation in flow seen in some experimental systems (see Section 5.4). This can be corrected for, however, by the inclusion of an “internal diffusion standard” in the labeled antigen reagent that is labeled with a spectrally-distinct fluorophore. The signal from the standard is then separated from the DIA accumulation with an appropriate optical filter set, and after smoothing and a slope calculation (using the same techniques described in Chapter 2 and Section 4.2.1) the actual midline for any individual image can be derived from the maximum value of the internal standard’s slope profile (The point of inflection of the error function that is the solution of the 2D infinite plane diffusion equations is located precisely at the location of the original interface<sup>34</sup>.) The most precise application of this standard would probably be to use a dual-bandpass optical filter and a color camera, and use the different color channels on the camera to separate the signals. This would insure exact spatial and temporal correlation between the internal diffusion standard and its cognate



DIA accumulation. Nevertheless, a dramatic reduction in signal variation in the CRP DIA (Chapter 6) was realized by using discrete optical filter sets and a monochrome camera, and separating the two signals by simply moving the filter cube back and forth to change filter sets, taking a separate image for each, and interleaving the diffusion image replicates with the accumulation image replicates (Figure 4.25). It is obvious that there is considerable variation between the replicates before midline correction (4.25A) that is eliminated after correction (4.25B).

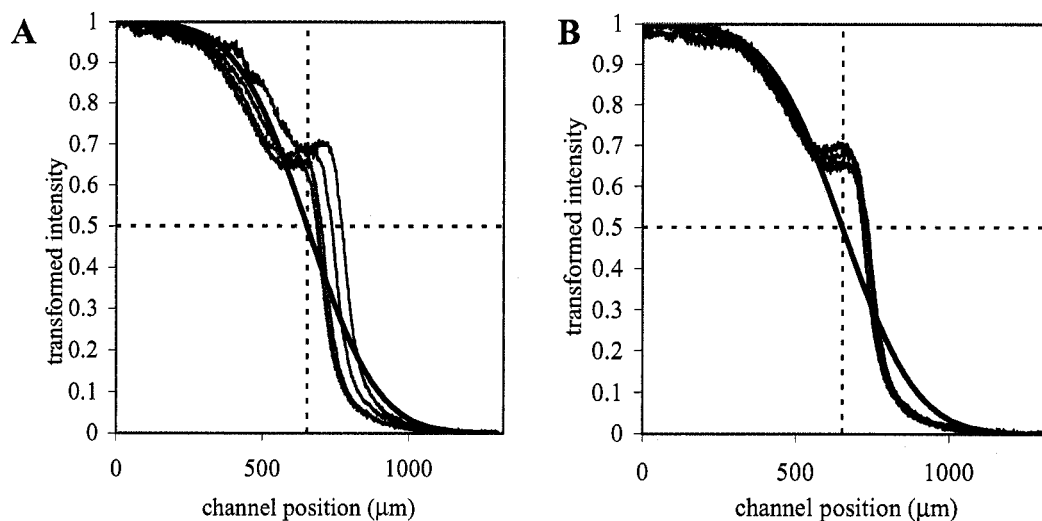


**Figure 4.25:** An experimental example of the application of the internal diffusion standard in the CRP DIA (formulation #4, see Chapter 6 for further discussion of this assay system). The colored lines are five replicate determinations of the blank signal, from different pump runs. The heavy black line is the predicted free-diffusion for the  $\text{Ag}^*$  -- the profile from which the accumulations are to be subtracted. The dotted lines are the physical midline of the channel (vertical) and the intensity at  $1/2[\text{Ag}^*]$  (horizontal), the intersection of which represents the point of inflection of the underlying diffusion profile; given for reference. A) The BFTN normalized accumulation profiles of the five replicates without correction by the internal standard. B) After correction by the internal standard, as described in the text.

For proper function, this standard should have a diffusivity similar to, or slower than, the labeled analyte, so that a good diffusion profile can be obtained with the same signal processing algorithms used for the DIA. Fluorophores that diffuse much faster will have a very low slope and no regions of the extremes of the channel where undiluted feed solution is present, both making correction of the raw diffusion images

problematic. The internal standard should also not react with any of the components of the DIA, or it will not be freely diffusing, and it could distort the assay results. For the CRP results shown (Figure 4.25), streptavidin labeled with Alexa-Fluor 594 was used.

Another disadvantage to this system is that the use of a non-directional difference disables the ability of the integration to filter out high-spatial-frequency (HF) noise that is randomly distributed around the true underlying accumulation. This type of noise results from the thermal noise of the camera. The camera noise is fairly constant for a properly working instrument; however, the BFTN processing amplifies this noise during the normalization process. The magnitude of noise thus observed in the profile appears greater when the background corrected intensity of the undiluted Ag\* reagent is less. The observed HF-noise does not vary appreciably for a given signal magnitude; as long as the fluorescence of the Ag\* reagent, illumination source intensity, background, and camera settings are kept constant – the normal case in operating the DIA. The HF-noise, is expected to introduce an “inaccuracy” relative to the true underlying accumulation, however. Unfortunately, performing a directional differencing would completely eliminate the signal. In the DIA, the mass of labeled analyte does not vary over the channel width relative to free-diffusion, only its distribution does.

The effects of these two noise sources are studied in more detail in Chapter 5 (Section 5.3). Despite these limitations, the integrated non-directional difference algorithm described here was chosen as the signal calculation for the remainder of this work. Its advantages over the slope algorithm were judged to outweigh its disadvantages.

#### **4.2.4 Summary of improvements to data analysis**

The results of this section indicate that significant improvements can be made in the performance of the germinal DIA for protein analytes through the application of a

number of signal processing and calibration revisions. The benefits of replacing the boxcar smoother of the germinal DIA with the Whittaker smoother have been clearly evinced -- the Whittaker smoother was used for all subsequent processing where a slope calculation followed. There are benefits of replacing the 4PLL NLLS calibration procedure with the 2PLL log-logit transformation for increasing the power of ANCOVA analysis through variance stabilization, but the transformation is detrimental to assay calibration. Finally, three techniques for leveraging more of the multivariate information into the response were investigated. The discrete Fourier transform showed initial promise, but was eventually rejected as providing few improvements for the processing cost. Multivariate calibration with the partial least squares algorithm displays potential for the protein DIA; but, is not a very intuitive technique. A simpler method of using all of the data is simply to integrate the difference of the observed accumulation from an appropriate free-diffusion curve. The integrated non-directional difference algorithm is the one that has been adopted for the second generation DIA.

### ***4.3: Biochemical modification of capture species***

As described earlier (Section 2.4.1), the ratio of diffusivity between the free labeled analyte and the immune complex of the labeled analyte and the antibody is a key parameter in the DIA – ratios approaching unity result in blank signals that are difficult to detect and modulate. The importance of this parameter is validated by the poor performance of the HRP DIA (Section 3.1) relative to the phenytoin DIA. The simulations performed in Chapter 5 also suggest that the biggest effect of altering the diffusivity ratio is seen as the ratio varies from unity to a value of about ten -- above that, there are diminishing returns. This suggests that large alterations to the ratio may not be required, especially if those alterations produce negative side effects.

There are a limited number of ways to alter the diffusivity ratio. The diffusivity of the analyte is not easily changed – it comes with the choice of analyte. The diffusivity of a protein analyte could be increased biochemically; e.g., the protein could be digested and an epitope-containing fragment used as the labeled analyte. However, it would be impractical to do this to unknowns, and the effect of having different diffusivities for the labeled and unlabeled analyte is not well understood. The most straightforward biochemical solution seems to be to modify the capture antibody so that it diffuses much slower.

There are a number of ways that the capture antibody could be made to diffuse more slowly.<sup>106</sup> Linking the antibody to a microsphere could alter its diffusivity by orders of magnitude, and microspheres are available surface functionalized and in different sizes. Microspheres are colloids, however, and care must be taken that solution conditions are manipulated so the microspheres do not aggregate and precipitate. Even with careful handling microspheres are notorious for clogging microdevices. Another way to slow the antibody diffusion is to link it to a very large protein. The enzyme  $\beta$ -galactosidase ( *$\beta$ -gal*) is large enough (MW=550 kD) to slow the antibody significantly, and can be readily obtained in functionalized form as well. Other slowly-diffusing, soluble molecules could be covalently linked to the antibody with standard conjugation chemistry, as well. Dextran is readily available in molecular weights approaching (and even exceeding) 1000 kD. Large polymers such as this are not usually monodisperse, however.

Each of these possibilities is assessed in this section. Several attempts at using microspheres are described, only one of which was marginally successful. Given the practical problems with microspheres, the feasibility of a DIA using two different soluble molecules as the diffusivity ratio amplifier has also been investigated. Modification with a soluble protein was simulated, but no actual experiments were performed. Experimental results with an antibody conjugated to dextran were

obtained, but the amplification was not as great as predicted, due to a reduction in binding activity of the conjugate.

#### **4.3.1. Modifying with Microspheres**

*4.3.1.1 Apparatus:* The same T-sensor system used for the germinal IgG DIA (Section 3.2) was used for this work.

*4.3.1.2 Reagents:* Three different systems were investigated: 1) 6- $\mu\text{m}$  microspheres covalently linked to anti-MsIgG (Amgen, Thousand Oaks, CA, USA); 2) 1- $\mu\text{m}$  streptavidin functionalized microspheres (Bangs Labs, Fishers, IN, USA) linked in-house to biotinylated anti-HRP (Jackson ImmunoResearch, West Grove, PA, USA); 3) 0.9- $\mu\text{m}$  microspheres covalently linked to anti-MsIgG (Spherotech, Libertyville, IL, USA). For all of these systems, the concentration of binding sites were made identical to the antibody reagent used for the germinal DIA, and all other materials were the same as the germinal DIA to facilitate direct comparison (Section 3.1).

The in-house linking required some additional steps. The 1- $\mu\text{m}$  streptavidin functionalized microspheres were incubated for one hour with the biotinylated anti-HRP to allow for the linking reaction. The unreacted antibody was then separated from the microspheres by centrifugation, and the microspheres were re-suspended in universal diluent to yield the correct concentration.

*4.3.1.3. Procedure:* The experiments were performed identically to the germinal DIA (Section 3.1). Simulations with the 2-D model (Section 2.2.4) were performed for all four systems. The Stokes-Einstein relationship was used to estimate the diffusivity of the microsphere for simulation purposes.

*4.3.1.4. Results:* The simulations all suggested that large increases in accumulation are expected with the various systems. An example is given (Figure 4.26A). In all

cases the diffusivity ratio expected with the beads is on the order of  $10^2$ ; i.e., much greater than any DIA previously investigated.

In preliminary testing only one system yielded any experimental results. The results with the 6- $\mu\text{m}$  microspheres linked to anti-IgG were invalidated because of sedimentation of the microspheres. An attempt was made to increase the density of the diluent to keep the microspheres suspended, but the supply of microspheres was consumed in the attempt, the results were not promising, so further experimentation was not attempted. The results with the 1- $\mu\text{m}$  streptavidin functionalized microspheres linked in-house to biotinylated anti-HRP did not differ significantly from free diffusion of the labeled antigen (data not shown). The 0.9- $\mu\text{m}$  microspheres linked to anti-IgG yielded two useable accumulations (Figure 4.26B). Note that the blank signal is much larger than predicted, and that the predicted modulation is present. Note also that the intensity of fluorescence is much higher on the side of the channel expected to contain only undiluted capture microsphere.

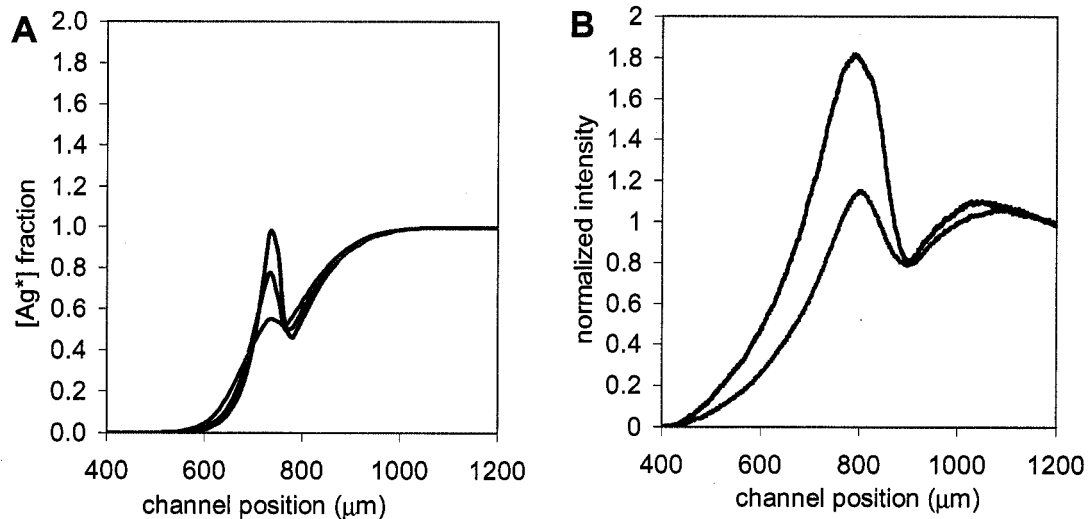


**Figure 4.26:** DIA accumulations when the capture analyte has been immobilized on a 0.9- $\mu\text{m}$  microsphere. For both figures, blue is the blank signal, red is the response to 400 nM sample Ag, and green is the response to 1500 nM sample Ag, as in Figure 3.2. A) Simulations from the 2D model. B) Observations from experiments.

*4.3.1.5. Discussion:* The failures of two of the systems highlight the difficulty of working with microspheres. These results suggest that using smaller microspheres helps to ameliorate some of these issues. We hypothesize that the lack of observed accumulation with the 1- $\mu\text{m}$  streptavidin functionalized microspheres linked in-house to biotinylated anti-HRP was due to failure of the linking reaction, resulting from the investigators inexperience with this system.

The simulations of the DIA using 0.9- $\mu\text{m}$  microspheres linked to anti-IgG do not match observations in magnitude, but do predict the general trend. It should be noted that some of the assumptions made in the modeling might not be valid when simulating the microsphere assays. The model assumes uniformly distributed and homogeneous binding sites. While this assumption is probably adequate for a bivalent antibody in solution, immobilizing a number of antibodies on a single microsphere introduces a dependency between these sites – many sites are linked to the same microsphere and cannot diffuse independently, creating inhomogeneity in binding site distribution. Also, the model may not account for the association rate and affinity of the antibody adequately. When immobilizing antibodies on solid surfaces the linkage method can affect the affinity of individual antibodies differently.<sup>105</sup> While the global effects of immobilization have been accounted for by changing the values of the association coefficients, we have not accounted for the heterogeneity in the association coefficients that can result from immobilization.<sup>105</sup>

An additional problem was encountered with the 0.9- $\mu\text{m}$  microspheres linked to anti-IgG. In order to formulate a reagent with the desired concentration of binding site, a very high microsphere concentration was required, due to the surface density of the anti-IgG. This resulted in a milky reagent that created artifacts from aggregation and light scattering. It is likely that scattering is responsible for the elevated signal on the side of the channel expected to contain only undiluted, unreacted capture microspheres. It also was a very expensive assay to perform, given the concentration

of microspheres required. The concentration of binding sites was chosen to enable comparison to the germinal DIA, however – it may not be necessary to use that concentration to produce a usable assay. There certainly appears to be a large blank signal available for modulation.

It should also be noted that the microsphere assay was performed at the same time as the germinal DIA for IgG, and before we understood the *in situ* aggregation hypothesized for the germinal IgG DIA. It seems likely that the microspheres could be cross-linking as well, similar to a latex agglutination assay technique. This could be responsible for the larger magnitude of the blank signal and response than predicted. It is unclear from these results what the contribution of *in situ* aggregation due to the multivalent nature of the analyte is (in the DIA using 0.9- $\mu\text{m}$  microspheres linked to anti-IgG). However, given that this assay was done with the presence of the microsphere as the only variable relative to the germinal DIA for IgG, it is clear that the contribution of the microsphere is significant.

#### **4.3.2. Modifying with a Soluble Protein**

We hypothesize that a streptavidin-functionalized  $\beta$ -gal (part #S3887: Sigma, St. Louis, MO) could be linked to biotinylated anti-HRP (Jackson ImmunoResearch, West Grove, PA, USA). While the binding of a single antibody and  $\beta$ -gal would only result in a diffusivity ratio of 2.5, some signal amplification is expected. Simulations were performed with the 2-D model using diffusivity estimates interpolated from similar sized proteins (Figure 4.27A). Amplification is seen, nevertheless, it is far less amplification than would be expected from 1- $\mu\text{m}$  microspheres (Figure 4.27B). No experiments have been performed with this system.



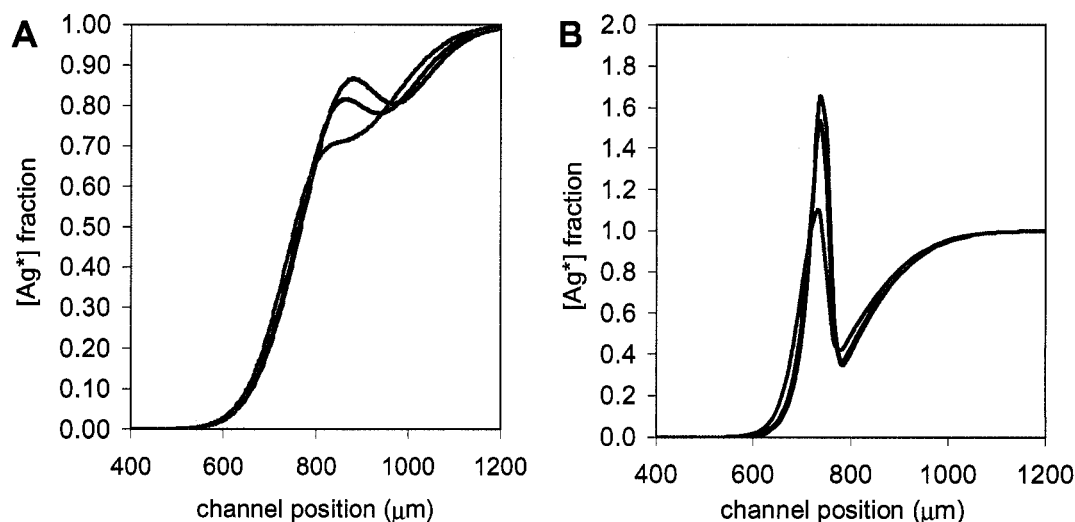


**Figure 4.27:** Simulations for HRP DIA with an increased diffusivity ratio. For both figures, blue is the blank signal, red is the response to 200 nM sample Ag, and green is the response to 800 nM sample Ag. A) Streptavidin functionalized  $\beta$ -gal linked to a single anti-HRP. B) 1- $\mu$ m microspheres linked to anti-HRP.

This system uses streptavidin as the linker on the  $\beta$ -gal, which is capable of binding up to four biotin molecule in solution. There are also a number of streptavidins on each  $\beta$ -gal molecule. It is hard to predict how many antibodies will bind to each  $\beta$ -gal, but multiple decorations could change the molecular weight considerably. To investigate the effect of this phenomenon, simulations were done assuming additional antibody mass. There was a small difference in the blank signal up to the addition of four antibodies (data not shown). It was this complication that motivated the custom conjugation of a high MW dextran, described next.

### 4.3.3. Modifying with an antibody conjugated to a dextran.

**4.3.3.1 Apparatus:** A second generation T-sensor device was used for all of the CRP DIA data, both here, and in Chapter 6. This device is identical in dimensions to the T-sensor used for the germinal DIA work (Section 3.1), with the exception that the channel depth was measured at 140  $\mu$ m, rather than the 150  $\mu$ m expected for the first generation device. The difference in depth arises from a change in materials and

manufacturing techniques. The second generation device is a monolithic solvent-assisted thermal laminated, PMMA device. Thus, it is adhesive free and displays a background auto-fluorescence less than the first generation glass/Mylar™-ACA/glass devices (see Section 4.1.1 and 4.1.3 for further explanation).

*4.3.3.2. Reagents and Procedure.* Hydrazine-modified antibody to C-reactive protein (CRP) was linked to a hydroxyl group of a 670 kD dextran to slow the diffusivity of the capture species approximately two-fold. (The CRP DIA is described in complete detail in Chapter 6.) Dr. David Schwartz, at Solulink Co., is an expert at this conjugation, and can manipulate the reaction to tune the degree of modification. He was retained to custom synthesize the dextran/CRP conjugate with approximately one Ab per dextran, so that there would not be a large distribution of molecular weights and, therefore, diffusivities of the capture species. It was judged that this would yield the most easily interpreted results. The rest of the materials, and the test procedure were exactly as described in Chapter 6.

*4.3.3.3. Results and Discussion.* The dextran-modified antibody did not produce the increases in accumulation predicted by a two-fold increase of diffusivity ratio alone (Figure 4.28). The product characterization provided by Solulink indicates that the conjugation procedure was successful, so an actual change in diffusivity seems highly probable. The discordant observations can be easily explained by the effects of the conjugation on the association rate of the antibody/antigen reaction. Predictions from simulations assuming a six-fold reduction in association rate along with the expected two-fold increase in the diffusivity ratio match observations quite well (Figure 4.28). As discussed in section 2.4.1, it is well known that the association rates of the antibody/antigen reaction are up to an order of magnitude slower when a large molecule is the antigen, relative to small antigens; presumably because of a slower rotational diffusion rate which renders a lower probability that the cognate binding sites are in the correct orientation relative to one another. It is no great leap to

conclude that the same factors are operating when the antibody is linked to a large molecule at an equimolar ratio. In retrospect, a six-fold reduction in association rate seems quite likely.

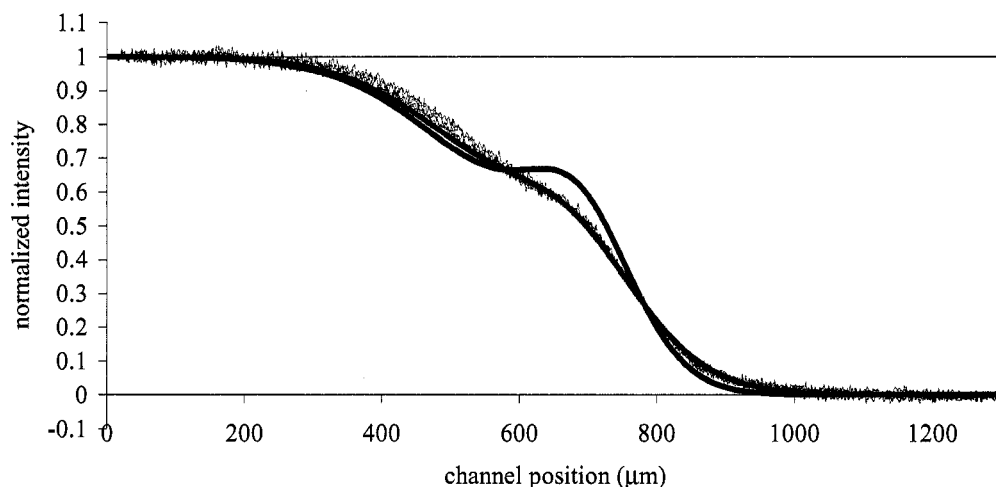


**Figure 4.28:** Results of the CRP DIA with a capture antibody conjugated to 670 kD dextran compared to simulations. Black line, (-) = predicted accumulation with a two-fold increase in the diffusivity ratio; Dark blue line, (-) = predicted accumulation with a two-fold increase in the diffusivity ratio and a six-fold reduction in association rate. The diffuse blue region around the blue line is a plot of eight separate accumulations gathered experimentally.

The initial slope of the dextran modified antibody system is 0.006 IU/nM-Ag, about half that of an unmodified system (0.014 IU/nM-Ag) because of the association rate reduction. This can be contrasted to the increase in initial slope (to 0.019 IU/nM-Ag) predicted by assuming the diffusivity ratio increase in the absence of association rate reduction. This system was not investigated further, because the net amplification gained by the modification was not significantly better than the simple antibody formulation for CRP -- in fact, it was worse. The results are placed in the context of model validation, noise estimation, and a clinically significant assay for CRP in Chapters 5 and 6.

### 4.3.3. Summary of biochemical modification

These results, coupled with the modeling in Chapter 5, suggest that significant signal amplification can result if the unmodified capture antibody is linked to something that will slow the antibodies diffusivity, without changing its reaction rates with the antigen. Microspheres give the most dramatic results, although care must be taken to choose a microsphere and buffer system that does not result in aggregation and precipitation. In addition, a typical surface density of the antibody may necessitate the use of a very high concentration of microspheres, which can create new types of artifacts such as light scattering. The use of soluble molecules linked to the antibody appears to alleviate some of these difficulties, and has resulted in predictable accumulation. Soluble molecules do not produce the magnitude of diffusivity ratio change associated with microspheres; however, are capable of increasing the diffusivity ratio in the most important range (from unity to ten, see Chapter 5). Unfortunately, when lightly labeled with antibody, soluble capture species can display a reduced association rate that cancels out the gains from increasing the diffusivity ratio; and, when labeled more densely, will display a range of diffusivities as additional antibodies bind to the complex.

## **Chapter 5: Exploring the Limits of the DIA with Modeling**

In this chapter, the effects of the physicochemical properties of the analyte on the DIA analytical signal and response are characterized through dimensional analysis and numerical modeling. In addition, the most important sources of variability are studied with simulation. Applying numerical models to predicting the DIA was deemed desirable for two reasons: 1) The model takes a few tens of seconds to yield an accumulation; whereas, an experimentally derived accumulation takes close to an hour when solution preparation, instrument set-up, clean-up, and preliminary image processing are all taken into account in the analysis time. Thus, the number of different parameter sets that can be explored is much greater with the model. 2) A model is inherently more general than a set of experiments. Any real analyte can have idiosyncratic characteristics that are lurking variables in extension of the results to other analytes. With a model, the assumptions about the system are stated in the model formulation, so the results apply to any analyte that satisfies those assumptions. The dimensional analysis enabled a reduction in the number of parameters that had to be varied, further generalized the result, and illuminated the true nature and interaction of the variables under study.

### ***5.1. Dimensional analysis***

#### **5.1.1 Background**

*5.1.1.1. Motivation.* There are several reasons why a dimensional analysis was undertaken. A two-dimensional finite-difference model, described in detail previously (Section 2.2.4) is capable of describing the behavior of the DIA when the system is operating in the regimes discussed (Section 2.2.3). This model, like the physical system it describes, has numerous dimensional variables (variables that have physical dimensions associated with them; e.g., concentration or time) that affect the result.

Adequately exploring all of them is daunting, and it is possible that many of them interact. Dimensional analysis reduces the number of variables that describe the behavior of the system by lumping dimensional variables into dimensionless groupings that describe the effects of several dimensional variables with a single group. In addition, if the analysis has been done properly, these dimensionless groupings are sufficient to define states of dynamic similitude; i.e., states of the system which display the same behavior in regards to the variable of interest. States that share the values for dimensionless groupings are dynamically similar, even if the values of the dimensional variables that make up those groupings are different. Two well-known examples of dimensionless groupings in fluid mechanics –  $Re$  and  $Pe$  -- are discussed in the Chapter 2. By performing a dimensional analysis on the important parameters in the DIA, similarly powerful dimensionless groupings have been identified.

In the past we have concentrated on the diffusivity ratio ( $D_{Ag}/D_{AbAg}$ ) as a key dimensionless quantity that captures important behavior, but it is not clear that this is the only, or even the most meaningful abstraction. A truly comprehensive analysis of the properties of the analyte that affect the DIA should start with the full set, and only eliminate those demonstrated to be unimportant.

*5.1.1.2. Theory.* The Buckingham pi-theory predicts how many independent dimensionless groupings there are, and outlines a formalism for determining what they are.<sup>24</sup> Using the theory, scaling laws can be determined, even in the absence of detailed governing equations, and a framework for experimental correlation is created.

The method of the pi-theory is well defined. The first step is to define the dimensional variables that are important in the analysis, and to identify the independent dimensions they contain (M=mass, L=length, T=time, etc.). Generally, one of the variables is hypothesized to be a function of the others, creating a simple model of the unknown

governing equation. The most useful form of this model is when a variable ( $y$ ) is assumed to be a product of the other variables ( $x_i$ ), of number  $M$ , each raised to an unknown power ( $a_i$ ):

$$17) \quad y = \prod_{i=1}^M [x_i]^{a_i}$$

The pi theory predicts that the number of independent dimensionless groupings ( $N$ ) can be found by subtracting the number of independent dimensions, from the number of dimensional variables. These groupings ( $Pi_i$ ) are related to the dimensional power law by:

$$18) \quad [y] = [y_0] \prod_{i=1}^{N-1} [Pi_i]^{b_i}$$

where  $y/y_0$  is the  $N^{th}$  dimensionless grouping arising from the formalism.

Once the problem has been formulated, the grouping of variables can be done in two ways: 1) Buckingham's indicial method, or 2) Taylor's shorthand method. Both methods are simple, although somewhat tedious algebra – the reader is referred to a good fluids mechanics textbook for details<sup>24</sup>. The result of the algebraic formalism is the  $N$  dimensionless groupings.

The dimensionless groupings resulting from the pi-theory can be used to guide experimental design so that the parameter space is spanned as desired with a minimum set of experiments (or simulations). By systematically varying one  $Pi_i$ , holding the others constant, and tracking  $y/y_0$ , a data set is quickly constructed that enables the deduction of the individual exponents in the power law ( $b_i$ ). By plotting  $\ln(y/y_0)$  versus  $\ln(Pi_i)$ , and taking advantage of the identities  $\ln(AB) = \ln(A) + \ln(B)$ , and  $\ln(A^b) = b \ln(A)$ ; the exponent  $b_i$  can be seen to be equal to the slope of the plot because:

$$19) \ln\left(\frac{y}{y_0}\right) = \ln([P_i]^{b_i}) + \ln\left(\prod_{j \neq i}^{N-2} [P_j]^{b_j}\right) = b_i \ln(P_i) + c$$

where  $c$  is a constant that results from holding the other  $P_i$  in the experiment constant.

These log-log plots are rich in information. As detailed above, the slope of a single plot corresponds to the exponent in a power law, for the set of conditions defined by the constant values of the other dimensionless groupings. (Note that the *y-intercepts* -- the  $c$  values -- are not terribly meaningful. They are simply the “bin” into which the effect of all the other groupings is segregated for that particular analysis.) If many plots for a particular  $P_i$  have a similar slope, it implies that the power law for that grouping hold true for the entire domain of the other  $P_{j \neq i}$  studied. They also are diagnostic of the problem statement – if there are key parameters left out of the problem description, non-monotonic plots may result. Many physical situations result in log-log plots that are well described by linear fits to the data. This is fortuitous, because it implies a simple power law. However, non-linear relationships are expected when the true, underlying governing equation does not follow a simple power law over the entire domain investigated. This does not indicate any problem with the problem statement.

This type of analysis can be applied to both experimental and model data. The focus in this dissertation is on the data generated by a numerical model, for the speed and generality advantages it confers, as discussed above.



### 5.1.2 Dimensional Analysis in the DIA

The formalism of the Buckingham pi-theory was applied to the DIA to reduce the number of parameters requiring systematic study, define states of dynamic similitude, and further generalize the conclusions of the numerical modeling.

*5.1.2.1. Setting up the analysis.* The first step was to determine all of the parameters thought to be important for describing the DIA (Table 5.1). We determined eight independent dimensional variables (the  $x_i$  in Section 5.1.1), and two dependant variables (the  $y$  in Section 5.1.1).

**Table 5.1.** The dimensional variables that define the DIA. Dimensional units denoted with standard abbreviations. Independent dimensions are: M=mass, L=length, T=time.

Variable Name	Symbol	Standard units	Independent Dimensions
Interaction time	$\tau$	s	T
Ag* diffusivity	$D_{Ag^*}$	$\text{cm}^2 \text{s}^{-1}$	$L^2 T^{-1}$
Ab diffusivity	$D_{Ab}$	$\text{cm}^2 \text{s}^{-1}$	$L^2 T^{-1}$
AbAg* complex diffusivity	$D_{AbAg^*}$	$\text{cm}^2 \text{s}^{-1}$	$L^2 T^{-1}$
Ag* concentration	$[Ag^*]$	moles $l^{-1}$	$ML^{-3}$
Ab concentration (binding sites)	$[Ab]$	moles $l^{-1}$	$ML^{-3}$
AbAg association rate	$k_{on}$	moles $l^{-1} s^{-1}$	$ML^{-3} T^{-1}$
AbAg dissociation rate	$k_{off}$	$s^{-1}$	$T^{-1}$
Blank DIA response	$R_i$	Fraction-Ag*	dimensionless
Initial slope of dose/response	$S_i (dR/d[Ag])$	fraction-Ag* moles-Ag $^{-1} l^1$	$M^{-1} L^3$

The dependant variables -- the blank response ( $R_i$ ) and the initial slope of the dose/response curve ( $S_i$ ) -- were chosen for investigation for the following reasons. The blank response represents the total signal available for modulation and, as such, should be correlated to all assay performance measures. The initial slope of the dose/response curve is a surrogate for the initial sensitivity, which is used to calculate a limit-of-detection (*LOD*) for a formulation. *LOD* is, arguably, the most important figure of merit for a protein DIA, given that many proteins are assayed as markers of disease states (clinically significant at concentrations above some low level), and that a low *LOD* is expected to be a design challenge for the DIA for high-molecular weight analytes.

Both these dependant variables interact with assay noise to impact the final figures of merit. Noise is assessed independently; both by simulation (Section 5.3) and by performing replicates of the DIA with an actual protein analyte for a variety of assay formulations (Chapter 6). It should also be noted, that the response investigated here is not the same slope response described for the germinal DIA, but is the modified integrated non-directional difference algorithm described and justified in Section 4.2.3.3.

The independent variables (the first eight rows of Table 5.1) conform to the assumptions of the T-sensor and of the 2-D model, and include self-evident deductions from the starting conditions. The flow rate and device dimensions are assumed to be captured by the interaction time ( $\tau$ ) – a reasonable assumption for high aspect-ratio devices under laminar flow; interrogated far downstream of the inlets so that flow development has been rendered unimportant and concentration gradients in the depth dimension have decayed. The diffusivity of the analyte ( $D_{Ag^*}$ ), immune complex ( $D_{AbAg^*}$ ), the association rate ( $k_{on}$ ) and the dissociation are ( $k_{off}$ ) are all assumed to be identical for both labeled and unlabeled forms of the antigen -- reasonable for large, lightly-labeled protein molecules. The concentration of the antibody ( $[Ab]$ ) and labeled analyte ( $[Ag^*]$ ) are variables manipulated in reagent formulation, but the concentration of sample analyte ( $[Ag]$ ) is an uncontrolled variable that is captured in the slope of the dose/response curve. (The concentration of immune complex results is not a variable in the dimensional analysis, since it results from the action of the reaction rates on the reactant concentrations; although it is tracked in the numerical model.) The concentration of the antibody ( $[Ab]$ ) tracked is actually the number of binding sites, assumed to be equivalent. Thus the actual antibody concentration is half the parameter  $[Ab]$ . In the germinal DIA, the dissociation rate is ignored, because it was assumed that the interaction times are insufficiently long for significant dissociation. Given the longer interaction times required for sufficient inter-diffusion

of large molecules, and the wide domain of interaction times to be studied, dissociation rate was included in the dimensional analysis.

It should be noted that  $Pi_i$  has been written as the inverse of what the pi-theory formalism actually returned. This type of transformation is acceptable in the formalism, and was done to make the results more intuitive (bigger complex returns a bigger number).

The two hypothesized, dimensional governing equations are given below:

$$20) [R_i] = [\tau]^{a_{1a}} [D_{Ag^*}]^{a_{2a}} [D_{Ab}]^{a_{3a}} [D_{AbAg^*}]^{a_{4a}} [[Ag^*]]^{a_{5a}} [[Ab]]^{a_{6a}} [k_{on}]^{a_{7a}} [k_{off}]^{a_{8a}}$$

$$21) [S_i] = [\tau]^{a_{1b}} [D_{Ag^*}]^{a_{2b}} [D_{Ab}]^{a_{3b}} [D_{AbAg^*}]^{a_{4b}} [[Ag^*]]^{a_{5b}} [[Ab]]^{a_{6b}} [k_{on}]^{a_{7b}} [k_{off}]^{a_{8b}}$$

Note that the  $a_i$  in Equations 20 and 21 are given an additional letter subscript to emphasize that the power laws may not be the same for the two dependant variables under study.

*5.1.2.1. Applying the pi-theorem and the algebraic formalism to the DIA.* The pi-theorem predicts that the behavior of the DIA in regards to a non-dimensionalized dependant variable should be described by five dimensionless groupings, given that we have eight independent variables having a total of three independent dimensions. Both the Buckingham and Taylor methods were used to do the dimensionless grouping, and identical results were obtained (Table 5.2).

**Table 5.2.** Dimensionless groupings that result from dimensional analysis of the DIA

Identifier	Dimensionless Grouping
Pi <sub>1</sub>	$\tau k_{on} [Ag^*]$
Pi <sub>2</sub>	$D_{Ag^*} / D_{Ab}$
Pi <sub>3</sub>	$[Ab] / [Ag^*]$
Pi <sub>4</sub>	$D_{Ab} / D_{AbAg^*}$
Pi <sub>5</sub>	$\tau k_{off}$
$(y/y_0)_1$	$R_i$
$(y/y_0)_2$	$S_i [Ag^*]$

Thus, in this problem statement, both  $R_i$ , and  $S_i$  are functions of these same five dimensionless groups ( $Pi_{1-5}$ ); but the exponents of the two power laws may be

different, and the power law relationship for  $S_i$  has a leading term ( $y_0=[Ag^*]^{-1}$ ), while the power law relationship for  $R$  does not (because  $R$  is already dimensionless).

Using the form of Equation 18, and the letter subscript introduced for Equations 20 and 21:

$$22) [R_i] = \prod_{i=1}^5 [P_i]^{b_{ia}}$$

$$23) [S_i] = [Ag^*]^{-1} \prod_{i=1}^5 [P_i]^{b_{ib}}$$

With the identification of these dimensionless groups, the proper simulations to perform with the numerical model were much easier to define.

## 5.2. Numerical Simulation

Using the insights arising from dimensional analysis, the two-dimensional FDT model, described in detail previously (Section 2.2.4) was used to generate blank responses and dose/response initial slopes for different combinations of the dimensionless variables that span the domain expected for real analytes. These simulations were then used to construct log-log plots (as described in section 5.1.2) to deduce power laws that govern the DIA.

### 5.2.1 Preliminary Simulations and Calculations

*5.2.1.1. Eliminating a dimensionless group.* Even with the reduction in the number of parameters to model from eight to five, the numerical task-at-hand was still quite large. Since we had assumed previously that the dissociation rate was unimportant, it was decided that some preliminary simulations to assess this assumption could enable a further reduction in the inputs to the full simulation set. Several values of  $\tau k_{off}$  were investigated for a selected set of the other  $P_{i,1-4}$  values. These simulations suggested that  $\tau k_{off}$  was unimportant for values less than  $\sim 0.3$ , and as it increased above this value, it rapidly became inversely correlated with  $R$  and  $S_i$ ; i.e., the response and initial slope went down rapidly as the value of  $\tau k_{off}$  went up (Figure 5.1). This led to

a decision to insure that all models and experiments were done at  $\tau k_{off} < 0.3$ . ( $\tau k_{off} > \sim 0.3$  also requires that this variable be considered for states of dynamic similitude.)

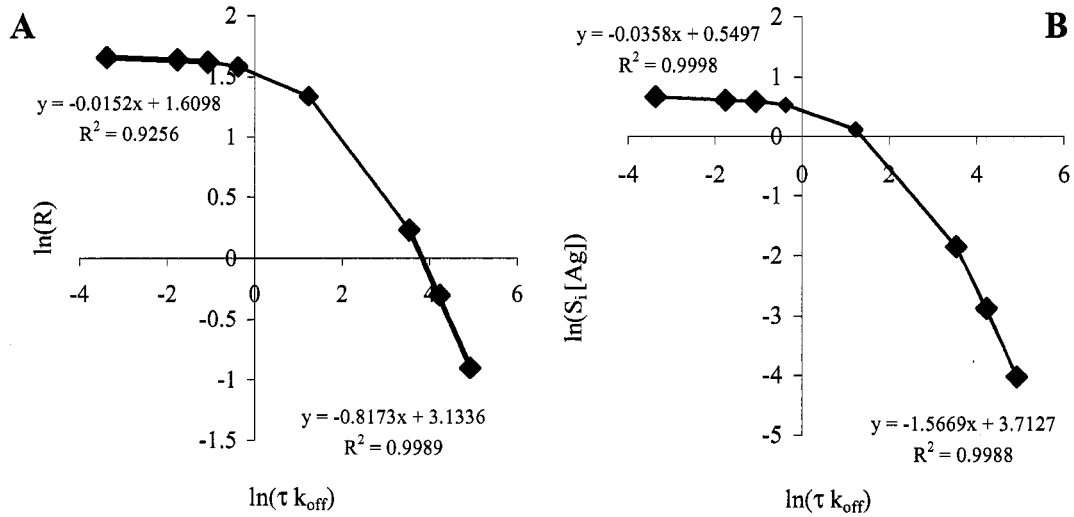


**Figure 5.1:** Summary of representative simulations that lead to the adoption of a  $< \sim 0.3$  criteria for the value of  $\tau k_{off}$ . The strong inverse relationship between this dimensionless group and both dependant variables of interest implies that a DIA formulated with a higher value for this dimensionless group will be sub-optimal. A) The log-log plot of the blank signal versus  $\tau k_{off}$ . B) The log-log plot of the dimensionless initial slope versus  $\tau k_{off}$ . Note that for both dependant variables, a linear fit of the relationship below  $\tau k_{off} \approx 0.3$  has a negligible slope, implying a vanishing power law exponent – the parameter can be ignored below that threshold. The opposite is true at the highest values of  $\tau k_{off}$ , with a strong inverse relationship.

**5.2.1.2. Other important dimensionless numbers.** There are two other dimensionless numbers that did not come from the dimensional analysis which were considered in the simulations that follow. The Kamholz number ( $Kz$ ) was discussed in detail previously (Section 2.2.4). To insure that these simulations were accurate descriptions of what would actually be observed in a DIA with those parameters, the Kamholz number was kept at  $> 5$ . The other number relates the device dimensions to the interaction time. We have denoted it the *T-number*, since it is unique to working in a T-sensor. It is defined as:  $T = d / (4D_{Ag} \tau)^{1/2}$ , where  $d$  is the width of the channel in the diffusion dimension (as defined in Section 2.2.1),  $D_{Ag}$  and  $\tau$  are as previously defined in this section. The number is derived from the solutions to the two-dimensional diffusion equations for an initial condition of an infinite plane source<sup>34</sup>. It is applied in

the following manner. The channel must be a sufficient width,  $d$ , to insure that, after the interdiffusion expected for a given interaction time, there is a sufficient fraction of the channel at each extreme which contains undiluted feed solutions to enable BFTN normalization (Section 2.2.1). A  $T$  value of  $>5$  insures that at least 10% of the channel at each extreme is undiluted feed solution. In addition, because we are integrating over a discrete data set to calculate the response, the same node-spacing in the channel (for models) and the same number and size of pixel (for experiments) must be sampled for each accumulation (or free diffusion) profile to produce an identical blank response and initial slope. Thus,  $T$  must be held constant to insure dynamic similitude. For these simulations,  $T$  was fixed at a value of 5.0.

*5.2.1.3. Evaluation of dynamic similitude.* A few tens of simulations were performed with the  $Pi_{1-5}$ ,  $T$ , and  $Kz$  held constant, but with different values of dimensional parameters contributing to several of the dimensionless groupings. As expected, changing dimensional variables made no detectable difference as long as the values for the dimensionless groups remained constant (data not shown). Thus, this set of dimensionless numbers defines states of dynamic similitude. It should be noted, that one additional variable must be tracked for dynamic similitude. As mentioned above in discussing the T-number, because of the nature of the discrete integration used to create the analytical signal, the number of nodes simulated or pixels sampled for each intensity profile affects the magnitude of the signal calculated. Signals calculated from a 200-node simulation do not match one from a 2000 node simulation, or a 781 pixel sample of an image. The relationship is that of a simple proportion, however... at least to a first approximation. (If the sampling is too course-grained, the representation of the underlying function may be inaccurate, and rescaling proportionally will not restore the lost accuracy.) For all the simulations done here, the same number of nodes was used.

## 5.2.2 A Comprehensive Simulation Set

5.2.2.1. *Description of Simulations.* A total of 480 different combinations of  $Pi_{1-4}$  were investigated (Table 5.3). For each combination accumulations for a number of different unlabeled antigen concentrations were simulated – a blank and several low concentrations. A good estimate of the initial slope was considered accomplished when the blank response and two low-concentration responses created a linear dose-response relationship. (The DIA algorithm produces smaller signals as the  $[Ag]$  gets greater. The absolute value of the slope was actually the parameter tracked, so that larger slopes would represent better performance.) Since some of the combinations investigated displayed non-linearity in the dose response closer to the blank than others, many cases investigated required more than three simulations. Close to two thousand individual simulations were performed, making this the most comprehensive investigation of the DIA to date.

**Table 5.3.** Values of the dimensionless groups used in simulations. All possible combinations of the values were investigated ( $5 \times 4 \times 6 \times 4 = 480$  combinations).

Dimensionless Grouping	Values Investigated
$Pi_1 = \tau k_{on} [Ag^*]$	0.01, 0.1, 1, 10, 100
$Pi_2 = D_{Ag^*} / D_{Ab}$	1, 10, 100, 1000
$Pi_3 = [Ab] / [Ag^*]$	0.1, 0.5, 1, 5, 10, 100
$Pi_4 = D_{Ag^*} / D_{AbAg^*}$	1, 1.14, 1.31, 1.5

It is illuminating to place these values in context. First, consider the domain of values for  $Pi_j$ . A value of 0.01 could be obtained by a low association rate typical of an antibody/protein-antigen reaction ( $\sim 10^5 \text{ M}^{-1}\text{s}^{-1}$ ), combined with a difficult to detect labeled antigen concentration ( $\sim 1 \text{ nM}$ ), and a reasonably fast interaction time (100 s). A value of 100 would result from an association rate more typical of a small molecule ( $\sim 10^6 \text{ M}^{-1}\text{s}^{-1}$ ), a relatively concentrated antigen reagent (100 nM) and an unacceptably slow interaction time (1000s).

For  $Pi_2$ , the low end of the domain corresponds to assaying for a ~150 kD protein with the germinal (whole antibody) capture species, or a ~47 kD protein with an  $F(ab')_2$ . The high end of the domain for  $Pi_2$  is only be achieved if the capture species is slowed with a biochemical modification of the kind described in Section 4.3 – even free ions do not diffuse in solution four orders of magnitude faster than whole antibodies. If a protein is the analyte, achieving a  $Pi_2$  of 1000 requires linking the antibody to a particle so large it will undoubtedly sediment or clog the device (see Section 4.3 for further discussion of these phenomena).

The domain for  $Pi_3$  is not intrinsically bounded by any properties of the analyte (except, perhaps, solubility limits and cost), so an arbitrarily diverse set of values was chosen.

Finally, consider  $Pi_4$ . The ratio of unity corresponds to a case where the analyte is much smaller than the capture species, so there is no change in diffusivity of the complex relative to the capture species. The ratio of 1.5 corresponds to a complex between a whole antibody and a ~530 kD analyte, or an  $F(ab')_2$  with a ~134 kD analyte.

So it appears that the  $Pi_i$  values chosen adequately span the parameter space of interest. For comparison, the phenytoin DIA as formulated could be represented by  $Pi_1 = 1.4$ ,  $Pi_2 = 7.4$ ,  $Pi_3 = 4.2$ ,  $Pi_4 = 1$ ,  $Pi_5 = 0.02$ ,  $K_z = 12.6$ ,  $T = 7.8$ .

*5.2.2.2. Summary of Results.* The log-log plots for the eight power law relationships investigated (two dimensionless dependant variables, each described by four independent dimensionless groups, as summarized in Table 5.2) illustrate the important results of the numerical modeling. Rather than display all 480 plots analyzed, many of which are redundant, representative example charts are provided for each of the eight cases (Figures 5.2–5.5), and deviations from the typical behavior



are noted in the accompanying discussion. Note that the results for  $Pi_3=100$  are omitted from the analysis. Dose-response curves in this part of the parameter space were very sigmoidal, and so presented difficulties for the calculation of initial slope. While their dynamic ranges are very large, their slopes were far from maximum, so they represent sub-optimal formulations compared to our stated criteria. It should also be noted that when  $Pi_2 = Pi_4=1$ , the signal and response vanish completely. Since the logarithm function is undefined at arguments of zero, these cases also cannot be plotted or included in the analysis. It is also difficult to imagine a physical case where both of these ratios could be unity – if the  $Ab$  and  $Ag^*$  have the same diffusivity, the combination of the two into an immune complex will not have the same diffusivity.

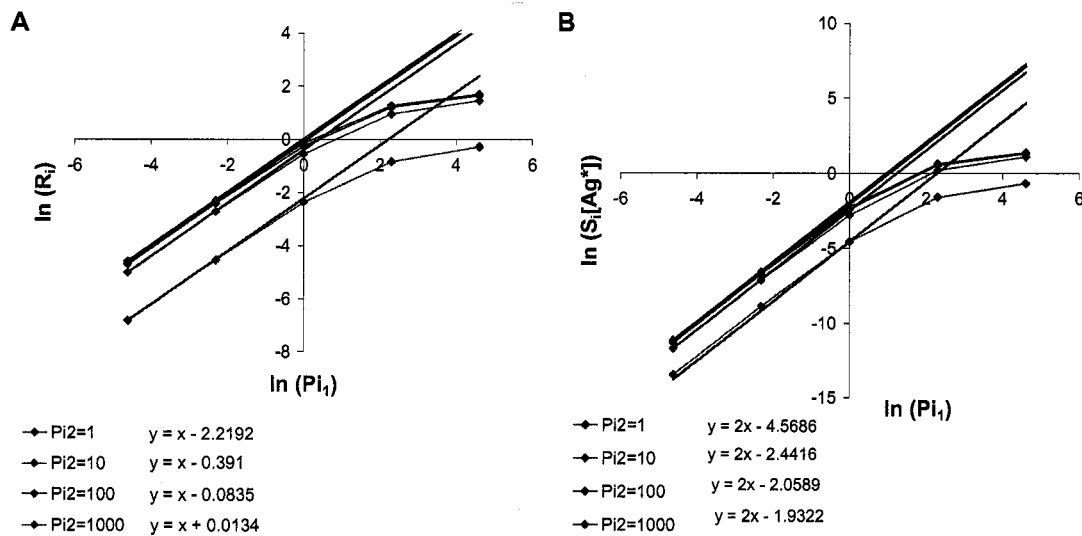


**Figure 5.2:** Representative summary of simulations for  $Pi_1 = \tau k_{on} [Ag^*]$ . Log-log plots of the dimensionless dependant variables versus  $Pi_1$  for all values of  $Pi_2$  (see legend),  $Pi_3=0.1$ , and  $Pi_4=1.31$ . Lines are fitted to the plots at low values of  $Pi_1$  only. A) The log-log plot of the blank response versus  $Pi_1$ . B) The log-log plot of the dimensionless initial slope versus  $Pi_1$ . See text for a discussion of data not shown for this case.

$Pi_1 = \tau k_{on} [Ag^*]$ : The blank response changes in direct proportion to  $Pi_1$ , (i.e., with a power of unity) for the low-values of  $Pi_1$ , and then with a decreasing dependence at the higher values of  $Pi_1$  investigated, up to almost no dependence at the extremes of  $Pi_1$ . There is no change in this behavior of when  $Pi_2$  is varied (with  $Pi_3$  and  $Pi_4$  fixed).

This non-linearity is dependant on  $Pi_3$  – increasing values of  $Pi_3$  (with  $Pi_2$  and  $Pi_4$  fixed) results in a faster “roll-off” of the dependence if  $R_i$  to  $Pi_1$  so that when  $Pi_3 > 1$ , the direct proportion stops at  $Pi_1 \approx 0.1$ , rather than  $Pi_1 \approx 1$  (data not shown). These observations are true for the dimensionless initial slope as well, although the power law exponent is equal to two in the linear, low- $Pi_1$  regime. Plots for other values of  $Pi_4$  (with  $Pi_2$  and  $Pi_3$  fixed) were indistinguishable from these examples (data not shown).

The dependence of  $Pi_1$  and  $Pi_3$  seems logical. Both  $Pi_1$  and  $Pi_3$  affect the mass of  $Ag^*$  that is involved in the immune complex:  $Pi_1$ , by specifying both the flux of  $Ag^*$  into the interdiffusion zone ( $\tau[Ag^*]$ ), and the frequency of reaction ( $k_{on}$ );  $Pi_3$ , by specifying the deviation from the ideal stoichiometric ratio. As  $Pi_3$  increases, the antibody is in excess in the interdiffusion zone, so the effect of increased flux of  $Ag^*$  and/or increased reaction rate is less important. This seems to indicate that at low values of both of these dimensionless groups, the blank response and slope are limited by the gross mass-action effects and at higher values they are limited by more subtle spatial and stoichiometric effects on the reaction.

The effect of  $Pi_1$  on  $R_i$  and  $S_i$  appears independent of  $Pi_2$  and  $Pi_4$ . This result suggests that the mass involved in the complex for a given set of  $Pi_1$  and  $Pi_3$  is not affected by the relative spatial position of that mass, as determined by the diffusivity ratios  $Pi_2$  and  $Pi_4$ .

It is not surprising that the blank response increases monotonically with this dimensionless group, given the known behavior of the DIA (Section 2.2.1). It is somewhat surprising that the initial slope increases monotonically – given that most competition assays use low concentrations of the labeled analyte to achieve low LODs -- until you recall that this is the relationship for the *dimensionless* slope. The power law for this group can be written  $S_i[Ag^*] = Pi_1^a = (\tau k_{on})^b ([Ag^*])^b$ , so for the actual *dimensional* slope, the relationship is  $S_i = (\tau k_{on})^b [Ag^*]^{b-1}$ . This implies that, if  $Pi_1$  is

manipulated by varying  $[Ag]$ , while leaving  $(\tau k_{on})$  fixed, you will see a maximum in the absolute value of  $S_i$  when the exponent of  $Pi_i$  is unity. (In Figure 5.2, this appears to happen at  $Pi_i \approx 10$ . This is an exciting and counterintuitive conclusion – LOD improves with increasing concentration of labeled antigen, up to a threshold, under many realistic DIA formulations! This conclusion was explicitly validated in Section 5.4.3.

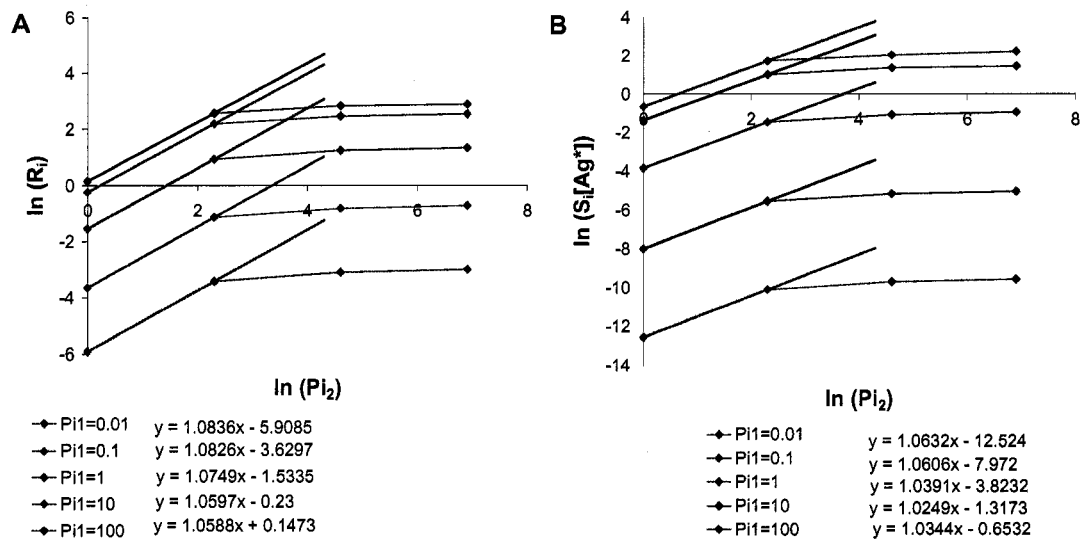


**Figure 5.3:** Representative summary of simulations for  $Pi_2 = D_{Ag^*} / D_{Ab}$ . Log-log plots of the dimensionless dependant variables versus  $Pi_2$  for all values of  $Pi_1$  (see legend),  $Pi_3 = 0.5$ , and  $Pi_4 = 1.14$ . A) The log-log plot of the blank response versus  $Pi_2$ . Lines are fitted to the plots at low values of  $Pi_2$  only. B) The log-log plot of the dimensionless initial slope versus  $Pi_2$ . See text for a discussion of data not shown for this case.

$Pi_2 = D_{Ag^*} / D_{Ab}$  : Both the blank response and initial slope change in direct proportion to  $Pi_2$  up to the  $Pi_2$  value of 10. Above that value,  $R_i$  and  $S_i$  are not significantly affected by  $Pi_2$ . There is no change in this behavior of when  $Pi_1$  is varied (with  $Pi_3$  and  $Pi_4$  fixed). This observation is somewhat surprising, given our initial hypothesis that larger capture species will increase the response dramatically (Section 2.4.1). It seems that once there is a detectable effect of accumulation, it matters little what the precise spatial distribution is – sharp tall bumps are not any better than more spread out bumps. This conclusion is probably the result of the change to a signal-algorithm

based on the integrated non-direction difference to free-diffusion (Section 4.2.3.3) – when the response was based on slope changes, the “peakiness” of the accumulation was important, but it is not when the difference from the infinite dose behavior for all modulated locations in the channel is integrated.

This relationship is dependant on  $Pi_4$  (with  $Pi_1$  and  $Pi_3$  fixed), with the direct proportionality appearing only at values of  $Pi_4=1.14$ . (Note the absence of meaningful data at  $Pi_2 = Pi_4=1$  noted earlier). At the higher values of  $Pi_4$ ,  $R_i$  increases as a lower power of  $Pi_2$ – as low as 0.6 in the extremes (data not shown). This can be explained by considering that both  $Pi_2$  and  $Pi_4$  have an effect on the underlying assay principal of the DIA – the slowing of the diffusion of the analyte once it is bound.  $Pi_2$  could be rewritten as  $(1/ Pi_4)(D_{Ag^*}/D_{AbAg^*})$ ; thus,  $Pi_2*Pi_4$  is the dimensionless grouping that relates most directly to the assay principal. It is acceptable as part of the pi-theorem formalism to transform a dimensionless group by multiplying it by another dimensionless group, as long as the total number of groups is not reduced. In retrospect, this may have been produced more easily interpreted results.

The effect of  $Pi_2$  on  $R_i$  appears independent of  $Pi_3$  (with  $Pi_1$  and  $Pi_4$  fixed, data not shown). This is concordant with the results of the  $Pi_1$  analysis, and can be explained with similar logic.

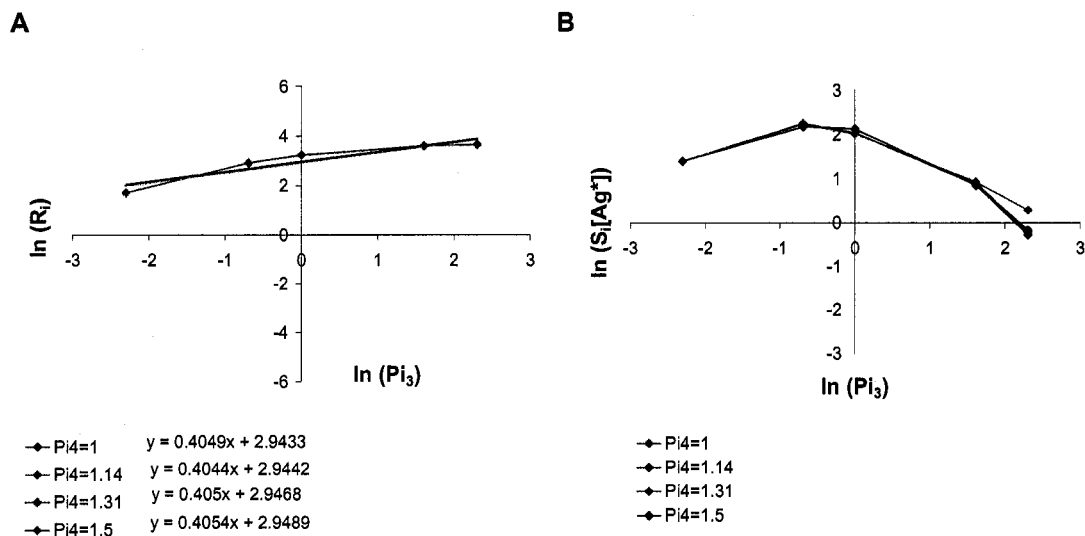


**Figure 5.4:** Representative summary of simulations for  $Pi_3=[Ab] / [Ag^*]$ . Log-log plots of the dimensionless dependent variables versus  $Pi_3$  for all values of  $Pi_4$  (see legend),  $Pi_1=100$ , and  $Pi_2=1000$ . Lines are fitted to the plots at all values of  $Pi_3$ . A) The log-log plot of the blank response versus  $Pi_3$ . Lines are fitted to the plots at all values of  $Pi_3$ . B) The log-log plot of the dimensionless initial slope versus  $Pi_3$ . No lines were fitted to this obviously non-linear relationship. See text for a discussion of data not shown for this case.

$Pi_3=[Ab] / [Ag^*]$ : The blank signal increases uniformly with increasing  $Pi_3$ , over the entire domain of  $Pi_3$  investigated, with the power of this relationship ranging from unity at low values of  $Pi_1$  to  $\sim 0.4$  for the highest values of  $Pi_1$ . The dimensionless slope, however, shows a maximum in value at an approximately equimolar ratio of Ag and Ab binding-sites. The relationships between  $R_i$  and  $S_i$ , and  $Pi_3$ , are not significantly affected by varying  $Pi_4$  (with  $Pi_1$  and  $Pi_2$  fixed). This maximum is only clearly noticeable at the higher values of  $Pi_1$  ( $\geq 1$ ), however. At the two lowest values of  $Pi_1$  the dimensionless slope increases with  $Pi_3$  in an identical fashion to  $R_i$  (data not shown). The relationships between  $R_i$  and  $S_i$ , and  $Pi_3$ , are not significantly affected by varying  $Pi_2$  (with  $Pi_1$  and  $Pi_4$  fixed, data not shown).

These observations can be explained by recognizing that an excess of Ab will increase the blank response by insuring that a larger fraction of the available  $Ag^*$  molecules are involved in an immune complex, but also will reduce the sensitivity of the  $Ab/Ag^*$

binding reaction to the introduction of competing Ag. The dependency of  $Pi_3$  behavior on  $Pi_1$  is explained with the same arguments invoked to explain the effect  $Pi_3$  of on  $Pi_1$  above.

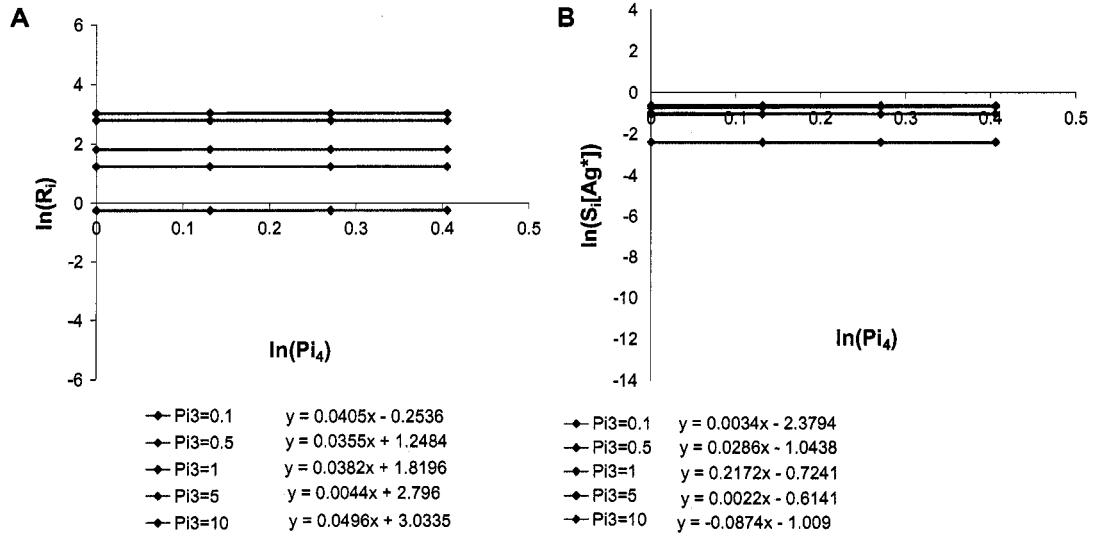


**Figure 5.5:** Representative summary of simulations for  $Pi_4 = D_{Ag^*} / D_{AbAg^*}$ . Log-log plots of the dimensionless dependent variables versus  $Pi_4$  for all values of  $Pi_3$  (see legend),  $Pi_1 = 1$ , and  $Pi_2 = 100$ . Lines are fitted to the plots at all values of  $Pi_3$ . A) The log-log plot of the blank response versus  $Pi_3$ . Lines are fitted to the plots at all values of  $Pi_3$ . B) The log-log plot of the dimensionless initial slope versus  $Pi_3$ . See text for a discussion of data not shown for this case.

$Pi_4 = D_{Ag^*} / D_{AbAg^*}$ : Neither the blank response or the dimensionless slope are significantly effected by varying  $Pi_4$  over the entire domain of  $Pi_4$  investigated. This behavior was not significantly changed when  $Pi_3$  is varied (with  $Pi_1$  and  $Pi_2$  fixed), nor did it change significantly when  $Pi_1$  is varied (with  $Pi_3$  and  $Pi_2$  fixed, data not shown), nor when  $Pi_2$  is varied (with  $Pi_3$  and  $Pi_1$  fixed, data not shown). For both  $Pi_1$  and  $Pi_3$ , there is a very slight change in  $Pi_4$  at the highest values of  $Pi_1$  and  $Pi_3$  that seems to reflect the effects of these two parameters on  $R_i$  and  $S_i$ , but it is not large enough to warrant inclusion in a power law relationship. It appears that for a course-grained description of the DIA, a single diffusivity ratio ( $Pi_2$ ) is sufficient to capture the important behavior.

It should be noted, that the case  $Pi_2 = 1$  is a degenerate case for  $Pi_4$ . When the diffusivities of the  $Ag^*$  and  $Ab$  are identical, a degree of freedom is lost and the value of  $Pi_4$  cannot vary. In this case,  $Pi_4$  reduces to  $0.5^{-1/3} \approx 1.26^{xviii}$ . It seems likely that there is some intermediate effect of  $Pi_4$  on  $R_i$  and  $S_i$  when  $Pi_2 = 1-10$ , but this simulation set did not investigate that narrow region.

5.2.2.2. *Power laws for dimensional variables.* From the analysis above, it seems that there are three regimes in which the DIA can operate. The *low-signal regime* is defined as  $Pi_1 < 10$ ,  $Pi_2 = 1-10$ ,  $Pi_3 \leq 1$ . The *high-signal regime* is defined as  $Pi_1 > 100$ ,  $Pi_2 > 10$ ,  $Pi_3 \geq 1$ . The parameter space lying between these two domains is a *transitional regime* where one regime blends into another. In the transitional regime, a simple power law will not apply.

For the low signal regime:

$$22a) [R_i] = [\tau k_{on} [Ag^*]]^1 [D_{Ag^*} / D_{Ab}]^1 [[Ab] / [Ag^*]]^1 [D_{Ab} / D_{AbAg^*}]^0$$

$$22b) R_i = \frac{\tau k_{on} D_{Ag^*} [Ab]}{D_{Ab}}$$

$$23a) [S_i [Ag^*]] = [\tau k_{on} [Ag^*]]^2 [D_{Ag^*} / D_{Ab}]^1 [[Ab] / [Ag^*]]^1 [D_{Ab} / D_{AbAg^*}]^0$$

$$23b) S_i = \frac{\tau^2 k_{on}^2 D_{Ag^*} [Ab]}{D_{Ab}}$$

In the special case, where  $Pi_3 = [Ab] / [Ag^*] \approx 1$ , (maximum in initial slope) these equations reduce to:

$$24a) [R_i] = [\tau k_{on} [Ag^*]]^1 [D_{Ag^*} / D_{Ab}]^1 [D_{Ab} / D_{AbAg^*}]^0$$

<sup>xviii</sup> This assumes a simple Stokes-Einstein relationship between molecular weight ( $M$ ) and diffusivity, and no viscosity or temperature change from complex formation. Under these assumptions,  $D_i = cM_i^{-1/3}$ , ( $c$  is a constant) and  $Pi_4 = cM_{Ab}^{-1/3} / c(M_{Ab} + M_{Ag})^{-1/3}$ . If,  $M_{Ab} = M_{Ag} \rightarrow M_{Ab} + M_{Ag} = 2 M_{Ab}$  then  $Pi_4$  reduces to  $0.5^{-1/3}$ .

$$24b) R_i = \frac{\tau k_{on} D_{Ag^*} [Ag^*]}{D_{Ab}}$$

$$25a) [S_i [Ag]^*] = [\tau k_{on} [Ag^*]]^2 [D_{Ag^*} / D_{Ab}]^1 [D_{Ab} / D_{AbAg^*}]^0$$

$$25b) S_i = \frac{\tau^2 k_{on}^2 D_{Ag^*} [Ag^*]}{D_{Ab}}$$

For the high signal regime:

$$26a) [R_i] = [\tau k_{on} [Ag^*]]^{0.3} [D_{Ag^*} / D_{Ab}]^0 [[Ab] / [Ag^*]]^{0.3} [D_{Ab} / D_{AbAg^*}]^0$$

$$26b) R_i = \sqrt[3]{\tau k_{on} [Ab]}$$

$$27a) [S_i [Ag]^*] = [\tau k_{on} [Ag^*]]^{0.3} [D_{Ag^*} / D_{Ab}]^0 [[Ab] / [Ag^*]]^{-0.3} [D_{Ab} / D_{AbAg^*}]^0$$

$$27b) S_i = \sqrt[3]{\frac{\tau k_{on}}{[Ab]}}$$

In the special case, where  $Pi_3 = [Ab] / [Ag^*] \approx 1$ , (maximum in initial slope) these equations reduce to:

$$28a) [R_i] = [\tau k_{on} [Ag^*]]^{0.3} [D_{Ag^*} / D_{Ab}]^0 [D_{Ab} / D_{AbAg^*}]^0$$

$$28b) R_i = \sqrt[3]{\tau k_{on} [Ag^*]}$$

$$29a) [S_i [Ag]^*] = [\tau k_{on} [Ag^*]]^{0.3} [D_{Ag^*} / D_{Ab}]^0 [D_{Ab} / D_{AbAg^*}]^0$$

$$29b) S_i = \sqrt[3]{\tau k_{on} [Ag^*]}$$

Equations 22-27 only apply when  $Pi_5 = \tau k_{off} < \sim 0.3$  and, therefore, can be ignored.

The limited analysis on  $Pi_5$  (Figure 3.1), combined with the power laws above, suggests that-- in the low signal regime -- at the high values of  $Pi_5$  possible by increasing  $\tau$ , the reduction of response and signal by  $Pi_5$  may not actually be as great as the gain in response and signal through  $Pi_1$ , resulting from the same increase in  $\tau$ .



However, in the high-signal regime, increasing  $\tau$  to the point where  $\tau k_{off}$  becomes important will most likely be counterproductive.

These power laws, and the plots from which they are derived, when combined with the estimates of noise, will enable the definition of limits and formulation of design rules.

### ***5.3. Noise Simulations***

Although it is always required to measure the variability of an assay system to identify lurking variables, a great deal can be learned about expected sources of variation through simulations with noise added in. Two sources of variation expected to be important are: 1) uncorrected variation in location of the midline, and 2) any variation in the random high-spatial-frequency (HF) noise during the experiment. These noise sources were briefly discussed previously (Section 4.2.3.3); but, in this section, they are studied explicitly, with special attention to their interaction.

#### **5.3.1. Procedure**

The interaction of midline variation and HF noise was studied by using simulated accumulations (with 781 nodes to more closely correspond with experimental observations) with added random noise of differing magnitudes, and simulated (noise-free) free-diffusion curves displaced different distances from the midline. These were combined pair-wise in signal calculations with the second generation DIA integrated non-directional difference algorithm, and the effects on the signal plotted. The study was repeated for several simulated accumulations of differing noise-free signal magnitudes (including the vanishing magnitude case -- a free-diffusion profile) to determine if the effects seen varied with the expected signal.

Random noise was added to the simulated accumulation profiles by creating a noise profile – a vector of random values with the same length as the simulated accumulation – and adding that vector to the accumulation. A “master noise vector” was created using the *RANDBETWEEN* function of Excel (Microsoft, Redmond, WA, USA), with the arguments (-100, 100) to randomly assign an integer in this range, and then re-scaling the vector so that all values were bounded by negative unity and unity. The magnitude of the noise was then varied to 0%, 1%, 5%, 10% and 20% by multiplying the master noise vector by an appropriate scaling factor prior to adding it to the accumulation.

Uncorrected midline variation was simulated by displacing the vector of simulated free-diffusion used in the signal calculation over a range of  $\pm 50$  pixels, in five pixel steps, using the same method used for midline correction of real data (changing the position indices of the vector). These displaced vectors were then applied to the signal calculation as normal.

Thus, a data set was created that varies only those two sources of variation under study, and enables evaluation of their effects alone, and in interaction, on a number of different signals. Plots of the profiles described above illustrate this study design (Figure 5.6).

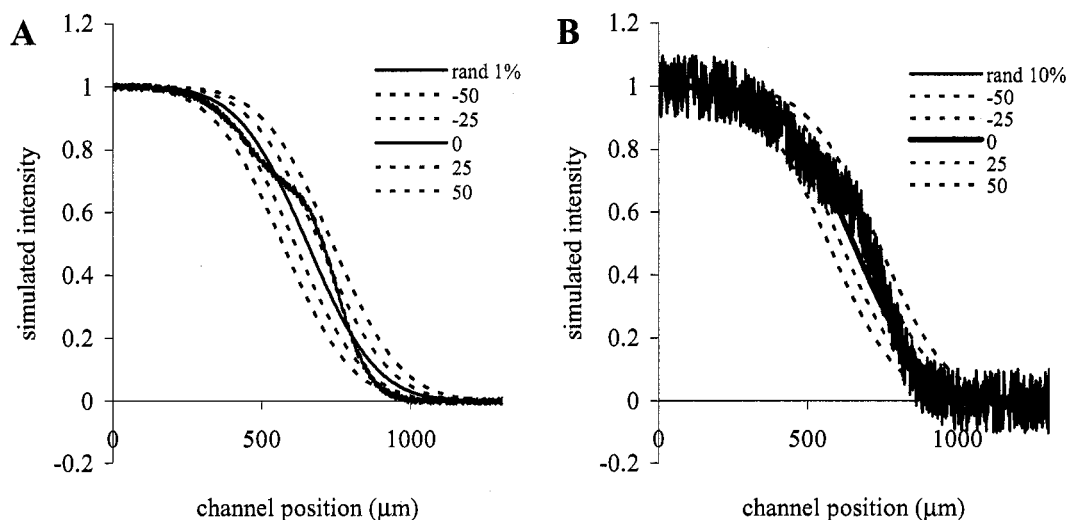


**Figure 5.6:** Plots that illustrate the study design used to investigate the expected primary sources of variation in the second generation DIA. Not all of the different midline displacement values (dotted lines) studied are plotted for clarity. Negative displacement corresponds to the Ab (low intensity) side of the channel. Not all of the HF frequency magnitudes, and signal magnitudes are shown for brevity. A) A plot of a middling signal intensity accumulation, with 1% added high frequency noise. B) The same accumulation with 10% added noise.

### 5.3.2. Results

Midline variation and HF noise variation are clearly both major contributors to signal variation in the second generation DIA (Figures 5.7 – 5.9). Signal versus midline displacement displays a quasi-parabolic relationship, with a steep slope and with a minimum in signal at vanishing displacement only when there is no HF noise. The quasi-parabola is not symmetric around the no-displacement axis, except for the limiting cases. Signal versus HF noise levels is a monotonically rising relationship, but is only linear for the free-diffusion, no displacement case (where the slope is  $\sim 4$ ).

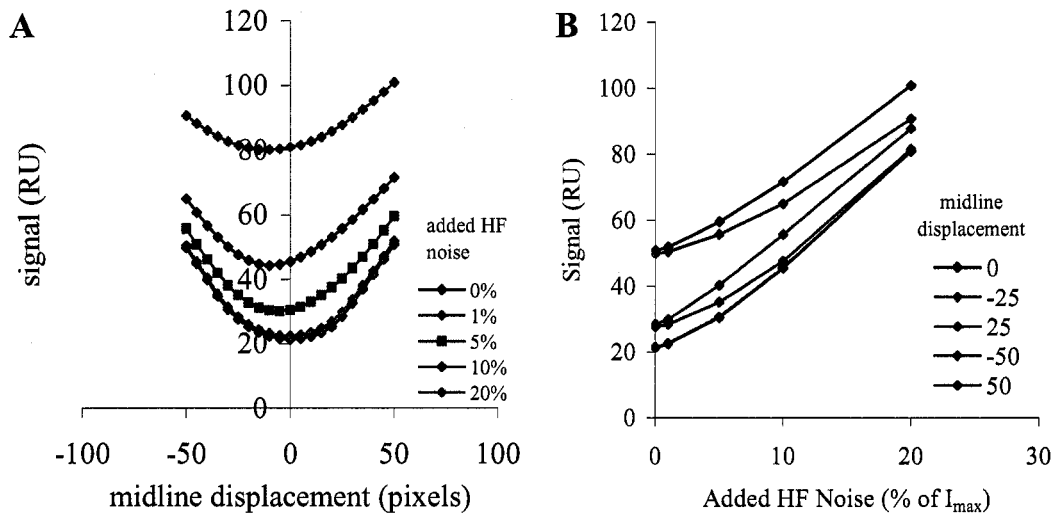


**Figure 5.7:** Representative plots of the signal variation observed in response to variation in the two most important sources of variation in the DIA for a middling signal intensity accumulation (the same accumulation shown in Figure 5.6) A) The signal versus midline-displacement plot, for the various added high-spatial-frequency noise cases (see legend). B) The signal versus HF-noise plot, for the various midline displacement cases (see legend).

There is a significant interaction between the two sources of variation. At higher HF noise levels, the minimum in the signal versus midline-displacement quasi-parabola moves to the “negative” (low intensity, Ab) side of the channel. The steepness of the quasi-parabola decreases as HF noise increases, suggesting that the HF noise begins to mask the effects of the midline displacement. The asymmetry of the quasi-parabola around the no-displacement axis also appears magnified as HF noise increases. At larger displacements of the midline, the signal versus HF-noise relationship is more nonlinear for low signals.

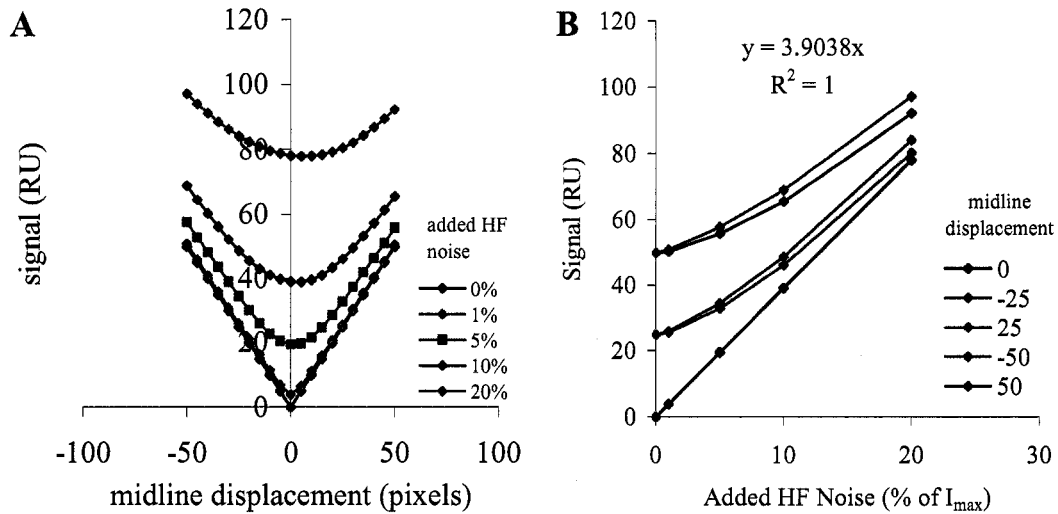


**Figure 5.8:** Representative plots of the signal variation observed in response to variation in the two most important sources of variation in the DIA for a vanishing signal intensity accumulation (the same free-diffusion simulation shown in Figure 5.6 before displacement) A) The signal versus midline-displacement plot, for the various added high-spatial-frequency noise cases (see legend). B) The signal versus HF-noise plot, for the various midline displacement cases (see legend). The statistics on the graph are for a line fitted to the vanishing displacement signal versus HF-noise relationship.

These general observations hold for all the different signal accumulations, but differ somewhat in magnitude as the signal is increased. In general, the lower signals are the most sensitive to midline displacement. The differences between the different signal levels are less apparent at higher HF values (as well as greater midline displacements) than at the low noise cases, indicating that modulation and response will be less detectable in the noisier cases.

### 5.3.3. Relating the Results to Real DIA Data

The simulations and associated analysis above (Section 5.3.2) can be applied to the actual DIA to predict assay variation, if an estimate of the HF noise and midline variation is made. Midline variation is explicitly corrected for in the second generation DIA by including an internal diffusion standard in the  $Ag^*$  reagent (Section

4.2.3.3). The efficacy of this method is difficult to evaluate, however. It is clearly necessary (as shown in Figure 4.25), indicating that there may still be some residual variation. (HF) noise that is randomly distributed around the true underlying accumulation, results from the thermal noise of the camera. As discussed earlier (Section 4.2.3.3), the camera noise is fairly constant for a properly working instrument; however, the BFTN processing amplifies this noise during the normalization process. Thus, the magnitude of noise observed in the profile appears greater when the background corrected intensity of the undiluted  $\text{Ag}^*$  reagent is less. The observed HF-noise does not vary appreciably for a given signal magnitude; as long as the fluorescence of the  $\text{Ag}^*$  reagent, illumination source intensity, background, and camera settings, etc., are kept constant – the normal case in operating the DIA. So for a given for a given formulation, HF-noise can be characterized.

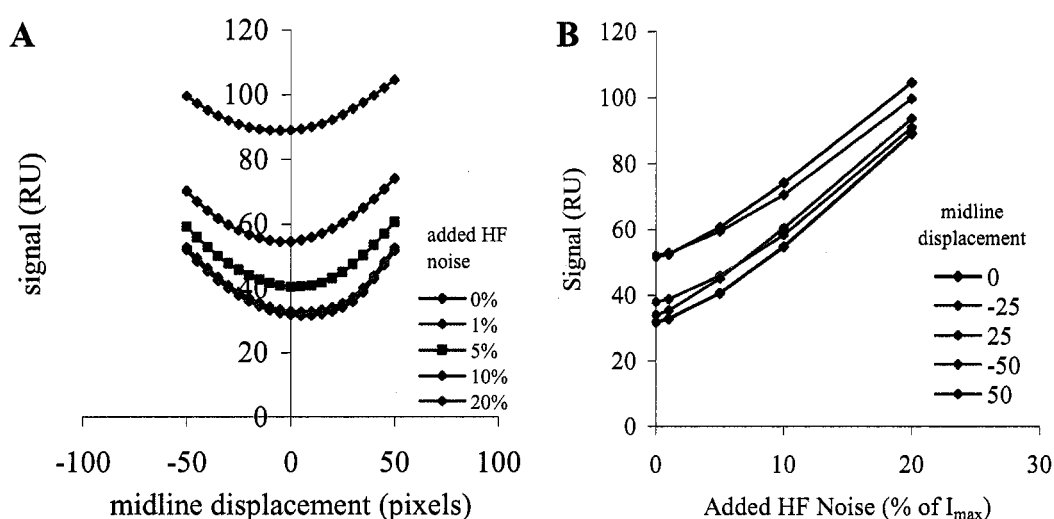


**Figure 5.9:** Representative plots of the signal variation observed in response to variation in the two most important sources of variation in the DIA for a moderately-high signal intensity accumulation (not shown) A) The signal versus midline-displacement plot, for the various added high-spatial-frequency noise cases (see legend). B) The signal versus HF-noise plot, for the various midline displacement cases (see legend).

In the absence of lurking variables, and given typical HF-noise levels, the signal variation observed should vary only slightly over the range of signals typically seen in protein DIA (since the slopes of the quasi-parabolas describing the do not vary greatly with signal magnitude in these cases). The magnitude of the signals seen, however, may differ significantly from those predicted by the simulations, unless the HF noise observed is accounted for. In Chapter 6, results for a DIA for C-reactive protein illustrate some of these conclusions.

#### ***5.4. Model Validation***

Comparison of the simulations derived from the numerical model to experimental data shows that the model is a good description of the DIA, if its limitations are respected ( $K_z$ ) and the stated assumptions are true. In this section, those comparisons are summarized.

##### **5.4.1 The Germinal DIA for phenytoin**

The DIA for phenytoin agreed reasonably well with the predictions of the numerical model, given the number of parameters in the phenytoin DIA that were unknown (a situation arising from the use of an off-the-shelf assay kit). These observations have been extensively discussed previously<sup>1</sup>, and will not be restated here.

##### **5.4.2 The Germinal DIA for HRP**

Accumulations for the HRP DIA agreed very well with the predictions of the numerical model for high-quality data (Figure 3.1). Some calculated responses in Section 3.1 did not match predictions, but subsequent analysis implicated both germinal DIA signal processing (Section 4.2), and reagent stability (discussed in Section 4.2.3).

### 5.4.3 The DIA for CRP

As a final check on the validity of the modeling done here, a more extensive data set with C-reactive protein was generated and analyzed. (The exact formulations of the CRP assays are described in more detail in Chapter 6.) This check included comparison of observed accumulations to predicted accumulations, comparison of observed signals to predicted signals, and verification that some of the more unexpected predictions of the power law analysis were true. A number of different formulations were evaluated that varied the composition of the assay, and thus varied the key dimensionless parameters, to verify that the predicted relationships occur.

*5.3.1.1 Accumulation Profiles.* All of the accumulations gathered matched the predictions of the numerical model well, within the variation displayed, with believable values for the parameters of the simulation (Figure 5.10, Figure 4.28 ).

*5.3.3.2 Signals.* The analytical and signals responses matched predictions well when the number of individual accumulation profiles gathered was large enough to result in a good estimate of the true underlying behavior of the accumulation (Figure 5.11).



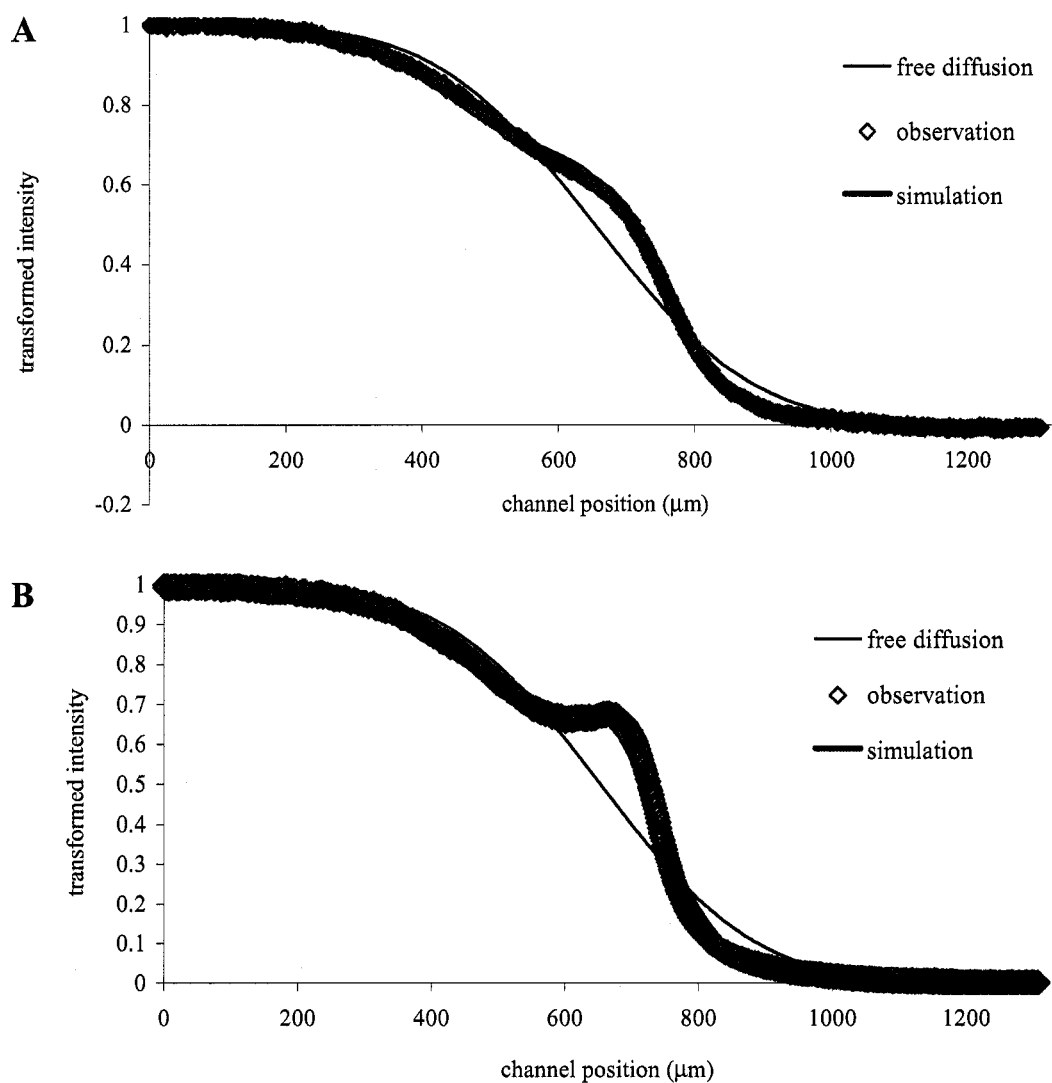


**Figure 5.10:** Observed and simulated accumulation profiles. Symbol sizes for observations have been adjusted to reflect the calculated error bars. A free-diffusion profile is provided for comparison, since it is the non-directional difference between these that comprises the signal. A) Mean accumulation profile for the blank signal of Formulation #1 (Table 6.2,  $n=8$ ). B) Mean accumulation profile for the blank signal of Formulation #2 (Table 6.2,  $n=5$ ). Note that the observations almost completely overlay the simulation.

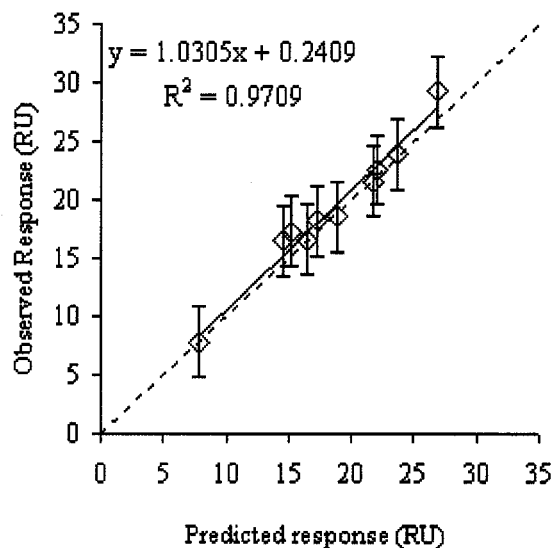


**Figure 5.11:** Comparison of representative mean observed analytical signals to predicted signals for five different CRP DIA formulations. The solid line is a fitted line with the statistics shown on the chart. The dotted line is a plot of  $y=x$ , provided for reference. The error bars represent typical noise observed for the CRP DIA, as discussed in more detail in Chapter 6

**5.3.3.3 Power law verification:** The extensive numerical simulations performed lead to formulation of power laws that had a few surprising implications (Section 5.2.2). The most counterintuitive of these was the conclusion that, at low signals, the initial slope of the dose-response relationship could be made steeper by increasing the concentration of labeled analyte in the Ag\* reagent. This seemed unusual for a competitive assay, and worthy of verification. Some additional simulations were done to identify a set of CRP DIA formulations that would test this relationship, and sufficient testing performed to verify that those formulations were modulated as expected (Figure 5.12).

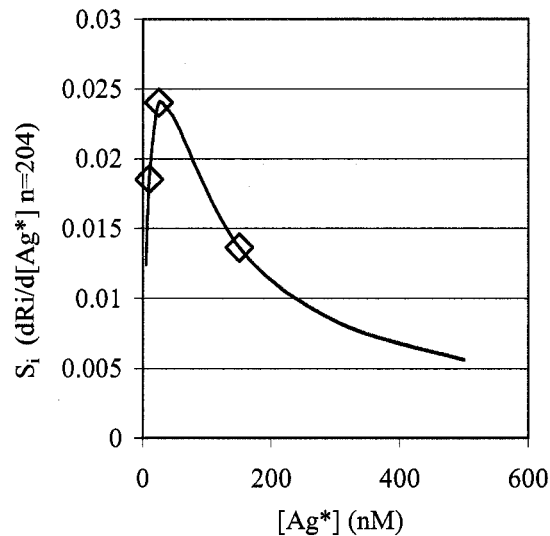


**Figure 5.12:** Validation of the prediction of the power laws that an increase in  $[Ag^*]$  will actually increase the magnitude of the initial slope in the low-signal regime. The solid line is the predicted relationship  $S_i$  versus  $[Ag^*]$  when all other variables are held constant, derived from performing numerical simulations similar to those that created the power law. The observed behavior for three germane formulations is plotted with the symbols ( $\diamond$ ).

### 5.5. Summary of Modeling

Through the application of dimensional analysis and numerical modeling, the range of behavior of the DIA over a wide domain of design parameter space has been characterized. Dimensional analysis has identified a set of dimensionless groupings of dimensional design variables that appear to be sufficient to describe the DIA in general, and which define states of dynamic similitude. Detailed simulations with a two-dimensional finite-difference model, guided by the insight of the dimensional analysis, enabled a comprehensive sampling of the parameter space. From the simulation results, power law relationships for the dimensional variables were formulated for both the blank signal and initial slope of the dose response. The results of the simulations and analysis were verified with experimental observations on a DIA for C-reactive protein.

## Chapter 6: The DIA for C-Reactive Protein

In this chapter, the DIA for C-Reactive Protein (CRP) is described in detail. The assay performance is shown by standard figures of merit to establish clinical acceptability in some POC settings. Estimates of variability described in this chapter are also used to relate the initial slope relationships derived in Chapter 5 to sensitivity and limit-of-detection in Chapter 7. The CRP assay is a second generation DIA. It makes use of several of the improvements discussed in Chapter 4, including: adhesive free, low background PMMA devices (Sections 4.1 and 4.3); BSA amended universal diluent (Section 4.2.2) Whittaker filtering for slope calculations (Section 4.2.1); and the integrated, non-directional, difference algorithm for signal calculation (Section 4.2.3).

### *6.1. Clinical Relevance of CRP*

Assay of a clinically relevant analyte is the ultimate demonstration of a new technique. Although much was learned from the model protein DIA in Chapter 3, the lack of reference methods for the model proteins in human fluids eliminated several important figures of merit from consideration. Thus, a DIA for a third analyte – CRP -- was performed.

CRP is a marker for systemic inflammation that has two distinctly different applications: 1) detection of acute-phase inflammation due to systemic insult, and 2) stratifying risk of cardiovascular disease. Hepatic production of CRP increases, sometimes a thousand fold, after systemic insults; e.g., infection, trauma, and ischemia<sup>178</sup>. Serum levels of CRP begin to rise within four to six hours of the onset of signs of the insult, and peak (generally >100 mg/L) within 24-48 hours. Serum levels return to normal (<10 mg/L) rapidly once the infection is resolved<sup>179</sup>. There is also a growing body of evidence that low-level inflammation is diagnostic of cardiovascular

disease, so CRP is now also considered useful as a tool to stratify risk for this disease<sup>180</sup>. The American Heart Association and the Centers for Disease Control define *low risk* as <1.0 mg/L, *average risk* as 1.0 to 3.0 mg/L, and *high risk* as >3.0 mg/L.<sup>179</sup>

CRP is a member of the pentraxin protein family. It is a cyclic homopentamer of non-covalently bound 23 kD subunits, with phosphocholine and calcium binding activity (Figure 6.1). It is thought to perform as a “surveillance molecule” and early defense mechanism by binding damaged tissue, nuclear antigens, and pathogenic organisms. CRP then activates the complement system and stimulates production of proinflammatory cytokines.

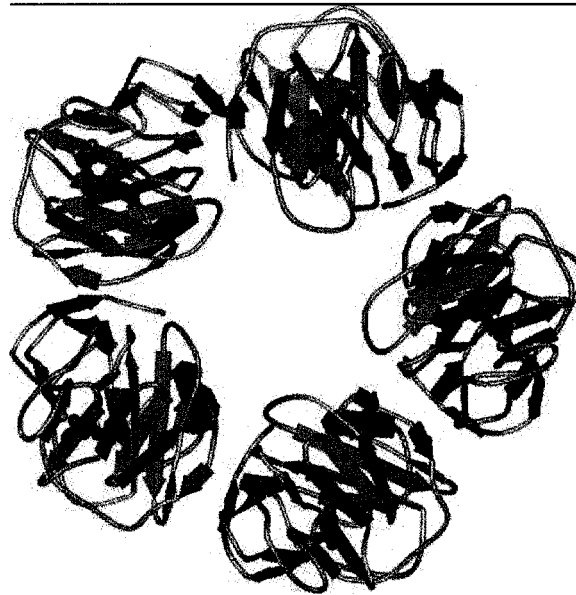


**Figure 6.1:** A diagram of the crystal structure of C-reactive protein complexed with phosphocholine. ViewerPro 4.2 software (Accelrys, San Diego, CA) was used to generate the ribbon diagram of the x-ray crystal structure of CRP-phosphocholine complex obtained from Brookhaven Protein Data Bank (PDB entry 1B09). The calcium ions are yellow, and phosphocholine is green. Reproduced with permission from Black et al<sup>181</sup>.

There are a number of available reference methods to which the CRP DIA could be benchmarked (Table 6.1). They include a qualitative point-of-care method, several quantitative methods (both POC and reference lab), and methods specifically

formulated for “high-sensitivity” (that is, methods with low limits of detection suitable for cardiac risk stratification). In general, the high-sensitivity methods have reduced dynamic ranges to accompany the increase in sensitivity, thus necessitating sample dilution if a quantitative result is desired. While quantitation increases diagnostic power, there is a demand for a qualitative POC assay as an initial screen by care providers. One could also visualize a potential at-home application as an indicator that a doctor visit is required. This POC test could be a “standard” CRP assay, to be used on or by patients experiencing symptoms of an infection or ischemia; or a high-sensitivity CRP assay to screen for potential cardiac risk.

**Table 6.1.** Examples of reference methods for CRP

Manufacturer	Intended Use	Assay Time (min.)	LOD (mg/L)	Upper Limit (mg/L)	Precision (%CV)
ABX Diagnostics	POC	<5	2	100	<10
Reference Diagnostics	reference lab	~15	0.5	10	<3
Murex Diagnostics	POC	10	10	qualitative	qualitative
Beckman	reference lab	?	0.2	80	?
Behring	reference lab	?	1	55	?

### ***6.2. Performing the CRP DIA***

Several assay formulations were investigated to assess the validity of the modeling and associated analysis (Section 5.3.1, Section 4.3.3). Except where otherwise noted (Table 6.2) all formulations shared the characteristics outlined in this section.

### 6.2.1. Reagents:

Phosphate buffered saline, pH 7.0 (Sigma Chemicals St. Louis, MO, USA) amended with 1-mg/mL bovine serum albumin (*BSA*, part # A7030: Sigma, St. Louis, MO) was used as a universal diluent for all solutions.

Affinity-purified monoclonal anti-CRP (part #10540A: TriChem, West Chester, PA, USA) or the same antibody conjugated to a 670 kD dextran molecule (Solulink Inc., San Diego, CA, USA) was diluted to the indicated concentration for the formulation. Purified human CRP (part #10542A: TriChem, West Chester, PA, USA) was labeled with AlexaFluor 488 (*AF488*, Invitrogen/Molecular Probes, Eugene, OR, USA), and this stock was diluted to the indicated concentration for the formulation. Analysis of free-diffusion of the CRP-AF488 suggests that it has dissociated into constituent subunits, probably because of the labeling. A few simulations indicate that the effect of differing diffusivities for the labeled and unlabeled CRP will be barely noticeable, as long as the correct diffusion profiles for the CRP-AF488 are used in processing (data not shown). Streptavidin labeled with AlexaFluor 594 (*SA-AF594*, Invitrogen/Molecular Probes, Eugene, OR, USA) was spiked into the labeled Ag\* reagent to a 25 nM final concentration as the internal diffusion standard required of midline correction (see Section 4.2.3.3). The antibody and antigen were purchased from this vendor because they were able to supply the antigen identical to that which the antibody was raised against. Thus, specificity and high affinity seemed assured.

**Table 6.2:** The different CRP formulations investigated

Formulation #	Differentiating Features
1	[Ag*] = 150 nM, [Ab] = 75 nM
2	[Ag*] = 1000 nM, [Ab] = 550 nM
3	[Ag*] = 25 nM, [Ab] = 12.5 nM
4	[Ag*] = 10 nM, [Ab] = 5 nM
5	[Ag*] = 150 nM, [Ab]-Dextran = 75 nM Ab

Test solutions for model validation and formulation assessment were prepared by spiking purified, unlabeled, human CRP (part #10542A: TriChem, West Chester, PA, USA) into the AF488-CRP stock solution to the indicated unlabeled-CRP concentration. The unlabeled-CRP stock was sufficiently concentrated that the dilution of AF488-CRP introduced by this preparation was negligible (<1%). Mock samples for the method comparison were prepared by spiking unlabeled-CRP stock into CRP-depleted human serum (Research Diagnostics Inc., Concord, MA, USA). After preparation these samples were divided into three identical aliquots and frozen. One aliquot was given to Research Testing Services at the University of Washington Hospital for quantification by nephelometry (Behring assay).

Formulation #1 (Table 6.2) was chosen as the “best formulation” CRP DIA to be evaluated by clinical figures of merit. This formulation did not have the  $S_i$  with the largest magnitude, and therefore did not have the lowest calculated limit of detection (LOD); however, the formulation that did (#2) has such a low blank signal, that the dynamic range was extremely small – the response at the LOD represented almost the entire modulated response, so quantitation would have been impossible (data not shown). Modeling predicted that a longer interaction time may have resulted in some improvements in both  $R_i$  and  $S_i$  for this formulation, especially given that the on-rate was higher than originally expected; however, the improvement was deemed not worth the costs in analysis time and equipment modification required. This formulation actually provides an excellent example of a marginally acceptable DIA on which to build projections on the limits to the technique (Section 7.2.1).

### **6.2.2. Apparatus**

The T-sensor used was a three-layer device made by solvent assisted thermal lamination of optically transparent poly-methyl methacrylate (*PMMA*: Rohaglas



formulation #99524, Cyro Industries, Orange, NJ, USA). The main channel was cut into the center layer with a CO<sub>2</sub> laser (Universal Laser Systems Inc., Scottsdale, AZ) to yield a straight channel with final cross-sectional dimensions of 140- $\mu$ m x 1320- $\mu$ m. Holes cut in an outer layer created access for the fluid vias. Accumulation images were gathered 40-mm from the confluence of the inlet streams. The finished device was mounted in a custom manifold to facilitate the leak-free connection of pump tubing.

The T-sensor device was mounted on the stage of a Zeiss ICM-405 inverted, epifluorescence microscope (Carl Zeiss Inc., Thornwood, NY) and imaged through a 10x objective. Excitation light came from a Zeiss HB 100W mercury arc source (Carl Zeiss Inc., Thornwood, NY). Two filter sets conditioned the light specific to the spectrally distinct labels in the CRP-AF488/SA-AF594 reagent: 1) excitation bandpass: 480/30 nm; dichroic beamsplitter: 505nm; emission bandpass: 535/40 nm (part# 31001, Chroma Technologies, Brattleboro, VT, USA) and, 2) excitation bandpass: 560/40 nm; dichroic beamsplitter: 595nm; emission bandpass: 630/60 nm (part# 31004, Chroma Technologies, Brattleboro, VT, USA). A Retiga 1300 (Q-Imaging, Burnaby, BC, Canada) cooled, 12-bit CCD camera was used for detection.

Two programmable, stepper-motor syringe pumps, both installed with 25  $\mu$ L syringes, provided pressure-driven flow at 42 nL/s(model # 50300: Kloehn, Las Vegas, NV). Pump control was accomplished with Windows Terminal Version 3.10.0.61 (Microsoft Inc., Redmond, WA).

### **6.2.3. Procedure**

Test solutions were introduced into the inlets of the T-sensor (after thorough priming) through a tee-valve and length of tubing by hand-injection with a sterile, disposable syringe. The tee-valve was then switched to be in-line with the pumps, and the solution in the lines was pumped into the device at a controlled rate. After a sufficient

time for wash-through of the frontal zone (~10 min for the current set-up) (diluted by Taylor dispersion) the steady state at the interrogation location was reached (interaction time,  $\tau=169$  seconds), and replicate images (5s integration time for each) were collected. Ten images were gathered, with a change of filter set (accomplished by sliding the filter cube back and forth) at every image. Thus, five replicates for each of the two spectral “cases” were temporally interleaved.

Geminal DIA sampling and signal processing algorithms were used (Section 2.2.1), except for the improvements noted at the outset of this chapter; i.e., Whitaker filtering of SA-AF594 free-diffusion curves prior to slope and midpoint calculations, and use of the integrated non-directional difference algorithm (Section 4.2.3.3).

Mock samples were assayed after a 1:1 dilution of the sample with a doubly-concentrated (2X) version of the appropriate CRP-AF488/SA-AF594 reagent. This sample/reagent mixture was then introduced into the T-sensor as normal. After all processing, the result was corrected by the dilution factor.

### **6.2.3. Results**

The results of the testing and analysis done to validate the modeling and assess the effect of conjugation of the capture antibody to a large dextran are documented in other, more appropriate sections of this document (Sections 4.3.3 and 5.3.1). In this section, the DIA for CRP is evaluated by criteria generally applied to mature clinical assays to assess the probability that development of the DIA into such a mature application is possible. Note, however, that the CRP DIA documented here is not a market-ready product – significant evolution and optimization to the formulation, instruments, and microfluidic cards would undoubtedly improve these results significantly should these efforts be undertaken. Such activities are beyond the scope of this dissertation.

**6.2.3.1: Signal Variation.** The variability in the calculated signals was almost entirely independent of signal magnitude for this formulation, from the maximum (blank signal) to minimum (free-diffusion) cases – the observed standard deviations range from  $\sim 1.5$  to 2 response units (*RU*). A pooled standard deviation of 1.7 *RU* was used for all calculations where this statistic is required. (Note that, given the 781-pixel sample size for this analysis, these units do not correspond exactly to the *RU* resulting from the 204-node simulations. See Section 5.2 for further discussion.) Examination of typical BFTN processed accumulation profiles for this formulation indicates that the high-spatial-frequency (HF) noise from the camera is  $\sim 2\%$  (Figure 6.2).

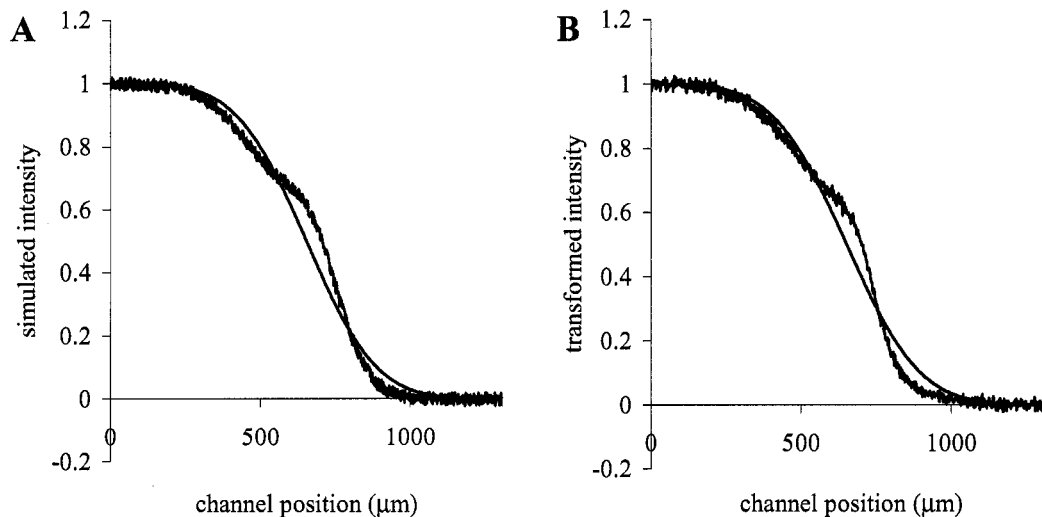


**Figure 6.2:** A comparison of a simulated blank accumulation for CRP DIA, with 2% added noise (A), to a representative observed blank accumulation (B). The simulation was done using the procedure described in Section 5.3.1.

Using this result, and the slope of a signal-versus-midline plot similar to the ones shown in Section 5.3.2, indicates that the variation in the CRP DIA observed can be accounted for by assuming that there is still sufficient variation in the position of the midline to produce a standard deviation of  $\sim 8$  pixels. This is similar to the observed variation for the midline position of the internal standards, so it is not unreasonable to assume that the midline correction algorithm is still not removing all of the midline variation.

This result also implies that underlying transport and reaction processes are very repeatable in this context (as expected, given the simple fluidics and low Re). The BFTN processing seems to correct for most experimental variation and correctly normalize each accumulation profile so that the resulting profile is, in essence, as predicted with an overlay the HF noise and some displacement in the channel position axis (due to variation in the midline). We hypothesize that the dominant source of variation in the DIA is the residual variation in the midline, and that further improvements of the midline correction algorithm will be the most productive method to improve the precision of the CRP DIA.

*6.2.3.1: LOD, Sensitivity, Dynamic Range, Assay Precision.* These important figures of merit are all related through the dose-response curve and the observed noise, as defined by IUPAC<sup>141</sup>.

The initial slope for this assay formulation is 2.54 RU/ (mgL<sup>-1</sup> Ag). Given the measured standard deviation ( $s$ ) of 1.7 RU discussed in the last section, and applying:

$$28) \quad LOD = 3s_{R_i} S = \frac{3s_{R_i}}{S_i}$$

where  $S = 1/S_i$  is the sensitivity as defined by IUPAC.  $S_i$  and  $R_i$  have the same meanings as defined previously (Section 5.1.2). The result: **LOD = 2.0 mg/L**.

Using the logic discussed in Section 4.2.2.3, the value of 3s can be considered to be the lowest signal distinguishable from the infinite dose (vanishing signal). For this formulation that signal (5 RU) corresponds to ~ 25 mg/L. Therefore, the standard curve shown Figure 6.3A, is the 4PLL NLLS fit to dose-response relationship  $\leq 25$  mg/mL.

Sensitivity is defined over the entire dynamic range as  $d[Ag]/dR^{141}$ . Since the standard curve is not linear, the first derivative can be derived from the standard curve, and inverted to plot sensitivity over the range (Figure 6.3B).

Relative precision (the standard deviation expressed as a percentage of the analyte concentration) is usually expressed at a few discrete analyte concentrations, however, since the standard deviation does not appear to be a function of the [Ag] for this assay, the pooled standard deviation can be applied to the sensitivity curve to display precision as a function of response (Figure 6.3.C).

The precision observed is not as good as generally expected for a quantitative assay (CV <10% in usable dynamic range). Thus, this assay may be most useful as a qualitative or “semi-quantitative” assay.

*6.2.3.1: Method Comparison.* The mock samples were compared to the Behring nephelometry assay to assess the ability of the assay to quantitate within its absolute dynamic range (Figure 6.3D). Although there is a lot of scatter due to the relatively poor precision of the assay and the single replicate determinations, the underlying trend compares reasonably well to the reference.

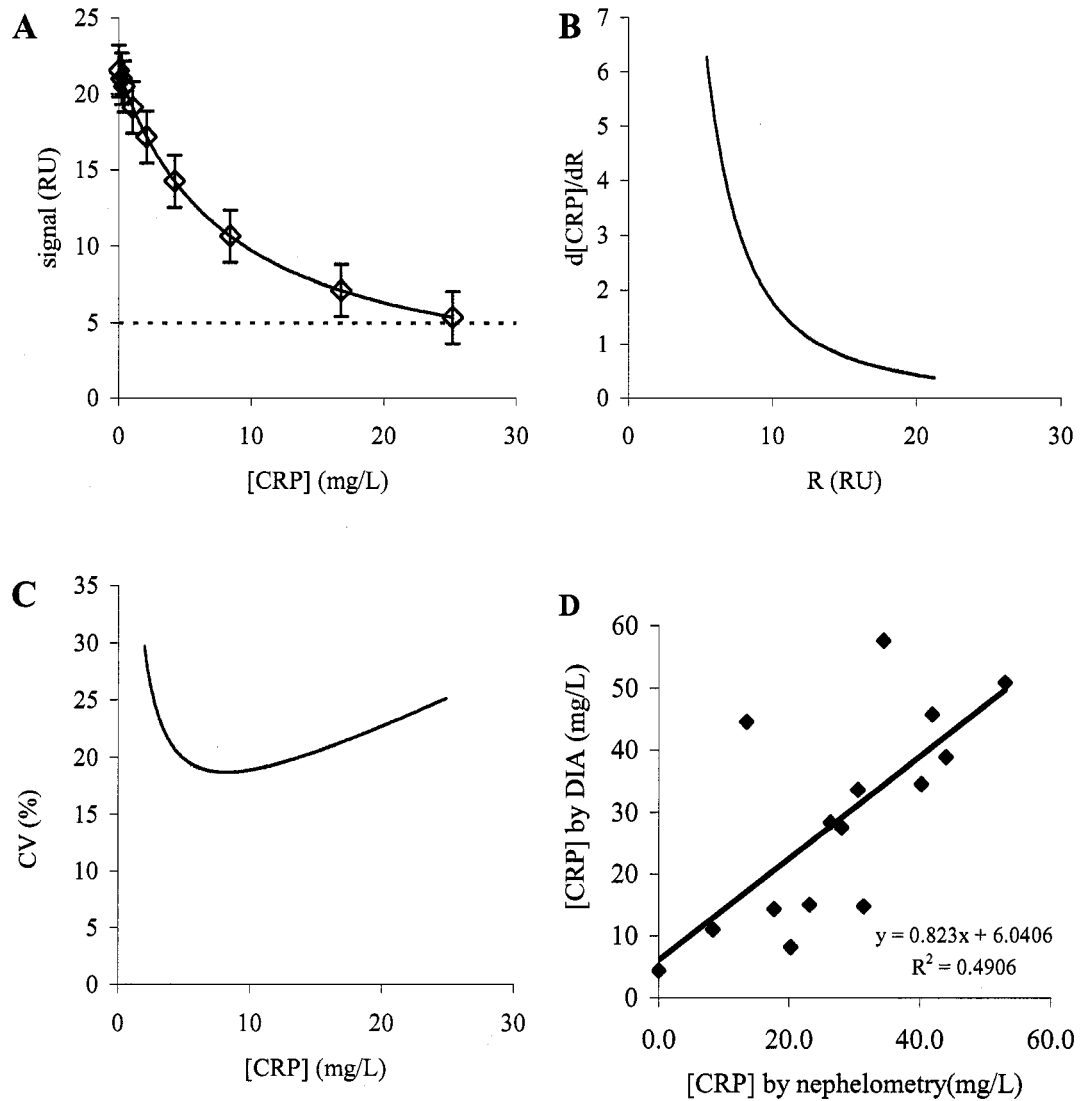


**Figure 6.3:** CRP figures of merit. A) The standard curve for the CRP DIA. Error bars correspond to the pooled standard deviation of all the responses observed. The red dotted line denoted the signal associated with the upper limit of the dynamic range as defined in the text. B) A plot of the sensitivity for the CRP DIA over the defined dynamic range. Note that the actual slope is negative. The absolute value is plotted here so that larger values for  $S$  correspond to the poorer sensitivity. C) The relative precision over the defined dynamic range. D) The comparison of quantitation by the CRP DIA to a reference (Behring nephelometry) method.

### **6.3. Summary**

The DIA for CRP displays performance that places it in proximity to existing CRP assays. It has a lower limit of detection than the qualitative POC assay from Murex, the potential for being faster, and (at least) semi-quantitative. The LOD is similar to the POC assay from ABX, but with a smaller dynamic range. Its performance is inferior to the reference lab assays, but was achieved without the aid of expensive fluid handling robotics and sophisticated control systems. The LOD displayed by the DIA is not quite low enough to make it attractive for the cardiac application, but it is not that far away. Considering the infant and protean nature of the DIA, even in the second generation, it seems that the inevitable improvements will eventually make this a competitive and attractive option for testing CRP.

## Chapter 7: Limits, Design Rules and Closure

In this concluding chapter, the validated modeling results and the noise estimates are used to determine what part of the design parameter domain will return DIA results in the functional range. A set of design rules is also outlined that can be used to guide the novice DIA designer toward a successful result with a minimum of “wandering” in the design parameter domain.

### *7.1. Defining the Molecular Weight Limits*

By applying the results of the numerical modeling and noise estimation, and making a number of assumptions about other parameters, the limits on the molecular weight of analyte that can be successfully assayed by the DIA can be deduced.

#### **7.2.1. Assumptions**

These projections assume:

- 1) The analyte diffuses by the Stokes-Einstein relationship; i.e., as a hard sphere. This is known to be a poor assumption for many proteins<sup>182</sup>, but for the “rule of thumb” projections desired, it is sufficient. The rigorous DIA designer will measure the diffusion profile of as many of the molecules as possible in the T-sensor before attempting precise and quantitative modeling.
- 2) The noise observed for the CRP assay is representative of typical analytes. This seems to be a reasonable assumption, as discussed in Section 6.2.3., as long as similar equipment is used.
- 3) Typical antibodies with a reasonably high affinity are used for the capture species.



- 4) An interaction time limit of 15 minutes. Longer times may enable DIA for larger molecules, but there are already well-developed techniques that can perform highly sensitive immunoassay given times longer than this. Also, longer interaction times will necessitate the use of wider channels to maintain the T-number at  $\geq 5$ , which are more difficult to wet out and prime.
- 5) Acceptance criteria similar to the CRP DIA. The definition of “what works” is dependant on how “works” is defined.

### 7.2.2. Projections

We can conclude from the results of the CRP DIA that a protein of  $\sim 20$  kD is essentially *at the limit* of the DIA with the given timing and equipment, making it a useful starting point for a projection. It also appears that we can treat this formulation as being in the transitional signal regime making application of the scaling laws formulated in Chapter 5 difficult. Instead, we can refer to the log-log plots on which the scaling laws are based to make a projection. If the interaction time is extended from the  $\sim 3$  minutes of the CRP DIA to the full 15 minutes,  $Pi_1(\tau k_{on}[Ag^*])$  changes from 20 to 100. On Figure 5.2 both the log-log plots have a slope of  $\sim 0.3$  in this region ( $\ln(20)=3$ , and  $\ln(100)=4.6$ ) so we assume an exponent of 0.3 in the scaling relationships for  $Pi_1$ . For the same gain in interaction time,  $Pi_5(\tau k_{off})$  changes from 0.14 to 0.72. On Figure 5.2 both the log-log plots have a slope of  $\sim -0.2$  in this region ( $\ln(0.14)=-2$ , and  $\ln(0.17)=-0.3$ ) so we assume an exponent of -0.2 in the scaling relationships for  $Pi_5$ . Thus, the net effect of increasing the interaction time on both  $R_i$  and  $S_i$  will scale by a power of 0.1 in this region of parameter space. For the CRP DIA,  $Pi_2(D_{Ag^*}/D_{Ag}) = 2.3$ , so the dependence of  $R_i$  and  $S_i$  on  $Pi_2$  is proportional, indicated in Figure 5.3 by the slope at  $\ln(2.3) = 0.8$ . Thus by increasing  $\tau$  by a factor of 5, we should be able to tolerate a decrease in  $Pi_2$  by a factor of  $5^{0.1} \approx 1.18$ , or to about  $Pi_2=1.98$ , and still get equivalent performance to the CRP DIA. The other

dimensionless parameters were not changed, as there is no net gain in overall performance to do so.

**For a DIA with an unmodified antibody, this projects to a molecular weight limit of ~33 kD.** To perform this assay a channel 2780- $\mu\text{m}$  wide would be required. If the same thickness film was used for the channel layer of the laminate, each pump would have to pump at 8.3  $\text{nLs}^{-1}$  flow rate. A simulation with these parameters yielded  $R_i = 20\text{RU}$  and  $S_i = 0.55 \text{RU/nM}$ , both very comparable to these parameters for the CRP DIA ( $R_i = 21\text{RU}$ ,  $S_i = 0.52 \text{RU/nM}$ ). This analysis clearly illustrates the use and utility of the log-log plots and scaling relationships.

The scaling relationships also indicate that decreasing the diffusivity of the capture species could enable a DIA for larger analytes; although, doing so frequently creates other, negative corollary effects (see Section 4.3). Assuming that these problems can be solved so that the other dimensionless groups are not affected by the decrease in  $D_{Ab}$  (at this juncture, an unproven hypothesis), the ratio of 1.98 can be applied to the  $D_{Ab}$ . **For a DIA with an antibody conjugated to 670 kD dextran, this projects to a molecular weight limit of ~148 kD.** Conjugating the antibody to an even larger particle will increase the size of a possible analyte correspondingly – if the problems can be solved.

If different performance to that seen with the CRP DIA is desired, these limits could change somewhat. For example, an analyte that does not require a low LOD could be made with a similar dynamic range and tolerate a lower value of  $Pi_2$ . Each analytical context can be re-evaluated using the scaling relationships derived in this dissertation. Nevertheless, the most dramatic extension of the analyte size range will be enabled by a reduction in signal variation.

## 7.2. Design Rules

The lessons learned in this research have been summarized in a set of design rules that can guide the optimization of a new design. These are formulated as a series of steps to be followed sequentially, with some iterative loops. They do not require access to the numerical models used in this research, only access to the analysis summarized in Chapter 5.

- Step 1: Obtain the highest affinity antibody available for your analyte and determine or estimate the reaction constants. (Iterative fitting of the numerical model the DIA may be the best method available for determining a rate constant, but equilibrium constants can be measured independently and are frequently provided by the vendor.)
- Step 2: Obtain a labeled version of the analyte and a similarly diffusive non-reactive internal diffusion standard, each labeled with spectrally distinct fluorophores. Estimate their diffusion coefficients using the Stokes-Einstein relationship, or by projecting from appropriate published values.<sup>182</sup>
- Step 3: Determine the design specifications, especially the target LOD, precision and dynamic range.
- Step 4: Choose a detector design and settings that result in the maximum number of discrete samples and a minimum of high-spatial-frequency noise in the sampled profiles. For a microscope/camera system this corresponds to the largest objective that images the entire width of the channel, a camera with as many pixels in the diffusion direction as possible, and the camera integration time that uses the full bit-depth of the camera (while avoiding saturation).
- Step 5: Using the scaling laws derived in Chapter 5 and the best available information for invariable parameters ( $D$ ,  $k$ , *etc.*), calculate the values for all dimensionless groupings, choosing values for the manipulated variables that result in  $R_i$  and  $S_i$  in concordance with your design specifications. For the first iteration, set  $Pi_3 =$

1,  $Pi_5 < 0.3$ ,  $T=5$ ,  $Kz < 5$ , and assume a standard deviation of  $0.0026N_p$  ( $N_p$  = the number of pixels that will be sampled for the profile).

Step 6: Fabricate a T-sensor of the appropriate dimensions to enable a DIA with these characteristics.

Step 7: Determine the diffusion coefficients of the labeled material in this T-sensor using the method of Kamholz.<sup>25-28</sup> Perform sufficient replicates that a good estimate of variation is obtained.

Step 8: Perform accumulations as needed to evaluate a formulation.

Repeat steps 4-8 as needed, improving the design each time, until a judgment about the feasibility of the DIA for the analyte is obtained. If required, consider decreasing the diffusivity of the analyte by one of the biochemical means in Section 4.3.

### **7.3. Closure**

The completion of this research significantly advances our understanding of how properties of the analyte interact with manipulated design variables and expected sources of variation to produce the final performance of the DIA. Shortcomings in the germinal DIA procedures have been identified, and improved upon in a second generation. This second generation DIA has been subjected to extensive analysis to create scaling laws that describe the relationship between two of the most important contributors to final assay performance – the signal of the blank, and the initial slope of the dose-response curve – and the analyte properties and design variables that produce them. Two sources of variation expected to be the dominant contributors to the variation observed – high spatial-frequency noise and midline variation – have been investigated through simulations. A second generation DIA for C-reactive protein has been characterized, both as an experimental validation of modeling predictions, and for its clinical significance. Finally, size limitations of the analyte were proposed and some design rules were formulated.

This work should prove to be a solid foundation for future investigations into the DIA. Several directions are immediately obvious: 1) Efficacy of biochemical modification to decrease the diffusivity of capture species as a strategy for improving assay performance is still an unresolved question. The modeling clearly indicates how beneficial this strategy should be, yet three attempts at achieving these benefits in a working DIA have been foiled by lurking variables. 2) Methods to decrease the variation in the analytical signal measurement/calculation are of paramount importance. Different equipment that enables the closer temporal association of the images of accumulations and internal standard diffusion profiles seems like a fruitful avenue of research. It seems that the time may have come to build a second generation DIA platform to go with the second generation assay. 3) It could be very illuminating to expand the numerical modeling into those parts of the parameter domain not yet explored, especially by investigating additional dimensions that are physically possible, but were eliminated by the assumptions of this work. For example, investigations into unequal diffusivity and reaction constants for the labeled and unlabeled analyte would be germane to many cases.

There appears to be several other potential dissertations suggested by this last paragraph alone. This will be the work of other investigators, grants, or laboratories.

## REFERENCES

- (1) Hatch, A.; Kamholz, A. E.; Hawkins, K. R.; Munson, M. S.; Schilling, E. A.; Weigl, B. H.; Yager, P. *Nature Biotechnology* **2001**, *19*, 461-465.
- (2) Weigl, B. H.; Yager, P.; Kamholz, A. E.; Hatch, A.; University of Washington: USA, 2002.
- (3) Christian, G. D. *Analytical Chemistry*, 6th ed ed.; Wiley,: Hoboken, NJ :, 2004.
- (4) Strobel, H. A.; Heineman, W. R. *Chemical instrumentation : a systematic approach*, 3rd ed ed.; Wiley,: New York :, 1989.
- (5) Hatch, A. Doctoral Thesis, University of Washington, Seattle, 2004.
- (6) Mathews, J. H., 1943- *Numerical methods using MATLAB.*, 3rd ed. / John H. Mathews, Kurtis D. Fink. ed.; Prentice Hall,: Upper Saddle River, N.J. :, 1999.
- (7) Maciel, R. J. *Journal of Clinical Immunoassay* **1985**, *8*, 98-106.
- (8) Harris, D. C. *Journal of Chemical Education* **1998**, *75*, 119-121.
- (9) Fylstra, D.; Lasdon, L.; Watson, J.; Waren, A. *Interfaces* **1998**, *28*, 29-55.
- (10) Kuehl, R. O. *Design of experiments : statistical principles of research design and analysis / Robert O. Kuehl*, 2nd ed ed.; Duxbury/Thomson Learning,: Pacific Grove, CA :, 2000.
- (11) Cook, R.; Wellington, D.; Syva Company: Palo Alto, CA, 1980, pp 23.
- (12) Weigl, B. H.; Yager, P. *Science* **1999**, *283*, 346-347.
- (13) Hatch, A.; Garcia, E.; Yager, P. *Proceedings of the IEEE* **2004**, *92*, 126-139.
- (14) Fu, E.; Foley, J.; Yager, P. *Review of Scientific Instruments* **2003**, *74*, 3182-3184.

- (15) Fu, E.; Chinowsky, T.; Foley, J.; Weinstein, J.; Yager, P. *Review of Scientific Instruments* **2004**, *75*, 2300-2304.
- (16) Nelson, K.; Foley, J.; Mashadi-Hosseini, A.; Yager, P., Boston, Massachusetts, USA 2005.
- (17) Nelson, K.; Foley, J.; Mashadi-Hosseini, A.; Yager, P. *Lab on a Chip*, manuscript in preparation.
- (18) Levicky, R.; Horgan, A. *Trends in Biotechnology* **2005**, *23*, 143-149.
- (19) Bancaud, A.; Wagner, G.; Dorfman, K. D.; Viovy, J. L. *Analytical Chemistry* **2005**, *77*, 833-839.
- (20) Darling, R. B.; Yager, P.; Weigl, B.; Kriebel, J.; Mayes, K., Banff, Canada 1998; Kluwer, Dordrecht, Netherlands.
- (21) Costin, C. D.; Olund, R. K.; Staggemeier, B. A.; Torgerson, A. K.; Synovec, R. E. *Journal of Chromatography A* **2003**, *1013*, 77-91.
- (22) Costin, C. D.; McBrady, A. D.; McDonnell, M. E.; Synovec, R. E. *Analytical Chemistry* **2004**, *76*, 2725-2733.
- (23) Chang, H. N. Masters Thesis, University of Washington, Seattle, 2005.
- (24) Wilcox, D. C., 2nd ed.; D. C. W. Industries: La Cañada, CA, 2000.
- (25) Kamholz, A. E.; Weigl, B. H.; Finlayson, B. A.; Yager, P. *Analytical Chemistry* **1999**, *71*, 5340-5347.
- (26) Kamholz, A. E.; Yager, P. *Biophysical Journal* **2001**, *80*, 155-160.
- (27) Kamholz, A. E.; Schilling, E. A.; Yager, P. *Biophysical Journal* **2001**, *80*, 1967-1972.
- (28) Kamholz, A. E.; Yager, P. *Sensors and Actuators B-Chemical* **2002**, *82*, 117-121.

- (29) Ismagilov, R. F.; Stroock, A. D.; Kenis, P. J. A.; Whitesides, G.; Stone, H. A. *Applied Physics Letters* **2000**, *76*, 2376-2378.
- (30) Beard, D. A. *Journal of Applied Physics* **2001**, *89*, 4667-4669.
- (31) Taylor, G. *Proceedings of the Royal Society of London. Series A, Mathematical and Physical Sciences* **1954**, *225*, 473-477.
- (32) Phillips, C. G.; Kaye, S. R. *Proceedings: Mathematical, Physical and Engineering Sciences* **1997**, *453*, 2669-2688.
- (33) Taylor, G. *Proceedings of the Royal Society of London. Series A, Mathematical and Physical Sciences* **1953**, *219*, 186-203.
- (34) Crank, J. *The mathematics of diffusion*, 2d ed ed.; Clarendon Press,: Oxford, [Eng] :, 1975.
- (35) Bird, R. B.; Stewart, W. E.; Lightfoot, E. N. *Transport Phenomena*, 1 ed.; John Wiley and Sons: New York, 1960.
- (36) Crowther, J. R. *The ELISA guidebook*; Humana Press,: Totowa, NJ :, 2000.
- (37) *Immunoassay / edited by Eleftherios P. Diamandis, Theodore K. Christopoulos*; Academic Press,: San Diego :, 1996.
- (38) Vanhercke, T.; Ampe, C.; Tirry, L.; Denolf, P. *Journal of Biomolecular Screening* **2005**, *10*, 108-117.
- (39) Nikolic-Vukosavljevic, D.; Todorovic-Rakovic, N.; Demajo, M.; Ivanovic, V.; Neskovic, B.; Markicevic, M.; Neskovic-Konstantinovic, Z. *Clinical & Experimental Metastasis* **2004**, *21*, 581-585.
- (40) <http://biomedtech.com>.
- (41) <http://www.bmg-labtechnologies.com>.
- (42) <http://www.celprogen.com>.
- (43) <http://www.dialab.at>.



- (44) Hill, A. S.; Skerritt, J. H.; Bushway, R. J.; Pask, W.; Larkin, K. A.; Thomas, M.; Korth, W.; Bowmer, K. *Journal of Agricultural and Food Chemistry* **1994**, *42*, 2051-2058.
- (45) <http://www.ssirobotics.com>.
- (46) Ma, H. C.; Horiuchi, K. Y.; Wang, Y.; Kucharewicz, S. A.; Diamond, S. L. *Assay and Drug Development Technologies* **2005**, *3*, 177-187.
- (47) MacBeath, G.; Schreiber, S. L. *Science* **2000**, *289*, 1760-1763.
- (48) Lueking, A.; Cahill, D. J.; Mullner, S. *Drug Discovery Today* **2005**, *10*, 789-794.
- (49) Jahn-Schmid, B.; Harwanegg, C.; Hiller, R.; Bohle, B.; Ebner, C.; Scheiner, O.; Mueller, M. W. *Clinical and Experimental Allergy* **2003**, *33*, 1443-1449.
- (50) Kersten, B.; Feilner, T.; Kramer, A.; Wehrmeyer, S.; Possling, A.; Witt, I.; Zanol, M. I.; Stracke, R.; Lueking, A.; Kreutzberger, J.; Lehrach, H.; Cahill, D. J. *Plant Molecular Biology* **2003**, *52*, 999-1010.
- (51) Song, X.; Cao, Y. *Progress in Biochemistry and Biophysics* **2001**, *28*, 819-821.
- (52) Holt, L. J.; Enever, C.; de Wildt, R. M. T.; Tomlinson, I. M. *Current Opinion in Biotechnology* **2000**, *11*, 445-449.
- (53) Arenkov, P.; Kukhtin, A.; Gemmell, A.; Voloshchuk, S.; Chupeeva, V.; Mirzabekov, A. *Analytical Biochemistry* **2000**, *278*, 123-131.
- (54) <http://www.affymetrix.com>.
- (55) Tomizaki, K. Y.; Usui, K.; Mihara, H. *Chembiochem* **2005**, *6*, 783-799.
- (56) Gayton-Ely, M.; Pappas, T.; Holland, L. *Analytical and Bioanalytical Chemistry* **2005**, *382*, 570-580.
- (57) Natishan, T. K. *Journal of Liquid Chromatography & Related Technologies* **2005**, *28*, 1115-1160.

- (58) Harrison, D. J.; Fluri, K.; Seiler, K.; Fan, Z. H.; Effenhauser, C. S.; Manz, A. *Science* **1993**, *261*, 895-897.
- (59) Fiorini, G. S.; Chiu, D. T. *Biotechniques* **2005**, *38*, 429-446.
- (60) Ghosal, S. *Electrophoresis* **2004**, *25*, 214-228.
- (61) Bange, A.; Halsall, H. B.; Heineman, W. R. *Biosensors & Bioelectronics* **2005**, *20*, 2488-2503.
- (62) Yin, X. B.; Wang, E. *Analytica Chimica Acta* **2005**, *533*, 113-120.
- (63) Simpson, D. C.; Smith, R. D. *Electrophoresis* **2005**, *26*, 1291-1305.
- (64) Michalke, B. *Electrophoresis* **2005**, *26*, 1584-1597.
- (65) Craig, D. B.; Wong, J. C. Y.; Dovichi, N. J. *Analytical Chemistry* **1996**, *68*, 697-700.
- (66) Horvath, J.; Dolnik, V. *Electrophoresis* **2001**, *22*, 644-655.
- (67) Rodriguez, I.; Li, S. F. Y. *Analytica Chimica Acta* **1999**, *383*, 1-26.
- (68) Kamande, M. W.; Fletcher, K. A.; Lowry, M.; Warner, I. M. *Journal of Separation Science* **2005**, *28*, 710-718.
- (69) Ruzicka, J.; Hansen, E. H. *Analytica Chimica Acta* **1980**, *114*, 19-44.
- (70) Ruzicka, J.; Hansen, E. H. *Analytica Chimica Acta* **1979**, *106*, 207-224.
- (71) Ruzicka, J.; Hansen, E. H. *Analytica Chimica Acta* **1975**, *78*, 145-157.
- (72) Kolev, S. D.; Pungor, E. *Analytical Chemistry* **1988**, *60*, 1700-1709.
- (73) Pollema, C. H.; Ruzicka, J. *Analytical Chemistry* **1994**, *66*, 1825-1831.
- (74) Ruzicka, J.; Pollema, C. H.; Scudder, K. M. *Analytical Chemistry* **1993**, *65*, 3566-3570.

- (75) Scudder, K. M.; Pollema, C. H.; Ruzicka, J. *Analytical Chemistry* **1992**, *64*, 2657-2660.
- (76) Wang, J. H. *Analytical and Bioanalytical Chemistry* **2005**, *381*, 809-811.
- (77) Economou, E. N. *Physical Review* **1969**, *182*, 539-&.
- (78) Gauglitz, G. *Analytical and Bioanalytical Chemistry* **2005**, *381*, 141-155.
- (79) Haes, A. J.; Van Duyne, R. P. *Analytical and Bioanalytical Chemistry* **2004**, *379*, 920-930.
- (80) Lofas, S.; Malmqvist, M.; Ronnberg, I.; Stenberg, E.; Liedberg, B.; Lundstrom, I. *Sensors and Actuators B-Chemical* **1991**, *5*, 79-84.
- (81) Haes, A. J.; Van Duyne, R. P. *Expert Review of Molecular Diagnostics* **2004**, *4*, 527-537.
- (82) Piliarik, M.; Vaisocherova, H.; Homola, J. *Biosensors & Bioelectronics* **2005**, *20*, 2104-2110.
- (83) Yuk, J. S.; Ha, K. S. *Experimental and Molecular Medicine* **2005**, *37*, 1-10.
- (84) Lyon, L. A.; Musick, M. D.; Natan, M. J. *Analytical Chemistry* **1998**, *70*, 5177-5183.
- (85) Lyon, L. A.; Pena, D. J.; Natan, M. J. *Journal of Physical Chemistry B* **1999**, *103*, 5826-5831.
- (86) Lyon, L. A.; Musick, M. D.; Smith, P. C.; Reiss, B. D.; Pena, D. J.; Natan, M. J. *Sensors and Actuators B-Chemical* **1999**, *54*, 118-124.
- (87) Sonvico, F.; Dubernet, C.; Colombo, P.; Couvreur, P. *Current Pharmaceutical Design* **2005**, *11*, 2091-2105.
- (88) Seydack, M. *Biosensors & Bioelectronics* **2005**, *20*, 2454-2469.
- (89) Ward, M. D.; Buttry, D. A. *Science* **1990**, *249*, 1000-1007.

- (90) Wessa, T.; Rapp, M.; Ache, H. J. *Biosensors & Bioelectronics* **1999**, *14*, 93-98.
- (91) Aizawa, H.; Kurosawa, S.; Ogawa, K.; Yoshimoto, M.; Miyake, J.; Tanaka, H. *Sensors and Actuators B-Chemical* **2001**, *76*, 173-176.
- (92) Zhang, C.; Caron, J. J.; Vetelino, J. F. *Sensors and Actuators B-Chemical* **2001**, *76*, 64-68.
- (93) Zimmermann, C.; Rebiere, D.; Dejous, C.; Pistre, J.; Chastaing, E.; Planade, R. *Sensors and Actuators B-Chemical* **2001**, *76*, 86-94.
- (94) Nomura, T.; Saitoh, A.; Horikoshi, Y. *Sensors and Actuators B-Chemical* **2001**, *76*, 69-73.
- (95) Wu, T. Z. *Biosensors & Bioelectronics* **1999**, *14*, 9-18.
- (96) Raiteri, R.; Grattarola, M.; Butt, H. J.; Skladal, P. *Sensors and Actuators B-Chemical* **2001**, *79*, 115-126.
- (97) Hansen, K. M.; Ji, H. F.; Wu, G. H.; Datar, R.; Cote, R.; Majumdar, A.; Thundat, T. *Analytical Chemistry* **2001**, *73*, 1567-1571.
- (98) Wu, G. H.; Datar, R. H.; Hansen, K. M.; Thundat, T.; Cote, R. J.; Majumdar, A. *Nature Biotechnology* **2001**, *19*, 856-860.
- (99) Wu, G. H.; Ji, H. F.; Hansen, K.; Thundat, T.; Datar, R.; Cote, R.; Hagan, M. F.; Chakraborty, A. K.; Majumdar, A. *Proceedings of the National Academy of Sciences of the United States of America* **2001**, *98*, 1560-1564.
- (100) Raiteri, R.; Butt, H. J.; Grattarola, M. *Electrochimica Acta* **2000**, *46*, 157-163.
- (101) Godin, M.; Tabard-Cossa, V.; Grutter, P.; Williams, P. *Applied Physics Letters* **2001**, *79*, 551-553.
- (102) Jensenius, H.; Thaysen, J.; Rasmussen, A. A.; Veje, L. H.; Hansen, O.; Boisen, A. *Applied Physics Letters* **2000**, *76*, 2615-2617.
- (103) Ji, H. F.; Hansen, K. M.; Hu, Z.; Thundat, T. *Sensors and Actuators B-Chemical* **2001**, *72*, 233-238.

- (104) Thaysen, J.; Boisen, A.; Hansen, O.; Bouwstra, S. *Sensors and Actuators a-Physical* **2000**, *83*, 47-53.
- (105) Vijayendran, R. A.; Leckband, D. E. *Analytical Chemistry* **2001**, *73*, 471-480.
- (106) Hawkins, K. R.; Hatch, A.; Chang, H.; Yager, P. *2nd Annual International Conference IEEE-EMBS Special Topic Conference on Microtechnologies in Medicine and Biology, May 2-4, 2002, Madison, Wisconsin, USA* **2002**.
- (107) Cecil, R.; Ogston, A. G. *Biochemical Journal* **1951**, *49*, 105-106.
- (108) Pellequer, J. L.; Vanregenmortel, M. H. V. *Journal of Immunological Methods* **1993**, *166*, 133-143.
- (109) Murthy, G. S. *Current Science* **1997**, *73*, 1097-1103.
- (110) Cumme, G. A.; Bublitz, R.; Ehle, H.; Horn, A. *Journal of Immunological Methods* **1990**, *128*, 241-248.
- (111) Tarun, E. I.; Karaseva, E. I.; Metelitsa, D. I. *Applied Biochemistry and Microbiology* **1997**, *33*, 147-154.
- (112) Munson, M. S.; Hasenbank, M. S.; Fu, E.; Yager, P. *Lab on a Chip* **2004**, *4*, 438-445.
- (113) Munson, M. S.; Hawkins, K. R.; Hasenbank, M. S.; Yager, P. *Lab on a Chip* **2005**, *5*, 856-862.
- (114) Klank, H.; Kutter, J. P.; Geschke, O. *Lab on a Chip* **2002**, *2*, 242-246.
- (115) Jensen, M. F.; Noerholm, M.; Christensen, L. H.; Geschke, O. *Lab on a Chip* **2003**, *3*, 302-307.
- (116) Wang, S. C.; Morris, M. D. *Analytical Chemistry* **2000**, *72*, 1448-1452.
- (117) Soutar, I. In *Multidimensional spectroscopy of polymers : vibrational, NMR, and fluorescence techniques*; Urban, M. W., Provder, T., Eds.; American Chemical Society,: Washington, DC :, 1995.

- (118) Boone, T.; Fan, Z. H.; Hooper, H.; Ricco, A.; Tan, H. D.; Williams, S. *Analytical Chemistry* **2002**, *74*, 78A-86A.
- (119) Wabuye, M. B.; Ford, S. M.; Stryjewski, W.; Barrow, J.; Soper, S. A. *Electrophoresis* **2001**, *22*, 3939-3948.
- (120) Baker, G. A.; Munson, C. A.; Bukowski, E. J.; Baker, S. N.; Bright, F. V. *Applied Spectroscopy* **2002**, *56*, 455-463.
- (121) Owens, C. V.; Davidson, Y. Y.; Kar, S.; Soper, S. A. *Analytical Chemistry* **1997**, *69*, 1256-1261.
- (122) Chen, X. Y.; Clarke, M. L.; Wang, J.; Chen, Z. *International Journal of Modern Physics B* **2005**, *19*, 691-713.
- (123) *Proteins at interfaces : physicochemical and biochemical studies / John L. Brash, editor, Thomas A. Horbett, editor*; American Chemical Society, Washington, DC :, 1987.
- (124) Castner, D. G.; Ratner, B. D. *Surface Science* **2002**, *500*, 28-60.
- (125) Czeslik, C. *Zeitschrift Fur Physikalische Chemie-International Journal of Research in Physical Chemistry & Chemical Physics* **2004**, *218*, 771-801.
- (126) Euston, S. R. *Current Opinion in Colloid & Interface Science* **2004**, *9*, 321-327.
- (127) Sun, S. D.; Yue, Y. L.; Huang, X. H.; Meng, D. Y. *Journal of Membrane Science* **2003**, *222*, 3-18.
- (128) Kidoaki, S.; Matsuda, T. *Colloids and Surfaces B-Biointerfaces* **2002**, *23*, 153-163.
- (129) *Proteins at interfaces II : fundamentals and applications / Thomas A. Horbett, editor, John L. Brash, editor*; American Chemical Society, Washington, DC :, 1995.
- (130) Miller, R.; Fainerman, V. B.; Leser, M. E.; Michel, M. *Current Opinion in Colloid & Interface Science* **2004**, *9*, 350-356.

- (131) Nakanishi, K.; Sakiyama, T.; Imamura, K. *Journal of Bioscience and Bioengineering* **2001**, *91*, 233-244.
- (132) Makamba, H.; Kim, J. H.; Lim, K.; Park, N.; Hahn, J. H. *Electrophoresis* **2003**, *24*, 3607-3619.
- (133) Jordan, C. E.; Corn, R. M. *Analytical Chemistry* **1997**, *69*, 1449-1456.
- (134) Cormack, A. N.; Lewis, R. J.; Goldstein, A. H. *Journal of Physical Chemistry B* **2004**, *108*, 20408-20418.
- (135) Jenkins, J.; Prabhakarandian, B.; Lenghaus, K.; Hickman, J.; Sundaram, S. *Analytical Biochemistry* **2004**, *331*, 207-215.
- (136) Towns, J. K.; Regnier, F. E. *Analytical Chemistry* **1992**, *64*, 2473-2478.
- (137) Shen, Y. F.; Xiang, F.; Veenstra, T. D.; Fung, E. N.; Smith, R. D. *Analytical Chemistry* **1999**, *71*, 5348-5353.
- (138) Sanders, J. C.; Breadmore, M. C.; Kwok, Y. C.; Horsman, K. M.; Landers, J. P. *Analytical Chemistry* **2003**, *75*, 986-994.
- (139) Walhagen, K.; Huber, M. I.; Hennessy, T. P.; Hearn, M. T. W. *Biopolymers* **2003**, *71*, 429-453.
- (140) Popat, K. C.; Desai, T. A. *Biosensors & Bioelectronics* **2004**, *19*, 1037-1044.
- (141) Thomsen, V.; Schatzlein, D.; Mercurio, D. *Spectroscopy* **2003**, *18*, 112-114.
- (142) Eisen, H. N. *Immunology: An Introduction to Molecular and Cellular Principles of the Immune Response*; Harper and Row, Medical Department: Hagerstown, Maryland, 1974.
- (143) Hawkins, K. R.; Yager, P.; UWTT: USA, 2004.
- (144) Hawkins, K. R.; Yager, P., Malmo, Sweden 2004; RSC Press; 129-131.
- (145) Hawkins, K. R.; Yager, P. **2005**.

- (146) Hawkins, K. R.; Yager, P. *Lab on a Chip* **2003**, *3*, 248-252.
- (147) Ellison, E. H.; Thomas, J. K. In *Multidimensional spectroscopy of polymers : vibrational, NMR, and fluorescence techniques*; Urban, M. W., Provder, T., Eds.; American Chemical Society, Washington, DC :, 1995, pp x, 604 p. .:
- (148) Gaigalas, A. K.; Wang, L.; Vogt, R. F. *Photochemistry and Photobiology* **2002**, *76*, 22-28.
- (149) Song, L. L.; vanGijlswijk, R. P. M.; Young, I. T.; Tanke, H. J. *Cytometry* **1997**, *27*, 213-223.
- (150) Moshrefzadeh, R. S.; Misemer, D. K.; Radcliffe, M. D.; Francis, C. V.; Mohapatra, S. K. *Applied Physics Letters* **1993**, *62*, 16-18.
- (151) Ganic, D.; Day, D.; Gu, M. *Optics and Lasers in Engineering* **2002**, *38*, 433-437.
- (152) Lakowicz, J. R. *Principles of fluorescence spectroscopy*; Plenum Press, New York :, 1983.
- (153) Straume, M.; Frasier-Cadoret, S. G.; Johnson, M. L. In *Topics in fluorescence spectroscopy*; Lakowicz, J. R., Ed.; Plenum Press, New York :, 1991, pp 177-.
- (154) Grushka, E.; Levin, S. In *Quantitative analysis using chromatographic techniques*; Katz, E., Ed.; Wiley, New York, , 1987, ch. 9, , pp pp.359-405.
- (155) Golay, M. J. E., Amsterdam 1958; Butterworths Scientific Publications, London.
- (156) Lenghaus, K.; Dale, J. W.; Henderson, J. C.; Henry, D. C.; Loghin, E. R.; Hickman, J. J. *Langmuir* **2003**, *19*, 5971-5974.
- (157) Hawkins, K. R.; Steedman, M.; Fu, E.; Ghosal, S.; Yager, P. *Lab Chip* **2007**, *7*, 281-285.
- (158) Sternberg, J. C. In *Advances in chromatography*; Giddings, J. C., Keller, R. A., Eds.; M. Dekker, New York :, 1966; Vol. 2.



- (159) <http://www.micronics.net>.
- (160) Vahey, P. G.; Smith, S. A.; Costin, C. D.; Xia, Y. N.; Brodsky, A.; Burgess, L. W.; Synovec, R. E. *Analytical Chemistry* **2002**, *74*, 177-184.
- (161) Aris, R. *Proceedings of the Royal Society of London. Series A, Mathematical and Physical Sciences* **1956**, *235*, 67-77.
- (162) Aris, R. *Proceedings of the Royal Society of London. Series A, Mathematical and Physical Sciences* **1959**, *252*, 538-550.
- (163) Sternberg, J. C. In *Advances in chromatography*; Giddings, J. C., Keller, R. A., Eds.; Marcel Dekker; New York, 1966; Vol. 2, pp 205-269.
- (164) Ghosal, S. *Journal of Fluid Mechanics* **2002**, *459*, 103-128.
- (165) Stokes, V. K. *Polymer Engineering and Science* **1989**, *29*, 1310-1324.
- (166) Wool, R. P.; Yuan, B. L.; McGarel, O. J. *Polymer Engineering and Science* **1989**, *29*, 1340-1367.
- (167) Kelly, R. T.; Pan, T.; Woolley, A. T. *Analytical Chemistry* **2005**, *77*, 3536-3541.
- (168) Perez, J. *Physique et mécanique des polymères amorphes. English Physics and mechanics of amorphous polymers / Jo Perez*; A.A. Balkema: Rotterdam ; Brookfield, VT :, 1998.
- (169) Stevens, M. P. *Polymer chemistry : an introduction / Malcolm P. Stevens*, 2nd ed ed.; Oxford University Press: New York :, 1990.
- (170) Liu, R. H.; Yang, J. N.; Lenigk, R.; Bonanno, J.; Grodzinski, P. *Analytical Chemistry* **2004**, *76*, 1824-1831.
- (171) Hawkins, K. R.; Steedman, M.; Fu, E.; Ghosal, S.; Yager, P. *Lab Chip* **2006**, DOI:10.1039/b612894g.
- (172) Lyons, R. G. *Understanding digital signal processing / Richard G. Lyons*; Addison Wesley Pub. Co.: Reading, Mass. :, 1997.

- (173) Stearns, S. D. *Digital signal processing with examples in MATLAB / Samuel D. Stearns*; CRC Press: Boca Raton, Fla. :, 2003.
- (174) Eilers, P. H. C. *Analytical Chemistry* **2003**, *75*, 3631-3636.
- (175) Savitzky, A.; Golay, M. J. E. *Analytical Chemistry* **1964**, *36*, 1627-1639.
- (176) Whittaker, E. T. *Proceedings of the Edinburgh Mathematical Society* **1923**, *41*.
- (177) Martens, H.; Naes, T., 1st ed.; Wiley: New York, 1989.
- (178) Pepys, M. B.; Debeer, F. C.; Dyck, R. F.; Hind, C.; Lanham, J. G.; Fagan, E. A.; Maton, P. N.; Starke, I.; Fox, K.; Allan, R.; Hodgson, H.; Chadwick, V. S.; Hughes, G. R. V.; Goldman, J.; Catovsky, D.; Galton, D.; Krikler, D.; Maseri, A.; Mallya, R. K.; Berry, H.; Hamilton, E. D. B.; Mace, B. E. W. *Annals of the New York Academy of Sciences* **1982**, *389*, 459-460.
- (179) AACC, 2004.
- (180) Danesh, J.; Wheeler, J. G.; Hirschfield, G. M.; Eda, S.; Eiriksdottir, G.; Rumley, A.; Lowe, G. D. O.; Pepys, M. B.; Gudnason, V. *New England Journal of Medicine* **2004**, *350*, 1387-1397.
- (181) Black, S.; Kushner, I.; Samols, D. *Journal of Biological Chemistry* **2004**, *279*, 48487-48490.
- (182) Liu, M.-K.; Li, P.; Giddings, J. C. *Protein Science* **1993**, *2*, 1520-1531.

**VITA**

Kenneth R. Hawkins is a native of San Jose, California, USA. He lived there for the first thirty-four years of his life, before leaving for greener climes. During his time in California, he graduated from Leland High School, attended the University of California at Davis, and San Jose State University – focusing on the sciences (particularly Biology) at each stop. He also worked for thirteen years at Syva Company, manufacturing and developing enzyme amplified immunoassays for various drugs. When circumstance permitted a return to the academy, he completed his Bachelor of Science in Molecular Biology and Biochemistry at University of Oregon in 1997. He completed his Doctor of Philosophy in Bioengineering at University of Washington in 2007.